SANDIA REPORT

SAND2016-11399
Unlimited Release
Printed November 2016

Heat Transfer Phenomena in Concentrating Solar Power Systems

Kenneth M. Armijo (PI) and Subhash L. Shinde (PM)

Prepared by
Sandia National Laboratories
Albuquerque, New Mexico 87185 and Livermore, California 94550

Sandia National Laboratories is a multi-mission laboratory managed and operated by Sandia Corporation, a wholly owned subsidiary of Lockheed Martin Corporation, for the U.S. Department of Energy's National Nuclear Security Administration under contract DE-AC04-94AL85000.

Issued by Sandia National Laboratories, operated for the United States Department of Energy by Sandia Corporation.

Available to DOE and DOE contractors from
U.S. Department of Energy
Office of Scientific and Technical Information
P.O. Box 62
Oak Ridge, TN 37831

Telephone: (865) 576-8401
Facsimile: (865) 576-5728
E-Mail: reports@osti.gov
Online ordering: http://www.osti.gov/scitech

Available to the public from
U.S. Department of Commerce
National Technical Information Service
5301 Shawnee Rd
Alexandria, VA 22312

Telephone: (800) 553-6847
Facsimile: (703) 605-6900
E-Mail: orders@ntis.gov
Online order: http://www.ntis.gov/search

SAND2016-11399
Unlimited Release
Printed November 2016

Heat Transfer Phenomena in Concentrating Solar Power Systems

Kenneth M. Armijo (PI) and Subhash Shinde (PM)
Concentrating Solar Energy Technologies Department
Sandia National Laboratories
P.O. Box 5800
Albuquerque, New Mexico 87185-MS1127

Abstract

Concentrating solar power (CSP) utilizes solar thermal energy to drive a thermal power cycle for the generation of electricity. CSP systems are facilitated as large, centralized power plants, such as power towers and trough systems, to take advantage of economies of scale through dispatchable thermal energy storage, which is a principle advantage over other energy generation systems. Additionally, the combination of large solar concentration ratios with high solar conversion efficiencies provides a strong opportunity of employment of specific power cycles such as the Brayton gas cycle that utilizes super critical fluids such as supercritical carbon dioxide (sCO_2), compared to other solar-fossil hybrid power plants. A comprehensive thermal-fluids examination is provided by this work of various heat transfer phenomena evident in CSP technologies. These include sub-systems and heat transfer fundamental phenomena evident within CSP systems, which includes receivers, heat transfer fluids (HTFs), thermal storage media and system designs, thermodynamic power block systems/components, as well as high-temperature materials. This work provides literature reviews, trade studies, and phenomenological comparisons of heat transfer media (HTM) and components and systems, all for promotion of high performance and efficient CSP systems. In addition, further investigations are also conducted that provide advanced heat transfer modeling approaches for gas-particle receiver systems, as well as performance/efficiency enhancement recommendations, particularly for solarized supercritical power systems.

ACKNOWLEDGMENTS

Sandia National Laboratories is a multi-mission laboratory managed and operated by Sandia Corporation, a wholly owned subsidiary of Lockheed Martin Corporation, for the U.S. Department of Energy's National Nuclear Security Administration under contract DE-AC04-94AL85000. This work was primarily funded by the US Department of Energy Solar Energy Technologies Program. This material is also based upon work partially supported by the U.S. Department of Homeland Security under Grant Award Numbers 2012-DN-130-NF0001-0202 and HSHQDC12X00059. The views and conclusions contained in this document are those of the authors and should not be interpreted as representing the official policies, either expressed or implied, of the U.S. Department of Homeland Security.

TABLE OF CONTENTS

1. INTRODUCTION

Solar thermally generated electricity is a low cost renewable energy source that employs highly-absorptive collectors to gather solar radiation for facilitating temperature power cycles to produce clean and affordable power. Overall conversion (system) efficiency of approximately 35% is feasible with intelligent thermal management [1]. Solar thermal radiation can be collected by different concentrating solar power (CSP) technologies for providing a high temperature heat source. These technologies however differ depending on whether they are line or point-focusing. There is also a distinction between either the distribution of an optical concentrator in the form of small planar fragments and continuous curved concentrators. Contemporarily, the four principal CSP technologies evident in commercialization are shown in Fig. 1.1 by their degree of commercialization (left to right).

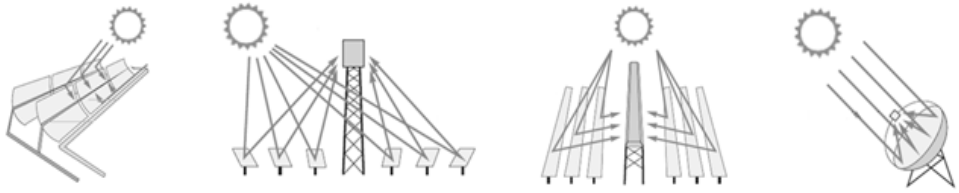

	Parabolic Trough	Central Receiver	Compact Linear Fresnel	Parabolic Dish
Operating Temperature [°C]	**350-550**	**250-565**	**390**	**550-750**
Plant Peak Efficiency [%]	14-20	23-35 Note – 35% achieved with combined cycle	18	30
Annual Capacity Factor [%]	25-28 (no TES) 29-43 (with TES)	55 (with 10h TES)	22-24	25-28
Collection Concentration [suns]	70-80	>1,000	>60 suns (with secondary reflector)	>1,300
Steam Conditions [°C/bar]	380-540 / 100	540 / 100-160	260/50	N/A
Water Requirement [m^3/MWh]	3 (wet cooling) 0.3 (dry cooling)	2-3 (wet cooling) 0.25 (dry cooling)	3 (wet cooling) 0.2 (dry cooling)	0.05-01 (mirror washing)

Figure 1.1. Principal CSP technologies used within industrial practice [2, 3].

In a CSP plant heat is used to operate a conventional power cycle, such as Rankine (stem engine), Brayton (gas turbine engine) or Stirling engine [1]. Stored heat can then be used during nighttime or overcast conditions for power generation. A simple overall schematic for a typical CSP system can be seen in Fig. 1.1, which describes the main general elements.

Typical market categories for CSP vary between small (<100 kW), medium (<10 kW) and large (>10 MW) where the systems can be composed of combinations of different collectors, power cycles and also thermal storage technologies. A CSP system processes heat like conventional power plants where the efficiency depends on the operating temperature. Therefore, the useful energy produced will depend on solar field collection and power cycle efficiencies as depicted in Fig. 1.2.

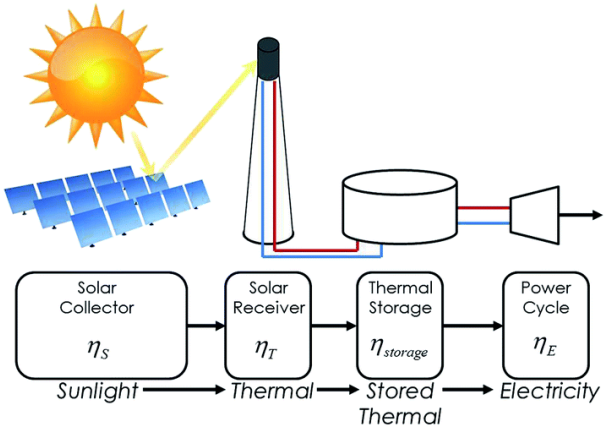

Figure 1.2. Main components of a Concentrating Solar Power (CSP) System [4].

Concentrated solar power systems use mirrors or lenses to concentrate a large area of sunlight, or solar thermal energy, onto a small area. Electrical power is produced when the concentrated light is converted to heat which drives a heat engine (usually a steam turbine) connected to an electrical power generator. Unlike the photovoltaic solar cells, converting energy from sunlight to electricity by CSP systems is based on the application of heat engine rather than photovoltaic effect which is directly transfer photon energy into electricity energy.

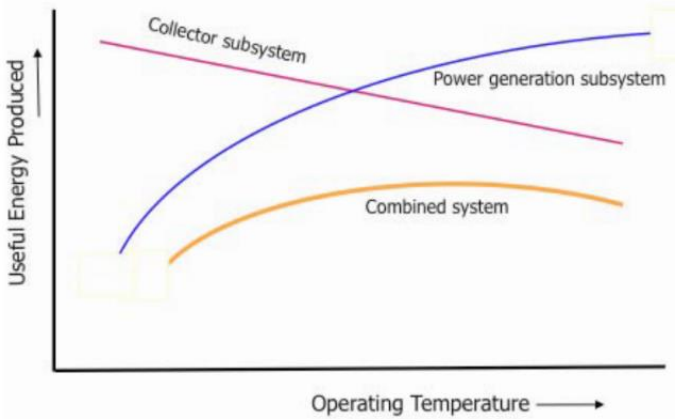

Figure 1.3. CSP system efficiency variation with operating temperature [1].

The collectors concentrate and collect solar thermal energy which is used to generate vapor that runs heat engines to produce electricity. The theoretical maximum efficiency that can be achieved is determined by the Carnot's cycle, where the efficiency of a heat engine is determined by the difference between the lowest and highest temperatures reached in one cycle. However, thermal losses of the solar receiver increase with the fourth power of its surface temperature [5], therefore, efficiency gains of the power block from a higher temperature can be potentially negated by the increasing thermal losses from the receiver due to higher temperatures. Therefore, the maximum efficiency can be increased and shifted towards higher temperatures when solar irradiation is further concentrated by CSP collectors. However, thermal losses remain constant for the same receiver surface area despite yielded solar power increasing. This is what allows CSP systems with higher concentration ratios to achieve higher system efficiencies. This is illustrated by Fig. 1.4 which presents CSP systems with varying concentration ratios and their respective maximum system efficiencies with respect to Carnot.

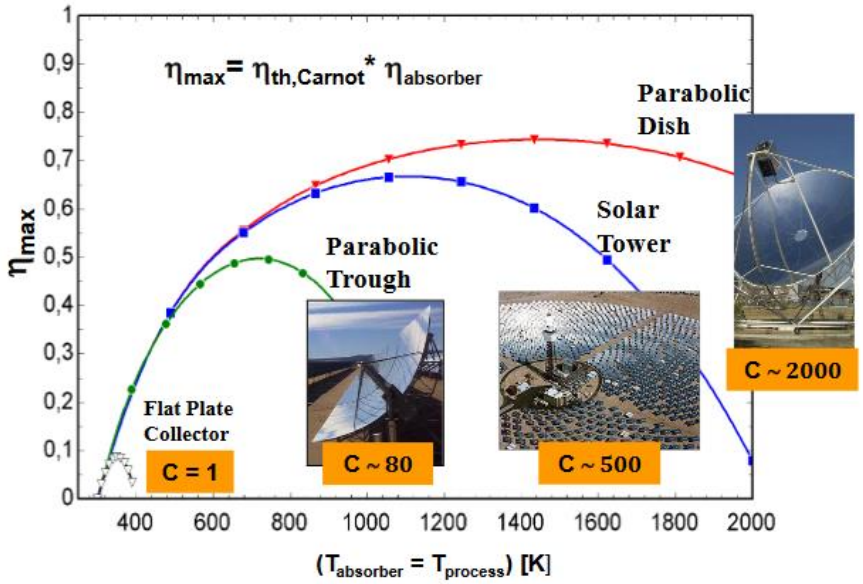

Figure 1.4. CSP technology theoretical efficiencies with respect to concentration ratio and absorber temperature [6].

Since the 2012 SunShot Vision Study, global deployment of concentrating solar power (CSP) has increased threefold to nearly 4,500 MW, with a similar threefold increase in operational capacity to 1,650 MW within the United States. Fig. 5 demonstrates that this deployment has led to dramatic cost reductions that have placed CSP well on the path to reaching the U.S. Department of Energy (DOE) SunShot Initiative goal of 6 cents/kWh by 2020 [8]. However enhanced power conversion systems are needed for responding to ever-increasing energy demands for the U.S. and globally. Efficiency in CSP systems is key for producing the most power for the smallest investment. A Brayton cycle typically operates at higher temperatures and pressures, which improves the overall efficiency compared to more universally-used Rankine cycle systems.

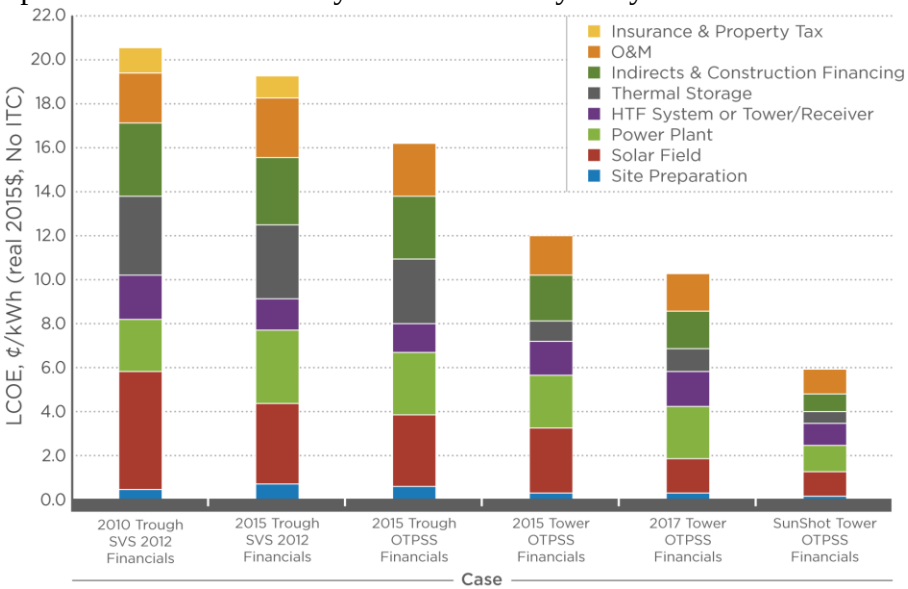

Figure 1.5. Cost reductions for parabolic trough and tower technologies since the original SunShot Vision Study (SVS) [7].

Brayton systems can be furthered improved through the employment of supercritical fluids such as water, carbon dioxide and helium that can avoid fundamental boiling/condensing phase change issues, as well as increasing Carnot temperature differences within the cycle. Incorporation of thermal energy storage is the key advantage of CSP plants and can be used to produce electricity when the sun is not shining. The round-trip efficiency of thermal storage can be very high ($\geq$ 99%), and costs are low relative to alternatives such as battery storage. SunShot goals for thermal storage include power-cycle inlet temperature $\geq$ 650 °C, energetic efficiency $\geq$ 99%, exergetic efficiency $\geq$ 95%, and a cost $\leq$ \$15/kW$_{th}$.

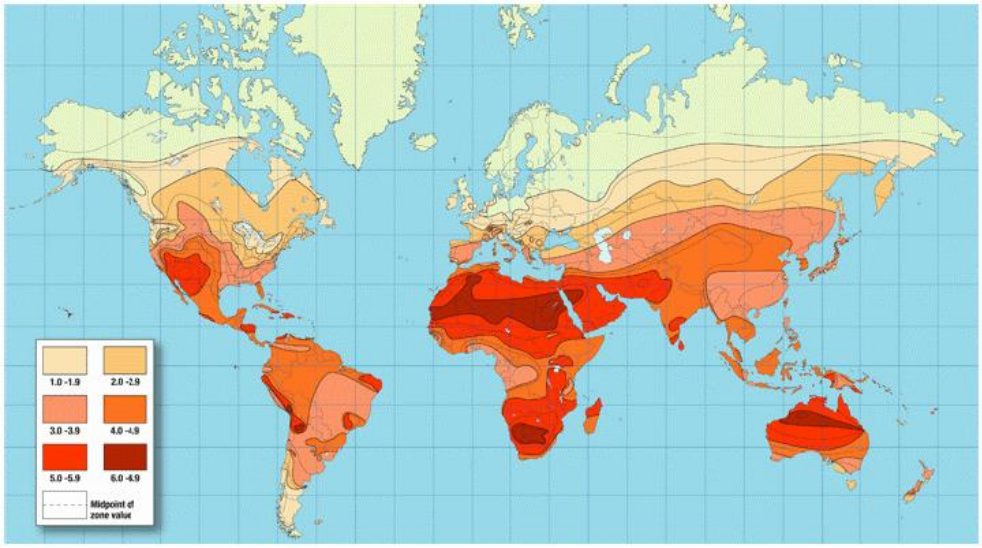

Figure 1.6. The solar insolation (kWh/m^2/day) on an optimally tilted surface. [1].

The potential for CSP implementation in any given geographic location is largely determined by the local solar radiation potential. Fig. 1.6 shows average solar insolation distributions globally for an optimally tilted surface during the strongest month of the year [6,7]. Regions represented by light and dark red colors are most suitable for CSP implementation, based on irradiance, measured in W/m^2.

The daily variation of the different components depends upon meteorological and environmental factors (e.g. cloud cover, air pollution and humidity) and the relative earth-sun geometry. The direct normal irradiance (DNI) is synonymous with the direct beam radiation and it is measured by tracking the sun throughout the sky. Fig. 1.3 shows an example of the global solar radiation that is measured on a stationary two flat plate and a plate that is tracking the sun. The measured DNI is also included and its lower value can be attributed to the fact that it does not account for the diffuse radiation component.

In CSP applications, DNI is important in determining available solar energy as its value is determined only by incident normal radiation, where collectors are designed to track the sun throughout the day. Fig. 1.7 shows the daily solar insolation on an optimally tilted surface during the worst month of the year around the world [6,7]. Regions represented by light and dark red colors are most suitable for CSP implementation. The annual DNI value will also greatly influence the levelized cost of electricity cost (LCOE), which will be discussed later. Typical values of DNI at different latitudes and selected locations around the world are given in Figure 6 and Table 1. Based on the information presented here it can be seen that desert and equatorial regions appear to provide the best resources for CSP implementation.

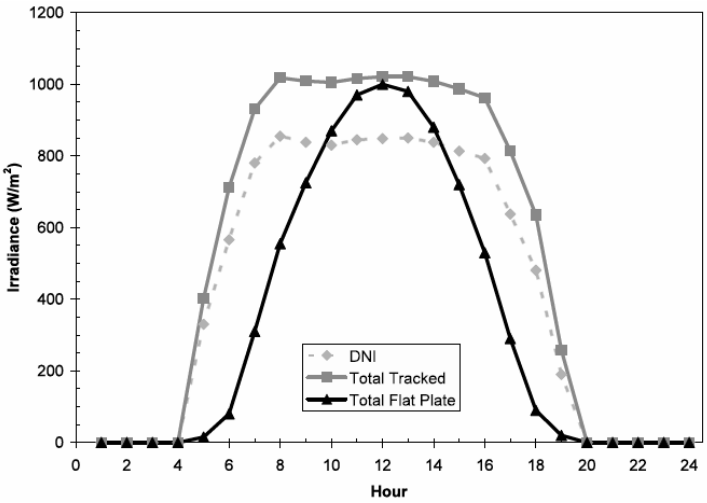

Figure 1.7. Solar irradiance variation within a day measured on a flat plate positioned horizontal and tracking system the sun and direct normal irradiance (DNI) [1, 8].

Equivalent radiation temperature of the sky depends on the air density and its moisture content. When the relative humidity is high and at sea level, the sky temperature can be assumed to be the same as ambient air temperature. However, for low relative humidity or at high altitudes, the sky radiation temperature can be 6 to 8 °C less than ambient temperature. If there is no atmosphere as with space applications, the equivalent sky temperature approaches 0 K.

For this work, radiation and other heat transfer principles will be discussed in a comprehensive overview for providing insight into the primary mechanisms of thermal-fluid behavior in CSP systems. In the subsequent chapters, a broad discussion will follow that provides the reader with greater detail of heat transfer phenomena and system-level design details for various CSP receivers currently in operation, as well as advanced concepts and design. Following this discussion, further heat transfer properties and general operational characteristics will be covered for a variety of heat transfer and working fluids employed in CSP and respective power block systems. These chapters will cover not just the ability for these fluids to transfer thermal energy, but also to store it. This dialogue will then be followed by two chapters that provide insight into current and advanced thermodynamic systems employed in CSP systems as well as heat transfer characteristics of components within the power block, for enhancing performance and reliability to further promote ubiquitous adoption of CSP for electrical energy generation.

2. CSP HEAT TRANSFER PRINCIPLES

Throughout the various stages of the CSP plant, heat transport is optimized to maximize conversion of solar heat to mechanical work by reducing thermal and optical losses. Fundamentally, an optimal CSP system design combines a relatively large, efficient optical surface (e.g., a field of high-reflectivity mirrors), harvesting incident solar radiation and concentrating it onto a solar receiver with a relatively small aperture area. To facilitate nominal CSP power generation ideal solar receivers would have negligible convection and conduction losses, where heat transfer to the rest of the solar thermal power plant is facilitated through maximum heat exchange to a working fluid with an outlet temperature high enough to feed a heat engine that produces electricity. For any heat transfer component, there are three principal modes of heat transfer: conduction, convection, and radiation where any energy exchange between bodies occurs through these modes or in combination based on temperature differences.

2.1 Radiation Heat Transfer

Radiation is energy emitted by a solid object, liquid or gas that is at a finite temperature. This matter can also dissipate radiant energy impinging on it by reflection and can be capable of absorption. For thermal energy processes there are several solar flux types which are illustrated in Fig. 2.1, where it is convenient to generalize by two wavelength ranges [9] short wavelength and long wavelength. Short wavelength radiation originates from the sun or high-temperature sources whereas long wavelength radiation typically originates from lower-temperature sources and is emitted in proportion to temperature to the fourth power.

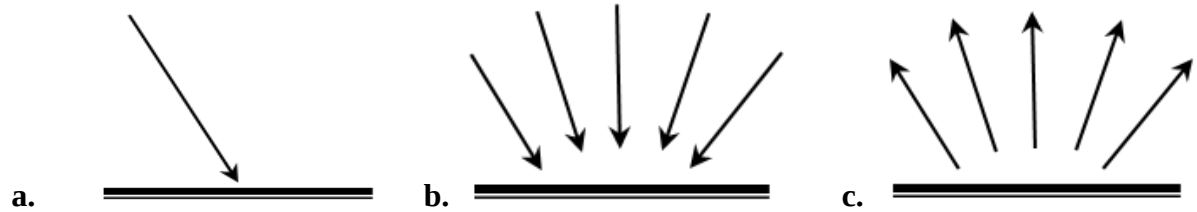

Figure 2.1. Radiation energy flux types which include a. direct beam radiation, b. diffuse radiation and c. reflected radiation.

Solar radiation at normal incidence, and at a particular surface on earth is subject to variations of extraterrestrial radiation, as well as atmospheric scattering and absorption by air molecules, water, dust and aerosols as described by Armijo *et* al. [10]. An illustrative description of irradiance attenuation from that of extraterrestrial irradiance, by various atmospheric aerosols and water, is shown in Fig. 2.2. For PV technologies the spectral response of a particular cell material can be susceptible to power generation reduction due to these atmospheric components; however, CSP is much more spectrally robust as it employs a significantly broader spectrum for power generation.

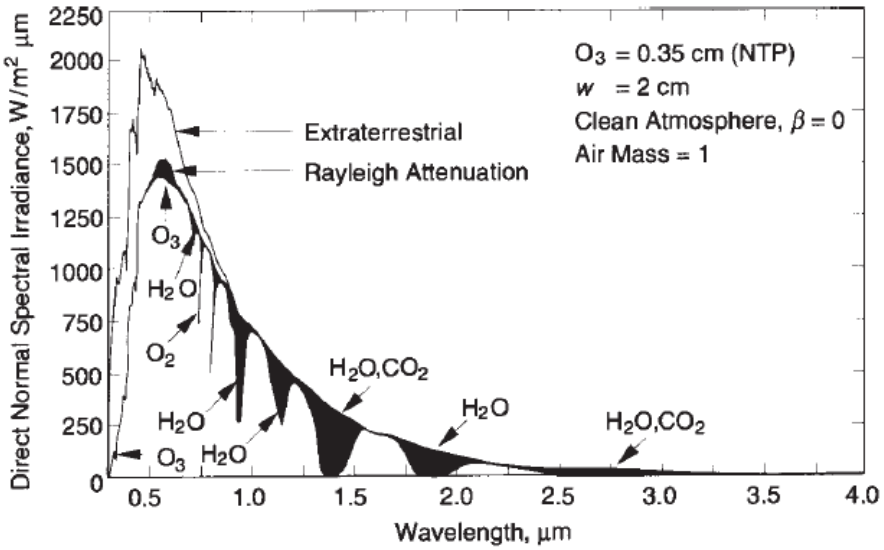

Figure 2.2. Solar irradiance spectrum comparison between extraterrestrial and atmospherically-attenuated irradiance with an air mass (AM) equal to unity [11].

Heat is also transferred by direct contact with solid objects (conduction), movement of air that carries heat away from the object (convection or sensible heat), and latent heat exchange in which heat is dissipated through a change in water from liquid to gas. The radiation that impinges on a surface or object must be conserved by the energy radiated back to the ambient, gained by sensible (conduction)/latent heat (convection) or thermal energy storage [458]. Accordingly, this radiation energy balance can be defined as:

$$(1-r)S\downarrow + L\downarrow = L\uparrow + H + \lambda E + G \tag{2.1}$$

The left side of the equation consists of absorbed solar radiation $(1-r)S\downarrow$ and longwave radiation ($L\downarrow$). The right side of the equation consists of the emitted longwave radiation ($L\uparrow$), sensible heat (H), latent heat (λE) and heat exchange by conduction (G) [458]. Therefore, the net radiation absorbed by an object is:

$$R_n = (1-r)S\downarrow + (L\downarrow - L\uparrow) = H + \lambda E + G \tag{2.2}$$

Net radiation (R_n) is balanced by sensible, latent and conduction heat transfer, where all surfaces except for those that are blackbody reflect or transmit sunlight. This amount is equal to rS, where S is the incident radiation onto the surface where r is defined as the fraction of S that is reflected by the surface [458]. The remainder term, $(1-r)S$, is the solar radiation absorbed by the surface. Emission of longwave radiation is a second means of radiative cooling. Terrestrial objects emit electromagnetic radiation in the infrared band at long wavelengths between 3 μm-100 μm. This emission is proportional to temperature raised to the fourth power, where the units are with respect to degrees Celsius:

$$L\uparrow = \varepsilon\sigma(T_s + 273.15)^4 \tag{2.3}$$

where σ = 5.67x10^{-8} W/m^2-K^4 is the Stefan-Boltzmann constant and emissivity, ε of an object generally ranges from 0.8-1.0 which is the emissivity of a blackbody. Most natural surfaces are considered "grey" which have an emissivity less than unity. However, unlike conduction and

convection, which require the presence of a temperature gradient in some form of matter to facilitate heat transfer, radiation heat transfer does not require matter and is an extremely relevant to many industrial processes that involve combustion and solar energy. The mechanism of radiative emission is related to the energy released as a result of oscillations or transitions of many electrons that constitute matter. These oscillations are sustained by internal energy and therefore the temperature of matter, where all forms of matter emit radiation [12]. For gases and semitransparent solids, such as glass and salt crystals at elevated temperatures, emission is a volumetric phenomenon, where the radiation that emerges from a finite volume of matter is the integrated effect of local emission throughout the volume. For the majority of liquids and solids radiation emitted from interior molecules is strongly absorbed by adjoining molecules, where this emitted radiation originates from molecules that are within a distance of approximately 1 μm from an exposed surface. Therefore, emission, or absorption, from solids or liquids into an adjoining gas or vacuum can be assessed as a surface phenomenon [12].

Sunlight, in the broad sense, is the total spectrum of the electromagnetic radiation given off by the Sun. Thermal radiation may be viewed as the transport of photons or the propagation of an electromagnetic wave, where for the propagation of radiation into a medium the frequency and wavelength are related as:

$$\lambda = \frac{c}{v} \tag{2.4}$$

where c is the speed of light in the medium, λ is the wavelength, and v is the frequency. For a vacuum the propagation of radiation follows that $c = 2.998 \times 10^8$ m/s. The complete electromagnetic spectrum is presented by Fig 2.3, where between approximately 0.1 to 100 μm thermal radiation is pertinent to heat transfer.

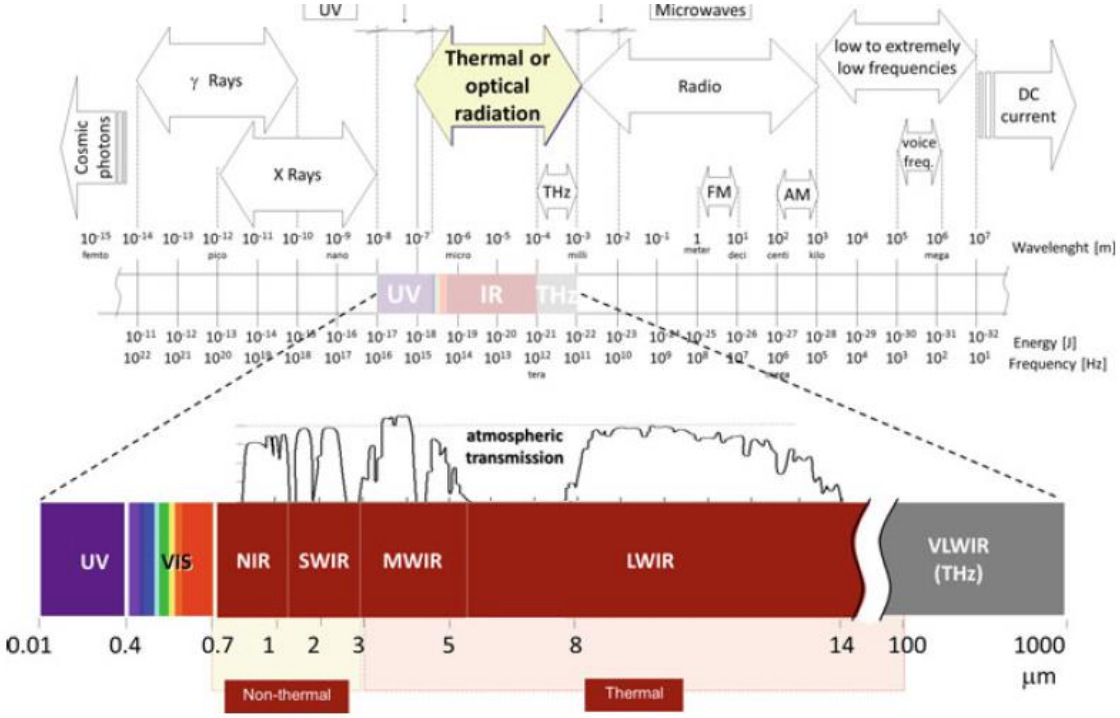

Figure 2.3. Thermal infrared radiation bands within the electromagnetic spectrum **[**13]

The thermal radiation band includes a portion of UV, all of the visible, as well as the IR which can be broken into four different subsections. First, the near infrared (NIR) band extends from 0.7 to

1 μm, while short-wave IR (SWIR) extends from 1 to 2.5 μm, where these spectra are generally the result of reflections from objects, which are similar radiation in the visible spectrum, however both NIR/SWIR light are not visible to humans, and can be considered as a non-thermal form of infrared radiation **[**13]. The mid-wave infrared (MWIR) region extends from 3 to 5 μm and the long-wave infrared (LWIR) extends from 7.5 to 14 μm, where both radiation spectra bands originate from an object's surface thermal emissions, and not reflections. Both MWIR and LWIR are considered the primary sources of thermal radiation. In addition, the terahertz region, which is between 100 and 1000 μm (0.3–30 THz), is part of the very long-wave infrared (VLWIR), from 14 to 1000 μm, where this radiation can be considered as a special case of thermal infrared radiation, sharing some properties with the infrared and others from the microwave bands **[**13]. In general, emitted radiation consists of a continuous, non-uniform distribution of monochromatic wavelength spectra, where the magnitude of the radiation at any wavelength, as well as the spectral distribution vary with temperature and directionality of the emitting surface [12]. Although radiation emitted by a surface propagates in all directions, radiation incident onto a surface may come from different directions, which can influence the surface response. For a radiative emitting surface of an arbitrary element of area dA_1 a differential solid angle dω may subtend a point onto a differential area dA_2 as shown in Fig. 2.4.

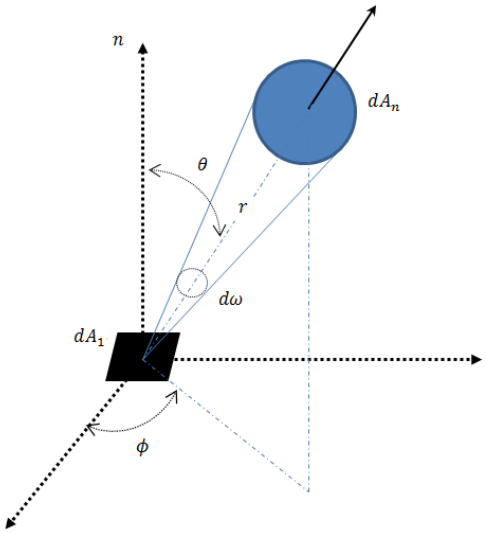

Figure 2.4. Radiation emission from an arbitrary differential element dA_1 into a solid angle dω subtended by dA_n at a point on dA_1 [12].

This direction can be specified in terms of zenith, θ and azimuth, ϕ angles of a spherical coordinate system. Additionally, if the midpoint within dA_2 were a sphere, the differential solid angle dω can be defined by a region between the rays of the sphere and measured as the ratio of the element area dA_2 on the sphere to the square of the sphere's radius as prescribed by Eqn. 2.5.

$$d\omega = \frac{dA_2}{r^2} \tag{2.5}$$

In contrast, as shown in Fig. 2.4 incident radiation from the area dA_2 can also subtend a solid angle dω onto a surface dA_1, where it can be related to a radiative flux or irradiation, which encompasses radiation incident from all directions [12]. With respect to wavelength, spectral irradiation G

(W/m^2-μm) is defined as the rate at which radiation of wavelength λ is incident on a surface per unit surface area and unit wavelength interval dλ about λ, Eqn. 2.6.

$$G_\lambda(\lambda) = \int_0^{2\pi} \int_0^{2\pi} I_\lambda(\lambda, \theta, \phi) cos\theta d\omega \tag{2.6}$$

where the unit solid angle dω = sinθdθdφ. If the total irradiation is taken with respect to the rate at which radiation is incident per unit area from all directions and all wavelengths, then one is provided:

$$G = \int_0^{\infty} G_\lambda(\lambda) d\lambda \tag{2.7}$$

However, if the incident radiation is diffuse, $I_\lambda(\lambda)$ is therefore independent of θ and φ, where it follows that:

$$G_\lambda(\lambda) = \pi I_\lambda(\lambda) \tag{2.8}$$

For radiation leaving a surface radiosity encompasses the reflected portion of irradiation, in addition to direct emission as shown by Fig. 2.5. Spectral radiaosity J_λ (W/m^2-μm) represents the rate at which radiation of wavelength λ leaves a unit area of the surface, per unit wavelength interval dλ. This parameter assumes surface radiation to leave in all directions and is related to the intensity associated with emission *e*, and reflection *r*, $I_{\lambda,e+r}(\lambda, \theta, \phi)$ by the expression:

$$J_\lambda(\lambda) = \int_0^{2\pi} \int_0^{2\pi} I_{\lambda,e+r}(\lambda, \theta, \phi) cos\theta sin\theta d\theta d\phi \tag{2.9}$$

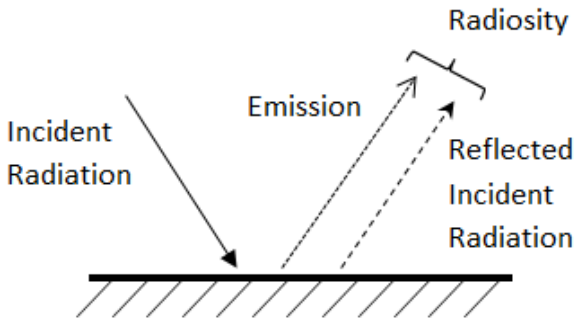

Figure 2.5. Graphical representation of surface radiosity [12].

In general, all incoming radiation must be reflected, absorbed or transmitted according to:

$$\rho_\lambda + \alpha_\lambda + \tau_\lambda = 1 \tag{2.10}$$

where for heat transfer applications, the dependence on incoming direction for absorptivity (as well as reflectivity and transmissivity) and outgoing direction for emissivity is generally weak and is commonly neglected, where it is assumed that the surface absorbs and emits diffusely. Therefore, for an opaque surface for any given wavelength the following expression can be applied:

$$\varepsilon_\lambda = \alpha_\lambda = 1 - \rho_\lambda \tag{2.11}$$

where the following definitions can be defined for the four fundamental radiative properties:

Reflectivity: $$\rho = \frac{reflected\ portion\ of\ incident\ radiation}{total\ incident\ radiation} \quad (2.12)$$

Absorptivity: $$\alpha = \frac{absorbed\ portion\ of\ incident\ radiation}{total\ incident\ radiation} \quad (2.13)$$

Emissivity: $$\varepsilon = \frac{emitted\ portion\ of\ incident\ radiation}{total\ incident\ radiation} \quad (2.14)$$

Transmissivity: $$\tau = \frac{transmitted\ portion\ of\ incident\ radiation}{total\ incident\ radiation} \quad (2.15)$$

When assessing real surfaces, blackbody radiation serves as a standard against which radiative properties of actual surfaces can be compared. Blackbody surfaces are perfect absorbers and emitters where $\alpha = \varepsilon = 1$, and where its emitted radiation is taken with respect to wavelength, independent of direction. Cavities with small apertures can be closely approximated as a blackbody, especially if its inner surface is at a uniform temperature where entering radiation is likely to experience many reflections before it can reemerge back to the ambient.

For surfaces with a prescribed temperature *T*, its emissivity is defined as the ratio of the radiation emitted by the surface to the radiation emitted by a blackbody at the same temperature. With respect to wavelength and direction, this parameter may be defined in terms of radiation intensity by:

$$\varepsilon_{\lambda,\theta}(\lambda,\theta,\phi,T) = \frac{I_{\lambda,e}(\lambda,\theta,\phi,T)}{I_{\lambda,b}(\lambda,T)} \quad (2.16)$$

For inclined surfaces, Fig. 2.6, the angle of incidence for surfaces sloped due north or due south can be determined with respect to the angle of inclination β, which has the same angular relationship to direct beam radiation as a horizontal surface does at an artificial latitude of $\phi - \beta$, where ϕ is the respective latitude. Therefore, the angle of incidence can be determined for the northern and southern hemispheres respectively by:

$$cos\theta = cos(\phi - \beta)cos\delta cos\omega + sin(\phi - \beta)sin\delta \quad (2.17)$$

$$cos\theta = cos(\phi + \beta)cos\delta cos\omega + sin(\phi + \beta)sin\delta \quad (2.18)$$

A more detailed description of these derived equations can be found by [14]. As prescribed by Duffie and Beckman [14] it is possible to increase the radiation incident on an absorber by use of planar reflectors, where the amount of radiation received from the reflector is a function of the view factor. A view factor is traditionally defined as the fraction F_{rc} of the radiation leaving a reflective surface A_r that is intercepted by a collector surface A_c. A reciprocity expression expressed by Eqn. 2.19 is also useful in determining one view factor from another.

$$A_r F_{rc} = A_c F_{cr} \quad (2.19)$$

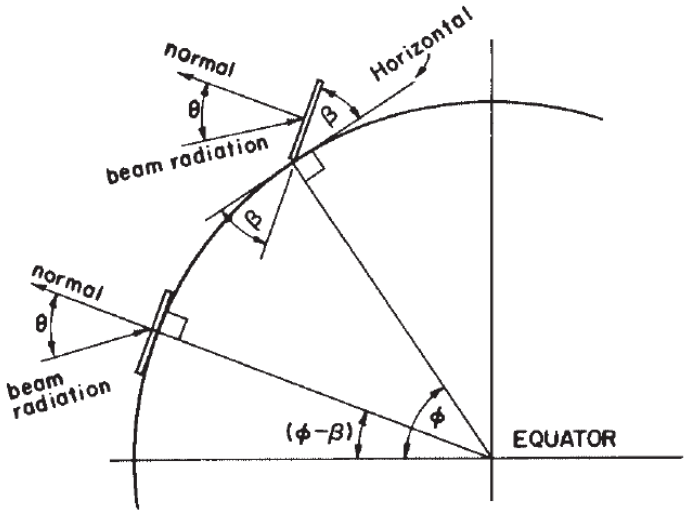

Figure 2.6. Solar collector reference angles with respect to the equator with respect to a northern hemisphere orientation [14].

As shown in Fig. 2.7, if one considers these two intersecting planes with an angle between the planes ψ, then the summation of the view factors must equal 1, as prescribed by Eqn. 2.20.

$$F_{rs} + F_{rc} + F_{rg} = 1 \tag{2.20}$$

where *s* and *g* represents the projected sky and ground respectively, and where *n* and *p* represent the respective lengths of the collector and reflector.

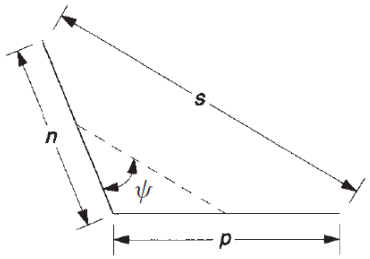

Figure 2.7. Cross-section of a collector and reflector [14].

Finally, in general for most engineering heat transfer applications Eqn. 2.21 is employed to characterize the radiative heat transfer interaction between an object and its environment with respect to wavelength.

$$\dot{Q}_{rad} = \sigma \varepsilon_{\lambda} A (T^4 - T_{\infty}^4) \tag{2.21}$$

where σ is the Stefan-Boltzmann constant, 5.67x10^{-8} W/m^2-K^4, A is the object surface area and T_{∞} is the ambient temperature.

2.2 Conduction Heat Transfer

Thermal conduction heat transfer through solids or stationary fluids occurs by a combination of two physical mechanisms: lattice vibration and particle collision. Heat is conducted through stationery fluids primarily by molecular collisions while in solids atoms are bound to each other by a series of molecular bonds. When there is a temperature difference in a solid, the hot side of the solid experiences more vigorous atomic movements which transfer thermal energy through vibrational motion. Eventually both hot and cold sides reach thermal equilibrium, where all atoms are vibrating with the same energy. Dense solids, especially metals have free electrons and are not bound to any particular atom where they can freely move. The electrons within the hot side of a solid will tend to move faster than those on the cooler side, and as the electrons undergo a series of collisions, faster electrons give off their energy to slower ones. Eventually, after many progressive collisions, equilibrium is reached where the majority of all electrons are moving at the same average velocity. Conduction through electron collision is more effective than by lattice vibration, which justifies why metals are generally better thermal conductors than ceramic materials, which do not have many free electrons [15]. In fluids the conduction mechanism is similar to metals where collisions between freely moving molecules facilitate heat transfer. The effectiveness by which heat is transferred through a material is measured by its respective thermal conductivity, *k*. A good conductor, such as copper, has a high thermal conductivity, whereas a poor conductor (an insulator) has a low thermal conductivity. The rate of heat transfer by conduction is given by Fourier's Law:

$$\dot{Q}_{cond} = kA\frac{dT}{dx} \tag{2.22}$$

where A is the cross-sectional area through which the heat is conducting, ΔT is the temperature difference between two surfaces separated by a distance dx. In heat transfer, a positive q indicates that heat is flowing into the body, and a negative q represents heat leaving the body.

For many CSP applications, heat transfer can be time dependent in nature for which unsteady or transient initial and boundary conditions apply. If the surface temperature of a system is altered, the temperature at each point in the system will also begin to change until a steady-state temperature distribution is reached. In certain situations, temperature gradients within a solid object can be approximately neglected where a lumped capacitance method may be applied to determine the variation of temperature with respect to time. For simple situations for which sudden changes in an environment facilitates transient conduction through an object initially at a uniform initial temperature T_i to a lower surrounding fluid environment at T_∞ the temperature of the solid will decrease for time $t > 0$ until it reaches the ambient temperature. This reduction is due to convection at the solid-liquid interface, where the lumped capacitance method can be utilized as long as the solid is spatially uniform at any instant during the transient process, but only for which the approximation that temperature gradients though the solid are negligible. To determine the time required for a solid to reach a steady state temperature T, Eqn. 2.23 can be used in this context of lumped capacitance.

$$\frac{T-T_\infty}{T_i-T_\infty} = exp\left(-\frac{hA_s}{\rho V C_p}t\right) \tag{2.23}$$

where the thermal time constant τ can be considered according to:

$$\tau = \frac{\rho V C_p}{h A_s} = RC \tag{2.24}$$

such that *R* is the resistance to convection and *C* is the lumped thermal capacitance of the solid, which can slow the response of the solid to its thermal environment as these values increase, analogous to an RC electrical circuit where a capacitive discharge through a resistor can facilitate a voltage decay. To determine if the lumped capacitance approximation is valid, the Biot number, Bi can be computed according to the form:

$$Bi = \frac{hL_c}{k} = \frac{R_{cond}}{R_{conv}} = \frac{L_c/kA}{1/hA} = \frac{Conduction\ Thermal\ Resistance}{Convection\ Thermal\ Resistance} = \frac{T_{s,1} - T_{s,2}}{T_{s,2} - T_\infty} \tag{2.25}$$

If the Biot number is less than 0.1 for a solid object, then the entire material will be nearly the same temperature with the dominant temperature difference will be at the surface where it can be considered to be thermally thin. The Biot number must generally be less than 0.1 to use the lumped capacitance approximation. This mathematical solution to the lumped system approximation provides the basis for Newton's law of cooling [12]. Finally, with the definition of the *Bi* number provided by Eqn. 2.25, rearrangement of Eqn. 2.23 provides Eqn. 2.26.

$$\frac{T - T_\infty}{T_i - T_\infty} = exp(-Bi \cdot Fo) \tag{2.26}$$

Here the parameter, *Fo* is dimensionless time which characterizes transient conduction problems that also has the form:

$$Fo = \frac{\left(\frac{k}{\rho C_p}\right) \cdot t}{L_c^2} \tag{2.27}$$

where L_C is the characteristic length which is defined according to its geometry, Table 2.1.

Table 2.1. Characteristic length based on geometry.

Rectangular	**Cylindrical**	**Spherical**
$L_C = \frac{V_{Rec}}{A_{Rec}} = \frac{L^3}{L^2} = L$	$L_C = \frac{V_{Cyl}}{A_{Cyl}} = \frac{\pi r^2 l}{2\pi r l} = \frac{r}{2}$	$L_C = \frac{V_{Sphere}}{A_{Sphere}} = \frac{{}^4/_3\,\pi r^3}{4\pi r^2} = \frac{r}{3}$

Under conditions for which temperature gradients aren't negligible, where 1D heat transfer is facilitated, exact heat equation solutions may be used to compute the temperature dependence with respect to time and space. These solutions exist for "finite solids" (plane walls, long cylinders with small wall thickness, and spheres) and semi-infinite solids [12].

In general, for good conductors with metallic bonds, electrons from each atom are not bound to any particular atom where they are very loosely held as free electrons, and can move throughout the metal material. Free electrons carry heat across a material very quickly through rapid collisions, where one electron gives some of its energy to another. In contrast, insulators do not collide as rapidly with each other and if the material is solid, then its electrons are going to be tightly held via covalent or ionic bonds. Gases and porous solids with large air-containing voids

can make the best insulators. Table 2.2 provides a list of common materials with their respective thermal conductivities.

Table 2.2. Approximate thermal conductivity and heat capacities of common industrial materials at 25 °C and 1 atm [16].

Material	Thermal Conductivity [W/m-K]	Heat Capacity [kJ/kg-K]
Aluminum	238	0.91
Copper	397	0.39
Gold	314	0.13
Iron	79.5	0.45
Silver	427	0.71
Brass (70% Cu, 30% Zn)	111	0.38
Bronze (75% Cu, 25% Sn)	26	0.435
Steel (Max 0.5% C)	36	0.49
Fiberglass	0.042	0.70
Concrete	1.3	0.88
Glass	0.084	0.84
Rubber	0.2	2.01
Brick	0.71	0.84
Sodium (s)	134	1.21
Potassium	100	0.75
Titanium	19-23	0.21
Nickel	90	0.44
Tin	62-68	0.21
Magnesium	159	1.05
Inconel	8-15	0.46
Hastelloy B	10	0.38
Haynes 230	8.9	0.40
Water (l)	0.6	4.18
Wood	0.1	1.76
Sand	0.15-0.25	0.29
Air	0.0234	1.02
Argon	0.016	0.52
Helium (g)	0.138	5.19
Nitrogen (g)	0.0234	1.04

When heat is added to a system, particles gain kinetic energy and since their average kinetic energy increases, the temperature increases. Since these particles have increased their kinetic energy, they move faster and further, where each particle takes up more room, so the material as a whole expands in all directions while the mean free path can grow.

Finally, it is important to design with respect to material expansion coefficient differences between adjacent materials, as a function temperature to reduce the onset of mechanical stress. There are effectively three types of thermal expansion that can occur during operation: linear, area and volume. If an arbitrary linear rod is heated up or cooled down, the rod will expand or contract respectively, where thermal linear expansion is defined by Eqn. 2.28:

$$\Delta L = \alpha L_0 \Delta T \tag{2.28}$$

such that ΔL is the change in length, α is the coefficient of linear expansion, L_0 is the original length of the rod, and ΔT is the temperature difference across the material. The change in length of a rod is directly proportional to the temperature difference in the material and the coefficient of thermal linear expansion. For a heated surface and volume, the coefficient αL_0 from Eqn. 2.28 is converted to 2 αA_0 and βV_0.

2.3 Convection Heat Transfer Systems

Convection heat transfer occurs between a fluid in motion and a bounded surface or secondary fluid, when the two are at differing temperatures. It may be classified according to the nature of the fluid flow where forced convection occurs due to external means such as a pump, a fan or mechanical energy source that facilitates motion as opposed to natural convection (or free) which is facilitated by buoyancy forces that arise from density differences. With natural convection fluid movement is created by the warm fluid itself. The density of the fluid decreases as it is heated; thus, hot fluids are lighter than those that are cooler. Here warm fluid surrounding a hot object then rises and is replaced by the cooler fluid, resulting in circulation. Although systems can be analyzed from a standpoint of natural or forced convection, often mixed convection conditions arise where velocities associated with a flow are small and/or buoyancy forces are large, and a secondary flow that is comparable to the imposed forced flow could be induced. The buoyancy-induced flow would be normal to the forced flow and could have a significant effect on convection heat transfer. Additionally, the impacts of mixed convection could also be represented by an external fan which could force fluid upward which would assist buoyancy, whereby a downward forced convective flow would hinder it. For these examples convective heat transfer is described by energy transfer occurring within the fluid due to combined effects of fluid conduction and bulk fluid motion where energy that is transferred is wither sensible or internal fluid energy. However, during phase change processes between a liquid to a vapor, latent heat exchange energy is added or removed based on the respective process of boiling or condensation. For any type of convection, the magnitude of heat exchange can be measured by the heat exchange coefficient h, prescribed by the rate Eqn. 2.29:

$$\dot{Q}_{Conv} = hA_S(T_S - T_\infty) \tag{2.29}$$

where $\dot{Q}_{Conv}$ is the convective power, proportional to the difference between the heated surface T_S and the ambient temperature T_∞. According to Incropera and Dewitt [12] convection heat transfer coefficients can be considered according to Table 2.3, where phase change processes can be many orders of magnitude higher than any conduction process. This dramatic heat transfer disparity has been exploited in CSP with heat pipes where various Dish Stirling investigations [17] have found marked performance improvements over sensible systems with heat pipes, which operate based on both boiling and condensation processes.

Table 2.3. General convection heat transfer coefficient values [12].

Process	h [W/m^2-K]
Natural Convection	
Gases	2-25
Liquids	50-1000
Forced Convection	
Gases	25-250
Liquids	100-20,000
Convection with Phase Change	
Boiling or Condensation	2,500-100,000

Generally, for single-phase heat transfer, the Nusselt number correlation is represented by an empirical expression of the form:

$$Nu = C \cdot Re^{p} \cdot Pr^{n} \left(\frac{\mu}{\mu_s}\right)^{0.14} \tag{2.30}$$

where *C*, *p* and *n* in are constants independent of the fluid used [18]. The last term in this expression accounts for the variable viscosity effect. This parameter is equivalent to the heat transfer coefficient by the expression:

$$Nu = \frac{h \cdot L_c}{k_f} \tag{2.31}$$

Where h is the convective heat transfer coefficient, L_c is the characteristic length and k_f is the thermal conductivity of the surrounding fluid. Modified Wilson plot technique is primarily used to determine the value of multiplier *C* and exponent of Reynolds number *p* in the Nusselt number correlation [19]. The magnitude of *n* is taken to be 1/3 in agreement with [20] and [21].

Many CSP applications involve internal flow applications with convection transport through varying cross-sectional geometries. To a first approximation a hydraulic diameter, used to determine Nu can be approximated as the characteristic length by:

$$D_h = L_C = \frac{4A_C}{P} \tag{2.32}$$

where A_C and P are the flow cross-sectional area and the wetted perimeter respectively. For turbulent flow conditions, $Re \geq 2300$, the Dittus-Boelter Eqn. 2.33 can be used for circular tubes, as well as the Petukhov model, Eqn. 2.33, used for flows that are characterized by large property variations.

$$\begin{matrix} Nu_{D_h} = 0.023 Re_{D_h}^{4/5} Pr^{n} \\ n = 0.4 \; for \; T_s > T_m \\ n = 0.3 \; for \; T_s < T_m \end{matrix} \quad for \begin{cases} 0.6 \leq Pr \leq 160 \\ Re_{D_h} \geq 10{,}000 \\ \frac{L}{D_h} \geq 10 \end{cases} \tag{2.33}$$

$$Nu_{D_h} = \frac{(f/8)\left(Re_{D_h} - 1000\right)Pr}{1.07 + 12.7(f/8)^{1/2}\left(Pr^{2/3} - 1\right)} \; for \begin{cases} 0.5 < Pr < 2{,}000 \\ 10^4 < Re_{D_h} < 5 \times 10^6 \end{cases} \tag{2.34}$$

For smaller *Re* numbers the Gnielinski modified correlation has been suggested [22].

$$Nu_{D_h} = \frac{(f/8)\left(Re_{D_h}-1000\right)Pr}{1.07+12.7(f/8)^{1/2}\left(Pr^{2/3}-1\right)} \; for \begin{cases} 0.5 < Pr < 2{,}000 \\ 3{,}000 < Re_{D_h} < 10^6 \end{cases} \tag{2.35}$$

For liquid metals with constant T_s the following correlation can also be used for *Pe* numbers greater than 100.

$$Nu_{D_h} = 5.0 + 0.025 Pe_{D_h}^{0.8} \tag{2.36}$$

For internal laminar flow through a duct with a uniform heat flux, the use of Eqn. 2.36 for various cross-sectional areas can be used to determine Nu_{D_h}. Conversely, external flow over solid surface boundary layers develop freely, without constraints imposed by adjacent surfaces.

Table 2.4. Laminar flow *Nu* numbers and friction factors for fully developed flow in tubes of various cross-sectional areas [12].

Cross-Section	$\frac{b}{a}$	Unifrom Heat Flux	Uniform Surface Temp. T_s	fRe_{D_h}
	------	4.36	3.66	64
	1.0	3.61	2.98	57
	1.4	3.73	3.08	59
	2.0	4.12	3.39	62
	3.0	4.79	3.96	69
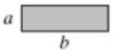	4.0	5.33	4.44	73
	8.0	6.49	5.6	82
	∞	8.23	7.54	96
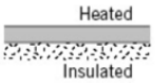	∞	5.39	4.86	96
	------	3.11	2.49	53

Laminar boundary layers develop at the leading edge (x = 0) and transition to turbulence at a downstream location, x_c when a critical Reynolds number, $Re_{x,c}$ is achieved [12]. Eqns. 2.39 and 2.40 provide respective laminar and turbulent correlations for flow over flat surfaces [12] where the ratio between the hydrodynamic and thermal boundary layers can be provided by:

$$\frac{\delta}{\delta_t} = Pr^{1/3} \tag{2.37}$$

where

$$\delta = \frac{5.0}{\sqrt{u_\infty/vx}} = \frac{5x}{Re_x} \tag{2.38}$$

Laminar:

$$\overline{Nu}_{L_C} = 0.664 Re_{L_C}^{1/2} Pr^{1/3} \; for \{Pr \geq 0.6 \tag{2.39}$$

Turbulent:
$$\overline{Nu}_{L_C} = \left(0.037Re_{L_C}^{4/5} - \varsigma\right)Pr^{1/3} \quad for \begin{cases} 0.6 \le Pr \le 60 \\ Re_{x,c} \end{cases} \le Re_{L_C} \le 10^8 \quad (2.40)$$
$$\varsigma = 0.037Re_{x,c}^{4/5} - 0.664Re_{x,c}^{1/2}$$

For free falling liquid drops Gourdon *et* al. [23] also provided a correlation for the average Nusselt number, Eqn. 2.41 where all fluid properties are evaluated at T_∞:

$$Nu_{L_C} = 2 + 0.6Re_{L_C}^{1/2}Pr^{1/3} \quad (2.41)$$

Heat transfer to or from fins in cross-flows are relevant to numerous thermal dissipation, boiling and heat exchanger applications in CSP. During heat exchange operation, a fluid can pass over a single tube where heat transfer can vary according to the cross-section as prescribed by Table 2.5.

Table 2.5. Average Nusselt number correlation equations for flow over varying single tube geometries [360].

Tube Cross-Section Geometry	Reynolds Number Validation Range	Average Nusselt Number	Restriction
	0.4-4	$\overline{Nu}_D = 0.989Re_D^{0.330}Pr^{1/3}$	$Pr \ge 0.7$
	4-40	$\overline{Nu}_D = 0.911Re_D^{0.385}Pr^{1/3}$	$Pr \ge 0.7$
	40-40,000	$\overline{Nu}_D = 0.683Re_D^{0.466}Pr^{1/3}$	$Pr \ge 0.7$
	4,000-40,000	$\overline{Nu}_D = 0.193Re_D^{0.618}Pr^{1/3}$	$Pr \ge 0.7$
	40,000-400,000	$\overline{Nu}_D = 0.027Re_D^{0.805}Pr^{1/3}$	$Pr \ge 0.7$
	6,000-60,000	$\overline{Nu}_D = 0.304Re_D^{0.590}Pr^{1/3}$	Gas Flow
	5,000-60,000	$\overline{Nu}_D = 0.158Re_D^{0.660}Pr^{1/3}$	Gas Flow
	5,200-20,400	$\overline{Nu}_D = 0.164Re_D^{0.638}Pr^{1/3}$	Gas Flow
	20,400-105,000	$\overline{Nu}_D = 0.039Re_D^{0.780}Pr^{1/3}$	Gas Flow
	4,500-90,700	$\overline{Nu}_D = 0.150Re_D^{0.638}Pr^{1/3}$	Gas Flow

For a bank of tubes, the geometries can either be solid or have a secondary fluid passing through them. The tubes can also either be aligned or staggered to the flow velocity, as shown in Fig. 2.8.

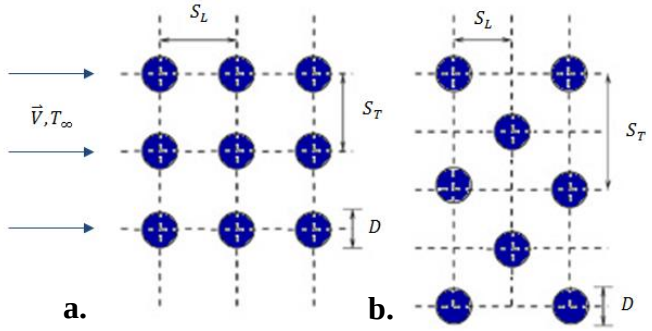

Figure 2.8. Tube bank arrangements for a. aligned and b. staggered configurations.

For the staggered configuration the tube diameter D, traverse pitch S_T, and longitudinal pitch S_L characterizes the tubes, measured between their respective centers. Values for these and other tube bank configuration performance parameters and theory can be found in [12], where correction coefficients C and m are provided and used to determine Nu numbers under specific flow conditions. For an airflow across a bank of tubes, with more than N_L rows of tubes, the average heat transfer coefficient can be determined from Eqn. 2.42 where all properties are evaluated at the film temperature [12].

$$\overline{Nu}_D = 1.13 C_1 Re_{D,max}^{m} Pr^{1/3} \; for \begin{cases} N_L \geq 10 \\ 2{,}000 < Re_{D,max} < 40{,}000 \\ Pr \geq 0.7 \end{cases} \tag{2.42}$$

Eqn. 2.43 by Zhukauskas [24] found improved accuracy for tube rows greater than 20, where all fluid properties with the exception of Pr_s, were evaluated at the arithmetic mean of the fluid inlet and outlet temperatures.

$$\overline{Nu}_\phi = C Re_{D,max}^{m} Pr^{0.36} \left(\frac{Pr}{Pr_s}\right)^{1/4} \; for \begin{cases} N_L \geq 20 \\ 1{,}000 < Re_{D,max} < 2 \times 10^6 \\ 0.7 < Pr < 500 \end{cases} \tag{2.43}$$

Finally as the fluid that passes through the tube bank it can experience a large temperature change, the heat transfer rate could be significantly overpredicted using the simplified expression from Newton's Law of cooling: $\Delta T = T_s - T_\infty$. As its temperature approaches T_s and ΔT decreases, the log-mean temperature difference, Eqn. 2.44 has been found to have enhanced results [12], where the outlet temperature can be predicted from Eqn. 2.45.

$$\Delta T_{lm} = \frac{(T_s - T_\infty) - (T_s - T_O)}{ln\left(\frac{T_s - T_i}{T_s - T_\infty}\right)} \tag{2.44}$$

$$\frac{T_s - T_O}{T_s - T_i} = exp\left(-\frac{\pi D N \overline{h}}{\rho V N_T S_T c_p}\right) \tag{2.45}$$

With the calculation of $\Delta T_{lm}$the heat transfer rate per unit length of the tubes within the bank can be determined by Eqn. 2.46 where N is the total number of tubes and $\overline{h}$ is the average heat transfer coefficient.

$$\dot{Q}' = N\left(\overline{h}\pi D \Delta T_{lm}\right) \tag{2.46}$$

2.4 Phase Change & Latent Heat Transfer

To provide electricity from CSP energy generation during off hours, latent HTFs and latent heat thermal energy storage (LHTES), using phase change materials (PCMs), is receiving considerable attention. Salts and other metallic-type materials are good candidates for utility as a PCM of high temperature facilities, although charging and discharging power of LHTES systems can be limited based on their respective thermal conductivities. Principally, latent heat is the energy absorbed or released from a substance during phase change from a gas to a liquid or a solid, or vice versa. If a substance is changing from a solid to a liquid, it will need to absorb energy from the surrounding environment to spread the molecules into a larger volume. If the substance is changing however

from matter with lower density to a phase with higher density, the substance therefore will give off energy as the molecules come closer together and lose energy from motion and vibration. As a liquid undergoes boiling, energy is absorbed from the heated surface and goes into expanding the liquid molecules into a vapor. Alternatively, when the liquid undergoes condensation, the liquid gives off energy as it solidifies. Fig. 2.9 provides a simplified graphical example for how this takes place, where a substance is in its solid phase at point 1 and is heated until its temperature reaches its melting point at point 2. As it is heated further between points 2-3, the energy from the heat source goes into breaking atomic bonds. At point 3 all of the solid phase has been transformed into the liquid phase and further heat input goes into kinetic energy of the particles raising the temperature until boiling, point 4. From points 4 to 5 thermal energy overcomes chemical bonds to allow the particles that have enough kinetic energy to escape from the liquid where the substance then enters into a gas phase. Beyond point 5, further heating under increased pressure can raise the temperature further. With sensible heat however, when an object is heated or cooled, its temperature rises or falls with the respective addition or removal of heat. However, the object does not undergo phase change.

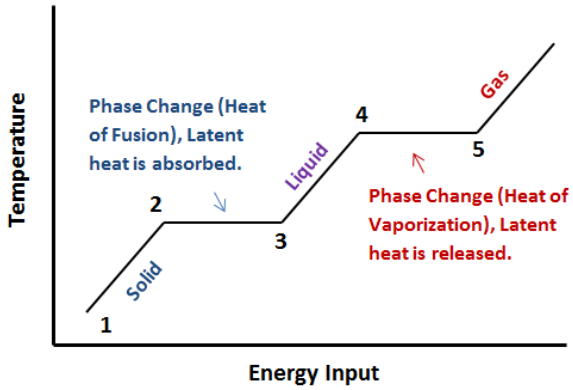

Figure 2.9. Phase change diagram based on temperature and input power.

During boiling, according to Carey [25] three mechanisms play important roles in boiling processes: 1. surface tension effects, 2. surface wetting characteristics of the liquid, and 3. metastable phase stability.

2.4.1 Surface Tension & Boiling

Surface tension σ corresponds to energy stored in the interface region per unit area [25]. The energy excess in this region is due to the slightly larger separation of the liquid phase molecules adjacent to the gas phase. The magnitude of the surface tension for a substance is directly linked to the strength of intermolecular forces in the material. Nonpolar liquids typically have the lowest surface tension. Water and other polar molecules have somewhat higher surface tension, and liquid metals, which exhibit metallic bond attraction, have very high surface tension. The surface tension of water at 20 °C is 0.0728 N/m, whereas liquid mercury has a surface tension of 0.484 N/m at the same temperature. The surface tension for any pure liquid varies with temperature. It decreases almost linearly with increasing temperature, vanishing altogether at the critical point where the distinction between the phases disappears [25]. Therefore to ensure bubble interfacial stability, the pressure inside a spherical bubble of radius r must exceed that in the surrounding liquid by $2\sigma/r$:

$$P_v - P_l + \frac{2\sigma}{r} \tag{2.47}$$

To ensure the bubble is in equilibrium with the surrounding fluid, the liquid must be superheated above the respective saturation temperature for the ambient liquid pressure where the amount of required superheating increases as the radius of curvature of the bubble interface decreases [25].

2.4.2 Wetting Characteristics

The wetting characteristics of a heat transfer fluid is generally quantified based on a contact angle between the solid heated surface and the tangent to the interface, at the point where it contacts the solid [25]. This angle is measured through the liquid phase (Fig. 2.10a) where it is generally determined based on liquid advancing over a solid surface, which tends to be larger than that of a liquid front receding over the surface, which is commonly termed as contact angle hysteresis Fig. 2.10b. The wetting behavior in combination with the surface tension effect, thus, determines the level of superheat required for the bubble to be in equilibrium with the surrounding liquid. The liquid must be heated above this superheat level for the bubble to grow. A steady boiling process can be sustained only if the liquid is heated above this threshold superheat level [25].

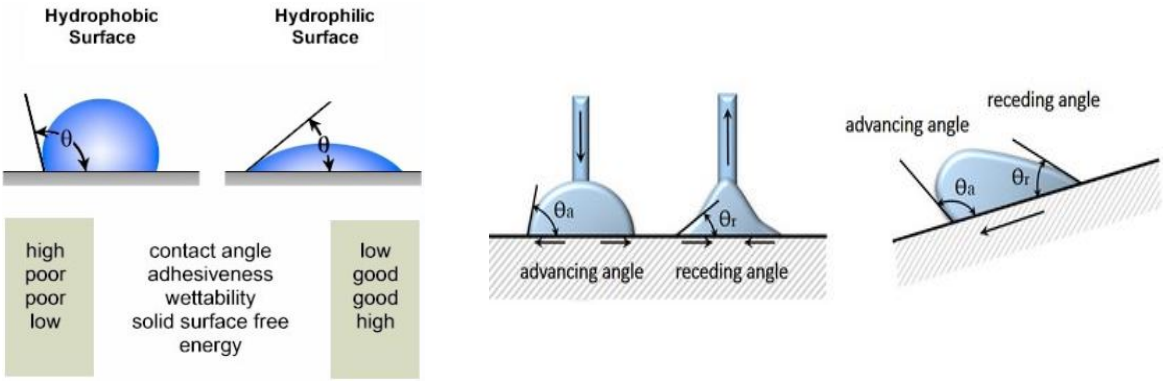

a. **b.**

Figure 2.10. Contact angle θ a. comparison between hydrophobic and hydrophilic surfaces [27] and b. hysteresis phenomena [28].

2.4.3 Phase Stability

It can be shown from basic thermodynamic analysis that a necessary and sufficient condition for phase stability where:

$$\left(\frac{\partial P}{\partial v}\right)_r < 0 \tag{2.48}$$

Below the critical temperature, extrapolation of the isotherms for the liquid and vapor phases consistent with an equation of state like the van de Waals equation results in an isotherm shape similar to that shown in Fig 2.11.

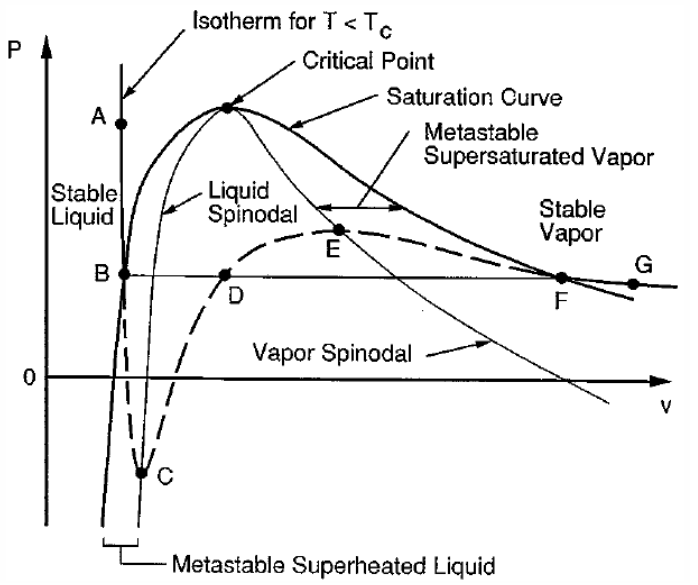

Figure 2.11. P-V diagram spinodal lines and metastable regions of boiling stability [25].

From Fig. 2.11 the locus of points where $(\partial P/\partial v)_T = 0$ are termed spinodal curves. Regions of metastable vapor and liquid exist between the saturation curve and the spinodal curves. The effects of surface tension discussed above require that fluid surrounding a vapor bubble be in the metastable superheated liquid region. Predictions of statistical thermodynamics imply that as $(\partial P/\partial v)_T$ approaches zero, the level of fluctuations in a fluid system increases. This, in turn, increases the probability that an embryonic new phase will form as a result of density fluctuations. Initiation of a phase change in this manner is termed homogeneous nucleation. Generally, a pure liquid must be heated to nearly 90% of its absolute critical temperature before homogeneous nucleation of vapor bubbles occurs [25]. In most physical systems of engineering interest, the bulk phase is in contact with solid walls of the containing structures, or solid particulate contaminants. These solid phases may provide nucleation sites where phase change may occur if the system state is driven into the metastable range. Nucleation of vapor bubbles may preferentially occur at low liquid superheat levels in crevices in the solid surface where gas is trapped [25].

Overall, phase transition from a liquid to a vapor state strongly depends on temperature and pressure, however forces, as a result of fluid motion can also impact bubble nucleation and stability. In general, although forced convection and pool boiling can prescribe liquid to vapor phase transition and resulting the appearance of vapor bubbles on a hot surface, forced convection however imparts a number of specific features to the conditions of bubble production and breakaway into the bulk of the liquid. The two-phase structures of vapor-liquid mixtures resulting from boiling, and mixing of liquid and vapor phases, also differ appreciably between pool and forced convection boiling. However, many leading investigators have previously [Kandlikar paper] approached characterization of forced convection boiling to include physical phenomena of pool boiling. Therefore, this work provides an overview of both boiling concepts, which are central elements to latent phase-change heat transfer in CSP systems.

2.4.4 Pool & Convective Boiling Heat Transfer

2.4.4.1 Pool Boiling Heat Transfer

For CSP systems, much sensible heating and storage takes place for general HTF operation of oil-based systems below 400 °C and 550 °C for molten salt systems [28], where Fig. 2.12 presents the relative range for these and other CSP HTFs.

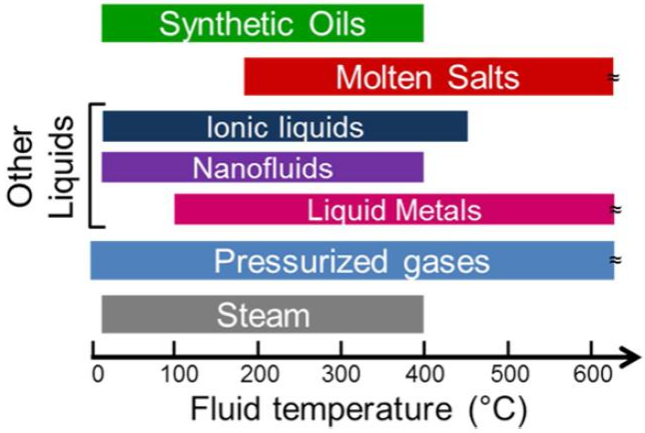

Figure 2.12. CSP heat transfer fluid relative operating range [139].

However, beyond these temperatures, phase change begins to occur according to the generalized boiling curve, shown in Fig. 2.1.3. This curve primarily represents the points beyond point 3 in Fig. 2.4.1, where initially natural convection heat transfer takes place between the heated surface and the fluid up to point A in Fig. 2.42. In this region the superheat ΔT is very low where there is insufficient vapor in contact with the liquid phase to facilitate boiling at saturation temperature. However, as superheat is increased, bubble inception will eventually begin at the ONB (onset of nucleate boiling) condition at point A. For the nucleate boiling region between $\Delta T_A \leq \Delta T \leq \Delta T_C$ two different flow regimes take place where first isolated bubbles form at nucleation sites, and as the surface if further heated these bubbles separate from the heated surface at an increased rate, which can cause considerable mixing and can enhanced the heat transfer coefficient h. As the superheat is further increased beyond point B, more nucleation sites become active with increased bubble formation causes bubble interference and coalescence. The heat flux in this region can be described by correlations of nucleate pool boiling heat transfer where data have typically been used as tools to predict nucleate boiling heat transfer in engineering systems and heat exchangers. A common correlation used by many investigators in various applications is Eqn. 2.49, developed by Rohsenow [29],

$$\frac{\dot{Q}''_{NB}}{\mu_l h_{fg}}\left[\frac{\sigma}{g(\rho_l-\rho_v)}\right]^{1/2} = \left(\frac{1}{C_{sf}}\right)^{1/r} Pr_l^{-s/r}\left[\frac{C_{pl}[T_w-T_{sat}(P_l)]}{h_{fg}}\right]^{1/r} \tag{2.49}$$

where the values of r = 0.33 and s = 1.7 are recommended for most fluids, though for water a value of s = 1.0 is suggested. The values of C_{sf} in this correlation vary with the type of solid surface and the type of fluid in the system. This empirically accounts for material property and/or wetting angle effects. Recommended values of C_{sf} for specific liquid–solid combinations are given by Rohsenow [29], but whenever possible, an experiment should be conducted to determine the appropriate value

of C_{sf} for the particular solid–liquid combination of interest. If this is not possible, a value of C_{sf} = 0.013 is recommended as a first approximation. Another common correlation for nucleate boiling is Eqn. 2.50 by Rohsenow [29] where the impacts of surface-fluid interactions are considered, such that surface-fluid and *n* coefficients provided for some materials are shown in Table 2.6.

$$\dot{Q}''_{NB} = \mu_l h_{fg} \left[\frac{g(\rho_l - \rho_v)}{\sigma}\right]^{1/2} \left(\frac{c_{p,l}\Delta T_e}{C_{s,f} h_{f,g} Pr_l^n}\right)^3 \tag{2.50}$$

Table 2.6. Nucleate boiling correlation surface-fluid configuration coefficients [29].

Surface-Fluid Configuration	$C_{s,f}$	n
Water-Copper		
Scored	0.0068	1.0
Polished	0.0128	1.0
Water-Stainless Steel		
Chemically Etched	0.0133	1.0
Mechanically Polished	0.0132	1.0
Ground & Polished	0.0080	1.0
Water-Brass	0.0060	1.0
Water-Nickel	0.0060	1.0
Water-Platinum	0.0130	1.0
n-Pentane-Copper		
Polished	0.0154	1.7
Lapped	0.0049	1.7
Benzene-Chromium	0.0101	1.7
Ethyl Alcohol-Chromium	0.0027	1.7

This condition allows vapor to escape as jets or columns, which then form into larger slugs that can blanket the heated surface. As this interfacial vapor blanketing increases, interference between densely packed bubbles inhibits further liquid motion near the surface, which leads to an inflection prescribing a heat transfer coefficient maximum, after which h begins to decrease with increasing ΔT to the critical heat flux (CHF) condition where a further increase in superheat makes it difficult for liquid to continuously wet the heated surface facilitating a dryout condition. For water/steam systems, the CHF condition slightly exceeds 1 MW/m^2.

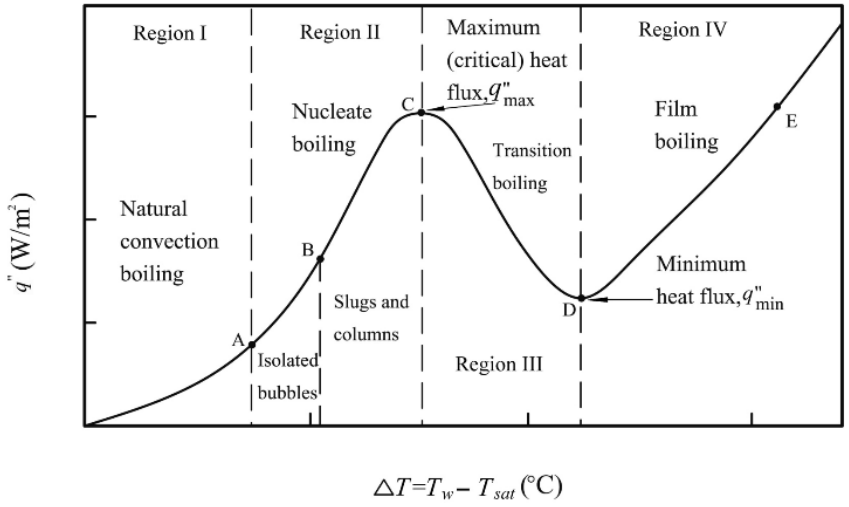

Figure 2.13. Generalized pool boiling curve for HTFs [30]

Since high heat transfer rates and convection coefficients are associated with small values of excess temperature, it is desirable to operate many types of CSP heat transfer equipment within the nucleate boiling region [12]. For water/steam systems, dividing q" by ΔT demonstrates that convection coefficients are higher (>10^4 W/m^2-K) than other boiling regions. These high heat transfer coefficients, especially for liquid metals (Add Table of Superheat, CHF and heat transfer coefficients for water/steam, oils and metals here), is what makes latent energy systems for high temperatures in excess of 550 °C considerably attractive when compared to sensible systems [28]. To determine the CHF condition, Carey [25] prescribes Eqn. 2.51 where C is 0.149 for large horizontal plates, and 0.131 for large horizontal cylinders, spheres and large finite heated surfaces.

$$\dot{Q}_{CHF} = C h_{lv} \rho_v \left[\frac{\sigma g(\rho_l - \rho_v)}{\rho_v^2}\right] \tag{2.51}$$

After the CHF condition is reached, further superheat increase facilitates operation within the transition boiling region. Here, unstable film or partial film boiling ensues, where bubble formation occurs so rapidly that a vapor film blankets the surface to where at any point on the surface, conditions may fluctuate between film and nucleate boiling. Since the thermal conductivity of the vapor is less than that of the liquid, h and q" continue to decrease with increasing ΔT where radiation heat transfer begins to become a more significant mode of heat transfer; however thermal-mechanical stress and fatigue of the surface becomes more problematic. It is advised that operation occur only up to the CHF condition to avoid system failures.

Boiling heat transfer, which can facilitate the highest heat transfer coefficients as illustrated by Table 2.3, can either occur with homogeneous or heterogeneous nucleation, where homogeneous occurs in the pure liquid state when a sufficient number of high-energy molecules come together to form a void, into which a vapor immediately diffuses to for a nucleus [31]. Conversely, heterogeneous nucleation occurs in the presence of two or three phases, which tends to occur more frequently considering homogeneous nucleation requires a relatively large amount of energy required to form the bubble surface and provide the work of expansion necessary to facilitate bubble growth up to the critical bubble radius. For liquid metals, as with ordinary liquids, bubble nucleation for incipient boiling occurs at gas-filled cavities in wetted solid-metal surfaces. Additionally, for any surface to boil, the heated surface temperature must be higher than the saturation temperature, where this difference is known as wall superheat. Whereas stable-nucleate boiling superheats for liquid metals are typically less than those for ordinary fluids, incipient-boiling wall superheats are often much greater. This indicates that for liquid metals wall temperature may have a large overshoot at boiling inception with a significant amount of hysteresis, where this overshoot is generally higher for pool boiling than forced convection boiling [31]. Dweyer indicated [31] that there are four reasons why liquid metals generally provide much higher incipient boiling superheats than with ordinary liquids:

1. Liquid metals usually wet solid metal surfaces very well, particularly in the range of temperatures encountered in boiling.
2. Alkali metals are very reactive chemically and act to reduce surface oxides of many metals and alloys.
3. Solubilities of inert gases in liquid metals increase with an increasing temperature.
4. Boiling pressures of liquid metals are generally low with respect to their critical pressures, which means that boiling occurs in that portion of the vapor pressure curve where the slope, dp/dt is low.

For pool boiling studies with alkali metals, Subbotin et al. [32] reported incipient-boiling superheats of Sodium up to approximately 90 °C, while Edwards and Hoffman [33] reported incipient-boiling superheats as high as 260 °C for potassium. For forced convection, Chen [34] observed incipient-boiling wall superheats over 37 °C with potassium, while Dweyer [32] found superheats up to 126 °C for sodium, with HTF flow faster than 0.3 m/s. Overall, the magnitude of incipient-boiling superheats in metals has been found [31] to be impacted by the following independent variables:

1. HTF operating pressure and partial pressure of inert gas in surface cavities.
2. Heat flux and heating method.
3. Flow rate or Reynolds number [35].
4. Pressure-temperature history of the system.
5. Liquid metal charging procedure, which can affect the amount of inert gas that can be trapped within surface cavities.
6. Inert gas and O_2 concentration in HTF.
7. Topography or microstructure and surface roughness.
8. Extent of natural convection (pool boiling), impacted by the system geometry.
9. Rate of temperature rise up to boiling temperature.
10. Operational time and reliability of the system.

2.4.4.2 Convective Boiling Heat Transfer

In contrast to pool boiling which is primarily facilitated by buoyancy-driven flow, forced convection boiling is due to forced bulk motion of the fluid, which can also include motion due to buoyancy effects. Convective boiling may also occur based on external flow over heated geometries [12], where vapor generation is not extensive and the liquid is subcooled, or with internal duct flow, commonly termed as two-phase flow. This type of flow is characterized by rapid evaporation of liquid to vapor in the flow direction.

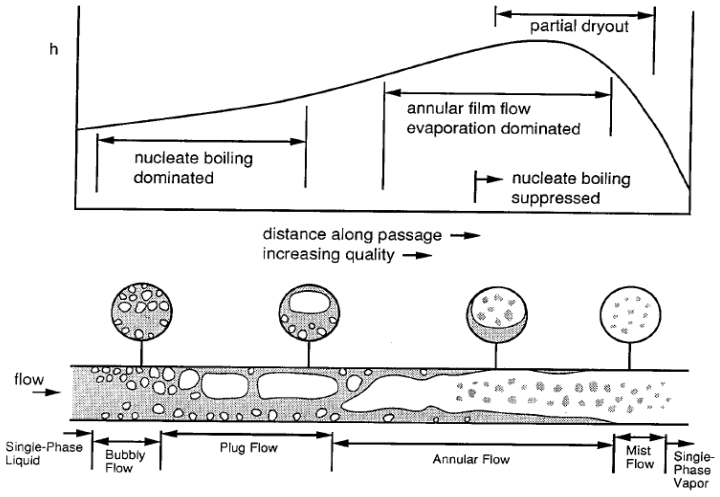

Figure 2.14. Convective flow boiling along a horizontal channel with qualitative variation of the heat transfer coefficient with respect to quality, under moderate wall superheat conditions [25].

Fig. 2.14 illustrates the vaporization process in a horizontal round tube where subcooled liquid enters prior to transitioning into two-phase flow. The regimes encountered depend on the entrance conditions and the thermal boundary conditions at the tube wall. At low quality the vaporization process is dominated by nucleate boiling, with convective effects being relatively weak. As the quality increases, the flow quickly enters the annular film flow regime in which convective evaporation of the annular liquid film is the dominant heat transfer mechanism.

At high wall superheat levels, transition boiling or film boiling can also occur. The transition from nucleate boiling to one of these regimes is termed a departure from nucleate boiling (DNB) or the CHF condition. However, the heat transfer performance of an evaporator under transition or film boiling conditions is so poor that equipment is not usually designed to operate under such conditions.

For convective flow boiling along a vertical channel, the impact of buoyancy can become significant for bubble departure from the heated surface which has an impact on regime transition with respect to the fluid. Fig. 2.15 presents convective boiling along a vertical channel where heat transfer to the entering subcooled liquid can be predicted by convection correlations presented in section 2.3 up to point B.

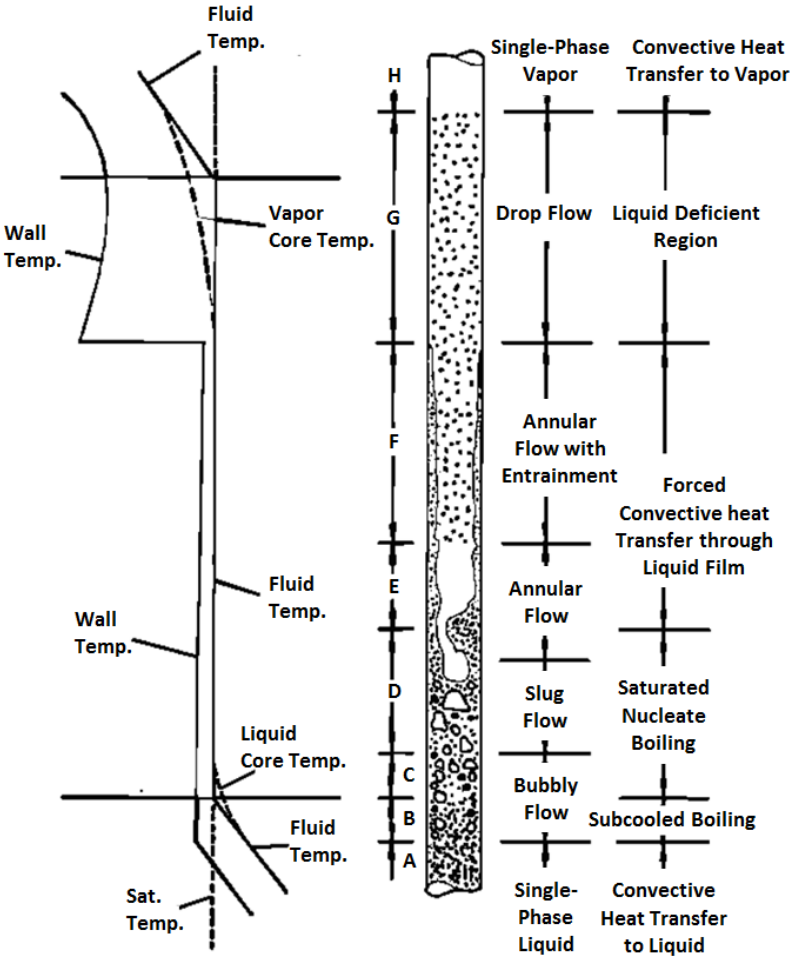

Figure 2.15. Flow convection heat transfer regions in a vertical tube [36].

In forced convection boiling, transitions into separate regimes occur as nucleate, bubbly, slug, annular and dryout which correspond to flow of increasing quality. Each of these regimes have

separate experimental correlations associated to them where their transition from one to another is typically not well defined. Bubble growth/separation and boiling regime transitions are strongly affected by flow velocity and other hydrodynamic effects [12]. When boiling is initiated, bubbles begin to nucleate on the heated surface and depart when a critical radius is achieved [25]. For this regime, the wall heat flux is predicted by Carey [25] for a constant heat flux, Eqn. 2.52, and isothermal boundary condition, Eqn. 2.53, where G is the Gibbs function: $G = H\text{-}TS$ and x is a prescribed position along the channel.

Const. Heat Flux B.C. $$\dot{Q}^{\parallel} = \left(\frac{D_h}{4z}\right) G c_{p,l}\left[T_l(z) - T_{l,in}\right] \tag{2.52}$$

Isothermal B.C. $$\dot{Q}^{\parallel}(z) = h_l\left[(T_w - T_{sat}) - \left(T_{sat} - T_{l,in}\right)\right] \exp\left(-\frac{4h_l z}{G c_{p,l} D_h}\right) \tag{2.53}$$

As the volume fraction of vapor increases, nucleate boiling is observed at low vapor qualities (x<0.1) which increases as individual bubbles coalesce to form slugs, which then proceed into an annular flow with increasing heat input. As this occurs saturated nucleate boiling becomes dominant where various investigators have proposed correlations to describe these phenomena [37-39]. Fig. 2.16 presents the boiling curve for flow convection where the heat flux is plotted verses the wall superheat, where the transition from forced convection to nucleate boiling is always at some wall temperature greater than the saturation temperature. The exact point where the boiling curve transitions from single phase to two-phase is dependent upon the amount of subcooling, mass flow rate, number and size of nucleation sites, and the fluid parameters. Most expressions for the prediction of ONB (onset of nucleate boiling) are derived by first determining the intersection of the forced convection (line 1-2) and fully developed boiling portions (line 3a-3b) of Fig. 2.16.

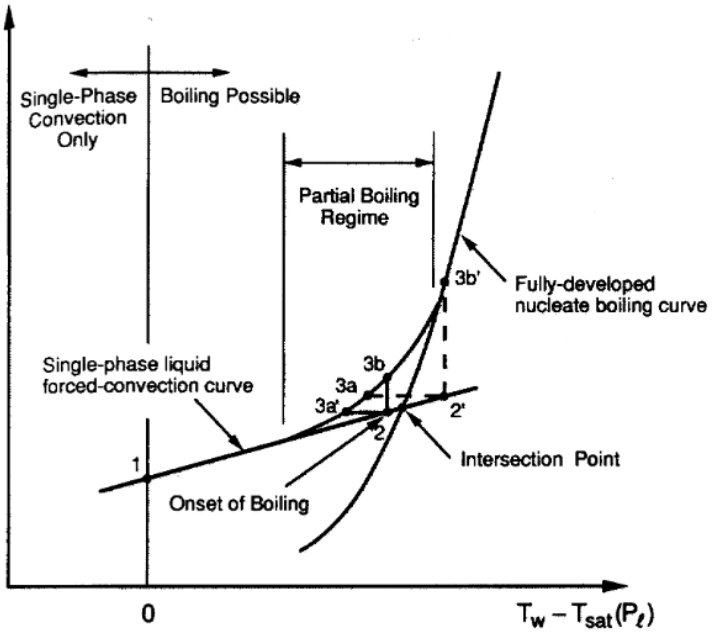

Figure 2.16. Convective Boiling curve at onset of nucleate boiling [25].

Carey [25] suggests for various fluids high accuracy can be attained with a heat transfer correlation by Kandlikar [40], based on either dominant contributions from nucleate boiling or convective boiling:

$$h_{sat} = maximum\ of \begin{cases} h_{NBD} \\ h_{CBD} \end{cases} \tag{2.54}$$

where for the nucleate boiling dominant regime:

$$h_{NBD} = 0.6683\left(\frac{\rho_l}{\rho_v}\right)^{0.1} x^{0.16}(1-x)^{0.64} f_2(Fr_l) h_l + 1058.0 Bo^{0.7} F_K (1-x)^{0.8} h_l \tag{2.55}$$

and for the convective dominant regime:

$$h_{CBD} = 1.1360\left(\frac{\rho_l}{\rho_v}\right)^{0.45} x^{0.72}(1-x)^{0.08} f_2(Fr_l) h_l + 667.2 Bo^{0.7} F_K (1-x)^{0.8} h_l \tag{2.56}$$

where F_K is a fluid constant provided by Kandlikar [41], which is 1 for water and 4.7 for nitrogen. In Eqn. 2.56 h_l is the single-phase heat transfer coefficient for the liquid phase only, and is computed according to correlations by Gnielinski [22]:

$$\begin{aligned} h_l &= \left(\frac{k_l}{D}\right)\frac{(Re_l - 1000)Pr_l(f/2)}{1+12.7\left(Pr_l^{2/3}-1\right)(f/2)^{0.5}} \quad for\ 0.5 \le Pr_l \le 200, \quad 2300 \le Re_l < 10^4 \\ h_l &= \left(\frac{k_l}{D}\right)\frac{Re_l Pr_l(f/2)}{1.07+12.7\left(Pr_l^{2/3}-1\right)(f/2)^{0.5}} \quad for\ 0.5 \le Pr_l \le 200, \quad 10^4 \le Re_l < 5\times 10^6 \end{aligned} \tag{2.57}$$

From the aforementioned relations, the friction factor f and function f_2 are computed according to:

$$f = [1.58 ln(Re_l) - 3.28]^{-2} \tag{2.58}$$

$$Re_l = \frac{GD}{\mu_l} \tag{2.59}$$

$$f_2(Fr_l) = \begin{cases} (25Fr_l)^{0.3}\ for\ Fr_l < 0.04\ for\ horizontal\ tubes \\ 1\ \ for\ Fr_l > 0.04\ for\ horizontal\ and\ vertical\ tubes \end{cases} \tag{2.60}$$

As with pool boiling, dry spots eventually appear on the inner surface, at which point the convection coefficient begins to decrease at the CHF condition. The reader is referred to [42-44] and CHF correlations by [25] for subcooled boiling and to [45-47] for CHF correlations associated with saturated flow boiling.

2.4.5 CSP Multimode Heat Transfer

During operation, most CSP components within a system experience more than one form of heat transfer where conduction, convection or radiation effects within an energy balance must be considered respectively. As illustrated in Fig. 2.17 for a generalized CSP receiver, all three effects can be evident within a prescribed control volume, where heat transfer analysis can be facilitated by an arrangement of the continuity, momentum and energy balance constitutive equations. As previously described, conduction assesses the diffusion of heat due to temperature gradients while convection impacts are facilitated by fluid flow heat transfer. However, for systems at high

temperature, radiation effects, which is the transfer of energy by electromagnetic waves between surfaces at differing temperatures, scale to the fourth power of temperature. This can have a tremendous impact on CSP systems, especially heat losses [434]. Additionally, although the heat transfer coefficient magnitude of these effects, as illustrated by Table 2.3, can vary widely depending on control volume geometry and solid/fluid material properties, conjugate heat transfer behavior for temperatures above 720 °C (DOE SunShot target temperature [8]) and pressures above 1 MPa are still not well understood with regards to heat losses for many CSP technologies.

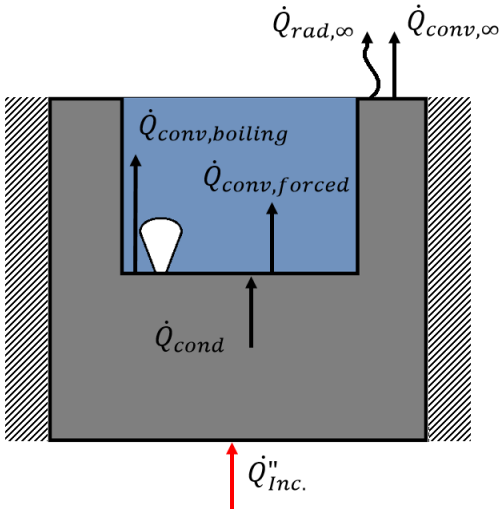

Figure 2.17. Multimode heat transfer of a generalized channeled receiver.

Much research is still ongoing to improve conjugate heat transfer performance and reliability of CSP receivers and other high-temperature systems including thermal energy storage (TES) and power block heat exchangers. The next subsequent chapters provide an overview of progress in CSP systems from the standpoint of heat transfer enhancement.

3. THERMAL COLLECTORS

3.1 Overview

Solar thermal concentrating receivers are designed to be a high-absorptance/transmittance, low reflectance, radiative/convective heat exchanger that emulates as closely as possible a radiative black body. Many concentrator varieties are possible for increasing the flux of radiation for CSP receivers. Duffie and Beckman [9] categorized these into two groups: reflectors and refractors, whereby these can be designed cylindrical to focus on a "line" geometry or circular to focus onto a "point." Examples of six configurations are shown in Fig. 3.1 where receivers can also be classified as concave, flat or convex. In general, concentrators with receivers much smaller than the aperture are effective only on beam radiation. It is also evident that the angle of incidence of the beam radiation on the concentrator is important and that sun tracking will be required for these collectors [9].

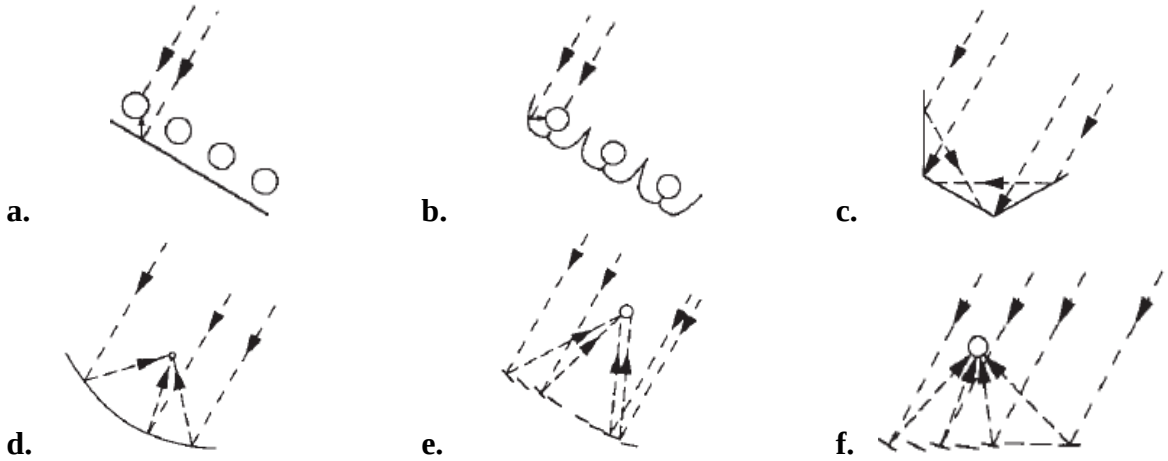

Figure 3.1. Concentrating solar collector configurations for a. tubular absorbers with a diffuse back reflector, b. tubular absorbers with specular cusp reflectors, c. plane receiver with plane reflectors, d. parabolic concentrator, e. Fresnel reflector and f. array of heliostats with a central receiver [9].

There are unique challenges associated with receivers for different CSP technologies that have distinctive requirements to push the envelope of performance. These include the development of geometric designs, high-temperature materials, HTFs as well as processes that maximize solar irradiance and absorptance, minimize heat loss, and have high reliability at high temperatures over thousands of thermal cycles [48]. Additionally, flat-plate collector systems are traditionally termed "absorber plates", while concentrating collectors are often referred to as "receivers." For CSP trough systems, the optical principle of a reflecting parabola is that all rays of light parallel to its axis are reflected to a point or a linear-focus translation. A parabolic dish (paraboloid), on the other hand, is formed by rotating the parabola about its axis; the focus remains a point and is often called point-focus concentrators. If a receiver is mounted at the focus of a parabolic reflector, the reflected light will be absorbed and converted into heat. These two principal functions, reflection to a point or a line, and subsequent absorption by a receiver, constitute the basic functions of a parabolic concentrating collector [48]. Depending on the optics design, certain receivers, such as

ominidirectional receivers, can achieve higher concentration ratios, and thus higher HTM temperatures than that of closed cavity receivers, Fig. 3.2.

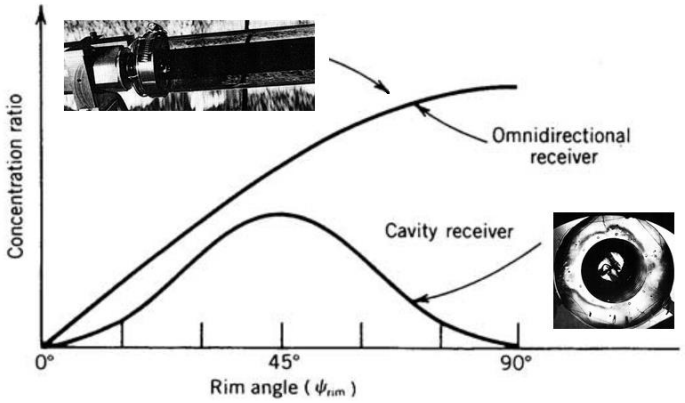

Figure 3.2. Variation of geometric concentration ratio with receiver rim angle [48].

As prescribed by Duffie and Beckman [9] the higher the temperature at which energy is to be delivered, the higher must be the concentration ratio, and the more precise must be the optics of both the concentrator and the orientation system. Fig. 3.3 shows practical ranges of concentration ratios and types of optical systems needed to deliver energy at various temperatures where A_a and A_r are the aperture and receiver areas respectively [9].

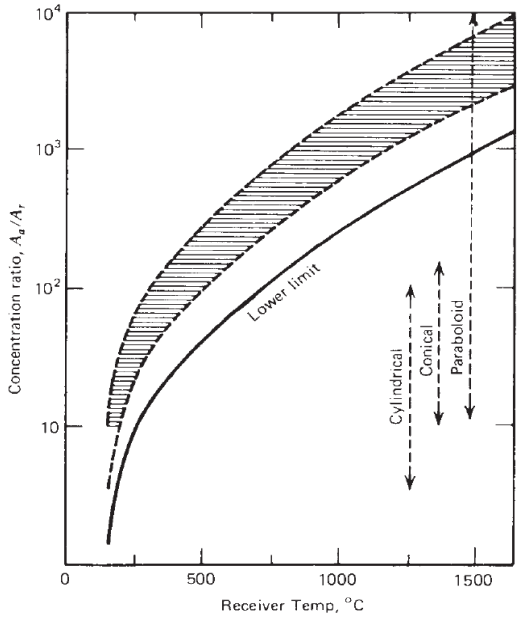

Figure 3.3. Concentration ratio and receiver temperature where the lower limit curve represents concentration ratios where thermal losses equal absorbed energy, shaded range corresponds to collection efficiencies of 40-60% of probable operation. Additionally, approximate ranges of three classes of collectors are shown [49].

The heat-transfer media can be a liquid, such as water, synthetic oil, or molten salt; a gas/vapor, such as air, helium or steam; a solid, such as sand or ceramic particles; or a supercritical phase, such as supercritical carbon dioxide. Liquids and supercritical fluids are typically contained and transported within a tubular receiver, whereas gases can be contained in tubes or volumetric

(honeycomb-like) receivers. Solid particles can be released into a cavity receiver for direct irradiance or across irradiated tubes as a fluidized bed or moving packed bed. Current DOE SunShot goals for a CSP receiver include exit temperatures ≥ 720 °C, thermal efficiency ≥ 90%, lifetime ≥ 10,000 cycles and cost ≤ \$150/kW$_{th}$.

Receivers should be highly absorptive within solar wavelengths of approximately 0.4–2.5 μm. However, at high temperatures, receivers can emit a significant amount of thermal radiation, thereby losing heat to the environment. At these high temperatures there is an overlap of the spectral absorptance and emittance, making it difficult to develop a truly selective absorber. Additionally, coatings and paints must endure high temperatures in an oxidizing environment for many thermal cycles and under potentially large thermal gradients. Overall, the challenges [50] that exist for improving the performance of high-temperature receivers are:

1. Development of optimized geometric designs.
2. High-temperature materials.
3. Heat-transfer fluids.
4. Maximize absorptance to minimize heat losses.
5. High reliability over thousands of thermal cycles.
6. Direct (no intermediate heat exchanger) vs. indirect (ability to store heat) heating.

3.2 Thermal Collectors Analysis

To perform an energy balance on a solar thermal collector, the incident surface is typically isolated where the heated surface absorbs incoming radiation, and balances energy losses by:

$$\dot{Q}_{Useful\ Loss} = \dot{E}_{opt,inc} - \dot{E}_{th\ loss} \tag{3.1}$$

where in general the losses can be evaluated based on an energy balance similar to the representation provided in Fig. 3.4

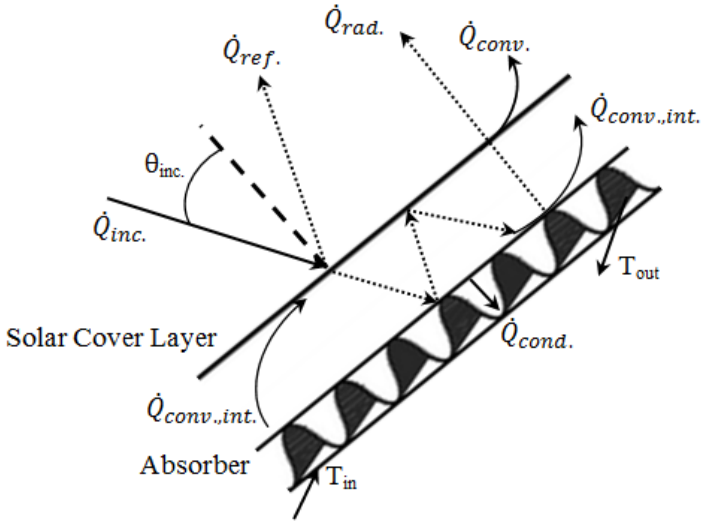

Figure 3.4. Energy balance on a generalized solar absorber/collector [48].

For omnidirectional receivers, the glass envelope temperature T_g is assessed as a function of the receiver tube temperature and the resultant rate of thermal energy exchange between the receiver tube and glass envelop [48]. In his investigation, Treadwell [51] presented the following simplified equation where the temperature of the glass envelope can be determined by evaluating the glass heat loss rate, Eqn. 3.2 with the receiver tube heat-loss rate producing Eqn. 3.3.

$$\dot{Q}_{loss,glass} = h_{glass}A_{glass}\left(T_{surf}^4 - T_\infty^4\right) + \sigma_{SB}\varepsilon_{glass}F_{rad}A_{glass}\left(T_{glass}^4 - T_\infty^4\right) \tag{3.2}$$

$$\dot{Q}_{loss} = \frac{\sigma_{SB}A_{surf}\left(T_{surf}^4 - T_{glass}^4\right)}{(1/\varepsilon_{surf}) + (A_{surf}/A_{glass})[(1/\varepsilon_{glass}) - 1]} + \frac{2\pi k_{eff} l_{rec}(T_{surf} - T_{glass})}{ln(r_2/r_1)} \tag{3.3}$$

where the subscripts "surf" and "rec" corresponds to the surface of the receiver tube and the receiver respectively, while $r_1$and r_2 are the respective radial lengths in Fig. 3.5.

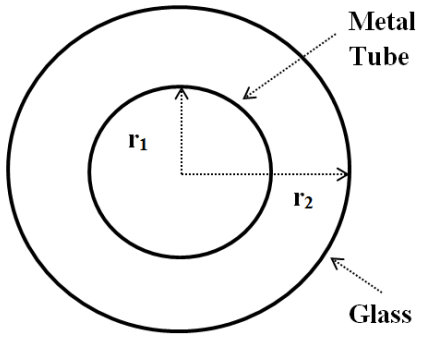

Figure 3.5. Omnidirectional metal tube receiver with outer glass tube diagram.

With Eqn. 3.3 a thorough derivation and values of k_e can be found in reviews by [52-54], however based on knowledge of k_{air} Table 3.1 [48] provides values of k_e/k_{air} for various Ra numbers. However, if an evacuated annulus receiver is employed then $k_{air} = 0$.

Table 3.1. Ratio of effective conductance of annulus k_e to air conductance with Rayleigh number [48].

Ra	(k_e/k_{air})	Ra	(k_e/k_{air})
1000	1.01859	10,000	1.62181
2000	1.10965	20 ,000	1.99668
3000	1.19208	30,000	2.25495
4000	1.27489	40,000	2.45820
5000	1.34809	50,000	2.62840
6000	1.40982	60,000	2.77617
7000	1.46467	70,000	2.90756
8000	1.51655	80,000	3.02640
9000	1.56918	90,000	3.13525
		100,000	3.23594

When performing an energy balance on the absorber plate of a solar collector, there are four general important mechanisms that reduce the amount of solar energy that is incident on the

collector aperture: imperfect reflection, imperfect geometry, imperfect transmission and imperfect absorption.

Based on a thermodynamic first law approach, Eqn. 3.4 provides a single expression for the rate of useful energy produced from a solar collector, equivalent to the difference of the optical (short wavelength λ) energy incident on the absorber surface and the respective heat losses by the different modes of heat transfer [48].

$$\dot{Q}_{Useful} = \dot{m}C_p(T_{out} - T_{in}) \\ = \Gamma\rho\tau\alpha I_{inc,a}A_{Aperature} - A_s\left[h_{comb}(T_s - T_{amb}) + \varepsilon\sigma\left(T_s^4 - T_{sky}^4\right)\right] \tag{3.4}$$

where h_{comb} is equal to the combined convection and conduction coefficient. Kalogirou [55] derived an expression for the energy transfer to a fluid at a local fluid temperature T_{f}:

$$q'_{useful} = F'\frac{A_a}{L}\left[n_0 G_b - \frac{U_L}{C}\left(T_f - T_a\right)\right] \tag{3.5}$$

From Eqn. 3.5, the collector efficiency is defined as:

$$F' = \frac{1/U_L}{\frac{1}{U_L} + \frac{D_0}{h_{fi}D_i} + \left(\frac{D_0}{2k} + ln\frac{D_0}{D_i}\right)} \tag{3.6}$$

where D_0 and D_{i} are the riser tube outer and inner diameters, U_{L} is the solar collector heat transfer coefficient, L is the distance half distance between two consecutive riser pipes defined by [55] where C is the concentration ratio, n_0 is the collector optical efficiency and G_{b} is the direct beam irradiation in units of (W/m^2).

The rate of optical (short wavelength λ) radiation incident on an absorber/receiver will be the solar irradiance absorption for that type of collector, also based on its direct and diffuse components. Since the capture area of the collector may not be aimed directly at the sun, this resource must be reduced to account for the angle of incidence [48]. The incident solar energy as a function of the collector opening area (aperture) is therefore:

$$\dot{E}_{inc} = I_{inc,a}A_{Aperature} \tag{3.7}$$

This solar resource encompasses a number of losses as it passes from the aperture of the collector to the absorber. These processes depend on the type and design of the specific collector where important optical loss mechanisms must also be included. The rate of optical (short wavelength λ) energy reaching the absorber or receiver is the product of the incoming solar resource multiplied by a number of factors, all less than 1.0:

$$E_{low\lambda} = \Gamma\rho\tau\alpha I_{inc,a}A_{Aperature} \tag{3.8}$$

where the capture fraction Γ is a parameter which represents the quality of the shape of the reflecting surface and size of receiver, which is often described as the fraction of the reflected energy not impinging on or entering the receiver or also termed "spillage." If the receiver is relatively small or the shape of the concentrator is poor, then this parameter will be considerably less than 1.0. The reflectance, ρ is a property of any reflecting surface where well designed

concentrators can have capture fractions of 0.95 or higher [48]. The τ transmittance is the fraction of solar radiation passing through all transparent cover material that sunlight passes through to the absorber. The transmittance is the average overall value and represents the total reduction in transmitted energy of the incident solar spectrum by all cover materials. Cover sheets of glass or plastic are used on flat-plate collectors, above the absorber to reduce convective heat loss. Absorptance α and emittance ε are experimentally determined parameters, where radiation properties of various surfaces are provided by Duffie and Beckman [9]:

Table 3.2. Radiation properties of various thermal collector materials [9].

Material	Type[a]	Emittance Temperature[b]	Absorptance[c]
Aluminum, pure	H	0.102/573, 0.130/773, 0.113/873	0.09–0.10
Aluminum, anodized	H	0.842/296, 0.720/484, 0.669/574	0.12–0.16
Aluminum, SiO_2 coated	H	0.366/263, 0.384/293, 0.378/324	0.11
Carbon black in acrylic binder	H	0.83/278	0.94
Chromium	N	0.290/722, 0.355/905, 0.435/1072	0.415
Copper, polished	H	0.041/338, 0.036/463, 0.039/803	0.35
Gold	H	0.025/275, 0.040/468, 0.048/668	0.20–0.23
Iron	H	0.071/199, 0.110/468, 0.175/668	0.44
Lampblack in epoxy	N	0.89/298	0.96
Magnesium oxide	H	0.73/380, 0.68/491, 0.53/755	0.14
Nickel	H	0.10/310, 0.10/468, 0.12/668	0.36–0.43
Paint			
Parson's black	H	0.981/240, 0.981/462	0.98
Acrylic white	H	0.90/298	0.26
White (ZnO)	H	0.929/295, 0.926/478, 0.889/646	0.12–0.18

[a] H is total hemispherical emittance; N is total normal emittance.
[b] The numerator is the emittance at the temperature (K) of the denominator.
[c] Normal solar absorptance.

High-temperature cavity revivers have been designed to employ quartz glass covers to reduce heat loss, to separate the gas in the receiver from the outside air, or used for facilitating pressurization of the gas within the cavity. The transmittance of the cover material also depends on the

wavelength of light passing through it where materials such as glass primarily transmits most radiation in the visible spectrum, however does not transmit much in the infrared. Therefore, an absorber covered with glass will receive most of the incoming, short wavelength radiation, while not transmitting much of the long wavelength radiation loss coming from the absorber [48]. Plastic however has high transmittance values at very long wavelengths, which tends to increase heat loss during night time, lower-temperature ambient conditions [48].

Although a black surface can have an absorption coefficient value greater than 0.98 [48], as the surface degrades this value can decrease. It is important to note that this property is for radiation in the solar or "visible" spectrum where for most real surfaces, the absorption varies as a function of the wavelength. This can be especially true for selective surfaces which are a class of solar collector surfaces that have higher absorptance in the visible spectrum that reduces thermal radiation losses [48]. As solar irradiance (short wavelength λ) reaches the surface of an absorber it then raises the temperature above that of the ambient, which initiates heat loss from the absorber. As the temperature difference between the collector surface and the ambient increases, this rate of heat loss can impact the overall energy balance, Eqn. 3.9.

$$\dot{Q}_{loss} = \dot{Q}_{loss,convection} + \dot{Q}_{loss,radiation} + \dot{Q}_{loss,conduction} \tag{3.9}$$

Adjusting the flow rate or having a large heated surface roughness can reduce the temperature of the absorber, reducing heat loss. However, if enough heat is not removed from the absorber, potentially due to interrupted flow or over insulated surface, the temperature of an absorber could increase hazards to flow channel material stress and thermal fatigue [48].

With regard to convection, this loss from a solar collector receiver is proportional to the surface area of the receiver and the temperature difference between the surface and ambient:

$$\dot{Q}_{loss,convection} = \bar{h}_c A_c (T_c - T_{amb}) \tag{3.10}$$

Although Eqn. 3.10 is a simplified representation, there are typically a number of convective and radiative processes based on surface geometries and boundary layer development that influence heat loss. The average temperature of a collector, T_c has uncertainty with its value as it's not a fixed or measureable quantity [48] since its temperature near the HTF inlet will be lower than near the outlet, and both locations will be lower than the intermediate surfaces not in contact with the HTF. Also, since convection is more of a surface phenomenon as it's assessed with respect to surface temperature, T_c may be driven by characteristics of a coating rather than the solid structural material. Overall, since convective losses are a major loss term for solar collectors, CSP design engineers tend to incorporate many features to collector designs to reduce its impact. Some of these include:

1. Multiple transparent cover sheets for flat-plate collectors.
2. Glass tubes surrounding linear absorbers with a vacuum drawn in the intervening space.
3. Concentration of solar energy so that the absorber area is small relative to the capture area.
4. Absorbers within cavities incorporating glass windows.

Based on Eqn. 3.10 radiation losses increase as the ΔT above the ambient temperature grows. For a black, vertical surface in still, ambient air at 25 °C, Fig. 3.6 exhibits the impact of radiation losses compared to convective losses, which is proportional to the surface emittance.

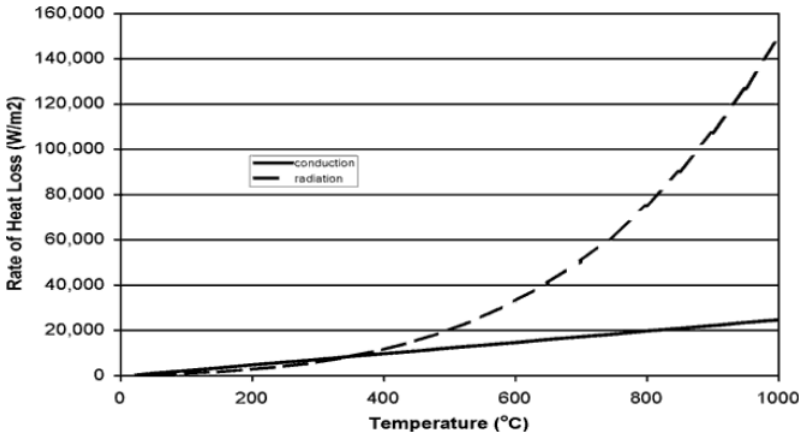

Figure 3.6. Convection versus Radiation Generalized Heat Losses for a Black, Vertical Surface in Free Air at 25 °C. [56**].**

Additionally, when determining an optimal size of a receiver many aforementioned factors of heat and optical losses can impact the energy absorbed by a receiver. Fig 3.7 by Stine and Geyer [56] illustrates that as the receiver size increases the amount of intercepted energy too increases as well as heat losses. The sum of energy intercepted by the receiver and heat from the receiver will show a maximum at an optimum receiver size [56].

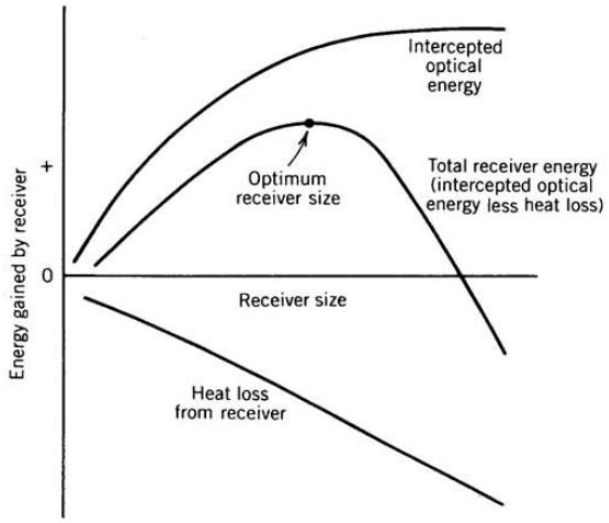

Figure 3.7. Optimization of the collector receiver size [56].

Even with an optimized receiver, heat transfer can still be limited to other geometrical limitations inherent to the type of system in operation. Fig. 3.8 provides daily energy performance data for dish, trough and flat plate collectors, averaged over a year. It is shown that for the same operating temperature of 288 °C, receiver dish systems are capable of higher absorption than N/S or E/W trough systems, for particular configurations, examined at Sandia National laboratories [48].

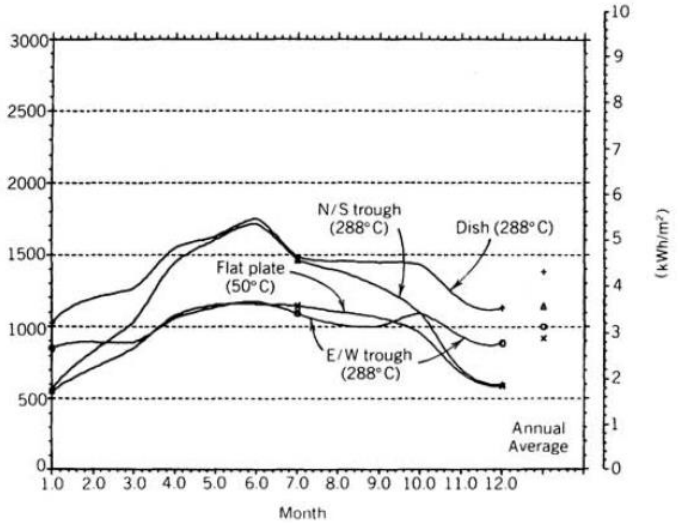

Figure 3.8. Annual performance summary of CSP collectors over a 1-year period at Sandia National Laboratories [48].

For high-temperature systems, second law analysis can have an impact in assessing overall performance based on entropy loss. An analysis by Kalogirou [55] based on a work by Bejan [57, 58] considered the maximization of power output based on the minimization of entropy, where the exergy inflow from incident solar radiation falling on a collector is provided by:

$$E_{x,in} = \dot{Q}_{Net}\left(1 - \frac{T_0}{T_{app}}\right) \tag{3.11}$$

where $\dot{Q}_{Net}$ is the net incident solar radiation on a collector, T_{app} is the apperant sun temperature as an exergy source, which according to Petela [59] is approximately equal to $3/4T_s$, where T_s is the apparent black body temperature of the sun at approximately 6000 K. Conversely the output exergy from a collector is provided [55] as:

$$E_{x,out} = \dot{Q}\left(1 - \frac{T_0}{T_r}\right) \tag{3.12}$$

The difference between $E_{x,in}$ and $E_{x,out}$ represents destroyed exergy where the entropy generation rate can be characterized by:

$$S_{gen} = \frac{1}{T_0}\left(E_{x,in} - E_{x,out}\right) \tag{3.13}$$

based on the expression:

$$S_{gen} = \frac{\dot{Q}_0}{T_0} + \frac{\dot{Q}}{T_r} - \frac{\dot{Q}_{Net}}{T_{app}} \tag{3.14}$$

Eqn. 3.14 can also be re-written as $E_{x,out} = E_{x,in} - T_0 S_{gen}$ where Fig. 3.9 illustrates the preceding entropy equations where maximum performance can be achieved with a minimum value of S_{gen}.

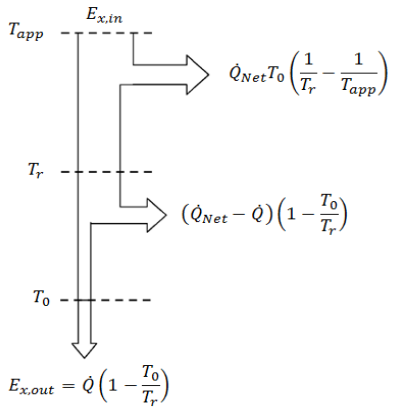

Figure 3.9. Exergy Analysis Flow Diagram [55]

Using Eqn. 3.14 in addition to a derived maximum dimensionless collector temperature θ_{max} [55] Kalogirou determined an expression for the minimum dimensionless collector temperature, θ_{opt} based on entropy minimization, Eqn. 3.15, which is derived based on Eqn. 3.16 [55]:

$$\theta_{opt} = \sqrt{\theta_{max}} = \left(1 + \frac{q_0^* C}{n_0 U_r T_0}\right)^{1/2} \tag{3.15}$$

$$\frac{S_{gen}}{U_r A_r} = \theta - 2 - \frac{q_0^* C}{n_0 U_r T_{app}} + \frac{\theta_{max}}{\theta} \tag{3.16}$$

where A_r is the receiver area, θ is dimensionless temperature, q_0^* is radiation falling on a receiver, n_0 is the collector optical efficiency U_r is the receiver-ambient heat transfer coefficient. By combining Eqns. 3.15 with 3.16 the minimum entropy generation rate, Eqn. 3.17 can be determined, where Kalogirou illustrates (Fig. 3.10) dimensionless entropy generation for three collector types based on measurements of stagnation temperature: parabolic trough (565 °C), parabolic dish (1285 °C) and a central receiver (1750 °C).

$$\frac{S_{gen,min}}{U_r A_r} = 2\left(\sqrt{\theta_{max}} - 1\right)\theta - \frac{\theta_{max}-1}{T_{app}/T_0} \tag{3.17}$$

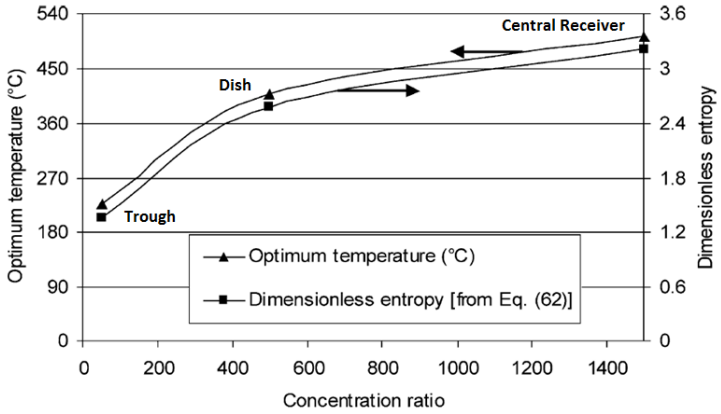

Figure 3.10. Entropy generation & optimum temperatures vs. collector solar concentration ratio for three solar collector technologies: parabolic trough, parabolic dish and central receiver [55].

3.3 Solar Selective Surface Coatings

CSP solar collectors must have high radiation absorptance in the solar energy spectrum, especially at elevated temperatures above 400 °C, where they may emit a significant amount of thermal radiation thereby losing heat to the environment [56]. It is also desirable to have long-wave emittance of the surface as low as possible to reduce losses. At very high temperatures there is an overlap of the spectral absorptance and emittance, making it difficult to develop a truly selective absorber. Selective coatings that have high absorptance for solar radiation and high transmittance for long-wave radiation can be applied to substrates with low emittance. Here the coating absorbs solar energy and the substrate acts as the poor emitter of long-wave radiation [14]. Additionally, coatings and paints must endure high temperatures in an oxidizing environment for many thermal cycles and under potentially large thermal gradients [56].

Generally, surfaces that have a low emittance value often have low absorptance, which also reduces absorbed solar energy. However, "selective coatings" facilitate surfaces that have a high absorptance (and emittance) for short wavelength (visible) light and have low average absorptance and emittance for long wavelength radiation (IR radiation) values during optimal CSP ambient conditions. These types of surfaces have property capabilities of selective tenability for both α and ε to optimize heat losses and thermal absorption with solar collectors [56]. As prescribed by the energy balance in Eqn. 3.18 to maximize the useful heat collected by a collector, high absorptance and a low emittance values are desired, where based on Kirchoff's Law, these parameters are only equal for radiation specific wavelengths:

$$\alpha_\lambda = \varepsilon_\lambda \tag{3.18}$$

From Eqn. 3.18 the employment of the subscript λ requires that these radiative terms be spectrally dependent requiring integration over all wavelengths to determine bulk property values. Principally, selective surfaces do not violate Kirchoff's law as they have high absorption for short wavelength radiation and low emittance, particularly in the IR portion of the spectrum, for long wavelength radiation. The end result is a surface that absorbs solar energy well, but does not radiate thermal energy very well [56]. This phenomenon is presented in Fig. 3.11 where 99.5% of CSP solar energy for absorption occurs generally at wavelengths below 5 μm [56]. This idealized surface is called a semi-gray surface, since it can be considered gray in the solar spectrum. However, the effect of using selective surfaces on higher temperature absorbers is less dramatic, where if the collector surface temperature is approximately 700 °C, only 43.6% of its radiated energy is at wavelengths above 5 μm and the integrated emittance is 64.5%.

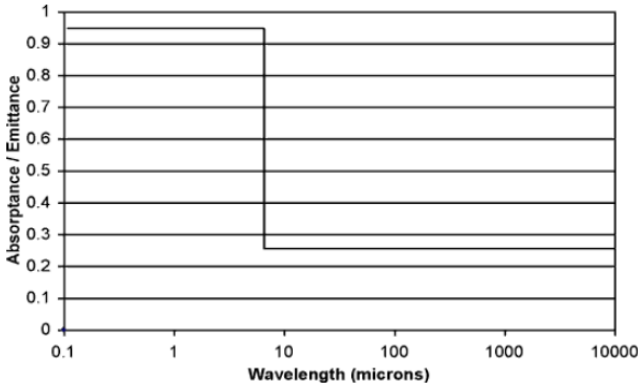

Figure 3.11. Radiation properties of a hypothetical selective surface [56].

These types of coatings, such as black chrome [60], are generally deposited as thin (2-3 μm) layers, such as by electro-deposition, where microscopic particles can effectively trap incident light, making the coating appear black. For black chrome, although it is highly absorbing in the visible spectrum, it is transparent in the IR region, therefore a collector can take on lower emittance of a potentially brighter substrate [56]. Additionally, the collector surface area can be modified to minimize radiative heat losses, where cavity receiver designs can be designed to have small openings through which concentrated solar energy can pass onto larger absorbing surfaces. Another heat loss mechanism, particularly with trough collectors is "end-loss" which is the fraction of energy being reflected from the curved surface that falls beyond the receiver due to the angle of incidence [56].

Another approach at facilitating solar selective surfaces is through geometrical surface modifications, as illustrated by Fig. 3.12. Here, directional selectivity can be obtained by proper arrangement of the surface, where deep grooves that are large relative to all wavelengths of radiation concerned, can be arranged for radiation from near-normal directions to the overall surface be reflected within the grooves absorbing a fraction of the beam. This enhanced absorption surface provides an increase in solar absorptance while increasing the long-wavelength emittance [9]. Hollands [61] demonstrated how a folded selective surface can have significantly enhance effective properties by proper configuration, where for a flat –plate collector surface that had α = 0.60 and ε = 0.05, the addition of 55° grooves, increased the average values to an effective α of 0.90 and an equivalent ε of 0.10.

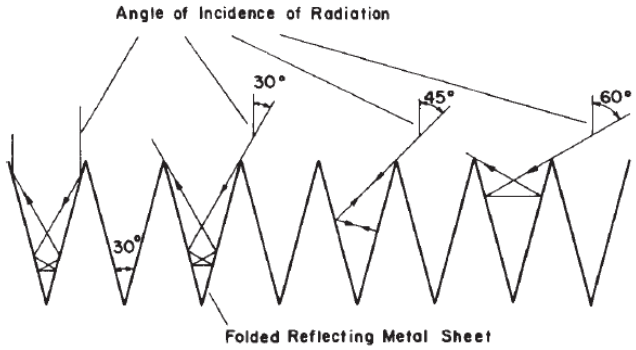

Figure 3.12. Selective geometrical surface modifications for absorption of radiation by successive reflections on folded metal sheets [9, 62].

With regards to conduction, this mode of heat loss is generally considered with respect to its cross-sectional area and temperature gradient as prescribed by Eqn. 3.19. In flat-plate collector designs, the sides and back surface of an absorber plate can facilitate heat loss, where they should incorporate good insulation properties (low k and relatively high thickness Δx) to reduce these losses. However, this heat loss mode is typically insignificant when compared to convective or radiative losses for any heat collector design, especially at high temperatures.

$$\dot{Q}_{loss,conduction} = \bar{k} \cdot \Delta\bar{x} \cdot A_{cross} \cdot (T_c - T_{amb}) \tag{3.19}$$

If insulation used within a heat transfer material facilitates a sufficiently high thermal resistance, the adiabatic approximation can typically be employed, whereby zero heat transfer occurs and Eqn. 3.19 approximately equals zero.

3.4 Collector Performance and Efficiency

The optimum azimuth angle for a flat-plate collector, considered to be the simplest form of a solar collector, is typically 0° in the northern hemisphere and 180° in the southern hemisphere [56]. A detailed overview for the calculation of solar radiation angles for flat-plate collectors can be found by [9]. There are several common methods for determining flat-plate thermal collector performance, where calculations and tests are performed on clear days with relatively high and constant solar irradiance [56]. Empirically, hot heat-transfer fluid is circulated through an absorber or receiver at a given mass flow rate, $\dot{m}$ to raise it to test temperature. For parabolic troughs, turbulent flow is maintained within the receiver tubes to ensure good heat transfer between the fluid and the wall of the tubes. A measurement is only made when the collector is at steady state, which is determined by a constant rise in heat transfer fluid temperature as it passes through the receiver [48]. There are essentially three methods for assessing collector efficiency for a flat plate collector, Fig. 3.13: collector balance, system balance and heat loss measurement methods [48]. The collector balance method is considered the most common method used for flat-plate and parabolic trough collectors where a temperature controller is typically connected to an auxillary heating and cooling device to ensure a constant fluid inlet temperature can be maintained. The rate of energy being transferred to the HTF at steady state is provided by Eqn. 3.20.

$$\dot{Q}_{useful} = \dot{m} C_p (T_{out} - T_{in}) \tag{3.20}$$

Test procedures developed at Sandia National Laboratories for this method are described by Dudley et al. [63].

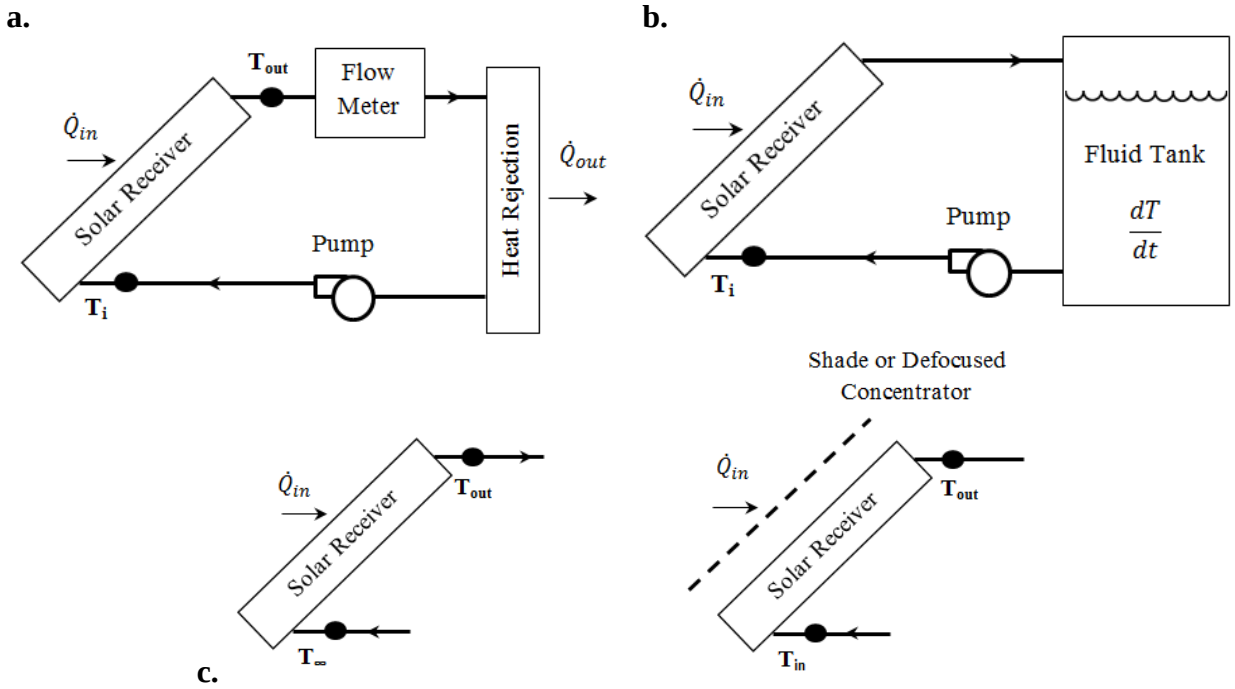

Figure 3.13. Three experimental methods for measuring collector efficiency based on a. collector balance, b. system balance and c. heat loss measurement methods [48].

For conditions where it is not easy to accurately measure fluid inlet or outlet temperatures or mass flow rate within the system, an insulated flow loop and tank can be used to facilitate a system energy balance:

$$\dot{Q}_{useful} = \dot{m}C_p \frac{dT}{dt} - \dot{W}_{pump} \tag{3.21}$$

where d*T*/d*t* represents the temperature rate increase of the tank with the HTF and $\dot{W}_{pump}$ represents the pump work entering the insulated system. For this method the amount of HTF must be large enough to ensure the bulk temperature rise does not inhibit a steady state temperature condition [48]. Normally the absorber surface should operate at a higher temperature than the HTF; however, when heat losses exist, (e.g. a defocused or shaded collector) the absorber surface will be cooler than the HTF which could result in measurement error that can indicate heat losses that are lower than would occur during normal operating conditions [48].

A third heat loss measurement method used for CSP collector systems involves two separate tests to determine thermal performance. Here the rate of optical energy collected by Eqn. 3.8 is measured where the collector HTF is operated close to ambient. Then with the second test, the collector is operated normally with a heat input where what will be lost from the receiver due to the collector-ambient temperature difference as described by Fig. 3.13c. Here the test is performed at varying collector operating temperatures where the rate of useful energy is given as:

$$\dot{Q}_{useful} = \dot{m}C_p(T_{out} - T_{in})|_{T_{HTF}-T_\infty} - \dot{m}C_p(T_{out} - T_{in})|_{\dot{Q}_{in}=0} \tag{3.22}$$

To determine solar collector efficiency, the collector aperture first needs to be aligned as close as possible to the DNI incident vector to eliminate any uncertainties due to off-normal incidence angle effects. Additionally, test data are obtained, typically at one temperature to determine the effect of varying incidence angles on collector performance [56]. Solar energy collection efficiency of thermal collectors is defined as the ratio of the rate of useful thermal energy leaving the collector to the useable solar irradiance falling on the aperture area as:

$$\eta_{col} = \frac{\dot{Q}_{useful}}{I_{inc,a}A_{Aperature}} \tag{3.23}$$

where the incoming solar irradiance falling on the collector aperture, $I_{inc,a}$, multiplied by the collector aperture area, $A_{Aperature}$ represents the maximum amount of solar energy that could be captured by that collector. Therefore, incorporation of Eqn. 3.23 into Eqn. 3.20 provides the thermal collection efficiency for flat plate collectors as:

$$\eta_{col} = \frac{\dot{m}C_p(T_{out}-T_{in})}{I_{inc,a}A_{Aperature}cos\theta_{inc}} \tag{3.24}$$

The thermal efficiency for receivers, based on collection efficiency is therefore:

$$\eta_{th} = \frac{\alpha\dot{Q}_{in}-\dot{Q}_{out}}{\dot{Q}_{in}} = \alpha - \frac{\varepsilon\sigma F_{view}T_{rec}^4 + f_{conv}\bar{h}_{conv}(T_{rec}-T_\infty)}{\eta_{field}E_{DNI}C} \tag{3.25}$$

where a parametric study by Ho and Iverson [64] found that receiver thermal efficiency was more sensitive to concentration factor *C* than with the view factor Fig. 3.14.

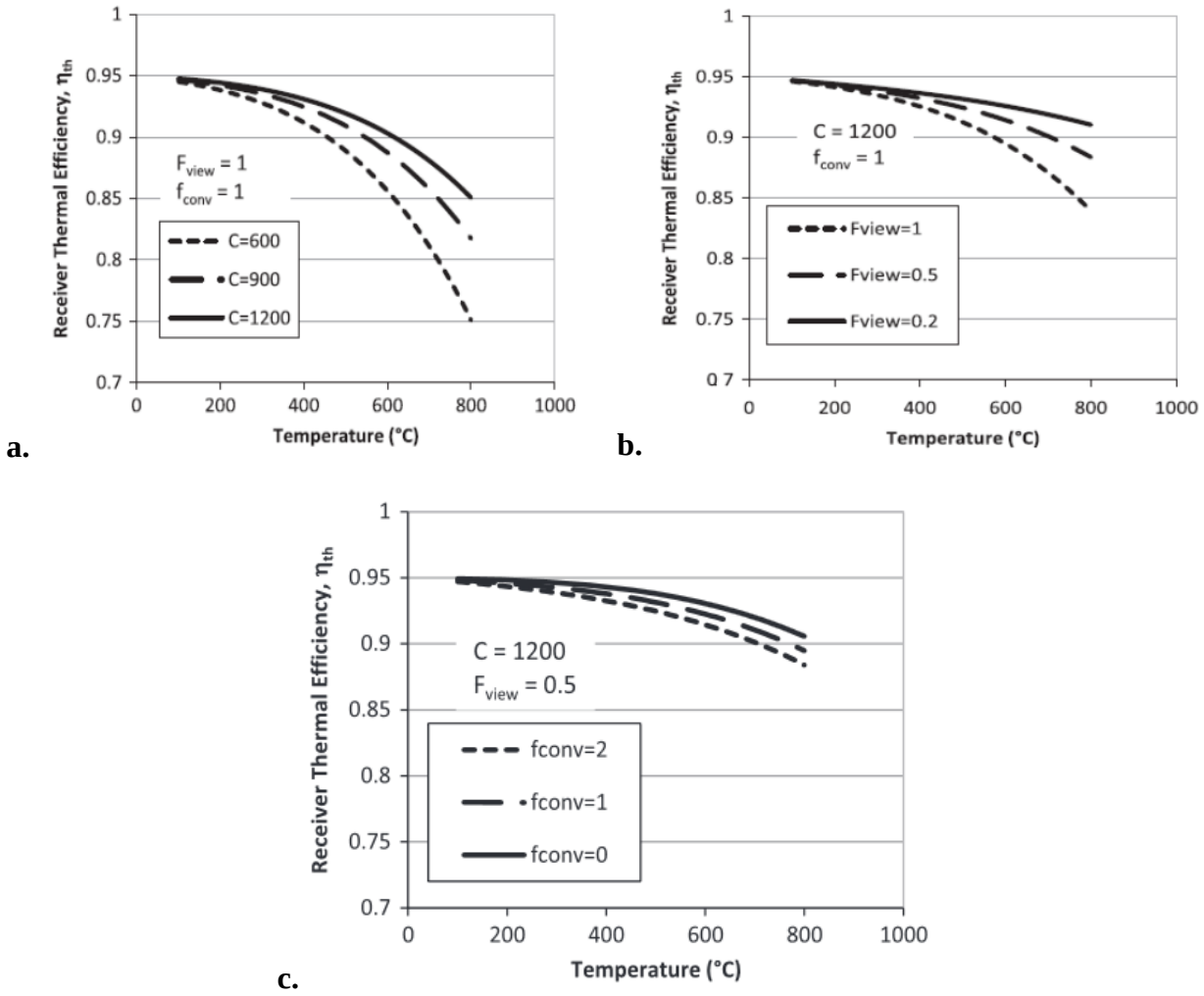

Figure 3.14. Thermal efficiency receiver plots of surface temperature with a. varying concentration ratio b. radiative view factor and c. convection heat loss [63].

Optical efficiency, as defined in Eqn. 3.26 which is defined as the rate of optical (short wavelength) energy reaching the absorber or receiver, divided by the appropriate solar resource [56]. It is determined by measurements while operating the collector at a constant inlet temperature while on-sun and then with it in a defocused orientation. This same test can be performed on a flat-plate collector by covering and uncovering the absorber with a sheet of opaque material. The efficiency of the on-sun collector to the rate of heat loss is divided by the same irradiance and aperture area with the result being optical efficiency [56].

$$\eta_{opt} = \Gamma\rho\tau\alpha \tag{3.26}$$

Finally, the balance of gains and losses within the receiver provides the total receiver efficiency as the product of Eqns. 3.25 and 3.26:

$$\eta_{Rec.} = \eta_{th}\eta_{opt} \tag{3.27}$$

Another method for enhancing optical and thermal efficiencies of CSP receivers, without the use of coatings, is through enhancement of light-trapping using fractal-like geometries. Ho *et* al. [443] developed novel fractal-like receiver geometries and features at both macro (meters) and meso (millimeters to centimeters) scales (Fig. 3.15) to increase light trapping and thermal efficiency at multiple length scales. According to the authors, advantages of this design approach could include increased solar absorptance with reduced thermal emittance.

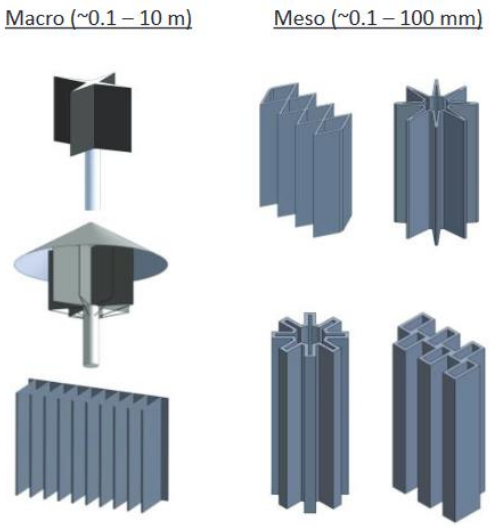

Figure 3.15. Fractal-like receiver geometries at the macro and meso-scales [443].

The results of their analytical/experimental investigation demonstrated that fractal-like structures and geometries can increase thermal efficiency by several percentage points at both meso- and macro-scales, depending on factors such as intrinsic absorptance. However, the impact was more pronounced for materials with lower intrinsic solar absorptance (<0.9) [443]. Additionally, modelling was also performed for macro-scale receiver geometries, where as illustrated by Fig. 3.16, modelled results found thermal efficiencies increased by nearly 5% with radial or linear bladed receiver configurations. Radiative losses were reduced with the fractal-like geometries due to reduced local radiative view factors in the hottest interior regions, while convective losses were slightly higher in the vertical panel configurations. Additionally, while convective losses were found to be reduced in the horizontal louvered panel configuration, the authors suggested for this configuration that heat losses from the higher temperature interior could potentially be recuperated in cooler regions which could reduce the overall convective heat loss [443].

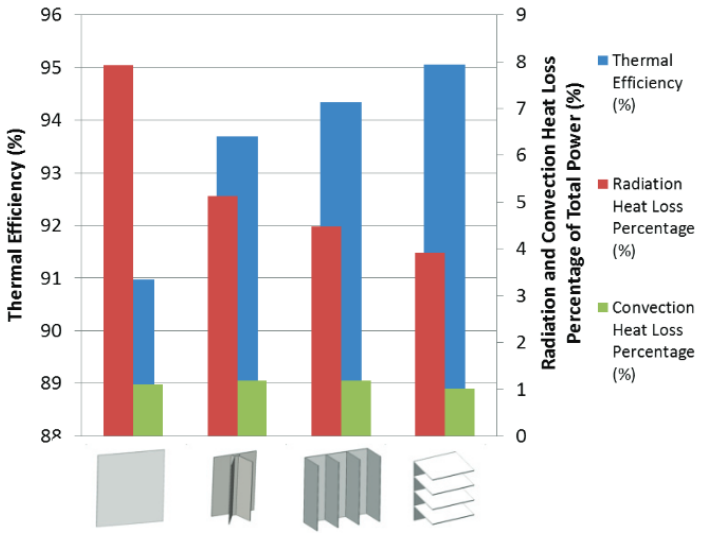

Figure 3.16. Thermal efficiency and heat losses for macro-scale receiver geometries with an average irradiance of 500 W/m2 [443, 444].

3.5 CSP System Receiver Technologies

Previous work has investigated solar transients and fluctuation in irradiance which can be mitigated by using oversized mirror fields (with solar multiples higher than 1) and making use of excess energy to load a thermal or chemical storage system [65]. However, these oversized mirror fields can increase costs where previous studies have focused on increasing receiver efficiency to reduce the overall receiver area [66]. Thermal losses for all CSP receivers include primarily convective and radiative heat losses to the ambient air and conductive heat loss through the receiver insulation. As previously discussed, radiative losses are dependent on receiver wall temperatures, shape factors and emissivity/absorptivity of receivers walls while conduction is dependent on receiver temperature and the type of insulation material employed [65]. Radiant flux and temperature are substantially higher in solar towers than in parabolic troughs, and therefore, advanced technology is involved in design as well as high-performance materials that can withstand high-temperatures. The solar receiver should mimic a blackbody by minimizing radiation losses where cavities, black-painted tube panels or porous absorbers are able to trap incident photons. For many designs the solar receiver is a single unit that centralizes all energy collected by concentrating mirrors [65]. There are different solar receiver classification criteria depending on construction solution, such as the use of intermediate materials as well as the type of HTF employed or other heat transfer mechanisms. According to geometrical configuration, there are essentially two types of design configurations: external and cavity-type receivers. Typical receiver-absorber operating temperatures are between 500-1200 °C where incident flux levels span a wide range between 300 to over 1000 kW/m^2 [65].

Receivers can also be directly or indirectly irradiated depending on absorber materials used to transfer energy to the HTF [67]. Directly irradiated receivers make use of fluids or particle streams able to efficiently absorb the concentrated radiation. Particle receiver designs however make use of falling curtains or fluidized beds, where darkened liquid fluids can also make use falling films [65]. The key design element if indirectly heated receivers is the radiative/convective

heat exchange surface. Essentially, two heat transfer options are used, tubular panels and volumetric surfaces. With tubular panels, HTF flows inside the tube and removes heat collected by the external black panel surface by convection, therefore acting as a recuperative heat exchanger. Based on the HTF properties and incident solar radiation, the tube may also undergo thermomechanical stress, and since heat transfer is through the tube surface, it may also be difficult to operate at an incident flux above 600 kW/m^2 [65]. As shown in Table 3.3 by Prakash *et* al. [65] high thermal conductivity liquids are able to better achieve operating flux levels above 1 MW/m^2 when compared to other common CSP working fluids.

Table 3.3. Operating temperature and flux ranges of solar tower receivers [65].

Fluid	Water/Steam	Liquid Sodium	Molten Salt	Volumetric Air
Average Flux (MW/m^2)	0.1-0.3	0.4-0.5	0.4-0.5	0.5-0.6
Peak Flux (MW/m^2)	0.4-0.6	1.4-2.5	0.7-0.8	0.8-1.0
Fluid Outlet Temp. (°C)	490-525	540	540-565	700-800

The operating temperature, heat storage system and thermodynamic cycle influence the design and can make selection of a receiver technology very complex. In general, according to Prakash *et* al. [65] tubular technologies allow either high temperatures (up to 1000 °C) or high pressures (up to 120 bar), but not both [68]. Directly irradiated or volumetric receivers allow even higher temperatures but limit pressures to below 15 bar [65].

3.5.1 Direct Absorption Receivers

3.5.1.1 Cavity Receivers

Cavity receivers are widely used especially with solar dish systems for providing industrial heat [69, 70] for generating electric power [71, 72] and for thermochemical reactions [73]. The cavity receivers used with these systems for process heat applications are generally cylindrical in shape, operate at medium temperatures (< 300 °C), have d/D ratios even greater than one, and may have non-uniform wall temperatures [77]. When compared to other types of receivers, cavity type receivers however have been shown to significantly reduce thermal and optical losses [74]. This receiver, as shown in Fig. 3.17a, typically consists of a receiver tube assembly enclosed within a cylindrical open cavity. Typically, the plane of the cavity aperture is placed near the focus of the parabola and normal to the axis of the parabola (also referred to as a focal plane receiver) Fig. 3.17b. Although the cavity could be linear and used with parabolic troughs, for parabolic dishes, a cavity receiver does not have stringent constraints on tube volume and pressure drop. In a cavity receiver, radiation reflected from heliostats pass through an aperture into an enclosed structure before impinging on the heat transfer surface. Cavities are constrained angularly and external receivers can be designed to be flat-plate tubular or a cylindrically shaped.

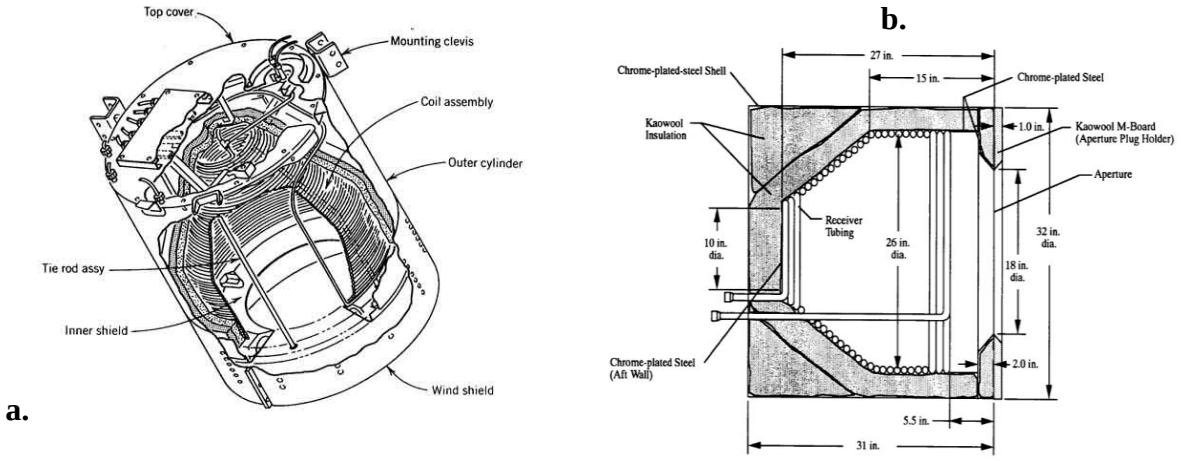

Figure 3.17. a. General overall solar cavity receiver design [75] and b. side profile of receiver cavity [76].

The effective absorptance of a cavity without a cover on its aperture, where the fraction of incident radiation absorbed by the cavity, is a function of absorptance of the inner surfaces and the ratio of the areas of the cavity as prescribed by Eqn. 3.28:

$$\alpha_{eff} = \frac{\alpha_i}{\alpha_i + (1-\alpha_i)A_a/A_i} \tag{3.28}$$

where α_i is the absorptance of the inner surface of the cavity, A_a is the area of the aperture and A_i is the area of the inner surface. Duffie and Beckman recommends as an approximation that α_i can be evaluated at the effective angle of incidence of diffuse radiation, around 60° [9].

The overall efficiency of these systems is dependent on the thermal losses occurring from the cavity receiver, where it is observed from literature that convective heat transfer constitutes the largest share of thermal losses [77-79]. These losses are found to be dependent on receiver inclination $\theta_{inc,rec}$ receiver wall boundary condition, aspect ratio (L/D), opening ratio (d/D) and magnitude/direction of the external wind [77]. Experimental and numerical investigations on natural convection losses in cavity receivers used with solar dish concentrators have been performed on different cavity shapes. Stine and McDonald [9] have performed experimental studies on conical frustum-cylindrical cavity receivers while Kugath et al. [445] has performed field studies on a similar receiver shape at medium temperature levels. Cylindrical shaped cavity receivers have been analyzed experimentally and numerically [65, 78, 80]. Numerical investigations on hemispherical cavity receivers have been carried out by Sendhil, Kumar and Reddy [79, 81]. Prakash investigated the impacts of wall temperatures, receiver inclination, and d/D ratio on natural convection losses and developed Nusselt number correlations to assess losses due to convection [77].

Radiation and conduction heat losses from the receiver can be predicted reasonably well by analytical techniques where convection from the cavity is much more complicated and generally not amenable to analytical predictions [76] due to wind effects and varying receiver orientation. Therefore, convective heat loss from cavity receivers is typically determined empirically [65]. Design correlations for estimating natural convective heat loss from cavity

receivers are usually derived experimentally. For cavity receivers convective heat loss can be directly calculated as [82]:

$$\begin{aligned} \dot{Q}_{Conv} &= \dot{Q}_{Forced} + \dot{Q}_{Nat} \\ \dot{Q}_{Forced} &= 7631 \frac{A}{W_{ap}^{0.2}} \\ \dot{Q}_{Nat} &= 5077 A_{Cav} \end{aligned} \tag{3.29}$$

where A is the aperture area, W_{ap} is the aperture width, and A_{cav} is the total area inside the cavity. Further detailed convection loss correlations for other types of solar receivers can be found by Becker and Vant-Hull [67]. Koenig and Marvin [83] performed experiments where they developed correlation Eqns. 3.30 and 3.31 for average natural convection. Stine and McDonald [80] found however that natural convective heat loss is better predicted if the coefficient of 0.78 is used instead of 0.52 and if the full geometric surface area of the cavity is used.

$$\overline{Nu}_L = \frac{\bar{h}_L}{k_f} = 0.78 P(\theta) l_C^{1.75} (Gr_L Pr)^{0.25} \tag{3.30}$$

$$\dot{Q}_{Conv.} = \bar{h}_L A \left(T_{Cavity} - T_\infty\right) \tag{3.31}$$

where all fluid properties are evaluated at $T = 11/16 T_{Cavity} + T_\infty$, θ is the receiver tilt angle, β is the coefficient of thermal expansion of air equal to $1/T$, where $l_C = R_{aperature}/R_{Cavity}$, $L = \sqrt{2} R_{Cavity}$ and T_{Cavity} is the average temperature of the cavity heat transfer tubing. Additionally, the following parameters are defined as follows:

$$\begin{aligned} P(\theta) &= cos^{3.2}\theta \qquad for\ 0° \le \theta \le 45° \\ P(\theta) &= 0.707 cos^{2.2}\theta \quad for\ 0° \le \theta \le 45° \end{aligned} \tag{3.32}$$

Siebers and Kraabel [84] reported the following correlation for predicting turbulent natural convection from a central receiver cavity, over a range of $10^5 \le Gr_L \le 10^{12}$:

$$\overline{Nu}_L = 0.088 Gr_L^{1/3} \left(\frac{T_w}{T_\infty}\right)^{0.18} \tag{3.33}$$

where T_w is the average internal wall temperature and L is the characteristic height of the cavity. Eqn. 3.33 was derived based on results of a large 2.2 m cubical cavity experiment developed by Kraabel [85], and experiments of 0.2 m and 0.6 m cubical cavities performed by LeQuere, Penot and Mirenayat [86]. Stine and McDonald [80] later performed natural convective cavity receiver heat loss experiments that included effects of different receiver temperatures, tilt angles and aperture sizes, which provided the correlation:

$$\overline{Nu}_L = 0.088 Gr_L^{1/3} \left(\frac{T_w}{T_\infty}\right)^{0.18} (cos\theta)^{2.47} \left(\frac{d}{L}\right)^s \tag{3.34}$$

where $s = 1.12 - 0.982(d/L)$, d is the aperture diameter and L is the receiver internal diameter at the cylindrical region. For this correlation the heat transfer area depends on whether solar

insolation is present, however for off-sun applications, only the portion of the receiver interior geometric surface area covered with heat transfer tubing should be considered [76].

Siebers and Kraabel [84] suggest as a first approximation that forced and natural convection components from a cavity receiver be simply added together to obtain the total convective heat loss. Clausing [87] performed simplified numerical experiments which calculated convective heat losses in a large central cavity receiver based on first law principles and the energy transferred from the hot receiver interior walls to the air inside the cavity. They also considered the energy transfer across the aperture by the combined influences of flow over the aperture due to wind and buoyancy-induced flow due to the cooler ambient air. The results of the numerical work by Ma [76] suggest that the influence of wind at 18 mph or less is minimal. This finding is in agreement with the experimental results of McMordie [88] who examined wind effects on convection from central cavity receivers. As a base line analysis, Fig. 3.18, Ma analyzed 3 different wind speeds on a receiver with a temperature of 277 °C and found that convective heat loss from the receiver was highest with the receiver facing horizontally (0°) and lowest with the receiver facing straight down (90°). With the receiver in a horizontally-facing orientation, natural convective heat loss was approximately 2 kW and with the receiver facing straight down these losses were presumed to be zero [76].

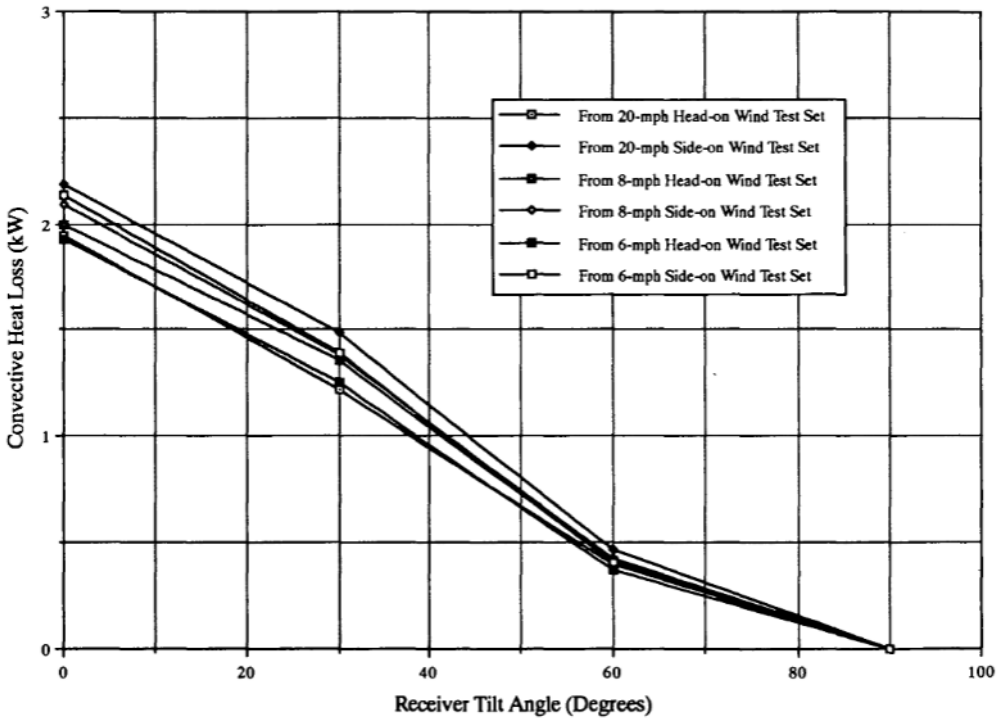

Figure 3.18. Natural convection heat loss from a cavity receiver at 277 °C [76].

The natural convective heat loss contribution was found to decrease as the receiver was tilted downward due to a larger portion of the receiver volume being in the stagnant zone as illustrated in Fig. 3.19. The authors found that convective currents are virtually non-existent and air temperature is high, as well as a smaller portion being in the convective zone where significant air currents exist. It has been observed by Siebers and Kraabel [84] and Clausing [87] that the interior

volume above the horizontal plane passing through the uppermost portion of the aperture is relatively stagnant, consisting of high-temperature air.

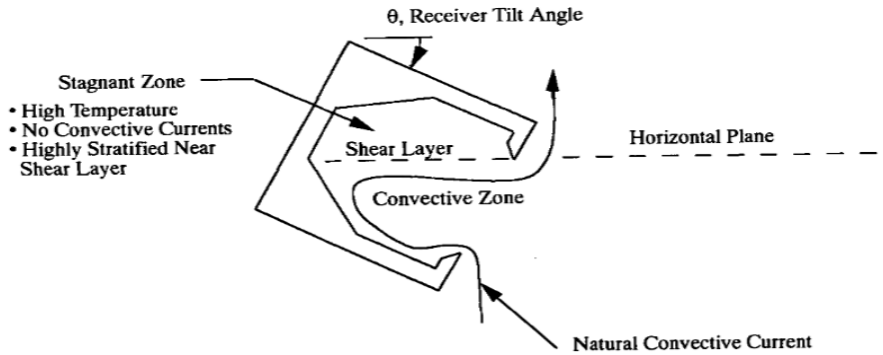

Figure 3.19. Cavity receiver diagram of stagnant and convective zones [76].

During nominal operation, natural convective currents flow inside the receiver from bottom to top, in a vertical plane. Several investigators [65, 76] have found that the orientation of a cavity receiver with respect to wind magnitude and direction can have a significant impact on forced convection heat losses. Numerical investigations by Prakash *et* al. [65] examined convective heat losses from a downward facing cylindrical cavity receiver, over varying inlet fluid temperatures between 50-300 ^{o}C and receiver inclinations between 0-90°. The investigators found that the convective losses increase with mean receiver temperature and decrease with inclination. The authors also found that wind induced convective losses are generally higher than with no wind (varying between 22-75% for 1 m/s wind speed and between 30-140% for 3 m/s wind speed). Fig. 3.20 provides a parametric view of convection phenomena for different wind directions and cavity tilt angles.

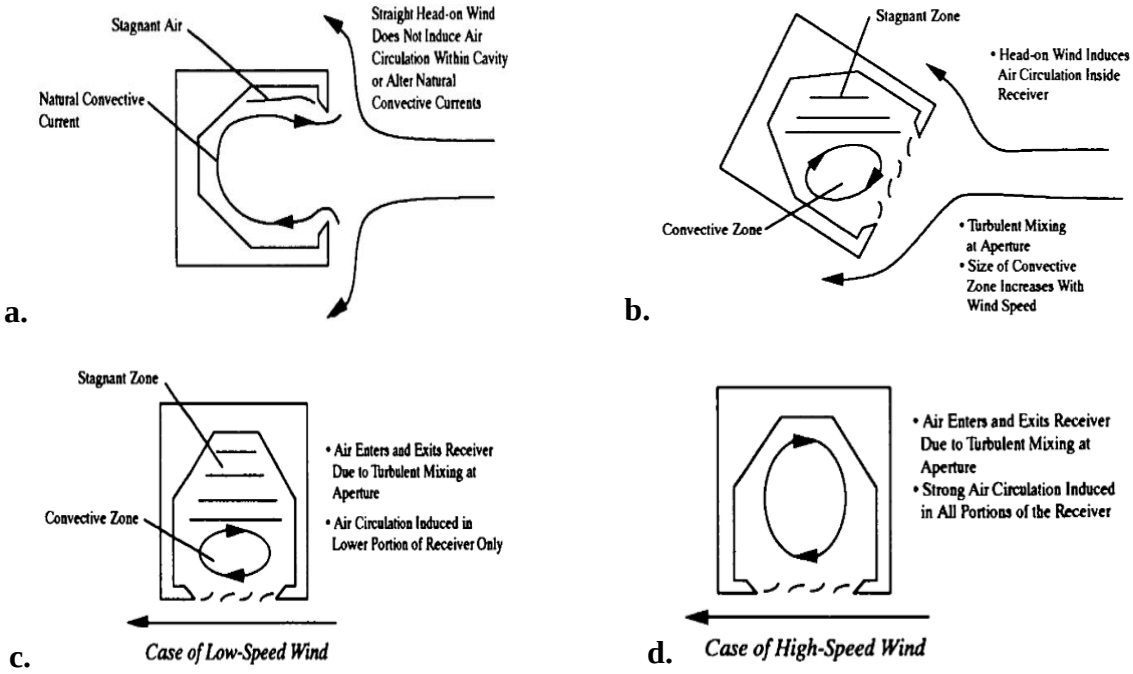

Figure 3.20. Graphical depiction of natural convection zones within a cavity receiver for tilt angle orientations of a. 0°, b. 30°, 60° and 90° [76].

For side-facing winds, forced convective currents are generally in a direction normal to the plane of natural convective currents. Because of this orthogonal relationship between natural and forced convective currents, it is reasonable to approximate that forced convection from the receiver is independent of natural convection. In addition, pure forced convection should change minimally as the receiver tilt angle changes. In the absence of gravity, side-on wind convective heat loss would be the same for any receiver tilt angle [76]. From data collected for side-on winds, Ma produced the Eqn. 3.35 curve fit for pure forced convection as a function of wind speed:

$$\bar{h}_{forced} = 0.1967V^{1.849} \tag{3.35}$$

where *V* is the velocity of side-on directional wind. This equation is based on full interior geometric surface area of the receiver, where the exponential value of 1.849 is much larger than the value of 0.8 provided by the general Nusselt correlation for turbulent heat transfer from a flat plate:

$$\overline{Nu}_L = \frac{\bar{h}L}{k_f} = 0.037Re_L^{0.8}Pr^{1/3} \tag{3.36}$$

According to Ma [76] the value of 1.849 is closer to that normally associated with shear stress, which suggests that the determining factor for heat transfer from the cavity may be the ability of wind to transfer mass and energy across the aperture via fluid shear and not necessarily the ability of the receiver walls to transfer energy to the air inside the cavity, which is consistent with findings by Clausing [87]. For head-on winds with the assumption that both natural and forced convection components are additive, Ma found that increased convective head loss was described by:

$$\bar{h}_{forced} = f(\xi)V^{1.401} \tag{3.37}$$

$$f(\xi) = 0.1634 + 0.7498sin\theta - 0.5026sin2\theta + 0.3278sin3\theta \tag{3.38}$$

McMordie found that for winds of 3 to 15 mph, wind speed and direction effects were also indistinguishable. However, Kugath et al. [69] measured effects of a 10 mph wind on convective heat loss from a cavity receiver and found convective heat loss to be highly dependent upon receiver orientation. The highest convective heat loss for that study was observed with wind blowing directly into the cavity, being as much as four times the level of natural convection. They also found that for wind blowing directly behind the receiver, total convective heat loss was not much higher than pure natural convection. An experimental investigation conducted by Faust et al. [89] showed that a noticeable increase in receiver convection occurred with a wind speed of only 2 mph. In their experiment the investigators observed winds parallel to the aperture plane result in the highest convective heat loss, where the authors concluded that with wind blowing in this direction, the aperture lies in the separation region and is subjected to the suction pressure of the air flow. However, the authors also found that winds perpendicular to the aperture plane were convective heat loss because flow stagnation supposedly decreases the responsible for natural convection.

Solar cavity receivers used for high temperature applications are generally modeled as plain walls with isothermal boundary conditions and have d/D ratios equal to or less than one [79, 90]. Numerical modeling of the cylindrical cavity receivers encountered in process heat applications (< 300 °C) is limited. Numerical studies performed by Prakash *et* al. [65, 91] have been carried out on such a cavity receiver. The use of Fluent CFD software for modeling the

receiver tubes and the flow within the tubes has been demonstrated by these studies for the cavity receiver having d/D ratio greater than one. It is therefore noticed that numerical study of natural convection loss from cylindrical cavity receivers of various diameters used for process heat applications at temperature levels of about 150°C–250°C having d/D ratio of 1 and 0.5 and inclined at different angles has not been performed. The use of Fluent CFD software for modeling the receiver tubes and the flow within the tubes has been demonstrated by these studies for the cavity receiver having d/D ratio greater than one.

3.5.1.2 Direct Absorption Particle Receivers

In a solar receiver, heat is transferred to an HTF, which transports this energy to a conversion sub-system that includes heat storage, heat exchangers, and a power block. Since existing CSP HTFs have drawbacks due to limited working temperatures such as salts (~240-565 °C), corrosion and safety limitations such as liquid metals, solid particles as an HTF have been demonstrated to reach operating temperatures as high as 750 °C and flux densities as high as 250 kW/m^2 [92]. Preliminary studies have shown that for a receiver design power of 395 MW_{th} and an outlet temperature of 800 °C a receiver efficiency of approximately 90 % can be achieved. Additionally, by applying a favorable operation strategy, a receiver efficiency of up to 67 % at 20%-part load condition can be possible [93]. The optimum applicable power range for one receiver is expected to be between 50 and 400 MW_{th} [94]. The maximum receiver temperature can be found in the HTF and on the receiver material which leads to decreased radiation losses and material stress and fatigue. Open particle receivers currently feature solid particles surrounded by a gaseous fluid. This can have several advantages such as increased radiation absorption, high heat capacity or lower material temperature towards the surroundings. Different particulate materials and designs have been studied for these systems, including direct-heating receivers with free-falling particles, Fig. 3.21a or obstructed particle flows Fig. 3.21b.

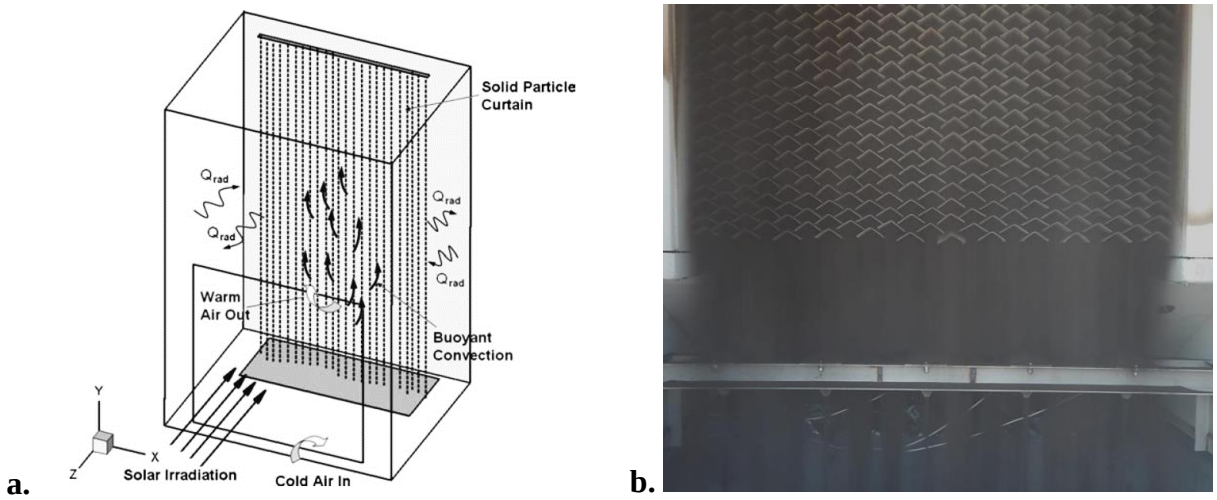

Figure 3.21. a. Illustration of a direct solid-particle receiver with hydrodynamic and thermal processes [96] and b. obstructed particle receiver flow design [95].

In another embodiment or the falling particle receiver Wu et al. [94] considered a cavity particle receiver with a non-rotating feed hopper inlet Fig. 3.20a and a centrifugal particle receiver Fig. 3.21b with rotating particle inlet. In their study the authors use bauxite particles as an HTM that had an absorption coefficient of approximately 0.8-0.9 and a heat capacity between 1000-1250 J/kg-K for the investigated temperature range. As shown in Fig. 3.20a the particles were transported to a feed hopper at the top of a face-down cylindrical cavity. While the particles fall down through an inlet slit to a collecting ring at the receiver bottom, a free falling curtain parallel to the inner cavity wall is formed. Solar radiation enters the receiver through the open aperture and is directly absorbed by the particle curtain. Similar to other cavity receivers, this design took advantage of reduced radiation losses due to the face-down design while allowing the particle curtain to be protected against the impacts of wind. An efficient recirculation strategy was also leveraged to realize optically dense curtains for high absorptivity and hence to increase the receiver efficiency. From their Matlab-based preliminary CFD models the instigators found for a face-down cavity, with a design power of 3 MW_{th}, that wind speeds between 5–15 m/s with particles lead to convective losses around 2.5–6.5 %. These losses were found to be significant, where consideration is required especially for large-scale power plants with tower heights up to 300 m [94].

A second particle receiver concept, Fig. 3.22b, entails a centrifugal particle receiver that combines high receiver efficiency which could be well-suited for decentralized small-scale CSP applications in the power range of 0.1 to 1 MW_{th}, as well as for systems up to 200 MW_{th}. Preliminary analysis for a 1 MW_{th} plant found for diameter to height ratio of 1.5, reflection losses of approximately 3% were determined. Using the Stefan-Boltzmann law the expected radiation losses for an aperture size of 1.13 m^2, over a temperature range between 600-1000 °C, were 9% [94]. Additionally, the investigators suggested that receiver rotation was able to reduce convection losses.

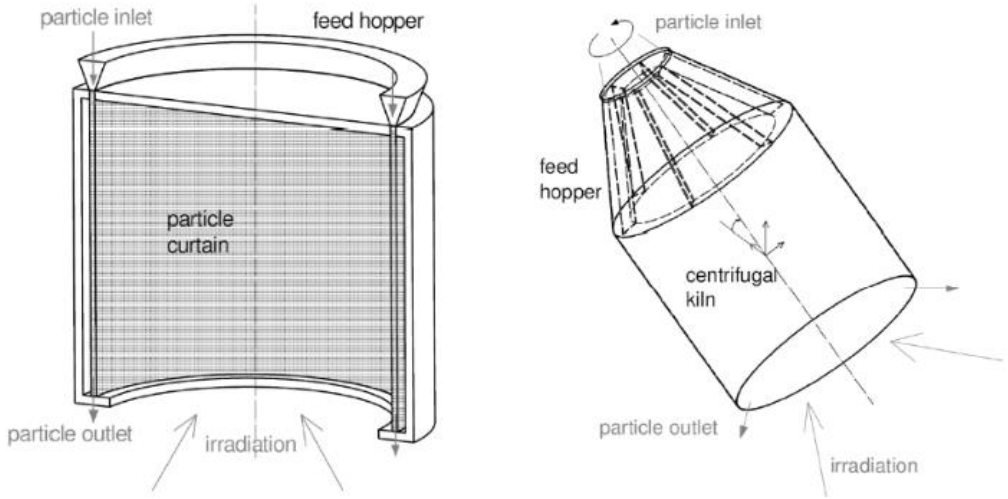

a. **b.**

Figure 3.22. Direct particle receivers by DLR for a. non-rotating particle injection cavity receiver and a b. rotating inlet centrifugal particle receiver. [94].

With regard to demonstrated falling particle receiver performance, at the National Solar Thermal Test Facility (NSTTF), Sandia National Laboratories recently completed a 3½-year project funded by the DOE SunShot Initiative to develop a high-temperature falling particle receiver, Fig. 3.23. Here, sand-like ceramic particles are heated as they fall through a beam of highly concentrated

sunlight [97]. The falling-particle receiver enables concentrated solar power with thermal storage for on-demand electricity production and process heat at significantly high temperatures (up to 1000 °C and higher), which can increase power cycle efficiencies and reduce levelized costs. Sandia constructed and successfully demonstrated this continuously, recirculating high-temperature 1 MW_{th} falling particle receiver achieving peak particle temperatures over 900°C with bulk temperatures over 800 °C [97]. The particle heating rate reached 100–300°C per meter of illuminated drop distance, at concentrated solar irradiances of approximately 1,000 kW/m^2 and thermal conversion efficiencies of approximately 80% [97].

Figure 3.23. Falling particle receiver at Sandia National Laboratories [97].

A design approach for CSP particle receivers is through fluidization of falling gas-particle mixtures. Fluidized flow heat transfer is the object of much research, especially in the area of combustion due to the potential of high heat transfer to immersed surfaces, which can reach temperatures on the order of 1000 K [98]. For large thermal input conditions, large gas flows are required when the temperature is raised to a point where agglomeration occurs [99, 100]. However, as agglomeration intensifies, convection heat transfer coefficients have been shown to reduce [100] due to decreased particulate mixing. This presents a fundamental challenge for particles at lower flow velocities which are required to enhance residence time. For fluidization, there are four primary modes of heat transfer [101]: bed-to-surface, inter-particle, gas-to-particle, and particle-to-particle heat transfer. Many studies have investigated bed-to-surface heat transfer, such as the work by Basu and Nag [102] who divided the overall heat transfer coefficient into components of particle conduction and gas convection. Particle convection has been previously modeled by a film model by Heered [103] and Mahalingam and Kolar [104], a packet or cluster renewal model by Mickley and Fairbanks [105] and Subbaro and Basu [106], single particle model by Brotteril and Williams [107] and Martin [108]. Gas-to-particle heat transfer components have been modeled by Eckert and Drake [109] and Wen and Miller [110]. Additionally, particle-to-particle heat transfer can result from three main mechanisms: heat transfer by radiation, heat conduction through the contact points between the particles, as well as heat exchange through the gas layer separating the particles. The first mechanism is only significant at temperatures higher than 600 °C, while the second occurs when moving particles collide and heat is conducted through the impact area.

Gas-solid particle systems in CSP applications use fluidized-bed technology for heat exchange and packed particles for thermal energy storage (TES) applications. When particle-TES is implemented in a fluidized-bed (FB) CSP plant, hot-solid particles discharge from the TES hot storage system to a FB heat exchanger for power generation. The separated outlet cold particles from the power block system then recirculate through a particle receiver for solar heat absorption and for charging the particle-TES [111].

Analytical modeling has increasingly been accepted as an effective method to study heat transfer phenomena of particle-fluid systems [112]. Current approaches for modelling particle flow and thermal behavior can be classified into two categories: the continuum approach (Eularian-Eularian) at a macroscopic level, and a discrete modelling approach at a microscopic/particle level (Eularian-Lagrangian). Table 3.4 provides a recommended modelling approach for various gas/solid models and scales.

Table 3.4. Model recommendations of solid particle and gas phase dynamics [113].

Name	Gas Phase	Solid Phase	Gas-Solid Coupling	Scale
Discrete Bubble Model	Lagrangian	Eularian	Drag Closures for Bubbles	Industrial (10m)
Two-Fluid Model	Eularian	Eularian	Gas-Solid Drag Closures	General Engineering Applications (1m)
Unresolved Discrete Particle Model	Eularian (Unresolved)	Lagrangian	Gas-Particle Closures	Laboratory-Scale (0.1m)
Resolved Discrete Particle Model	Eularian (Resolved)	Lagrangian	Boundary Condition at Particle Surface	Laboratory-Scale (0.01m)
Molecular Dynamics	Lagrangian	Lagrangian	Elastic Collisions at Particle Surface	Mesoscopic-Scale (<0.001m)

For the continuum approach, the macroscopic behavior is described by conservation equations of mass, momentum and energy that are then closed with constitutive relations with initial and boundary conditions [114-116]. One of the most widely used models, the two-fluid model (TFM), accounts for both fluid and solid-phases, treated as interpenetrating continuum media in a computational cell, which is much larger than individual particles but still small compared with the size of process equipment [114]. However, it's utility depends on the constitutive or closure relations for the solid phase and the momentum exchange between phases which is often difficult to obtain [112].

The discrete approach however considers a finite number of discrete particles interacting by means of contact and non-contact forces. When coupling with fluid flow, DPS is often coupled within a computational fluid dynamics (CFD) framework [112]. Here, the flow of a continuum fluid can be determined by solving Navier-Stokes equations while coupling CFD and DPS through particle-fluid interaction forces [117, 118]. The main advantage of DPS-CFD is that it can generate detailed particle-scale information, such as the trajectories and forces pertaining to individual particles, important for determining mechanisms governing complex flow behavior [112]. With the DPS-CFD approach, information such as particle-particle or particle-wall contact, local porosity and local gas-solid flow structure can be produced, which is essential in determining heat transfer behavior of individual particles [112]. Chen *et* al. [96] developed a CFD model for an open particle receiver in the form of a curtain of ceramic particles between 200 μm and 600 μm in size, where their simulations show good agreement with experimental results. The calculated receiver efficiencies were found to be approximately 70% for particle outlet temperatures of less than 1000 K. Cocker and Miller [119] modeled a cylindrical volumetric receiver with air and carbon nanoparticles as the HTF. Their initial CFD simulations suggest fluid outlet temperatures

of up to 1430 K. As new particle and receiver material stability issues are resolved for temperatures greater than 750 °C [95], thermal efficiencies of solar particle receivers are expected to reach 90% [120], however there are still heat transfer issues, such as particle-fluid and particle-wall-fluid interactions that still need to be resolved.

Zhou *et* al. [121, 122] proposed a comprehensive model taking into account most known heat transfer mechanisms. This approach considers particle-fluid convection, particle-particle conduction, and particle radiation. The extended DPS-CFD model offers a useful numerical technique to elucidate the fundamentals governing heat transfer in packed/fluidized beds at a particle scale. Overall, various methods have been developed for DPS simulation [123]. In general, a particle passing through a particle-fluid flow system can either exhibit translational and/or rotational motion, determined by Newton's second law of motion [112]. The corresponding governing equations for a particle *j* acting on a particle *i* that has a radius *r*, mass *m* and moment of inertia *I* can be written as:

$$m\frac{d\vec{V}_i}{dt} = f_{int,i} + \sum_{j=1}^{N_p}\left(f_{e,ij} + f_{d,ij}\right) + m_i g \tag{3.39}$$

$$I_i\frac{d\omega_i}{dt} = \sum_{j=1}^{N_p}\left(M_{t,ij} + M_{r,ij}\right) \tag{3.40}$$

where $\vec{V}$ and ω are the translational and angular velocities of the particle respectively. The forces f considered within these equations are: particle-fluid interaction force $f_{int,i}$, the gravitational force $m_i g$, and inter-particle forces between particles which include the elastic force $f_{e,ij}$ and viscous damping force $f_{d,ij}$. These inter-particle forces can be resolved into the normal and tangential components at a contact point [123]. The torque acting on particle *i* by particle *j* includes two components: $M_{t,ij}$ which is generated by tangential force and causes particle *i* to rotate, and $M_{r,ij}$ which is generated by asymmetric normal forces that slows the relative rotation between particles. A particle may undergo multiple interactions where the individual interaction forces and torques are summed over the N_p particles interacting with particle *I* [123]

Interaction forces and torque determined between two particles (approximated as spheres) have previously been established by several investigators [123]. According to Zhou *et* al. [112] there are approximately nine particle-particle interaction forces which impact solid-particle heat transport and are non-linear. Additionally, many correlations are available in the literature to calculate the fluid drag acting on individual particles [124, 125]. The heat transfer of particle *i* and its surroundings is considered to be controlled by three mechanisms: particle-fluid convection, particle-particle or particle-wall conduction, and radiation. According to the energy balance, the governing equation for particle *i* can be generally written as [112]:

$$m_i C_{p,i}\frac{dT_i}{dt} = \sum_{j=1}^{N_p}\dot{Q}_{i,j} + \dot{Q}_{i,f} + \dot{Q}_{i,rad} + \dot{Q}_{i,wall} \tag{3.41}$$

where N_p is the number of particles exchanging heat with particle $\dot{Q}_{i,j}$ is the heat exchange rate between particles *i* and *j* due to conduction. Additionally, $\dot{Q}_{i,f}$ is the heat exchange rate between particle *i* and its local surrounding fluid, $\dot{Q}_{i,rad}$ is the heat exchange rate between particle *i* and its surrounding environment by radiation, and $\dot{Q}_i$,wall is particle-wall heat exchange rate. $C_{p,i}$ is the particle specific heat.

Convective heat transfer between particles has been previously studied with various equations proposed [126, 127] where originally the convective heat transfer rate between particle *i* and fluid *f* was calculated according to Eqn. 3.42.

$$\dot{Q}_{i,f} = h_{i,conv} A_i \left(T_{f,i} - T_i\right) \tag{3.42}$$

where A_i is the particle surface area, $T_{f,i}$ is fluid temperature in a computational cell where particle i is located, and $h_{i,conv}$ is the convective heat transfer coefficient. $h_{i,conv}$ is associated with the Nusselt number for air, which is a function of particle Reynolds number and gas Prandtl number:

$$Nu_i = \frac{h_{i,conv} D_i}{k_f} = 2.0 + a Re_i^b Pr^{1/3} \tag{3.43}$$

where k_f and D_i are the fluid thermal conductivity and particle diameter, respectively. Re_i is the local relative Reynolds number for a particle *i*. The constant, 2.0, represents the contribution by particle-fluid natural convection where *a* and *b* are parameters determined empirically [112]. Kunii and Levenspiel [127] suggest a value of b = 0.5, with a potential range based on bed conditions of 0.6-1.8. For heat transfer at the fluid-wall interface Eqn. 3.44 is suggested [112] for determining the heat transfer coefficient $h_{f,wall}$ where D is the hydraulic diameter, and the exponent n is 0.4 for heating, and 0.3 for cooling [128].

$$Nu_i = \frac{h_{f,wall} D}{k_f} = 0.023 Re^{0.8} Pr^n \tag{3.44}$$

For conduction heat transfer between particles, Fig. 3.24, there are two primary mechanisms that are generally considered by several authors [129, 130] which include: a. particle-fluid-particle conduction and b. particle-particle conduction as described by Zhou *et* al. [121].

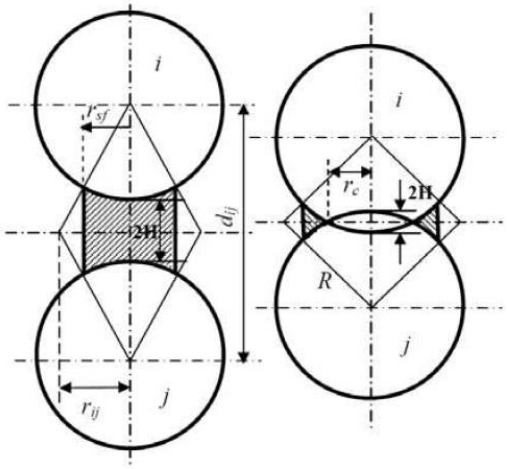

Figure 3.24. Diagram for the relative positions of two particle spheres that are in a. non-contact and b. contact with overlap [121].

A model developed by Cheng *et* al [130] and Zhou *et* al. [112] is provided by Eqn. 3.45 where the heat flux between two particles *i* and *j* are approximated as spheres and where k_{pi} and k_{pj} are the respective thermal conductivities.

$$\dot{Q}_{i,j} = \left(T_j - T_i\right) \int_{r_{sij}}^{r_{sf}} \frac{2\pi \cdot r dr}{\left(\sqrt{R^2 - r^2} - r\,(R+H)/r_{ij}\right) \cdot \left(1/k_{pi} + 1/k_{pj}\right) + 2\left[(R+H) - \sqrt{R^2 - r^2}\right]/k_f} \tag{3.45}$$

For this formulation conduction heat transfer between particles occurs through the contact area or between particles and the wall, due to elastic deformation based on two mechanisms: 1. conduction due to particle-particle static contact (packed bed) and 2. conduction due to particle-particle collision (typically associated with a fluidized bed) [112]. For static particle-particle conduction a formulation by Cheng *et* al. [130] can be employed:

$$\dot{Q}_{i,j} = \frac{4r_c(T_j - T_i)}{(1/k_{pi} + 1/k_{pj})} \tag{3.46}$$

Conversely, for particle-particle heat transfer due to collision, a modified formulation of the Sun and Chen [131] model by Zhou *et* al. [112] can be used:

$$\dot{Q}_{i,j} = c' \frac{(T_j - T_i)\pi r_c^2 t_c^{-1/2}}{(\rho_{pi} c_{pi} k_{pi})^{-1/2} + (\rho_{pj} c_{pj} k_{pj})^{-1/2}} \tag{3.47}$$

where r_c and t_c are particle-particle contact radius and contact duration respectively. As prescribed by Zhou *et* al. [112] for a particle-wall static or collision contact, a wall can be treated as a particle with an infinite diameter and mass.

With regard to radiation heat transfer contributions, an environmental temperature is generally assumed to represent the enclosed surface temperature around a particle according to Eqn. 2.21 where the parameter T can be taken as an averaged temperature between the particles and the fluid by volume fraction in an enclosed spherical domain Ω provided by [121] where $T_{f,\Omega}$ and k_Ω are the fluid temperature and number of particles located in the domain Ω.

$$T = T_{local,i} = \varepsilon_f T_{f,\Omega} + \left(1 - \varepsilon_f\right) \frac{1}{k_\Omega} \sum_{j=1}^{k_\Omega} T_j (j \neq i) \tag{3.48}$$

For high temperature gas-particle systems, radiation heat transfer can become the dominant mode of energy transport, where it is important to resolve the processes of absorption, emission, and scattering for an investigated media. However, particle-gas prediction modelling may also take a stochastically distributed [448, 449] approach, where attenuation of radiation in a randomly-distributed particulate medium can be derived using the Poison Eqn. 3.49:

$$P_N = \frac{\lambda^N exp(-\lambda)}{N!} \tag{3.49}$$

where P_N is the probability, and λ is the expectation of the number of particles, N in a specified volume. However, the attenuation of radiation in a particulate medium can deviate from traditionally-employed Poison distributions, as illustrated by Fig. 3.25a, due to impacts related to time evolution and/or external forcing such as with turbulent flow [450, 451]. During turbulent particle-laden flows, particles are carried by the surrounding fluid that may undergo frequent velocity fluctuations. This can impact the particle inertia and cause particle velocities to lag the

local fluid velocity, leading to a segregation of particles out of regions of high fluid vorticity and into regions of high shear [447].

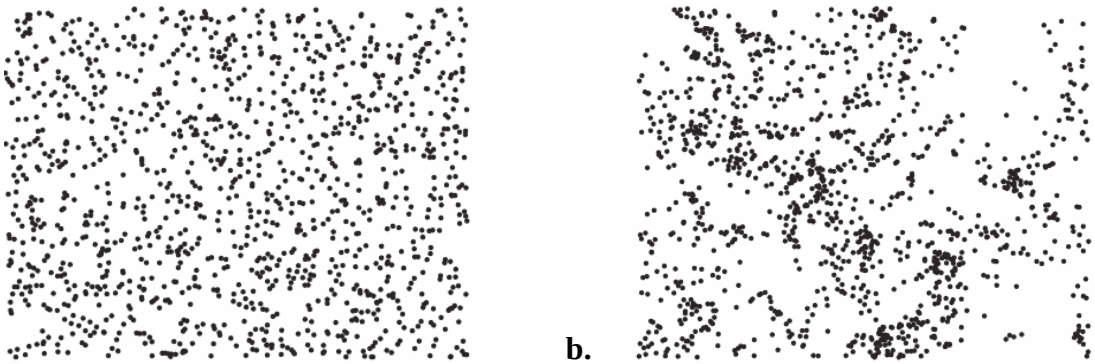

a. **b.**

Figure 3.25. Illustrative comparison of an a. Poison particle distribution and b. turbulence-clustered particle distribution [447].

Radiation transport can be further complicated as the participating medium is not continuous, as in the case of a cloud of small particles [447] or clusters, Fig. 3.25b. Resolving the interaction between the radiation and the individual particles in a very large system is impractical, whereas continuum-based representations of the particle field lend themselves to efficient numerical techniques based on the solution of the radiative transfer equation. In an investigation by Frankel et al. [447] the investigators assessed radiation transport through discrete and continuum-based representations of a particulate medium. Exact solutions for radiation extinction were developed using a Monte Carlo model in different particle distributions which were then projected on to a concentration field of varying sizes. The Bouguer–Beer law was also applied to the model to compute transmission through the domain using a concentration field, determined from the same particle fields. A solution for radiative transport was validated with a particle-resolved Monte Carlo experiment where computed transmission was shown to produce deviations from the Bouguer–Beer law based on the assumption of a uniform particle concentration [447].

Fluidized bed heat transfer at a microscopic scale has also been examined experimentally [132-134]. In these studies, the authors described heat transfer to a particle by at least three mechanisms: convection from fluid, conduction from particles or wall, and radiation where the heat transfer of a particle was found to be strongly affected by the local gas-solid flow structure, and therefore vary spatially and temporally. This suggests that information derived for a single particle may not be reliable due to difficulty in quantifying such local structures in a particle bed.

3.5.1.3 Advanced Magnetic Falling Particle Receivers

Although previous falling particle receiver designs have proven outlet temperatures above 800 °C, and thermal efficiencies between 80-90%, performance challenges still exist to operate at higher concentration ratios above 1000 suns and greater solar absorptance levels. To increase absorptance, these receivers will require enhanced particle residence time within a concentrated beam of sunlight. However, depending on particle size and external forces (e.g., external wind and flow due to convective heat losses), optimized particle flow can be severely affected, which can reduce receiver efficiency. To reduce particle flow destabilization and increase particle residence

time on the receiver an imposed magnetic field can be utilized based on a collimated design for three different methodologies [135].

Generally, magnetohydrodynamics (MHD) considers fluid flow of electrically conducting media in the presence of an electro-magnetic field where previous CSP research has included electrically conducting liquid metal fluid flow in the presence of a magnetic field [136]. However, many of these studies [137] considered fluidized solid particles operating temperatures under 600 °C. To date, research does not exist for CSP applications that leverage magnetic falling particles as the HTM. However, previous work [138] has shown that increasing heat-flux residence time and inter-particle collisions for particles, with a high heat capacitance, can increase heat transfer absorption rates considerably. Increases in particle mass loading ratios (seeded particle specific mass to carrying gas specific mass) have also previously found heat exchanger enhancement by orders as high [138] as 10, which could have implications for CSP falling particle receivers.

There are several classes of magnetic particles that can be leveraged for CSP falling particle applications. The main distinction between these types is that some have no collective interaction of atomic magnetic moments, whereas in other materials there is a very strong interaction between atomic moments [135]. Ferromagnetic particles exhibit long-range magnetic order below a certain critical temperature. Even though electronic exchange forces in ferromagnets are very large, thermal energy eventually overcomes the exchange and produces a randomizing effect. This occurs at a particular thermal limit called the Curie temperature *T*, at which point they begin to lose their magnetic properties and would drop from the magnetic field through the receiver once they reach the desire temperature. This class of materials can also be magnetized by an external field, and remain magnetized after the field is removed. For iron oxides, such as Fe_2O_4, these temperatures can be as high as 1043 K [135].

Finally, electrically charged particles moving through a magnetic field tend to move in circles orthogonal to the field, tracing out helical paths. An equivalent magnetic moment can be assigned to the particle based on the time average of the particle's circular motion. If the magnetic field is non-uniform but has a small gradient, then the equivalent magnetic moment and the resulting force from the non-uniform field are such that the charged particle, independent of the sign of the charge, tends to be repelled by regions of strong magnetic field [135].

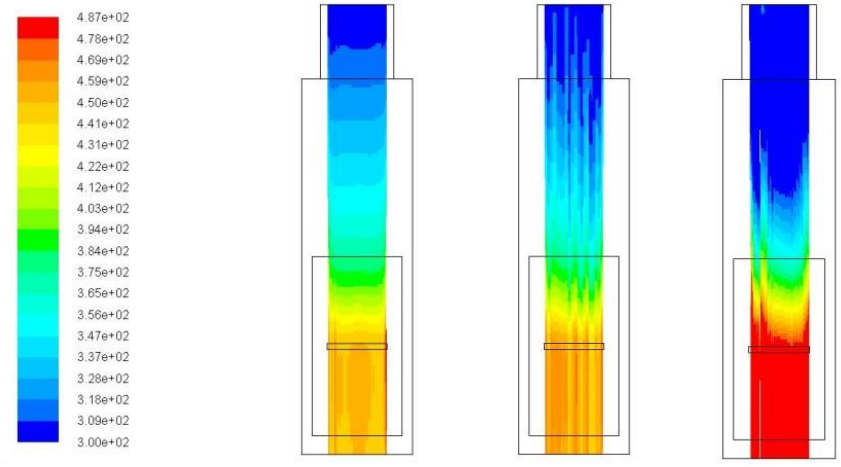

Figure 3.26. Particle temperatures (K) with downward particle acceleration of 9.81 m/s^2 (left), 5 m/s (middle) and 2 m/s^2 (right) [135].

In a study by Armijo *et* al. [135], the authors investigated high magnetic field strength materials such as bismuth ferrite with melting temperatures >1100 °C were assessed. The authors produced a 3D DPM model for solid-particle flow employed where the ambient air is treated as a continuous fluid (primary phase), and the dispersed solids (secondary phase) as an interpenetrating continua. Particle-particle interactions were accounted for based on kinetic theory of granular flow. The results of the investigators suggested that if induced magnetic fields are capable of reducing particle acceleration from 9.81 m/s^2 to 2 m/s^2, the average particle velocity at the bottom of the receiver is reduced from approximately 10-4.7 m/s [135]. This has the potential to increase the average particle temperatures in this location from 449 K to 520 K (Figs. 3.26 and 3.27).

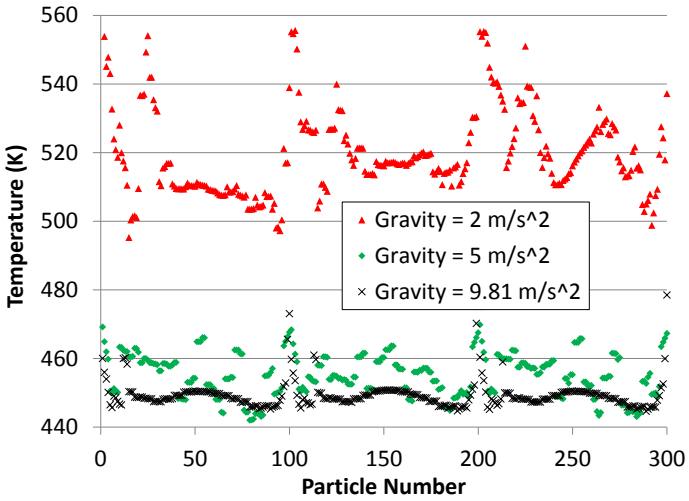

Figure 3.27. Particle temperature at bottom outlet for three Fluent runs with particle accelerations of 2, 5, and 9.81 m/s^2 [135].

3.5.1.4 Other Advanced Direct Receivers

Advanced direct receiver designs have been examined over a broad spectrum of other designs. The use of a quartz window for cavity receivers has been investigated to reduce convective heat losses, but potentially at the expense of reflected solar losses [140]. Quartz windows also limit the ability to use pressurized gases and limit the size of the cavity opening [140]. Additionally, multi-cavity receivers and microchannel designs are being pursued to increase the available heat-transfer area to high-temperature, high-pressure fluids and media in compact designs, with the goal of reducing heat loss and increasing thermal efficiency [141]. Additionally, extended heat-transfer surfaces within tubes can increase heat transfer and structural reliability [142] and are being investigated for high-temperature, high-pressure applications such as direct supercritical carbon dioxide sCO_2 receivers [143]. These higher receiver temperatures are being investigated to enable higher-efficiency power cycles such as sCO_2 closed Brayton cycles. However, at higher temperatures, radiative and convective losses from the receiver are increased. Heat transfer challenges also exist across walls and surface interfaces during heat-transfer media transport to the storage system or power block.

3.5.2 Indirect Absorption Receivers

3.5.2.1 Indirect Absorption Particle Receivers

For instances where heat is transferred through walls of a duct from a solar heat source to a gas, heat transfer to the gas may be enhanced if the gas is seeded with small particles, where the particles are at a higher temperature. This effect can be significant in cases where gases, which have low heat carrying capacity, must be used in favor of high heat capacity liquids, due to high temperature, reliability or other practical constraints. An optimization is then required for transferring as much heat as possible to the gas to limit the necessary size of the heat transfer surfaces.

Principally, for gas flowing through a tube without particles, heat is only transferred by convection from the tube walls to the gas molecules. If the gas is radiatively participating, surface emission from the interior of the tube walls is also effective in heating the gas. The presence of particles therefore contributes to a third heat transfer mechanism where heat is transferred from the particles to the gas by radiation, conduction and convection. In addition, heat is transferred from the walls to the particles by radiation, especially if the radiative absorption coefficient of the gas is low [138]. Heat is then passed on to the gas from the heated particles. Jones developed a heat transfer model to study heated particles that are seeded in a heat exchanger running through a furnace in order to enhance heat transfer to a gas flowing through the tubes. It was found that the inclusion of particles heated to temperatures approaching the furnace temperature, and mass loading ratios (seeded particle specific mass to carrying gas specific mass) up to an order of ten, facilitated significant heat transfer enhancement from the walls to the gas [138]. Such enhancement had the effect of reducing the required heat exchanger tube length and furnace size for the same overall heat transfer.

Knowledge of temperature profiles within a packed bed and the heat removal rate is essential for achieving particle flow homogeneity and optimal concentrating solar power (CSP) productivity within channels. Predictive modeling for packed bed thermo-hydraulics is very complex due to the interaction of different heat and mass transfer mechanisms on different scales and geometries [144]. The study of heat transfer mechanisms between a packing material and a channel wall, of a particle-gas fluid passing through a single tube, has traditionally been an area of research for nuclear packed bed reactors and combustion research [145, 146]. For packed bed particle configurations, inter-particle collisions are important thermal-physical phenomena that must be adequately characterized for accurate heat transfer predictions, especially at high temperatures [147]. Three approaches have been employed that address inter-particle collisions [148] for packed beds. Again, as mentioned previously in section 3.5.1.2, these can include Eulerian-Eularian models [149-153], Eularian-Lagrangian models [154-156], in addition to stochastic collision models [157, 158]. Particle collision has been shown to affect the particle velocity field [159, 160] and heat transfer in gas-particle flows. However, these models, which are considered as a standard framework for investigating gas-particle heat transfer, have not to-date been validated for temperatures as high as 720 °C: the temperature SunShot goal for CSP [7]. Experimentally, for packed bed heat exchangers, previous fundamental heat transfer research have only examined operating temperatures up to 400 °C for gas-particle flows containing alumina spheres, with Reynolds numbers between 30-150 [161]. Hydrodynamically, although research has been performed for Reynolds numbers as high as 10400, investigations to date have not examined packed bed heat transfer beyond 12 MPa operating pressures [144]. Solid particles as an HTF

have been shown to reach operating temperatures as high as 750 °C and flux densities as high as 250 kW/m^2 [162]. However, an understanding of thermal-fluid transport phenomena of particle beds for CSP applications is still relatively limited, especially for high temperature CSP particle receivers. Accurate fundamental characterization of the particle-gas flow, as well as the particles themselves, is necessary to improve heat transfer performance between the bulk fluid and heat exchange walls, as well as to ensure reliability of the system for long-duration, nominal reliability operation.

Interphase heat transfer between dispersed particles and a semi-continuous gas within a channel has been studied by Jones [138] by formally modeling combined radiation, conduction, and convection heat transfer between a particle and a semi-infinite medium. His results demonstrated that with seeding particles, simple correlations for combined mode heat transfer can be accurate. It was also found that the critical particle spacing at which interphase heat transfer is interfered with by neighboring particles is smaller for radiation dominated cases than for conduction dominated cases. Additionally, particle-particle and particle-wall collisions have also been shown by investigators [164] to impact both the gas and bulk flow temperatures. Simulation results by Mansoori *et* al. [164] indicate that the level of thermal turbulence intensity and heat transfer are strongly affected by particle collisions. Inter-particle collisions were found to attenuate the thermal intensity near the wall but somewhat amplify temperature fluctuations in the pipe core region. The hydrodynamic-to-thermal time-scale ratio and the turbulent Prandtl number in the region near the wall were also found to increase due to the inter-particle collisions. Results later found by Mansoori *et* al. [163] showed that the effect of particle-particle heat transfer was more significant for smaller particle sizes, lower flow Reynolds numbers, and for higher loading ratios. It was also demonstrated that the particle volume concentration significantly affects the ratio of inter-particle to gas-particle heat transfer.

For cases where interphase heat transfer is very rapid with small interphase temperature differences, the gas/particle medium is often considered to be a single homogeneous phase. This is the case for very small particles at the micron scale, especially when the initial temperatures of the phases are the same [98]. Due to these fine particle sizes, studies of such cases tend to concentrate on turbulent particle transport and the effect on the total medium radiative properties of the distribution of particle number density and size [138]. For turbulent gas-solid particle flow regimes, experimental evidence suggests that the Nussselt number is increased by adding hot particles to a fluidized bed with large particles and low gas velocities, while it can be decreased when the particles are small or the gas velocity is high. Research by Mansoori et al. [165] validated this finding with particles that ranged between 600-1200 μm and velocities between 11-21 m/s. Their research found for flow within the turbulent regime that a Lagrangian-Eulerian modelling framework was able to show agreement with their experimental results for the particle sizes and flow velocities considered.

Advances have been made in characterizing different particulate flow regimes and their respective transitions, which impact thermal convection between the bulk gas-particle fluid and the heat exchange walls. For these systems, the analogy with gas-liquid two-phase flow can be applied for investigating hydrodynamic regimes in gas-solid systems [166]. If particle flow is dispersed, such as the case of particle separation being greater than 10 diameters, turbulent conditions are then considered along with particle mixing theory [166]. Although issues still remain pertaining to gas-particle instability theory based purely on hydrodynamic considerations, most fluidization researchers believe that interparticle forces play an important role for powders less than 100 μm [167]. However, work by Rosenweig [168], demonstrated that limiting bubble-

free hydrodynamics was important for increasing heat transfer. In their vertical particle-gas hydrodynamic studies, Flammant *et* al. [162] demonstrated that dense particle flows (with SiC particles having a solid fraction in the range of 30-40%), with optimally low-levels of air voids or "bubbles," help to facilitate homogeneous temperature distributions between the particles and the continuum gas by enhancing agitation and thermal mixing, which is favorable for heat transfer [167].

For some thermochemical processes heat transfer in two-phase systems involving gas and solid particles are encountered, fluidized beds operate in either the bubbling regime or the fast-circulating regime. In the first case, particles are retained in the fluidized bed while gas passes upward past the particles, partially as rising bubbles. In the second case, gas velocities exceed terminal velocity for the individual particles and the two phases flow through the fluidized bed in concurrent upward flow [169]. As the velocity increases various hydrodynamic regimes of gas-particle fluid flow occur, which are presented in Fig. 3.28.

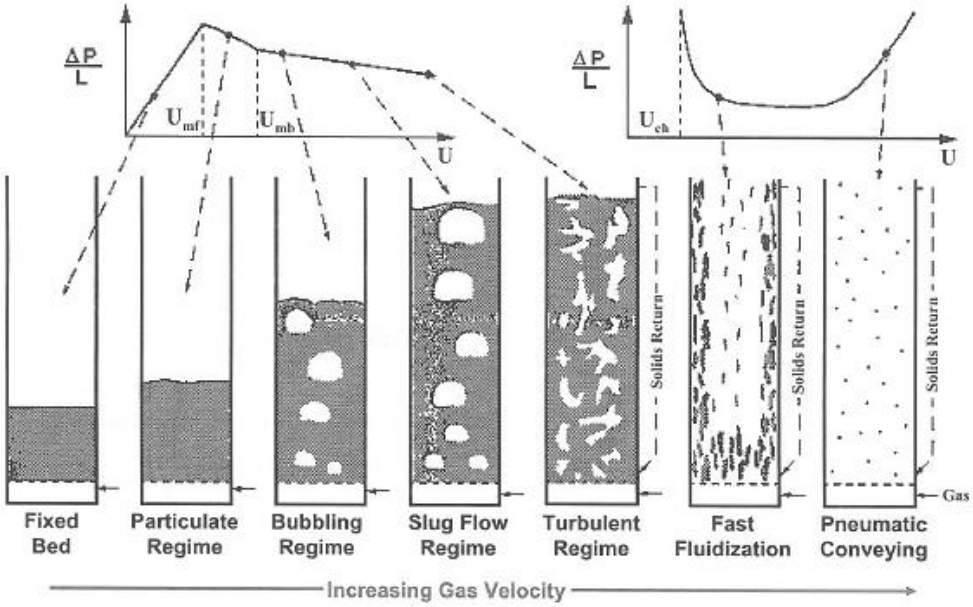

Figure 3.28. Hydrodynamic regimes of fluidization [170].

From Fig. 3.28 increased flow facilitates dispersion ("bubbling") between the particles and increased turbulence, where Wen and Yu 171] developed Eqn. 3.50 to estimate the minimum fluid velocity for spherical particles. Their results suggested that increasing gas velocity beyond minimum fluidization causes the excess gas to collect into discrete bubbles that grow and rise through the fluidized matrix of solid particles.

$$Re_{mf} = \frac{U_{mf} D_p \rho_g}{\mu_g} = [(33.7)^2 + 0.0408 Ar]^{1/2} \tag{3.50}$$

$$Ar = \frac{D_p^3 \rho_g (\rho_s - \rho_g) g}{\mu_g} \tag{3.51}$$

Typically, tubes carrying HTFs are often immersed in fluidized beds to extract or add thermal energy [167]. Data for the circumferentially averaged heat transfer coefficient for horizontal tubes are shown in Figure 3.29 for various types of solid particles.

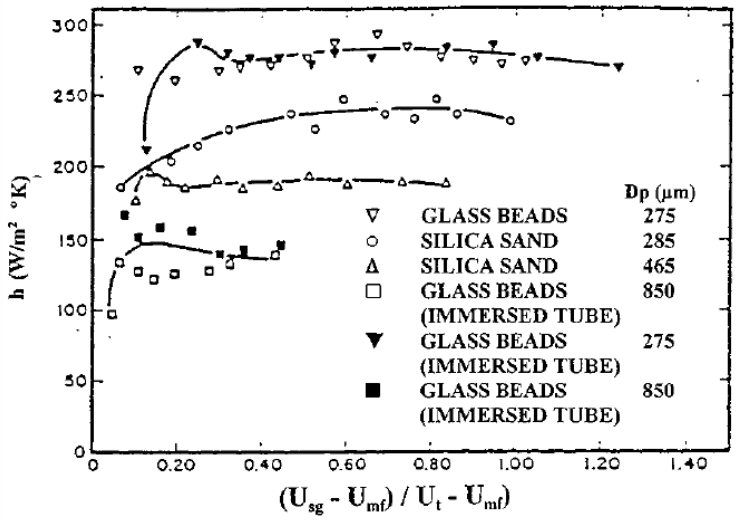

Figure 3.29. Average heat transfer for horizontal tubes immersed in bubbling fluidized beds for various solid particles [172].

Additionally, Kunii and Levenspiel [127] have shown that increasing gas pressure and density significantly increases the magnitude of the heat transfer coefficient as well as promoting the occurrence of minimum fluidization at a lower value of superficial gas velocity. The effect of bundle spacing is insignificant at 1-atm pressure but becomes increasingly more important as gas pressure and density increase [167].

For fast fluidization, when the superficial gas velocity exceeds the terminal velocity of the solid particles, the particles are generally suspended in concurrent upward flow with the gas. This upward flow occurs in rise reactors where desired physical or chemical reactions occur. In most applications, the two-phase flow exits the top of the riser into a cyclone where the gas phase is separated and exhausted while the solid particles are captured and returned for reinjection at the bottom of the riser [167]. Volumetric concentration of solid particles in fast fluidized beds (FFBs) tends to be fairly diluting [127] however. Heat exchange with the particle/gas suspension is usually accomplished through the vertical wall surfaces or through vertical tubes immersed in the duct. The heat transfer coefficient on the vertical surfaces of FFBs has been found to increase with increasing solid concentration, aside from other second-order parametric effects. It is generally accepted that the effective heat transfer coefficient for surfaces in FFBs has contributions for gas-phase convection, particle-induced convection, and radiation as prescribed by Eqn. 3.52.

$$h = h_g + h_p + h_r \tag{3.52}$$

In contrast to the situation in dense-bubbling fluidized beds, the relatively dilute concentration of solid particles in FFBs often results in significant contributions from all three heat transfer mechanisms [127]. The radiation coefficient can be obtained by a gray body model suggested by Grace [167]. The contribution of the gas phase convection (h_g) is commonly estimated based on correlations for gas flow alone at the same superficial gas velocity. Although the presence of particles may alter the turbulence characteristic of this gas flow, any errors caused by this procedure are usually small since h_g is generally smaller than the particle-phase convective coefficient hp. For most FFBs, the particle convective contribution to heat transfer is most

important and the prediction of h_p is the major concern in thermal design [167]. Unfortunately, mechanistically based models are still lacking and most design methods rely on empirical correlations which often combine the contributions of gas and particle phases into a single convective heat transfer coefficient (h_c). One such correlation proposed by [173] where V_t is the terminal velocity of the particles:

$$Nu_{D,p} = \frac{h_c D_p}{k_g} = \left(\frac{C_{pp}}{C_{pg}}\right)\left(\frac{\rho_{sus}}{\rho_p}\right)^{0.3}\left(\frac{V_t}{gD_p}\right)^{0.21} Pr_g \quad (3.53)$$

For high thermal input conditions, much higher values of gas flow than predicted by purely hydrodynamic approaches are required when the temperature is raised to a point where agglomeration occurs [174]. However, as agglomeration intensifies, convection heat transfer coefficients have been shown to reduce [175] due to decreased particulate mixing. However, external fluidization techniques such as imposed acoustic fields [176] and magnetic fields [168, 178] can cause disaggregation of particle clusters into smaller units composed of a few relatively large agglomerates and many smaller ones, allowing in some cases large particle sizes of up to 45 μm to be fluidized as if they were smaller materials [176, 177]. Research by Chirone *et* al. [176, 177] indicated that acoustical field effects extend to gas velocities well above minimum fluidization and result in much more reproducible behavior of cohesive powders.

3.5.2.2 Tubular Receivers

Tubular receiver designs have previously been employed by parabolic dish receivers as well as liquid–metal heat pipes for improving heat exchange from a solar heat input to a gas [179]. The internal heat transfer coefficient in a liquid-metal heat pipe is on the order of 30,000W/m^2-K compared to 300W/m^2-K for heat transfer to gases [179]. Therefore, higher solar fluxes can be tolerated with heat pipes yielding more compact receivers, lower metal temperatures, and lower pressure drops where disadvantages include potentially higher receiver costs [64]. Design specifications included an air-outlet temperature of 815 °C with an air-inlet temperature of 565 °C, air mass flow rate of 0.24kg/s, pressure drop of 2%, and thermal efficiencies up to 85% [180].

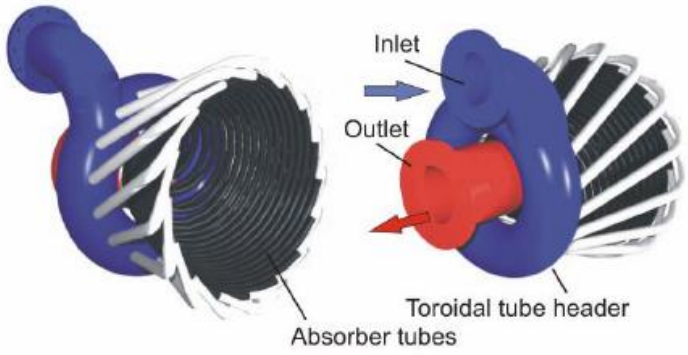

Figure 3.30. SOLGATE tubular receiver for 600 °C air outlet temperature [180].

More advanced designs for this type of system have been conducted by DLR for a solar-hybrid microturbine system operating in a central receiver for applications on the order of 100kW–1 MW [181-183]. In one study, investigators as part of the SOLGATE project, developed a solar-hybrid cogeneration system with a micro-turbine, which was able to operate under varying contributions

of solar power input and fuel. A novel profiled multilayer tubular receiver, shown in Fig. 3.30, demonstrated operation at a power level of 230 kW_e and temperatures of approximately 600 °C [180].

During development of a low temperature tube module, analyses by Heller [180] were conducted to evaluate the upper limit of a tubular receiver for solar hybrid gas turbine systems. Typically, there is a strongly inhomogeneous heat load on the absorber tubes, with solar fluxes up to 500 kW/m^2 on the front side and low fluxes on the backside of the tubes [180]. Two limiting factors were identified: 1. low heat conductivity of high temperature metal alloys and 2. poor ratio between heat transfer coefficients and pressure drop. Finite element calculations of the temperature and stress distributions at the cross-section of the absorber tubes demonstrated high thermal gradients in the tube walls (up to 220 K), caused by low thermal conductivity of the tube material and relatively low heat transfer coefficients between the tube wall and air at the inner side of the tube [64]. This led to high inhomogeneous stresses, reduced life time, as well as a relatively low air outlet temperature compared to the maximum allowable surface temperature [180]. To reduce thermal gradients between the irradiated front side and the non-irradiated back side of the absorber tubes the concept of a "profiled multilayer tube" (PML) technology was developed, which consists of using three metallic tube layers: a high temperature alloy at the outer side, copper as intermediate layer and another high temperature alloy layer at the inner side of the tube, Fig. 3.31.

a. 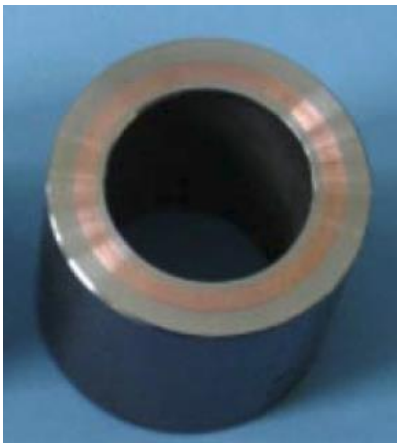 **b.** 

Figure 3.31. a. Profiled multilayered tube b. PML tube sample of normal steel and copper [180].

The function of the copper within the PML is to leverage its heat conductivity to distribute the heat by conduction throughout the circumference. The outer layer however provides the structural strength while the inner layer protects the copper from corrosion at high temperatures. In addition, a spiral profile was implemented on the inner surface to improve the heat transfer coefficient. Preliminary calculations for this solar receiver concept revealed that the temperature gradient in the tube wall could be significantly reduced, in addition to the maximum temperature of the tube [180]. Figs 3.32a and 3.32b presents the simulated temperature distribution in standard and multi-layer absorber tubes respectively.

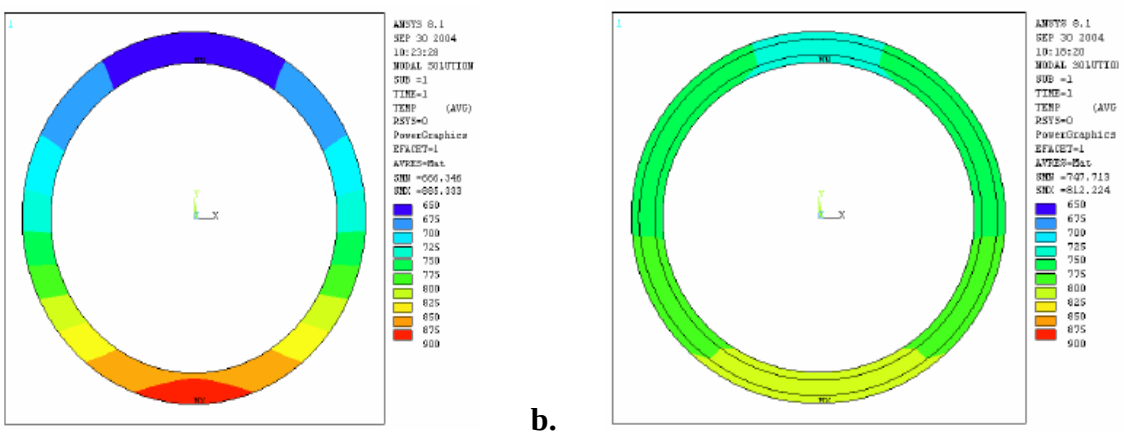

a. **b.**

Figure 3.32. Temperature distribution in an irradiated a. standard tube and b. multi-layer tube [180].

The empirically validated results in Fig. 3.33 demonstrated that the temperature difference between the irradiated and non-irradiated sides of the tube section can be reduced from 106 °C to 31 °C when utilizing PML tubes. Therefore, the investigators concluded that the application of PML tubes instead of common mono tubes leads to a noticeable decrease of the maximal overall temperature and also to a significant reduction of the temperature gradient relating to the tube circumference and, hence, to a reduction of the internal stresses [180].

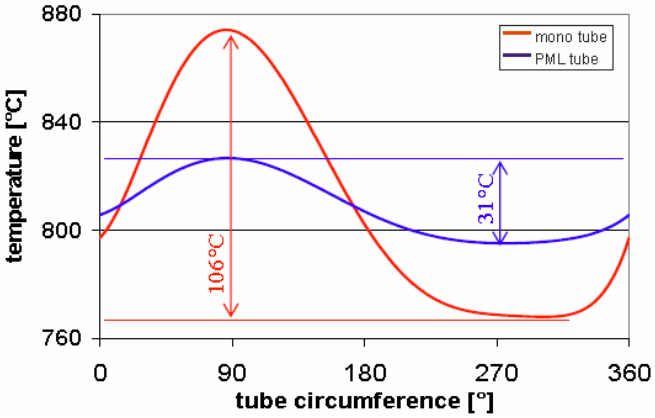

Figure 3.33. Local temperature distribution comparisons of a mono-tube and a PML tube [180].

Tubular receivers however have many challenges associated with large convective and radiative heat losses from receivers operating at higher temperatures, as well as difficulty in transferring heat effectively from irradiated tubes to the gas. They are also subject to rapid transient thermomechanical loads that can adversely affect the fatigue life of the receiver [64]. Uhlig conducted tests and developed a Chaboche-type plasticity model to predict the fatigue life of nickel-based alloy tubes subject to transient thermal stresses, where the model was used to reduce the stresses in the receiver [184]. Kolb compiled low-cycle fatigue data for Incoloy 800HT, Inconel 625-LCF, and Haynes 230 alloys and performed analyses to determine allowable flux limits on these materials [185]. Tubular receivers are a likely possibility for employment in supercritical carbon dioxide (sCO_2) systems as small diameter tubes can enable high pressures required for the supercritical phase. At the turbine inlet, pressures of approximately 15–25 MPa may be expected for sCO_2 Brayton cycles [64].

3.5.2.3 Volumetric Receivers

Air-cooled tubular receivers can experience challenges due to lower heat transfer coefficients, as discovered in the German–Spanish GAST project where two tubular receivers, one metal and one ceramic, were tested at the PSA in Spain [186]. To improve the contact surface, volumetric absorbers with very porous wire, foam or appropriately shaped materials within a volume, allow radiation to penetrate deeply into the structure where thin substructures (wires, walls or struts) ensure good convective heat transfer [186]. A well-designed volumetric absorber produces the so-called "volumetric effect" as the irradiated side of the absorber is at a lower temperature than the fluid leaving the absorber. Under specific operating conditions, volumetric absorbers tend to have an unstable mass flow distribution [187]. Receiver arrangements with mass flow adaptation elements (e.g., perforated plates) located behind the absorber can reduce this tendency, as well as appropriate selection of operating conditions and the absorber material [187].

During operation, the HTM is heated to temperatures between 800-1000 °C for metals, up to 1200 °C for ceramics, and up to 1500 °C for SiC [188]. The HTM can then be used to heat another working fluid for a power block [189], charge a storage medium [190], or pass directly into a gas turbine [64]. Two prominent applications of volumetric air receivers provided by Ho and Iverson [64] are a. open-loop atmospheric receiver system and b. closed-loop pressurized (windowed) receiver system for a Brayton Cycle. A comprehensive review of volumetric receivers can be found by Avila-Marin [188].

Losses due to radiation can be mitigated by a two-slab selective volumetric receiver in which the irradiated front slab was composed of solar transparent glass beads or a silica honeycomb, and the second slab was composed of silicon carbide particles [191]. These semitransparent multi-layer systems allow solar radiation to penetrate through the first slab and into the second slab. Infrared emission from the second slab can be absorbed by both slabs and as a result, the location of maximum temperature can be found within the interior of the volumetric absorber, therefore decreasing radiative heat loss. Experiments by Avila-Marin [189] found for a windowed receiver, thermal efficiencies of approximately 90% could be attained with gas outlet temperatures of approximately 700 °C could be attained. Pitz-Paal *et* al. [192] also suggested a similar concept utilizing square glass channels that cover a ceramic foil receiver where their results suggested that the efficiency could be improved by up to 10% with gas outlet temperatures up to 1000 °C.

The potential for unstable flow and non-uniform heating in the volumetric receiver, leading to overheating and local failures in the receiver material [64] is another challenge for volumetric air receivers [193]. These instabilities are caused by changes in temperature-dependent air properties (viscosity and density), but may be mitigated by using low-porosity absorber materials [64]. Karni *et* al. suggested the use of a volumetric solar receiver employing ceramic pins which helped achieve gas temperatures near 1000 °C [194].

4. HEAT TRANSFER FLUIDS FOR CSP SYSTEMS

4.1 Overview

To achieve high conversion efficiencies for CSP systems, high temperatures at the receiver and heat engine, along with low temperatures at its energy sink, are inherently necessary. These temperatures are limited by the HTFs (or heat transfer media (HTM)) in the receiver and the working fluid in the heat engine. For some systems the HTF and working fluid can be the same, as in the case of water/steam [195]. Additionally, the selection of an HTF must entail consideration of its ability to retain and store energy, as this is an important feature for CSP. HTFs can be classified by their states of matter during their respective operating conditions. In addition to the three standard states (solids, liquids and gases), HTFs can also experience higher heat transfer coefficient levels as they undergo phase change processes and achieve supercritical thermodynamic states.

Previous work rated the potential of various HTFs for CSP applications by their thermal and transport properties, where Becker [196] developed the following comparisons according to their density Fig. 4.1a, specific heat Fig. 4.1b, dynamic viscosity Fig. 4.1c and thermal conductivity Fig. 4.1d.

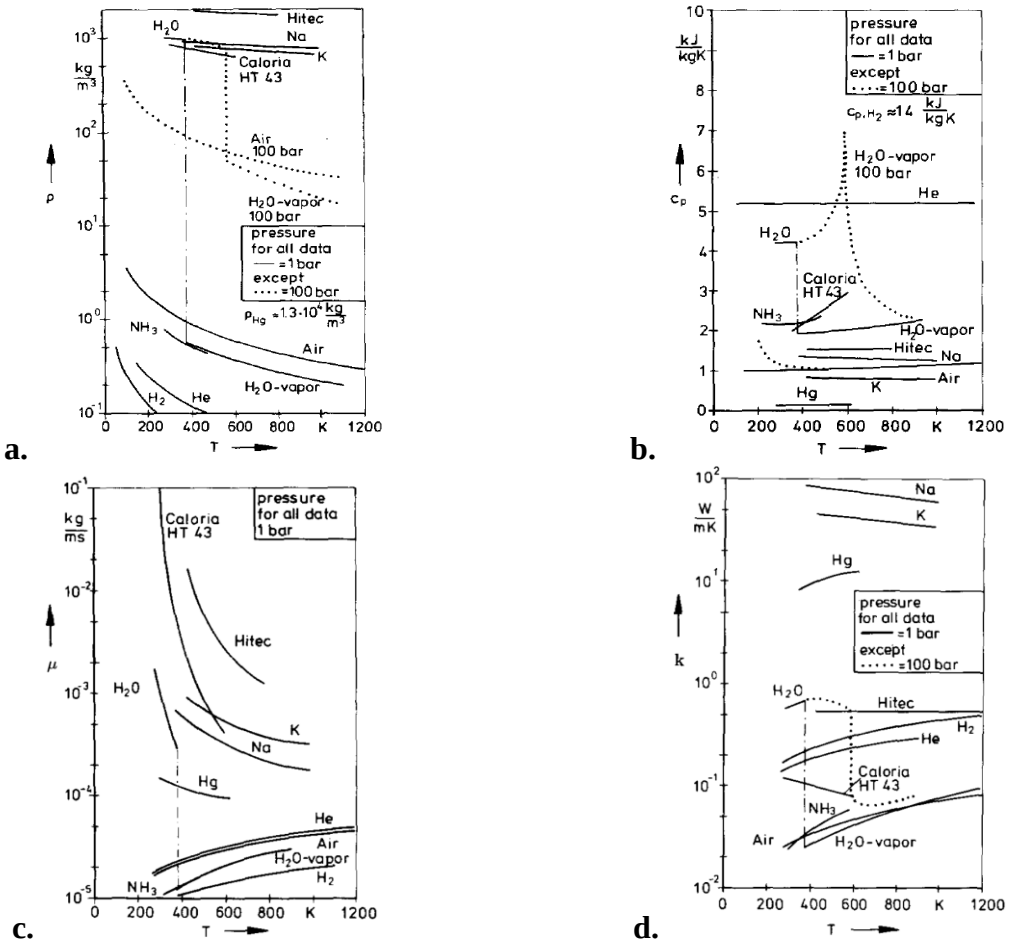

Figure 4.1. Selected CSP HTF comparisons according to a. density, b. volumetric heat capacity, c. dynamic viscosity and d. thermal conductivity [196].

When combining respective properties from Fig. 4.1, the Prandtl number PR can be determined as the ratio of the momentum diffusivity to the thermal diffusivity, where from Fig. 4.2, fluids such as water, Hitex and air have Prandtl numbers greater than one, while alkali fluids, which were found to achieve the highest operating temperatures, had values less than one [196].

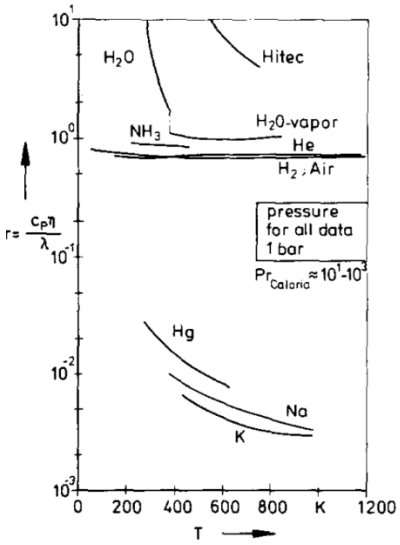

Figure 4.2. Computed *Pr* values for selected CSP fluids. [196].

Heller [197] notes that for ideal CSP systems, important thermophysical properties of HTFs to consider are:

- Low solidification temperature.
- High evaporation temperature and thermal stability limit.
- High material or bulk fluid thermal conductivity.
- Low viscosity which can contribute to low pumping power requirements.
- High densities and heat capacities which can facilitate ideal storage requirements.
- The ability for the fluid to be used as a power block working fluid to reduce exergy losses.
- Chemical compatibility with contact metals with low corrosion/oxidation activity values.
- Low cost and high availability
- Low toxicity, flammability, explosivity and other environmental hazards.

High performance HTFs have the requirement of gaining heat from the receiver but also efficiently rejecting heat to a thermodynamic cycle. This heat transfer capability is based on convective heat transfer characteristics, as outlined in section 2.3, which includes a high thermal conductivity that enables efficient transfer of heat from the absorber to the power block, a high density and specific heat capacity that enables high heat flux levels at reasonable mass flow rates, and low HTF viscosities that minimize pumping power [139]. To capture these requirements, HTF figures of merit (FOM) have been developed where Mouromtseff [295] proposed Eqn. 4.1 FOM to compare the performance of HTFs based on the Dittus-Boelter correlation for internal turbulent flow.

$$FOM_{Mo} = \frac{\rho^{0.8} C_p^{0.33} k^{0.67}}{\mu^{0.47}} \tag{4.1}$$

Other FOMs suggested by Weinstein *et* al. [139] include one by Bonilla *et* al. [296] for axial heat flow, Eqn. 4.2 which excludes flow of heat from a wall, as well as an FOM by Lenert et al. [297] Eqn. 4.3, which is based on the minimization of pumping power given a certain temperature rise in the collector tube.

$$FOM_{Bonilla} = \frac{\rho^2 C_p^{2.3}}{\mu^{0.2}} \tag{4.2}$$

$$FOM_{Lenert} = \frac{\rho^2 C_p^{2.3}}{\mu^{0.2}} \tag{4.3}$$

Weinstein *et* al. provided a comparison for these FOMs for several CSP HTFs where they found FOMs by Mouromtseff and Lenert *et* al. had similar trends, as illustrated in Fig. 4.3. The values where found highest for liquid metals due to their high thermal conductivities. Additionally, saturated water was found to be very high for all FOMS due to its high heat capacity while air and pressurized water vapor had the lowest FOMs due to their low viscosities [139].

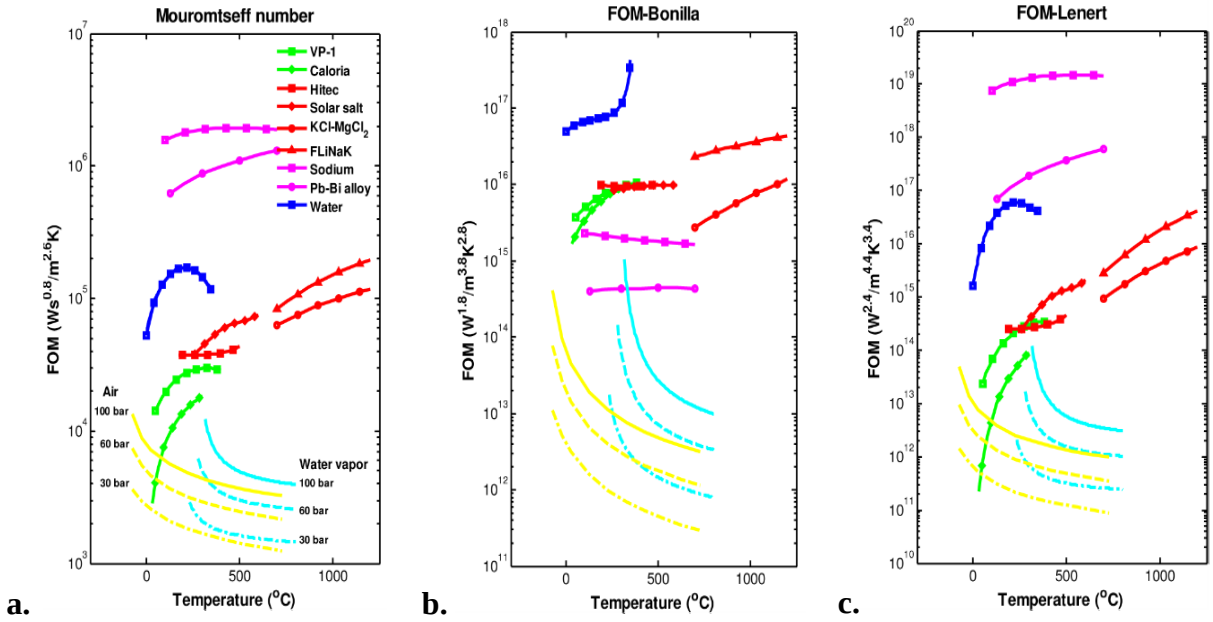

Figure 4.3. Several selected CSP HTF materials comparisons by Weinstein [139] for FOMs by a. Mouromtseff [295], b. Bonilla *et* al. [296] and c. Lenert *et* al. [297].

Finally, with regard to the thermodynamics of HTFs, the fundamental equation of state can be assessed to evaluate their ability to operate under high pressure conditions (e.g. for sCO_2 and sH_2O systems). Traditional approaches for formulating equations of state are: 1. methods of mechanical statistics, which take a rigorous approach for assessment of the interaction between molecules, and 2. empirical or semiempirical equations to describe their behavior based on experimentation. The semiempirical equations of state generally express pressure as the sum of two terms, a repulsive term P_R and an attractive term P_A. According to this model, no single molecule can move freely, but interacts with nearby molecules via forces of cohesion and repulsion. For most analyses one can utilize the van der Waals equation of state Eqn. 4.4, to describe the properties of a real gases qualitatively [198].

$$P = P_R + P_A = \frac{RT}{V-b} - \frac{\Theta(V-\eta)}{(V-b)(V^2+\delta V+\epsilon)} \tag{4.4}$$

The acentric factor, ω was introduced by Pitzer *et* al. [199] as a measure of the difference in the structure of a molecule of any substance compared to that of a gas with a spherical molecule defined as:

$$\omega = -log\left[P_{vp,r}\right]_{T_x=0.7} = -1 \tag{4.5}$$

where $\left[P_{vp,r}\right]_{T_x=0.7} = \left[P_{vp}\right]_{T_x=0.7}/P_{cr}$ which is the reduced vapor pressure calculated at the reduced temperature *T*r = 0.7. By introducing reduced variables $T_r = T/T_{cr}$, $P_r = P/P_{cr}$ and $V_r = V/V_{cr}$, into the Van der Waals equation, on can arrive at the reduced pressure Eqn. 4.6, where the compressibility factor at the critical point is defined by Eqn. 4.7.

$$P_r = \frac{T_r}{Z_{cr}V_r - b^*} - \frac{a^*_{cr}\alpha(\omega,T_r)}{Z^2_{cr}V_r^2 + 2b^*Z_{cr}(b^*)^2} \tag{4.6}$$

$$Z_{cr} = \frac{P_{cr}V_{cr}}{RT_{cr}} \tag{4.7}$$

with b^* = 0.077796, and a^*_{cr} = 0.457235. Eqn. 4.3 corresponding to the critical point where T_r = P_r = V_r =1, Z_r has previously been found to be a constant 0.307 for any fluid [198]. In a study by Intermizzi [198] the investigator found for all fluids tested, the same volumetric behavior except for those with a varying acentric factor ω. The results can be seen below in Fig. 4.4 for various working fluids tested.

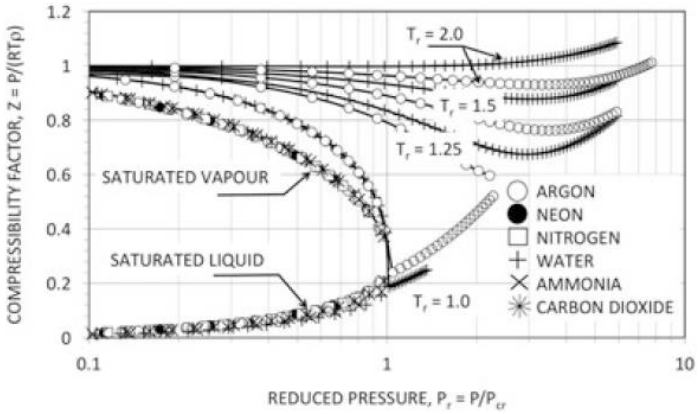

Figure 4.4. Working fluids compressibility chart where the values of the compressibility factor *Z* are calculated from the Van der Waals equation of state [198].

Overall, the sole purpose of an HTF is to transmit heat from one location to another. There are very diverse types of HTFs for CSP technologies that are typically employed based on their thermodynamic property limits and costs. A CSP design consideration that impacts these property limits is whether the HTF is directly or indirectly heated. As illustrated Figs. 4.1-4.4, most thermodynamic properties are strongly dependent on temperature and pressure and can vary significantly if its fluid motion is bounded or unbounded. Additionally, since many CSP technologies may also have inherent optical concentration constraints, relative operating

temperatures can also be assessed, in addition to costs, to determine the best HTF for a particular application. In this chapter, various HTF fluids, spanning various phases of matter will be assessed for CSP applications, temperatures and pressure conditions.

4.2 Synthetic Oils

Parabolic trough collectors capture and focus solar radiation onto a linear receiver tube that is placed in the focal line of the parabolic trough collectors. The HTF in these systems is typically a synthetic oil [200], which circulates through the receiver tube and transports the thermal energy to a heat exchanger system in a power block, where high-pressure superheated steam is generated [452]. A receiver tube loop runs through the solar field and is composed of a modular series of heat collection elements (HCE), which include steel tubes that contain synthetic oil with an outer glass tube that maintains a vacuum around the hot steel tube. This vacuum annulus serves as a thermal insulator while allowing for maximum absorption of the solar thermal radiation by each HCE [452].

Common synthetic oil HTFs have previously included mineral oil, silicone, aromatics and polyalkylene glycols due to their employment at relatively low pressures [433]. However, in most cases synthetic oils are composed of a eutectic mixture of 26.5% Biphenil and 73.5% Diphenil Oxide [432], with commercial names such as Therminal VP-1® or Dowtherm® synthetic oils [197]. These fluids have stable molecules that remain liquid under low pressures from ambient temperatures up to about 400 °C [201]. The most commonly used grades of these HTFs in CSP plants typically have a purity as high as 99.9%, with chlorine levels below the detection limit of 0.2 parts per million (ppm). Disadvantages for employment of these oils are degradation reliability issues and high costs. Overall, since their upper limit is relatively low, they are generally unable to be used in in high efficiency power cycles [197]. Additionally, previous work has also identified degradation mechanisms that can limit their utility over time where specific synthetic oil grades with high chloride and sulfur levels may not be suitable for use in CSP plants due to the risk of leaks and expensive equipment replacements from stress corrosion cracking. Lang and Lee [432] indicated that thermal degradation is impacted by many factors which include:

- Fluid temperature
- Initial impurity concentration (organic and inorganic)
- Concentration of degradation products in HTF
- Low boiler / high boiler ratio in the HTF
- Degradation product composition
- Oxygen accessed to the fluid (e.g. lack of cover gas quality)
- Metal surface to HTF mass ratio due to catalytic effects from construction materials
- Contamination of HTF (e.g. pipe conservation oil, residues from construction, oil from pump seal system, etc.)

In their work, the investigators developed a model (Eqn. 4.8) for thermal degradation, k of the eutectic diphenyl oxide/biphenyl fluids in a parabolic trough CSP plant was built based on laboratory testing results and average fluid analysis results from operating CSP plants.

$$k = e^{aT^2+bT+c} \tag{4.8}$$

From Eqn. 4.8, *T* is the temperature of the fluid where the three coefficients are determined empirically with respect to the fluid concentration. Fluid degradation was compared between a high quality product at 99.9% purity and commercially available products with reduced purities of around 99.5%. A range of 1.7-2.4 times more degradation was determined for 99.5% purity fluids compared to the 99.9% quality for the operating conditions in a CSP plant. These results indicate that more frequent degradation separation mitigation operations would be needed for lower 99.5% purity fluids, which ultimately would require higher costs where, additional new fluid refills over a 25 years of operation would be approximately $2/kg [437].

Another issue using synthetic oils as an HTF is the formation of hydrogen gas over time as a result of thermal degradation, which proceeds at a very low rate at 400°C, but accelerates considerably between 400°C and 425°C [452]. H_2 forms within steel receiver tubes and permeates into a vacuum annulus over a very long time period, where it can facilitate heat loss. Research by Moens and Blake [452] provided mechanistic evidence for the degradation process which involves a radical reaction where hydrogen gas is formed as a by-product, as well as aromatic oligomers with higher molecular weights. Additionally, the authors also suggest that organic impurities in the fluid can catalyze the thermal breakdown of the HTF through the thermal formation of highly reactive hydrogen atoms (radicals). Here, the authors recommend the HTF should be of the purest grade and kept free of organic impurities to mitigate hydrogen formation [452]. Another contribution to hydrogen formation is the presence of oxide layers at the surface of the steel receiver walls that can have sufficient catalytic activity to convert DPO into dibenzofuran. Further research is still required however to understand the fundamental chemistry behind this catalytic reaction which has never been thoroughly investigated [452].

4.3 Molten Salts

The biggest advantage of molten salt as a HTF is the possibility of direct storage at relatively low costs. Molten salt power tower systems are generally limited to receiver outlet temperatures of approximately 565-600 °C and employ heat exchangers to produce superheated steam at 540 °C and 130 bar, as well as reheated steam at 538 °C and 28 bar [202]. The resulting gross thermal efficiencies are typically 42% with wet cooling [203].

Commonly used nitrate salts (60% $NaNO_3$ and 40% KNO_3 by mass) are stable to higher temperatures of up to 600 °C their lower maximum temperature can be limiting as further increased temperatures increases the corrosion rate with stainless steel [204]. Generally, heat transfer characteristics of molten salts are mediocre where a reasonably high density and low specific heat capacity enable a low volume flow but the low thermal conductivity can lead to elevated thermal losses [197]. To reduce these losses and increase receiver efficiency, heat transfer between a pipe and HTF can be improved by increasing fluid velocity and turbulence [205], while optical efficiency can be improved with pyramid-like spikes of which the HTF circulates [206].

The high solidification temperatures of liquid salts can present challenges, especially with linear receivers where the HTF could freeze during evening hours or during times of low irradiance [197]. In central receiver systems, salt will normally be drained into a tank during receiver filling with a cover gas, though the freezing of the salt, which could block pipes and valves, could cause severe damage to a system [207]. Just as with molten metals, solutions to freezing, aside from draining, could include trace heating or circulation of stored salts. However, these solutions could

result in higher heat losses, electrical power consumption and investment costs. Research has been conducted to address this issue for the development of salts with lower melting points [197], as well as higher maximum operating temperatures to facilitate higher efficiency power cycles [207]. Kolb *et* al [185] estimated the economic benefits of raising the salt HTF's receiver exit temperature to approximately the same temperatures as investigated by Kelly [208], and predicted LCOE reductions of up to 8%. Advanced salt concentrations have in turn been more recently studied in an effort to raise the power cycle operating temperatures. Raade *et* al. [209] found a quinary composition of LiCl, NaCl, KCl, CsCl and SrCl to have a melting point of 253 °C at ambient pressure, and a thermal stability of up to approximately 750 °C. This novel salt consisted of more than 70% by weight of CsCl and LiCl, which however are both expensive materials.

Earlier studies have previously been performed to understand molten salt thermal-fluid behavior in advanced CSP molten salt reactor applications [211, 212], where the majority of the literature on molten salt heat transfer studies have been limited to relatively low Re numbers less than 45000 [210]. Hoffman [213] investigated turbulent heat transfer for molten NaOH for Re values of 6000-12000 where the authors determined heat transfer characteristics followed the correlation:

$$Nu = 0.021Re^{0.8}Pr^{0.4} \tag{4.9}$$

A wider range of *Re* was studied by Grele and Gedeon [214] between 5300-30000, where the authors measured values of Nu were 20% higher than those of the widely-used Dittus-Boelter equation, Eqn. 2.33. Hoffman and Cohen [215] studied molten $NaNO_2$-$NaNO_3$-KNO_3 for heat transfer for *Re* between 4850-24710 and between heat flux up to 614 kW/m^2, where the authors also found good agreement between their data and the Dittus-Boelter equation. In another study, Yu-Ting *et* al. [216] researched molten $LiNO_3$ salt flowing through a test section that rejected heat to a cooling oil flowing a jacket around a test section with a *Re* range 4100-9850 where the authors showed good agreement between their experimental data and the Gnielinski equation [217] and the Hausen equation [216]. Additionally, a study by Das *et* al. investigated molten nitrate salt [210] (60% $NaNO_3$ and 40% KNO_3) up to *Re* values of 2x10^5 and heat flux levels up to 1,000 kW/m^2. The authors found good agreement between their developed *Nu* correlation and their data, where two major effects were observed: 1. the *Nu* values gradually plateaued for the highest *Re* tested and 2. at higher *Re* values, positive interaction of heat flux on *Nu* was observed [210].

Salts containing lithium have also been studied for thermal energy storage (TES) systems applications because of their optimal thermophysical properties. Lithium nitrate has been considered as a great additive to improve the thermal performance for sensible heat storage of molten salts, due to its ability to increase the salt mixture's working temperature range [435]. In their research, Fernández *et* al. [436] characterized thermophysical properties of lithium nitrate containing salts with corrosion evaluations of carbon and low chromium steels at 390°C for 1000 hours. Thermophysical properties, such as melting point, heat capacity and thermal stability of saline nitrates were measured using a simultaneous thermogravimetric analyzer (TGA) and differential scanning calorimeter (DSC), which included $NaNO_3$ and KNO_3 (SQM-SSR grade), $Ca(NO_3)_2$*$4H_2O$ and $LiNO_3$ (Panreac 98%) [436]. Their results, as shown in Table 4.1, showed that using lithium and calcium nitrate, in small quantities (10 wt.%), enabled the salt mixture energy density to increase by 19%. Their results also found a reduction in thermal stability due to the incorporation of corrosion products into the salt. A steep reduction in weight % was observed around 350 °C in the salts after the corrosion tests.

Table 4.1. Thermophysical properties of lithium nitrate containing molten salts [436].

Molten salt mixture (wt.%)	Work temp. range (°C)	Viscosity at 250°C (cP)	Corrosion rate of A516 Steel at 390°C (mm/year)	Electrical conductivity at 390°C ($\Omega^{-1}m^{-1}$)	Energy density (MJ/m^3)	Salt Price (US$/Ton)	Two-tanks system cost/stored energy (US/kWh_{th})
Solar Salt	221–589	5.51	0.97	0.37	550	893	11.67
20 $LiNO_3$ – 52 KNO_3 – 28 $NaNO_3$	130–600	6.3	0.31	0.67	513	1161	16.35
30 $LiNO_3$ – 10 $Ca(NO_3)_2$ – 60 KNO_3	134–567	5.72	0.027	0.56	607	1274	15.07
10 $LiNO_3$ – 10 $Ca(NO_3)_2$ – 60 KNO_3 – 20 $NaNO_3$	132–580	5.78	0.013	0.45	680	1038	10.98

To address corrosion issues, especially with chloride salts which are extremely corrosive to stainless steels, nickel alloys can be employed, however their costs can be prohibitive. However, chemically resistant coatings can also be applied to ensure system internal surfaces have low wettability and can withstand long-term exposure to these materials at temperatures greater than 600 °C [440]. When power turbines and containment alloys reach temperatures greater than 700 °C, the salts form a thin film of molten fluid that attacks the substrate metal alloy (hot corrosion). The applied coatings are designed to limit degradation of the underlying substrate [437, 438] where they must be very dense with minimal defects during application to ensure good resistance [439]. Protective coatings are formulated to corrode at an established rate (µm/yr. normal to the surface) when in contact with the HTF. This corrosion rate determines the coating thickness that is required to protect the substrate for a 30-year lifetime of a respective plant. To protect storage tank walls and piping from corrosion and eventual failure, coatings are being developed that have a target corrosion rate of 30 µm/yr. with a minimal thickness of 900 µm [440].

Chloride salts have not been observed to form stable passivated oxide layers and are susceptible to high corrosion rates in the presence of moisture and oxygen. Purification techniques however can be employed to ensure formation of protective layers do not readily occur where ullage gas may also be employed to reduce corrosion, though a study by Kruzenga [441] showed that oxygen content must be lower than 10%. Impurities in the form of oxygen and moisture are much less of an issue in carbonate salts. For carbonate salts ullage gases are typically high in CO_2 content, where formation of protective oxide layers has been found to inhibit corrosion from the base alloy [441]. Additionally, Ren *et* al. [454] and Olivares *et* al. [455] proposed replacing molten nitrate salts with mixed carbonate salts since their corrosion-reducing ability could further increase operation temperatures to between 700 °C and 850 °C. Research by de Miguel *et* al. [453] investigated corrosion behavior of an austenitic steel HR3C in a eutectic ternary carbonate molten salt mixture ($Na_2CO_3/K_2CO_3/Li_2CO_3$) through an isothermal immersion test at 700 °C for 2000 hrs. A microstructural and compositional study was performed using SEM – EDX and XRD analysis where they observed corrosion products arranged in a multilayer structure, with $LiFeO_2$, $LiCrO_2$, NiO and $FeCr_2O_4$ being the main compounds in different layers (from molten salt to the

unaffected substrate interface). The weight loss observed through gravimetric analysis was attributed to soluble chromates initially formed (K_2CrO_4). Despite this weight loss the utility of carbonate steels in CSP applications still appears promising, however further research over longer time periods at high temperatures (~700 °C) is still required to ensure compatibility of carbonate salts that the HR3C steels [453], as well as other CSP materials.

4.4 Metals

Traditionally, latent metal HTFs typically don't have the problematic upper, and lower operating temperature limitations as experienced molten salts. Latent metal HTFs can operate at lower and safer pressures, while still achieving temperatures required for next-generation Rankine, Brayton and other power cycles. These materials can possess outstanding heat transfer with low viscosity and high thermal conductivities which can facilitate small thermal gradients of the flow inside the receiver pipe wall. Additionally, the pipe thickness can be kept small as well due to the low pressure, which leads to maximum pipe temperatures close to the fluid's exit temperatures [222], resulting in higher receiver efficiencies and reduced strain inside the pipe caused by thermal expansion [223]. Eventually, these properties may allow higher maximum solar fluxes on the receiver and a higher thermal efficiency of it. Kelly [208] determined the maximum allowable incident flux on a molten salt receiver with an operating pressure of 20 bar and a 696 °C outer max pipe temperature, to be as high as 2.5 MW_{th}. It is believed however that liquid metal receivers can tolerate even higher influx levels [197].

Thermodynamically, latent metal receiver systems have the potential for having an enhanced exergetic fit to higher temperature CSP systems as shown by Fig. 4.5 [218]. Here Andraka *et* al. demonstrated that latent HTF CSP engines have significantly reduced exergy losses compared to sensible systems, especially when combined with a latent storage system [226]. Liquid metals have garnered growing attention as a potential replacement for more conventional HTFs in CSP systems due to their high thermal conductivity, which have a strong potential for increasing receiver efficiency and operational temperatures that could facilitate more advanced power cycles. They also have very high potential as HTFs due to their wide range of practical operating temperatures and their superior heat transfer characteristics.

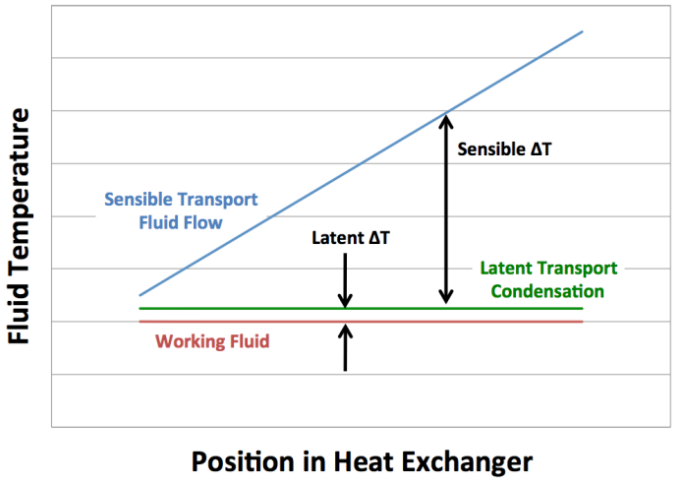

Figure 4.5. Comparison of sensible and latent heat transport into a Stirling engine [219].

Latent metal systems also allow for high maximum fluid temperatures at low pressures, high receiver efficiencies and low pressure drops. For binary cycles the utility of alkali metals as a working fluid for topping cycles (as shown in Fig. 4.6 for saturation pressure curves [220]) are generally considered as a means of increasing the operating temperature beyond that of standard steam cycles. As shown in Table 4.2. Liquid-metal HTFs can facilitate high absorption from very high solar flux levels and efficiencies where the utility of heat pipes is also being evaluated as a way to increase heat transfer from receiver tube or panel surfaces.

Table 4.2. Peak Flux comparison of common CSP HTFs with liquid Sodium [221].

Heat Transfer Fluid	Configuration	Peak Flux (MW/m^2)
Liquid sodium	In tubes	1.5
Liquid sodium	In heat pipes (transferring to air)	1.2
Molten nitrate salt	In tubes	0.7
Liquid water	In tubes	0.7
Steam vapor	In tubes	0.5
Air	In metal tubes	0.22

In conjunction with a combined cycle the use of alkali metal HTFs in latent form can also improve performance of Rankine power cycles. As illustrated by Fig. 4.6, an analysis performed by Angelino and Invernizzi [220] at a maximum temperature equal to that of steam, potassium was shown to dramatically reduce major thermodynamic limitations of the steam cycle by increasing the overall average temperature of the heat input from the primary source.

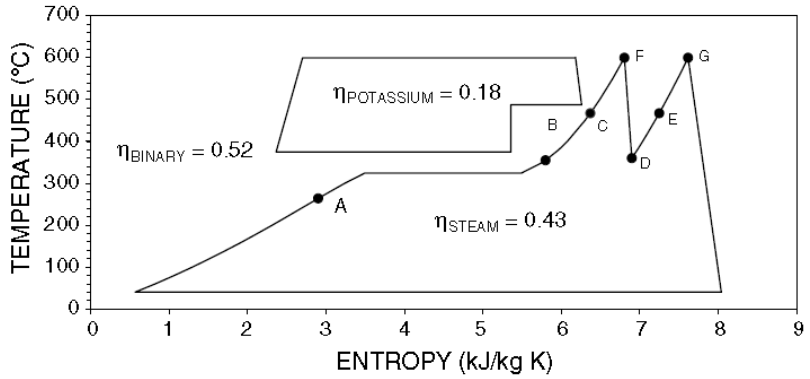

Figure 4.6. Conceptual topping cycle comparison between potassium and steam at the same maximum temperature [220].

Alkali metals have been proposed for high-temperature topping cycles in Rankine-Rankine combined cycle configurations [220], where these systems have the potential to provide good temperature-matching with bottoming steam cycles due to higher phase change heat transfer coefficients. Thermal efficiencies of an alkali Rankine topping cycle and steam Rankine bottoming cycle have however been shown to reach 56% for 1000 °C maximum HTF temperatures, with the potential of reaching as high as 60% [203]. However, turbomachinery for the metal vapor cycles is estimated to be large, requiring a 3.9 m turbine tip diameter for potassium and 2.8 m for rubidium, for a 50 MW turbine [220]. Latent metal systems can also promote isothermal operation requirements for many thermodynamic cycles including Stirling engines [224]. To achieve high operating conditions, alkali metals [225], have high thermal conductivities that improve heat

transfer and allow a receiver to operate at high heat flux levels, while maintaining an acceptable temperature difference between the absorber inner surface and the fluid [226].

4.4.1 Potassium and NaK

A research program for the development of a Rankine cycle based nuclear power plant for space application in the 1960s demonstrated that potassium is a much better high temperature working fluid compared to mercury. It is less corrosive to stainless steel at 870 °C than mercury at 480 °C or steam at 540 °C. Additionally, potassium stainless steel boilers were operated from 5000 to 16,000 hrs. at 815–870 °C with virtually no corrosion [227, 228]. Furthermore, a niobium system worked for 10,000 hrs. at 1100 °C with no trace of corrosion [228]. On the whole, potassium boiling systems were operated for more than 200,000 hrs. at temperatures above 815 °C in the development of long range nuclear electric space power plants [228]. Potassium compatibility with stainless steel systems at a temperature much higher than that of standard steam cycles is due to the favorable corrosion characteristics and to the low saturation pressure which implies minimal stresses in heat exchanger tubes [220]. In Russia in 1972, a vapor potassium system was built and successfully operated for more than 20 years. Evaporators, turbines, condensers, pumps and valves were tested for around 10,000 hrs. at vapor temperatures up to 1030 °C [220]. A temperature of 930 °C was found to be compatible with the use of chromium–nickel stainless steel [227]. The use of refractory metals (e.g. niobium, molybdenum, tantalum) has become attractive for high temperature applications with potassium, whereas steel corrosion seems to be due largely to the solubility of the constituting elements in this element. In the case of refractory metals this solubility is extremely low; however, these materials do have oxidation issues and can have high costs [220].

For NaK the eutectic sodium-potassium alloy NaK78 (22.2-77.8 mass percentage [197]) melts at ambient pressure at -12.6 °C and boils at 785 °C [229]. Despite the inferior heat transfer characteristics of NaK78 as compared to sodium, the low solidification point makes it very attractive for transient power plants, like CSP such as Nuclear. However, freezing issues in pipes, vents and receivers are practically eliminated. Other non-eutectic NaK alloys could show more favorable thermodynamic properties for plants, like higher densities, at the cost of high solidification temperatures [197]. Diver *et* al. [230] presented the state of the art in parabolic dish CSP systems at the beginning of the 1990s where the investigators focused on indirectly heated Stirling engines with liquid metal HTF that are evaporated in the receiver and condense on the heat exchanger to the engine.

4.4.2 Lithium

At the highest temperatures predicted for molten metal utility in CSP plants [220], the use of lithium as a heat transfer fluid could be attractive, owing to its minimal vapor pressure (normal boiling point at 1310 °C). Extensive tests on its corrosion characteristics at moderate temperatures were performed worldwide owing to its essential role in nuclear fusion future reactors [220]. Unfortunately, its interaction with high alloy steels seems much worse than that of sodium (same corrosion rate for lithium at 450 °C and sodium at 700 °C, [231]). Refractory metals, on the contrary, seem compatible with lithium even at very high temperatures [220]. Additionally, lithium has previously been proposed as heat transfer and heat storage medium at 1230 °C top temperature

using a molybdenum alloy as building material [232]. In an investigation by Davis and Kikin, [233], a 30 kW Rankine cycle system was operated for more than a 1000 hrs. at the Jet Propulsion Laboratory (JPL) featuring a lithium heat carrier loop and a potassium power plant at a lithium top temperature of 1150 °C. Refractory metals were extensively used as a material for the hottest components.

4.4.3 Sodium

Sodium is a capable HTF option for advanced high-temperature CSP receivers due to its high operating temperatures and thermal conductivity, which results in high heat-transfer coefficients and minimized heat-transfer surfaces. Sodium is relatively inexpensive and has a number of distinct advantages over oils and salts in CSP applications, such as: raising the maximum receiver temperature, increasing the maximum thermal flux of the receiver, lowering the operational pressure of the primary HTF loop, and preventing solidification in the receiver piping [226]. HTFs such as nitrate salt mixtures currently used in central receiver plants are capable of achieving bulk temperatures of 600 °C, which is not suited for higher-efficiency power cycles such as ultra-supercritical steam power cycles (~590-620 °C) [224] or advanced power cycles under development (e.g. sCO_2 Brayton cycle, 700 °C+) [64]. Previous sensible receiver systems using sodium as a HTF have demonstrated enhanced receiver efficiencies between 90-96% ±10% [226] at power levels up to 2.85 MW_{th}, as well as systems with thermal efficiencies as high as 76% based on daily energy averages [234]. For sensible sodium systems, it has been shown that external receiver systems perform significantly better than cavity receivers due to reduced convection losses and improved heat distributions [235]. However, receivers with latent sodium for Dish-Stirling systems [237] have demonstrated evaporation operating temperatures between 700 °C-850 °C. For a Dish-Stirling engine with a heat pipe containing latent sodium, efficiencies as high as 93% were found for a peak absorber surface temperature of 830 °C [219], where a 20% performance improvement was realized with a directly illuminated receiver [226].

Latent sodium, being electrically conductive, can also be pumped by electromagnetic pumps, thereby reducing the need for mechanical systems susceptible to operational mechanical fatigue [226]. Sodium also does not need to be pressurized since its boiling point is much higher than the receiver system's operating temperature. Utility of latent sodium can achieve higher receiver efficiencies and also reduce fatigue found with sensible systems. Although sodium pool boiling has been studied extensively in both CSP and nuclear applications [64], forced convection boiling has been studied far less, and has improved potential safety, principally due to lower latent transport pumped mass. Latent systems exhibit lower pressures than pumped sensible systems, where at 800°C system pressures are half an atmosphere and any failures result in air ingress rather than sodium egress. Coupling a phase change storage material in the cycle minimizes hazards by eliminating the need to have sodium and water in close proximity [226]. Latent sodium under a low oxygen state is also compatible with many structural materials and does not have corrosion issues (if O_2 is properly controlled [226]) as found with sensible and other high-temperature HTF's, including molten salts. Boerema *et* al. [222] conducted a comparison of HITEC® Heat Transfer Salt and sodium as HTFs for central receivers, where the main advantages for sodum, as illustrated in Fig. 4.7, were higher operating temperatures, with lower pipe temperatures due to the high thermal conductivity. This enables higher radiation fluxes, smaller aperture areas and subsequent heat losses [222].

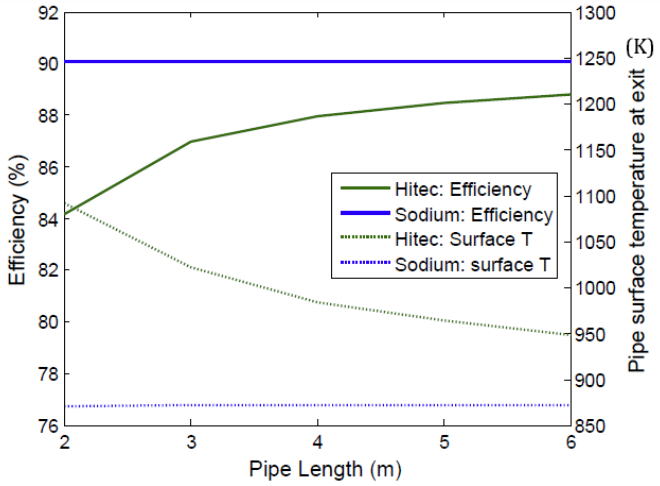

Figure 4.7. HITEC® heat Transfer Salt and sodium receiver efficiencies and maximum surface temperatures for various pipe lengths [222].

4.4.3.1 Sodium Safety Issues

Sodium reacts with air and is inherently a potent reducing reagent and reacts violently with water to form hydrogen and sodium hydroxide. It normally has an oxidation state of +1, and its single valence electron is lost with great ease, yielding a colorless sodium ion, Na^+ [226]. It reacts violently with mineral acids, halogens, and reacts exothermically with oxidizing agents, organic and inorganic halides, and protic media [229]. Sodium also reacts to generate shock-sensitive products with sulfur oxides and phosphorous, and reacts with incandescence and many metal oxides such as mercurous and lead oxides. Sodium dissolves in many other metals such as potassium with great evolution of heat. The reactivity of a sample of sodium is largely related to its surface area. Therefore, reactions involving solid pieces of sodium, especially with an oxide or hydroxide coating, may be slow and controlled, whereas reactions with high-surface area sodium dispersions may be vigorous [237].

4.4.3.2 Reactivity with Liquid Water

Contact of sodium with water or chlorinated hydrocarbons causes a violent exothermic reaction and may cause detonation of the released hydrogen. Although sodium has a high chemical reactivity with water, the heat release rate and heat of combustion is lower compared to conventional hydrocarbon fuels [237]. However, in contact with water sodium often ignites the hydrogen formed. Pure sodium begins to absorb hydrogen appreciably at approximately 100°C [238], where the rate of absorption increases with temperature. The reaction between sodium and water can be divided into two half-reactions, where Eqn. 4.10 describes the loss of electrons from sodium atoms, and Eqn. 4.11 describes when water molecules gain those electrons.

$$2[Na \rightarrow Na^+ + e^-] \tag{4.10}$$

$$2H_2O + 2e^- \rightarrow H_2 + 2OH^- \tag{4.11}$$

The balanced equation for this reaction can then be written as:

$$2Na(s) + 2H_2O(l) \rightarrow 2Na^+(aq) + 2OH^-(aq) + H_2(g) \quad (4.12)$$

For the reaction of water with liquid sodium, the ease of surface area expansion can produce more explosive results since the reaction can be highly exothermic; where for a reaction at 25 °C, where sodium is a solid, approximately only 33.67 kilocalories per mole of heat is released [238]. Additionally, secondary reactions accompany violent reactions with water, with the liberation of hydrogen gas which can be explosive. The heat liberated in Eqn. 4.13, is sufficient to cause the reaction in Eqn. 4.14.

$$Na + H_2O \rightarrow NaOH + \frac{1}{2}H_2 + \dot{Q}_{Heat} \quad (4.13)$$

$$2H_2 + O_2 \rightarrow 2H_2O \quad (4.14)$$

4.4.3.3 Reactivity with Air and Water Vapor

When exposed to air, sodium may ignite spontaneously at a temperature as low as 115 °C, depending on such conditions as humidity, dispersion, etc. For water vapor, sodium begins to absorb hydrogen appreciably at approximately 100 °C where the rate of absorption increases with temperature [238]. A sodium fire can be recognized by a very low flame with many bright yellow nodes. Sodium fires produce a dense white caustic smoke that contains highly alkaline material, sodium monoxide (Na_2O) and sodium hydroxide (NaOH), which can cause irritation and rapid tissue destruction through chemical and thermal burns. As the temperature increases above 650 °C, sodium can begin to spall concrete (which can cause secondary hazards such as flying debris), consume asbestos, firebrick, transite and other similar materials [237]. Under high pressure conditions, and temperatures above 300°C, the formation of sodium peroxide is facilitated as the very reactive sodium material is consumed before each O_2 molecule can combine with enough sodium to from Na_2O, Eqn. 4.15.

$$2Na + O_2 \rightarrow Na_2O_2 \quad (4.15)$$

Data on the combustion and burning rate of sodium in air and reduced oxygen atmospheres are required to predict the rate of energy release for a fire of a given size. Conversely, when sodium peroxide or monoxide are dissolved in water, oxygen is evolved and an alkaline solution is then formed containing sodium hydroxide (Eqns. 4.16 and 4.17).

Peroxide:
$$Na_2O_2 + H_2O \rightarrow 2NaOH + \frac{1}{2}O_2 + \dot{Q}_{Heat} \quad (4.16)$$

Monoxide:
$$Na_2O + H_2O \rightarrow 2NaOH + \dot{Q}_{Heat} \quad (4.17)$$

During fires, a CO_2-contianing atmosphere can arise that can transform sodium hydroxide particles/droplets into solid sodium carbonate particles at a rapid rate, and as a function of relative humidity (RH). As illustrated by Jordan *et* al. [239], this conversion at 50% RH occurs 5 times faster than at RH levels less than 3% [239]. This may be explained that as the surface of wet particles are already converted to solid crystal carbonate, it may act as a diffusion barrier, where

smaller particles have a higher content of sodium carbonate than larger ones. As shown in Fig. 4.8, after 260 sec., only at RH levels above 50% is 100% sodium carbonate realized [239], which would facilitate a safer environment after a fire since all volatile sodium aerosols will have progressed fully through reaction.

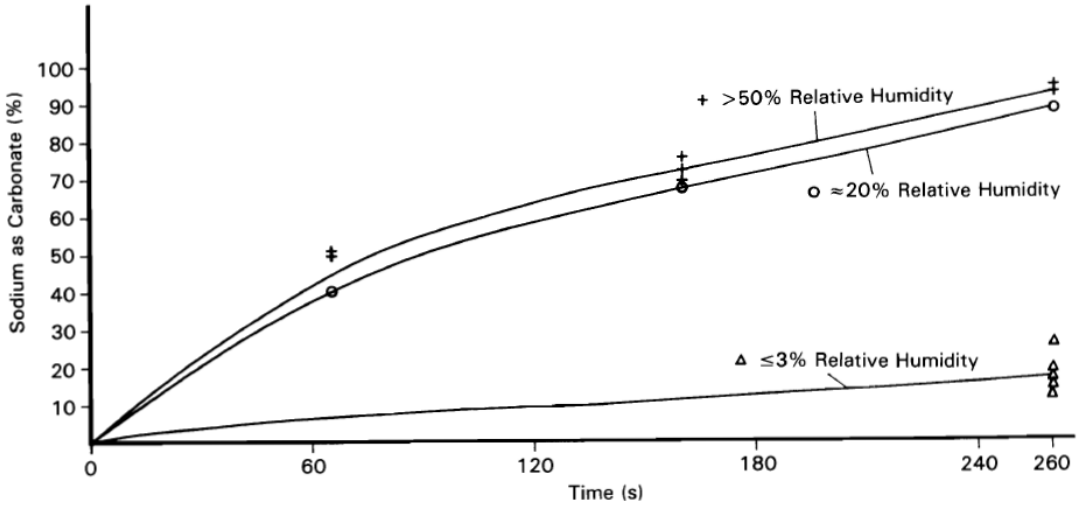

Figure 4.8. Carbonate formation from sodium fires under varying relative humidity [239].

Through implementation of handling and engineering controls [31, 226], safe and optimal heat transfer performance of CSP receivers using sodium can be realized. Solutions to address safety can be broadly categorized according to prevention and extinguishment. Design controls of receiver piping, such as utility of high conduction metals and absorber coatings, [64] have been shown to reduce thermal stress, while design optimization [240] can be leveraged to reduce cycle fatigue from induced vibration, which occurs in the direction of sodium flow. Flow boiling instabilities can be abated through addition of small amounts of heavy inert gas (e.g. Xenon or Argon) which provides pre-existing bubbles that can be inflated with minor superheat that consistently provides low superheat startup and more stable operation [226].

4.4.4 Lead Bismuth Eutectic (LBE)

The lead bismuth eutectic composition Pb-Bi (44.5%-55.5%) has been investigated for applications in CSP [241]. LBE alloy is a reasonably standard industrial HTF with a low melting temperature (~124.6 ℃ at 0.1MPa), though high boiling temperature (~1669.9 ℃), with low safety risks [242]. The density of LBE changes little upon melting/solidification, however after solidification, it is known to show a notable and time dependent volume evolution which could cause unexpected material breakage. Prior research has provided the following operating correlation recommendations for LBE [243], Table 4.3.

Table 4.3. Recommended thermophysical property correlations for LBE at 0.1 MPa and a Pb 44.5%, Bi 55.5% composition [243].

Properties	Correlation	Temperature Range (K)
Density	$P(kg/m^3) = 11{,}096\text{-}1.3236T(K)$	403-1,300
Dynamic Viscosity	$M(Pa\text{-}s) = 4.94x10^{-4}exp(754.1/T(K))$	400-1,100
Heat Capacity	$C_p(J/kg\text{-}K) = 159\text{-}2.72x10^{-2}T(K) + 7.12x10^{-6}T(K)^2$	400-1,100
Thermal Conductivity	$k(W/m\text{-}K) = 3.61+1.517x10^{-2}T(K)\text{-}1.741x10^{-6}T(K)^2$	403-1,100
Sat. Vapor Pressure	$P(Pa) = 1.11x10^{10}exp(-22{,}552/T(K))$	508-1,943

Like most molten metal HTF systems, temperature measurements are performed indirectly by welding a thermocouple onto the outer surface of piping and heat exchange equipment. Since LBE is a good conducting material, the error of these measurements has been generally approximated to be negligible for relatively thin walls (approximately <1 in) [242]. Additionally, for LBE applications, cover gas is generally recommended to displace oxygen down to levels less than 0.025%, where operating processes for LBE in CSP systems include: 1. Use of trace heaters to be used to prevent solidification of LBE during pumping and transport and 2. Storage tanks and heat exchange equipment charged with cover gas, such as argon [243].

According to Pacio and Wetzel [244], LBE has problematic drawbacks when compared to sodium or NaK (reaction with water), and has a very high density, leading to much lower flow speed requirements. The boiling temperature of LBE (1670 °C) is even higher than that of sodium but the solidification temperature (125 °C) is higher as well, so that freezing is an issue. In a study by Kim et al. [243] LBE was utilized in a developed test system where approximately 1000 kg of LBE was successfully used to capture 35 MJ of solar energy. The test successfully transferred heat from the solar air receiver to the LBE, with the temperature of stored LBE reaching 770 °C.

4.5 Gases

The upper temperatures of gaseous HTFs in CSP systems are usually only limited by the materials of the receiver pipes, ducts, etc. They are therefore especially suited for high-temperature applications. Gases, however, have the downside of comparable low heat transfer coefficients and densities. Gases can be used to directly power a gas turbine, thus making use of the very high temperatures which can be generated in a central receiver. The exhaust gases can also be used to power a bottoming cycle, which renders possible high thermal system efficiencies [197].

4.5.1 Air

Air is by far the most investigated gaseous HTF used in thermodynamic cycles as it is abundant, with extensive experience with its utility as a heat transfer working fluid. It can be readily used in a Brayton cycle, is non-hazardous, theoretically free of cost and does not necessitate a heat exchanger for co-firing. The high operating temperatures of the fluid can enable combined cycle plants with high efficiencies, however its heat transfer can be problematic due to its low density and thermal conductivity. Therefore, it has unfavorable heat transfer characteristics, requiring large heat exchangers and receivers for its application. For the implementation of a CSP receiver

in a gas turbine, it has to be pressurized, where performance is highly dependent on the pressure drop between the compressor and expander [197].

Air can be used as an HTF as well as the power block working fluid where it can also drive a Rankine steam cycle through a heat exchanger. For this application, an open air receiver is typically used for simplicity reasons. The air doesn't have to be pressurized (except to overcome pressure drops in the receiver, piping and heat exchanger) and the turbine is not directly coupled with the receiver outlet flow. However, the advantage of using a high temperature working fluid cannot be made use of, since Rankine cycles are typically limited to approximately 640 °C [197]. The only commissioned demonstration plant using this technology for grid-power is the Jülich Power Tower, as described by Hennecke *et* al. [245]. In the AlSol project, this technology is also used in a 7.1 MW_e hybridized solar-natural gas power tower [246]. Additionally, Wilson Solarpower [247] proposed a system in which unpressurized air is used as the HTF in a closed receiver. This hot air then heats pressurized air in a regenerative heat exchanger, Fig. 4.9, to be used in the microturbine within a Brayton cycle.

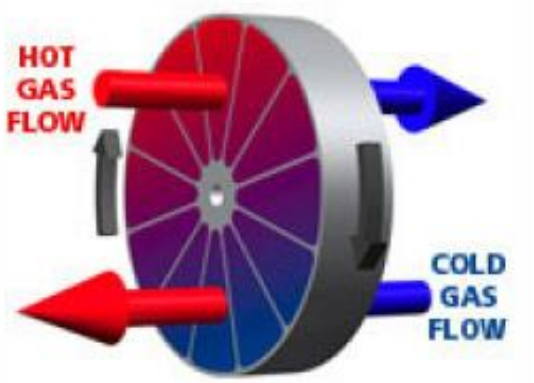

Figure 4.9. Regenerative air-air heat exchanger [247].

4.5.2 Helium

Helium possesses good heat transfer characteristics which could be beneficial in the design of a solar receiver or combined power block cycle. Angelino and Invernizzi [220] suggested that a closed helium cycle could be useful in cogeneration applications, as rejected heat is typically available at relatively high temperatures. Based on system design parameters from a solar application by Frutschi [248], the authors found that the Helium cycle was able to achieve an 800 °C top temperature with a computed overall efficiency of 40.2%. Results of their analysis can be seen in Table 4.4, where they also computed a potential top pressure for this system to be approximately 20-60 bar. They concluded that the closed helium cycle lent itself intrinsically to cogeneration where the heat of cooling of the working fluid prior to compression is available at a comparatively high temperature [220].

Table 4.4. Solar closed helium Cycle Study Results by Angelino and Invernizzi [220].

Type of compression	Inter-refrigerated
Compressor inlet temperature	25 °C
Turbine inlet temperature	800 °C
Compressor pressure ratio (optimized)	2.9
Turbine adiabatic efficiency	0.90
Compressor adiabatic efficiency	0.85
Recuperator effectiveness	0.92
Electro-mechanical efficiency	0.95
Overall cycle efficiency	40.2%

4.5.3 Water/Steam

Steam and supercritical steam (sH_2O, $P_{crit,H2O}$ = 221 bar) has traditionally been used as a working fluid in conventional power plants. For molten salt power towers that produce supercritical steam for the power block, the efficiencies have seen a 2-3% improvement over superheated water systems [203] since they have the potential to operate at higher temperatures and pressures [249, 250]. Operation with steam above the supercritical point can allow for higher temperatures and fluid behavior that shares the compressibility of a liquid while avoiding complications due to multi-phase heat exchangers, such as intrinsic instabilities. Supercritical water was an early candidate for supercritical power cycles due to extensive operating knowledge of water with Rankine cycles [241]. Ultra-supercritical (USC) steam plants have found high performance conditions as high as 620 ^{o}C / 310 bar [252]. USC turbines have found utility in coal plants where their ratings can range between 200 MW_e and 1050 MW_e and reach net efficiencies in excess of 45%. Next generation advanced USC (A-USC) plants are expected to run at turbine inlet temperatures of between 700 °C and 760 °C, with efficiencies above 50% [253].

Due to the high critical pressure of water, sH_2O can require high cost materials for piping, turbomachinery and heat exchangers. Additionally, it has been found that supercritical water is extremely corrosive, not allowing its utility for use with turbines, compressors and recuperators in Brayton cycles. Coventry and Pye [254] proposed a parabolic dish system, employing sH_2O or superheated (subcritical) water as the HTF and working fluid, with a molten salt storage system. The advantage of sH_2O systems is the lack of evaporation processes which lead to smoother isobaric heating processes as compared to other superheated fluids [197]. The heat transfer between sH_2O and another single phase fluid, such as molten salt, is exegetically preferable as demonstrated by Fig. 4.10 [254].

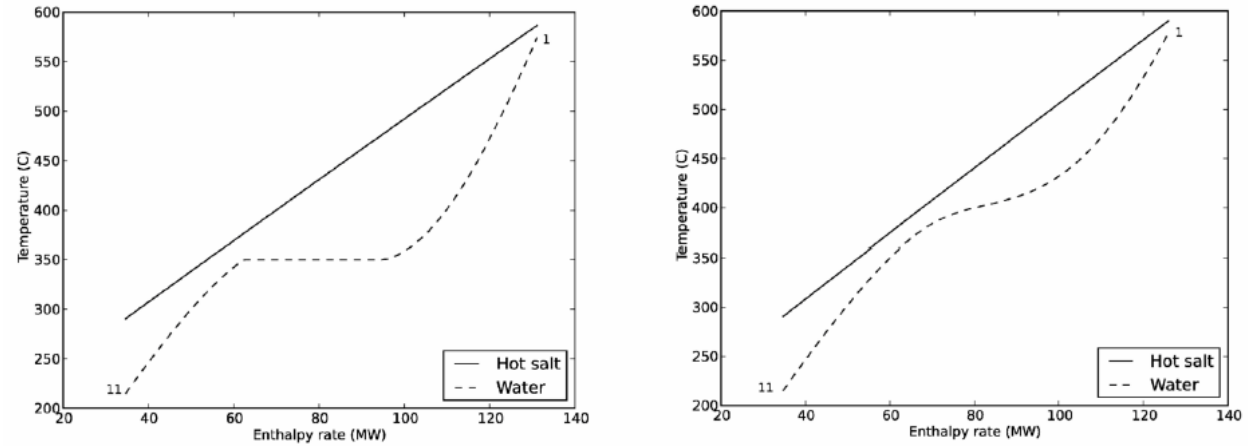

Figure 4.10. Subcritical and supercritical heat transfer in systems with one HTF [254].

There has however been fouling concerns expressed as steam temperatures exceed 627 °C due to limitations of standard ferritic steels, where the requirement of more expensive high-nickel alloy materials has been suggested [203].

4.5.4 CO_2

Compared to water, carbon dioxide is less corrosive and has a much lower critical pressure of 73 bar, yet supercritical CO_2 (sCO_2) is relatively dense at approximately 0.6 kg/m^3 [257]. These characteristics can decrease stress on pipes, as well as flow speeds, which can reduce the size of the power block turbomachinery and heat exchangers compared to steam. Additionally, sCO_2 cycles show higher efficiencies than current [255] steam or air cycles. Other benefits of its higher density is smaller machinery geometries and simpler plant design [258], where these benefits have shown demonstrated promise in next generation nuclear [251] and conventional power plants, as well as for cooling applications [256].

Although disadvantages may exist as outlined by Turchi [258] for sCO_2 as an HTF and a working fluid in CSP plants, Gary [259] suggested advantages for using sCO_2 in combined cycle solar power tower systems as a means of reducing the LCOE to 0.06 USD/kWh$_e$. Chapman and Arias [260] compared three parabolic trough configurations with synthetic oil, subcritical CO_2 and sCO_2 as HTFs, where they found higher magnitude pumping power requirements necessary for subcritical loops as compared to synthetic oil. However, due to the higher density of sCO_2, pumping power was significantly reduced even below that of synthetic oil. Though the high pressure dramatically increased the requirements on pipes, where its utility will most likely not be feasible in line-focus systems, but only in central receiver systems [197].

Chapman and Arias [260] as well as Ma and Turchi [261] addressed the problem of adding a thermal energy storage system (TESS) to a sCO_2 system, where a molten salt storage medium was found to limit the turbine inlet temperature during discharging processes to temperatures less than 600 °C. Active direct and passive storage systems however do not appear viable due to the need for high pressure tanks. Cox [262] found that standard heat transfer correlations are in general applicable to sCO_2 heat exchangers, though in close proximity to the critical point the measured heat transfer noticeably differed from the calculated values.

Rouillard *et* al. [263] compared the corrosion effects on a ferritic-martensitic and different austenitic steels in contact with sCO_2 at a temperature of 550 °C and a pressure cycle of 250 bar. Their research was aimed at the development of components for the secondary cycle for advanced nuclear reactors. It turned out that corrosion had a much more profound effect on ferritic-martensitc steels as compared to austenitic ones [197]. Dostal *et* al. [264] gave an elaborate overview on sSO_2 as a working fluid and HTF in nuclear power plants [197]. The information found in their report is applicable to CSP, as they investigated different configurations for liquid metal cooled reactors with sCO_2 as the working fluid. One safety advantage realized is that there is no direct heat exchanger between a potentially volatile liquid metal and a water/steam cycle [197]. CO_2 also reacts exothermally with liquid metals, such as sodium, but no hydrogen is created in the reaction, therefore greatly decreasing the hazards associated with liquid metals, which have the capability of realizing high temperatures and subsequent efficiencies [224]. Dostal *et* al. [264] built a model for different sCO_2 cycles for preheating, reheating, precooling or intercooling applications, and compared them to a supercritical water and ideal gas Brayton cycle with helium as the working fluid. In this analysis they investigated the influence of heat exchanger (pre-cooler, regenerator, etc.) sizes on thermal efficiency and pressure losses. The investigators found great potential for sCO_2 cycles due to the simple layout of Brayton cycles as compared to Rankine cycles, and high efficiencies at moderate pressures/temperatures [197]. The latter caused by the cycles' low compression work due to the low compressibility factor of sCO_2 at the critical point.

5. THERMAL ENERGY STORAGE

5.1 Overview

The extended operation of solar thermal power plants using stored thermal energy can significantly improve the power dispatch ability [267]. Thermal energy storage systems use materials that can be kept at high temperatures in insulated containers. The heat retrieved can then be used in conventional thermal power plants for power generation at times when sunlight is not available or when weather conditions are not favorable [266]. Thermal energy storage can be less expensive overall than electric batteries and capacitors, which have many reliability issues [293]. The reduction in costs for thermal energy storage can allow CSP plants to increase the capacity factor and dispatch power as needed. Although direct energy storage in batteries and capacitors may have a high efficiency, it is still very challenging and expensive, particularly when storing a large quantity of electrical energy [265]. Storage provides heat necessary for operation of thermal power plants when sunlight availability is out of phase, and thus increases their operational capacity (in terms of the daily operational time).

From an energy efficiency perspective, direct use of solar thermal energy for heating is much more efficient than using electricity for heating, as electricity generation requires much more input of other types of energy than the generated electricity [266]. Financially, TES reduces mismatch between solar energy supply and utility demand [267], where TES systems can be integrated within CSP systems to facilitate buffering during transient shading events (clouds, dust, etc.), where the power block of a CSP facility can be severely affected that can reduce turbine efficiency and contribute to start-up losses [268]. Although many HTFs, and even the solid walls of heat exchange equipment can retain some thermal inertia during operation [269], at a utility-scale, turbine shut down can still become imminent under shading conditions [270]. TES has the ability to dramatically improve this buffering to not only improve the performance of CSP systems, by allowing for continued power production, it can also impact the reliability of power block components by reducing thermal-mechanical stresses induced by system losses [268].

Table 5.1 shows the capacity-credit results for a subset of solar multiples and thermal storage capacities [271]. Configurations with less than six hours of energy storage capacity would result in lower capacity credit [272]. The flexibility of CSP should also allow it to meet "flexible capacity" requirements, such as the California Public Utility Commission (CPUC) requirement that all load-serving entities procure capacity with sufficient flexibility to address the largest predicted 3-hour ramp rate in each month [273].

Table 5.1. Capacity credit (%) for various configurations of CSP-TES [265].

	Solar Multiple						
TES (hours)	**0.7**	**1.0**	**1.3**	**1.7**	**2.0**	**2.5**	**3.0**
6	93%	96%	97%	98%	98%	–	–
9	–	–	–	98%	98%	99%	–
12	–	–	–	–	–	99%	–
15	–	–	–	–	–	99%	99%
18	–	–	–	–	–	–	99%

Fig. 5.2 describes the result of a recent NREL study comparing the combined operational and capacity benefits of CSP-TES relative to PV under varying levels of renewable penetration in California [265]. The analysis found that the value of CSP, compared to variable-generation PV, demonstrated an increase in value of up to 6 cents/kWh under a 40% RPS [274].

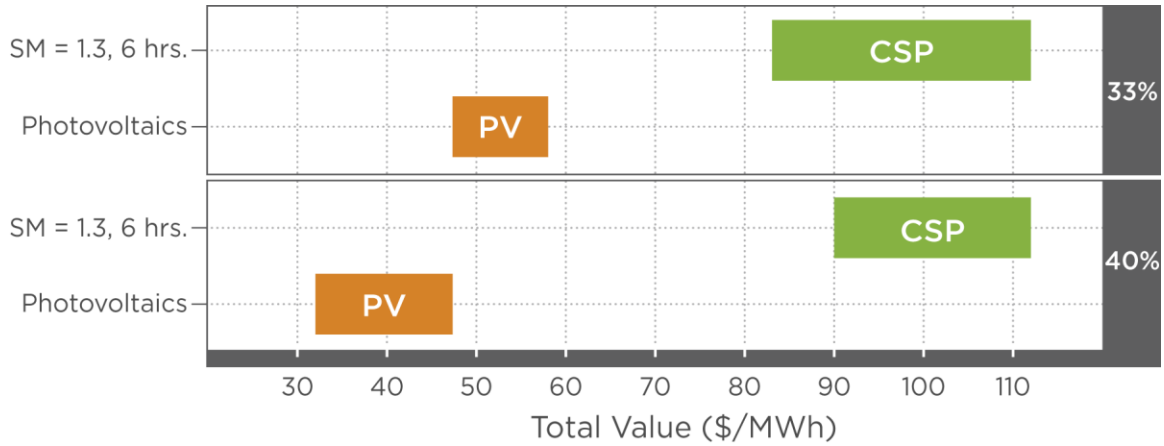

Figure 5.2. Total value, which includes operational and capacity value, of CSP-TES and PV under 33% and 40% RPS scenarios [274].

The necessity of thermal storage purpose is twofold: to increase the value of the power generated by strongly reducing its aleatory character and to improve the plant economics by using the available hardware (structures, piping, power block, grid connections, etc.) for more hours a year [220]. CSP with thermal energy storage (or CSP-TES) provides considerable flexibility, increasing its own value to the grid and even enabling greater grid penetration of other variable-generation technologies such as PV and wind [274]. Previous analysis has demonstrated the ability of CSP to provide frequency-response reserves that can help maintain grid stability [275]. Another significant benefit of CSP-TES is its ability to provide firm capacity, which is the capacity available to the power system at times of greatest need, which is most often the hours of highest net demand [272, 276]. Variable-generation resources such as PV and wind tend to be limited in availability during these hours at high penetration of renewables on the grid because these hours typically occur when the solar or wind resources are unavailable [277]. As a result, installation of these technologies alone cannot meet system peak demand, especially as older fossil plants are retired and new capacity additions become necessary to maintain system reliability [274].

According to Heller [197] there are two primary means for storing energy in CSP systems. The active direct methodology is considered [200] the simplest way of storing heat, which uses the primary HTF as the storage medium, Fig. 5.3a. This has been shown to work particularly well when using synthetic oil [197] or molten salts [185] that remain in a liquid state at elevated temperatures.

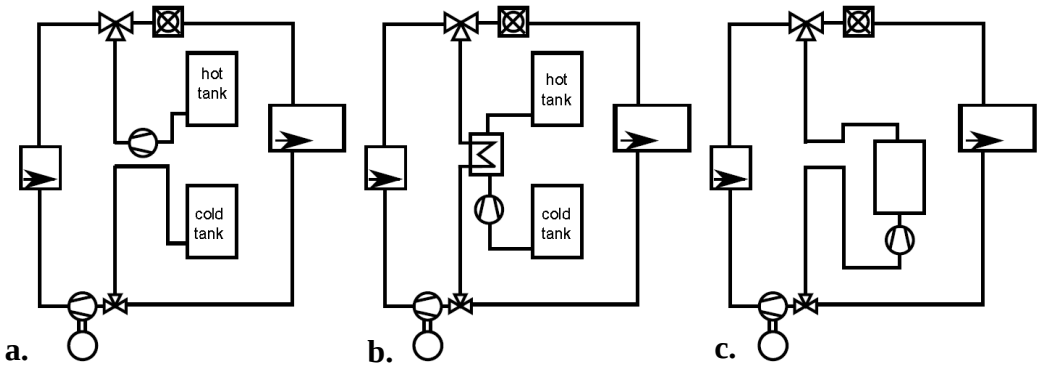

Figure 5.3. Types of thermal energy storage, a. active direct, b. active indirect and c. passive [197].

In DSG pants or when gas is the primary HTF, either a gaseous medium would have to be stored, resulting in low volumetric energy capacities, or a high pressure needs to be maintained inside a tank to condense the medium, reducing long-term storage viability [197]. In active indirect storage systems (Fig. 5.3b), the storage medium is separated from the primary HTF by a heat exchanger, which has the advantage of not requiring the HTF to serve as the heat storage medium, providing more design flexibility.

Concentrating solar plant projects like Andasol in Spain [278] incorporate heat storage that allows a system to operate for approximately 6 to 12 hrs. in the absence of incident solar irradiance, where advanced TES technologies use a two-tank salt system, such that the hot and cold tanks store liquid salts separately [197]. This system can be used since components associated with molten-salt handling (pumps, valves, tanks, and heat exchangers) are available at commercial scale for nitrate salts ($NaNO_3$ and KNO_3), within salt applicable temperatures [279]. In a two-tank CSP system, salt flows from the cold tank to the solar receiver, is heated, and enters the hot tank. During power generation, hot salt flows to a steam generator and returns to the cold tank [197].

Current research and industrial applications with CSP thermal energy storage can be principally divided into three primary categories: 1. sensible, 2. latent and 3. chemical (sorption and thermochemical), which are illustrated by Fig. 5.4. This figure by Pfleger *et* al. [442] provides some examples of different forms of thermal storage media which will be discussed further in the next subsequent sections.

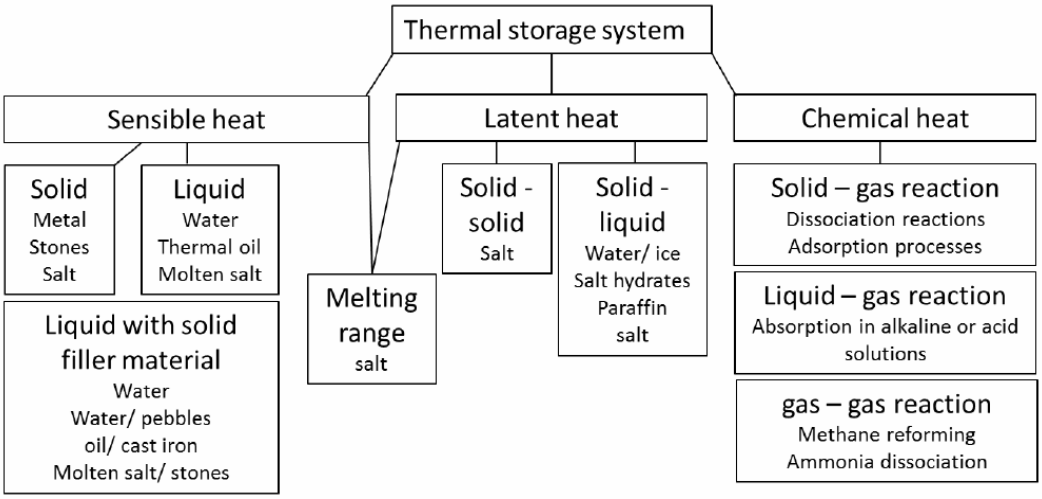

Figure 5.4. Classification of CSP thermal storage media [442].

5.2 Sensible Energy Storage

"Sensible heat" indicates that the storage process can be sensed by a change in temperature, where the relation of the change in temperature and the stored heat is directly related by the heat capacity C_p. TES systems for CSP generally store energy by changing the temperature of the storage medium, which is then retained for later utility in power production. In sensible TES systems, heat energy is stored or released by heating/cooling an HTM [139]. The amount of energy input to a TES in a sensible heat system is related to the mass of storage material and its heat capacity, as well as the temperature difference of the storage medium between its initial and final states. This heat transfer $\dot{Q}_{Sensible}$ can be expressed as:

$$Q_{Sensible} = V\rho C_p(T_{i+1} + T_i) = mC_p\Delta T \tag{5.1}$$

where V is the volume of the storage materials, m and C_p denote the mass and specific heat of the storage material, and ΔT is the temperature difference before (at an arbitrary time i) and after the storage operation (at an arbitrary time i+1). The specific heat of solids can be estimated by the Dulong-Petit law:

$$q_{Cp,solid} \cong 3R\Delta T \tag{5.2}$$

$$C_p \cong \frac{3R}{M} \tag{5.3}$$

where $q_{Cp,solid}$ is the heat stored per mole, R is the universal gas constant and M is the molar mass. An investigation by Weinstein *et* al. [139] found that a mole of sensible TES material almost always has the same heat stored for an identical ΔT, which is approximately 25 J/(K-mol) or equivalently as a heat capacity of $3k_BT$ for each atom from the equipartition theorem, where k_B is the Boltzmann constant. The investigators also determined from Fig. 5.5 that the relative volume of atoms in the lattice (packing fraction) does not change significantly between materials, which leads to similar volumetric energy densities ρC_p (<one order of magnitude).

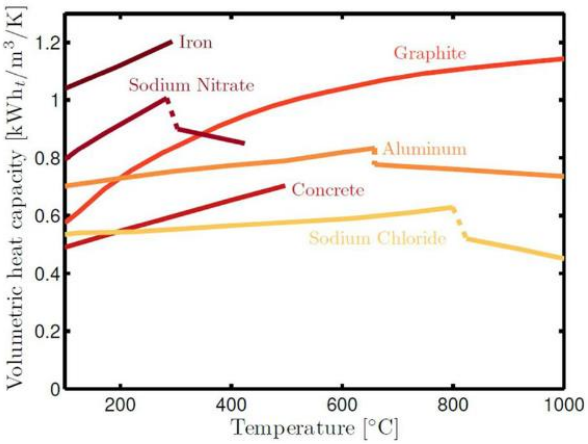

Figure 5.5. Volumetric heat capacity of TES materials, where curve discontinuities correspond to phase change [139].

Energy storage in sensible TES systems are determined largely by the volume of the system where total capacity of the system (kWh$_t$/m^3) can be determined by integration of the volumetric heat

capacity over the operating temperature range [139]. Values for some sensible TES materials with these volumetric heat capacity values are shown in Table 5.2 provided by Weinstein *et* al. [139].

Table 5.2. Sensible CSP TES materials, where material properties are representative of the specified operating range [139].

material	operating temperature range (°C)	thermal conductivity (W/m·K)	density (kg/m^3)	specific heat capacity (kJ/kg·K)	volumetric heat capacity (kWh$_{th}$/m^3·K)
		Liquids			
water	200–300	0.7	800	4.9	1.09
mineral oil	200–300	0.12	770	2.6	0.56
synthetic oil	250–350	0.11	900	2.3	0.57
silicone oil	300–400	0.10	900	2.1	0.52
liquid sodium	270–530	71	850	1.3	0.31
nitrite salts	250–450	0.57	1825	1.5	0.76
nitrate salts	265–565	0.52	1870	1.6	0.83
carbonate salts	450–850	2	2100	1.8	1.05
Hitec	220–600	0.46	1900	1.5	0.79
HitecXL	120–500	0.52	1990	1.4	0.77
		Solids			
cast iron	200–400	37	7200	0.56	1.12
cast steel	200–700	40	7800	0.60	1.30
sand/rocks/gravel	200–300	1	1700	1.30	0.61
concrete	200–400	1.5	2200	0.85	0.52
castable ceramic	200–390	1.35	3500	0.87	0.84
advanced concrete	200–390	1.0	2750	0.92	0.70
NaCl	200–500	7	2160	0.85	0.51
silica fire brick	200–700	1.5	1820	1.00	0.51
magnesia fire brick	200–1200	5	3000	1.15	0.96
graphite	200–2000	40	1900	1.75	0.92

Sensible systems can also be comprised of solid particles, such as those used in falling particle receivers. Dense gas-particle suspensions of approximately 50% of the solid, have been proposed for application in direct and indirect tubes as a HTF. This relatively new HTF behaves like a liquid with extended working temperatures as it remains in a fluidized state at any temperature above freezing and permits working temperatures up to 700 °C or more. Moreover, it can be used as an energy storage medium because of its high thermal capacity and potential ability to be employed in heat exchangers for power block dispatchable energy generation. The addition of nanoparticles in fluidized HTFs have also been explored to facilitate nanofluidic transport, which has been found to further enhance physical and transport properties, where work by Nagarajan *et* al. demonstrated a collector efficiency increase as high as 23.3% when using an Al_2O_3/water nanofluid, with a weight concentration of 0.2%. [446].

5.2.1 Molten Salts

The use of molten salts in a sensible storage medium is the standard against which most current storage options are compared. Conventional molten nitrate/nitrate salts become unstable at approximately 600 °C, however freeze at approximately 228 °C [7], which can be favorable for high-efficiency CSP receivers. Achieving higher-temperature, higher-efficiency power cycles requires new higher-temperature compositions [7]. However, many molten salts solidify at temperatures above ambient, causing blockage and potential damage to piping and heat exchangers. To address this, lower freezing-point salts would aid in the mitigation of freezing events in addition to achieving much higher temperatures [280]. Carbonate salts also appear to be

suitable for operation up to 850 °C [281]. Further work by Fraas [228] is described for a molten salt cooled nuclear reactor with a top temperature of 980 °C. Research with chloride salts have also been investigated as a thermodynamically stable means for achieving higher CSP operating temperatures (>700 °C) [7]. Sand, sintered bauxite, alumina, and ceramics have also been investigated as a heat-transfer and storage media [282]. Desirable features include a high solar absorptance (for direct irradiated particles), low thermal emittance, good durability, resistance to sintering, high heat capacitance, ease of flow, and low cost. Studies [7] have shown that commercial ceramics particles (sintered bauxite) used as proppants for hydraulic fracturing have many of the desired properties for directly irradiated receivers.

Additionally, solid-state storage systems have recently been researched [283] due to the relative low cost of many potential solid-state storage media and their ability to achieve higher-temperature operation. However, heat transfer into and out of the solid-state materials represents the largest challenge in developing these systems.

5.3 Latent Thermal Energy Storage

Most thermal energy storage systems in operation are sensible; however, storing heat in the form of latent heat of PCMs can significantly increase energy density [290]. Latent thermal energy storage (LTES) is facilitated by converting a storage media from one phase to another within an isothermal process. This can provide enhanced storage capacity when compared to sensible heat thermal energy storage (STES) systems of the same temperature range since STES materials are limited by the need to store at higher temperatures to achieve the desired output temperature for turbine systems [456]. The latent heat of phase change can store or retrieve large amounts of energy and are generally smaller, and on a weight basis LTES materials, have the potential to be more effective than sensible heat storage materials. LTES commonly leverages phase change phenomena between solid and liquid states, due in large part to its lower volumetric expansion, compared to liquid-gas, and its high latent heat compared to solid-solid transition [456]. In latent TES systems, energy is stored during phase change, and due to the specific heat of a typical medium the latent enthalpy change is usually greater than the sensible heat change for a given system size [284].

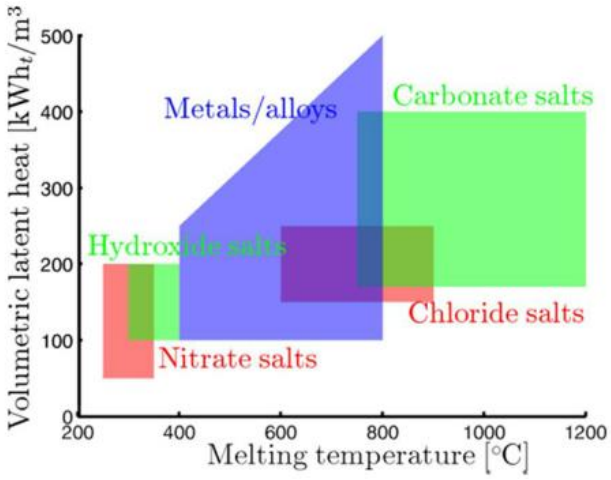

Figure 5.6. Volumetric latent heat with respect to melting temperature for latent heat TES PCM materials [139].

The U.S. DOE requirements for TES under the SunShot Initiative seeks to improve heat transfer and thermal energy storage medium, lower the systems costs to less than 15 kW/h, increase the exegetic efficiency to greater than 95%, and lower material degradation due to corrosion to less than 15 m/year [457]. A variety of LTES have been proposed to achieve desired CSP efficiencies and energy capacities, where in general these systems are categorized in two groups. First, active systems, where the storage medium is a fluid and flows between the tanks (common in sensible heat thermal energy storage). The second or passive systems, is where the storage medium is solid, contained in one tank, and the heat transfer fluid passes through the storage material only for charging and discharging [456]. However, most LTES systems are passive to ensure phase change within a controlled environment.

As can be noted from the boiling curve Fig. 2.3 in section 2, latent heat storage materials are usually useful over a small temperature range. The stored energy during a latent storage process can be assessed as:

$$Q_{Latent} = V\rho\Delta h_m = m\Delta h_m \tag{5.4}$$

where m denotes the mass and Δh_m is the specific latent enthalpy difference (heat of fusion) of the PCM material. Weinstein *et* al. [139] suggested that latent heat of melting roughly scales linearly with melting temperature for various classes of materials, where higher energy densities can typically be achieved for PCMs with high melting temperatures, Fig. 5.6. The investigators also pointed the advantages of latent heat PCMS over sensible materials where the energy density is typically higher as $h_m \gg C_p\Delta T$ and that charging and discharging processes usually occur at constant temperature, which is advantageous for alignment with system design heat engine operating temperatures [139].

An investigation by Angelino and Invernizzi [220] demonstrated that cooling of a molten salt from 550 °C to 300 °C facilitates an available specific energy of 387 kJ/kg while solidification of LiF at 848 °C supplies a specific energy of 1087 kJ/kg. A large number of pure salts or mixtures (typically fluorides of Ca,Mg, Na, K, etc.) are available with melting temperatures ranging from 750 to 1250 °C [220, 285]. Technical challenges still need to be addressed for the large volume change during melting with low thermal conductivity of the liquid and of the solid, where solutions have been proposed [286, 287]. A wide preliminary screening [288], where the fluoride salt is completely free from water, demonstrated that many metals and alloys are available with a sufficient corrosion resistance at temperatures around 900 °C. In particular, mild steel and pure nickel exhibits a relatively good resistance [285]. At high temperatures for binary cycles, phase-change heat storage seems the most promising option, where the thermal characteristics of melting PCMs, that exchange heat at a fixed temperature, simplifies insertion of the heat storage in the plant layout [220]. An instance of CSP plant layouts which includes a phase change thermal storage is given by Wallin and Dustin [286].

However, the process is isothermal, so unless the power cycle relies on nearly isothermal conditions (e.g., Stirling cycle, heavily recuperated sCO_2 cycles), high exergetic losses may occur. It has been demonstrated that TES systems that employ a latent phase change material (PCM) can maximize storage of useful energy (or exergy) and at the system level, increase the efficiency of a power system [289]. Nithyanandam *et* al. [291] illustrated that the energy required to melt one kilogram of sodium nitrate by latent heating, is 75% higher compared to the energy required to raise the temperature of one kilogram of the same substance by 1 K through sensible heating. Thus TES systems using latent sodium-based phase change materials have the advantage of being

volumetrically compact in size with enhanced heat transfer coefficients. Thermodynamically, sensible systems have been shown to be a poor exergetic fit for high temperature CSP systems, which include highly recuperated sCO_2, phase change storage, hybrid storage and chemical processing [7].

Finally, advanced research of various encapsulation methods for PCM have been evaluated to address challenges with heat transfer while the system is discharging [17]. Examples include encapsulation of small amounts of PCM within a solid that will not undergo phase change and impregnation of PCM into metal or graphite foams. The use of PCMs with an embedded thermosyphon or heat pipes have also been investigated to reduce thermal resistances [292].

5.4 Thermochemical Energy Storage

More compact TES can be achieved based on energy storage designs that utilize chemical reactions. Thermochemical storage (TCS) is based on the heat capacity and its change as function of temperature accompanied with chemical reaction. Here, TCS makes use of the enthalpy of reaction ΔH where reactions featuring a positive change of ΔH (endothermic reaction) heat can be stored [284]. Conversely, energy can also be released by a backward reaction ($\Delta H < 0$) which can provide energy input to a power block. This class of energy storage includes sorption and thermochemical reactions. In thermochemical energy storage, energy is stored after a dissociation reaction and then recovered in a chemically reverse reaction. Thermochemical energy storage has a higher storage density than the other types of TES, allowing large quantities of energy to be stored using small amounts of storage substances. Energy storage based on chemical reactions is particularly appropriate for long-term storage applications, e.g., seasonal storage of solar heat, because the process involves almost no energy losses during the storing period [284]. In their work, Abedin and Rosen [284] performed a comparison between sensible, latent and thermochemical energy storage where their results can be seen in Table 5.3, where the authors found that each had different operating characteristics and distinct advantages and disadvantages.

The main principle of thermochemical TES is based on a semi-reversible reaction [284]:

$$C + heat \leftrightarrows A + B \tag{5.5}$$

In Eqn. 5.5, a thermochemical material, *C* absorbs energy and is converted chemically into two components, *A* and *B*, which can be stored separately. The reverse reaction occurs when materials *A* and *B* are combined together and *C* is formed [284]. Energy is released during this reaction and constitutes the recovered thermal energy from the TES material. Storage capacity of this system is dependent on the heat of reaction when material *C* is formed. The charging process for this state is endothermic where thermal energy is absorbed from an energy resource and used for dissociation of the thermochemical material. This is equivalent to the heat of reaction or enthalpy of formation [284]. After the charging process, components *A* and *B* are separately stored with little or no energy losses where the materials are stored at ambient temperatures, leading to no thermal losses (except during the initial cooling of components *A* and *B* after charging) [284].

Table 5.3. General comparison between thermochemical energy storage with sensible and latent systems [284].

Performance Parameter	Type of Thermal Energy Storage		
	Sensible TES	**Latent TES**	**Chemical TES (Sorption and Thermo-chemical)**
Temperature range	Up to: 110 °C (water tanks) 50 °C (aquifers and ground storage) 400 °C (concrete)	20-40 °C (paraffins) 30-80 °C (salt hydrates)	20-200 °C
Storage density	Low (with high temperature interval): 0.2 GJ/m^3 (for typical water tanks)	Moderate (with low temperature interval): 0.3-0.5 GJ/m^3	Normally high: 0.5-3 GJ/m^3
Lifetime	Long	Often limited due to storage material cycling	Depends on reactant degradation and side reactions
Technology status	Available commercially	Available commercially for some temperatures and materials	Generally not available, but undergoing research and pilot project tests
Advantages	Low cost Reliable Simple application with available materials	Medium storage density Small volumes Short distance transport possibility	High storage density Low heat losses (storage at ambient temperatures) Long storage period Long distance transport possibility Highly compact energy storage
Disadvantages	Significant heat loss over time (depending on level of insulation) Large volume needed	Low heat conductivity Corrosivity of materials Significant heat losses (depending on level of insulation)	High capital costs Technically complex

Any other energy losses are due to degradation of the materials. Finally, during the discharge process, constituents *A* and *B* are combined in an exothermic reaction. The energy released from this reaction permits the stored energy to be recovered. After discharging, component *C* is regenerated and can be used again in the cycle. The discharging reaction can be written as:

$$A + B \rightarrow C + heat \tag{5.6}$$

Another thermochemical process, sorption (adsorption and absorption) is based on a chemical processes and thus are also considered chemical heat storage. Adsorption occurs when an adsorptive material accumulates on the surface of an adsorbent and shapes a molecular or atomic layer [284]. The adsorptive material can be a liquid or gas while the adsorbent can be a solid or liquid. Absorption is a process that occurs when a substance is distributed into a liquid or solid and forms a solution. Storing solar energy in the form of chemical bonds is attractive because the energy can be stored indefinitely, and thermal boosting can occur in the form of reduction/oxidation reactions [284]. There has been much research in this area where investigations by Weber and Dorer [294] analyzed long-term heat storage using a closed sorption system with NaOH and water as the working pair and compared the results with a conventional storage system, focusing on system volume [298]. An investigation based on bromide strontium as the reactant and water as the working fluid, in a system using flat plate solar collectors and applied to direct floor heating, demonstrated the relationship between attained power levels and the heating storage capacities of reactive composites [284]. Mauran *et* al. [299] analyzed

experimentally the same working pair for heating and cooling purposes (heating in winter or mid-season and cooling in summer). Zondag *et* al. [300] characterized magnesium sulphate as a storage media and examined cycling behavior of $MgSO_4$ and the dehydration temperature of the reactant. Thermal energy storage based on a $Ca(OH)_2$ and CaO cycle is also an example of thermochemical energy storage, where the reversibility and efficiency of this system was investigated in Azpiazu *et* al. [301]. Thermochemical energy storage based on ammonia and water has also been investigated in conjunction with a solar thermal plant [284]. General characteristics of these working fluis, as well as a dissociation and synthesis reactor were studied in [302], where the optimization of a related heat recovery device has been reported [303]. Overall, kinetics, energy density, and techno-economic costs present challenges and limitations to applying thermochemical energy storage [284].

6. CSP THERMODYNAMIC POWER SYSTEMS

6.1 Overview

Solar energy has a high exergetic value as it originates from processes occurring at the sun's surface with a blackbody equivalent temperature of approximately 5777 K [187]. Therefore, more than 93% of the energy generated may be theoretically converted to mechanical work by thermodynamic cycles [304], or to Gibbs free energy by chemicals and solarized chemical reactions [305], including promising hydrogen production processes [306]. Previous techno-economic analyses have shown a significant potential for cost reduction through efficiency improvement of the power block [66, 307]. Due to widespread use of turbomachinery and heat engine technology, CSP has some unique challenges with respect to other renewable energy technologies as a heat source in that it stands to benefit from economies of scale and thermodynamic technological advances from industries such as coal, natural gas and nuclear industries. While modern subcritical steam cycles (which are also common thermodynamic power cycles to date for CSP) may be limited to thermal efficiencies up to approximately 42% [66], supercritical steam cycles have been developed with thermal efficiencies exceeding 47% [249], with its relative comparison to other thermodynamic cycles as presented in Fig. 6.1. Combined cycles, which use rejected heat from a high-temperature cycle to drive lower-temperature cycles to supplement the power output, typically offer higher thermal efficiencies (potentially exceeding 60%) and have been used in traditional power cycles for decades [308]. Such high-performance cycles have been shown to be adaptable for CSP systems [309, 310], and represent an important step in reducing LCOE, while promoting CSP as a true competitor to traditional methods for utility-scale power generation. Currently, there is much effort to increase thermal conversion efficiency to meet the U.S. department of Energy (DOE) SunShot Initiative target of >50% thermal efficiency in an effort to reduce the cost of solar energy [7].

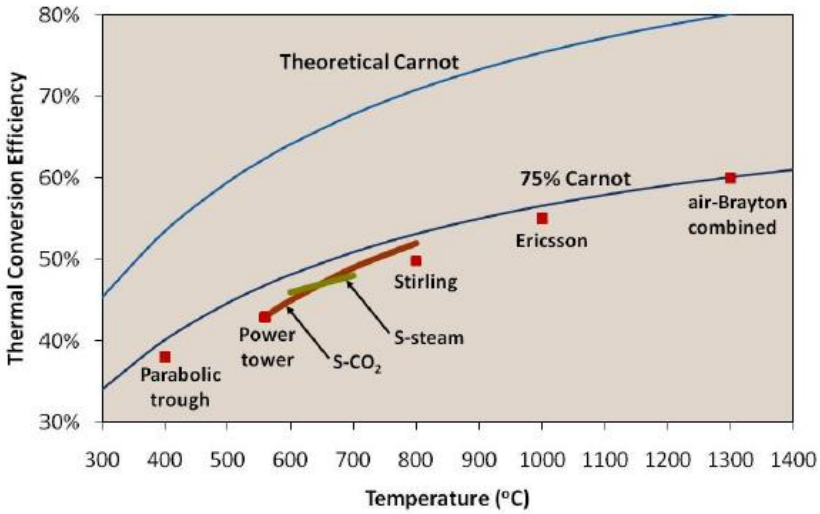

Figure 6.1. CSP thermodynamic cycle thermal conversion efficiency comparisons [311].

In order to achieve high conversion efficiencies, high temperatures at the heat engine and low temperatures at its energy sink are necessary. These temperatures are limited by the HTF in the receiver, as well as the working fluid in the heat engine cycle [197]. Overall, most ideal

thermodynamic cycles operate based on four processes of compression, heat input, expansion and heat rejection. Table 6.1 provides a breakdown comparison between various cycles that CSP currently, and potentially, can employ for research and application depending on whether the respective system operates independently or in combination with an internal or external combustion cycle.

Table 6.1. Thermodynamic Cycle Process Comparisons.

	Cycle	Process 1-2 (Compression)	Process 2-3 (Heat Input)	Process 3-4 (Expansion)	Process 4-1 (Heat Rejection)
External Combustion Cycles	Carnot	Isentropic	Isothermal	Isentropic	Isothermal
	Rankine	Adiabatic	Isobaric	Adiabatic	Isobaric
	Stirling	Isothermal	Isochoric	Isothermal	Isochoric
	Ericssson	Isothermal	Isobaric	Isothermal	Isochoric
	Hygroscopic	Adiabatic	Isobaric	Adiabatic	Isobaric
	Scuderi	Adiabatic	Variable Pressure and Volume	Adiabatic	Isochoric
	Stoddard	Adiabatic	Isochoric	Adiabatic	Isobaric
	Bell Coleman	Adiabatic	Isobaric	Adiabatic	Isochoric
Internal Combustion Cycles	Brayton	Adiabatic	Isobaric	Adiabatic	Isobaric
	Diesel	Adiabatic	Isobaric	Adiabatic	Isochoric
	Otto	Adiabatic	Isochoric	Adiabatic	Isochoric
	Lenoir	Isochoric	Isochoric	Adiabatic	N/A

Single cycles represent the simplest thermal power plant configurations, and are traditionally the baseline in identifying high-efficiency systems. A combined cycle however utilizes multiple thermodynamic cycles: one primary high-temperature (topping cycle) and one or more lower-temperature cycles (bottoming cycle), driven by heat rejected from the higher-temperature cycle. According to Dunham and Iverson [203] although significant improvements have been made with single cycle systems, it has been widely believed [312, 313] that operation above 50% thermal efficiency requires implementation of combined cycles with traditional HTFs. However, it has also been suggested that advanced sCO_2 and helium Brayton cycles could potentially achieve 50% [203]. For example, this can be attained by a Brayton-topped, combined cycle which can allow for optimum use of highly concentrated solar energy where the ideal operating temperature is beyond high-temperatures ever attained by sub-critical Rankine cycles [314]. While modern subcritical steam cycles may be limited to thermal efficiencies up to approximately 42% [66], supercritical steam cycles have been developed with thermal efficiencies exceeding 47% [249]. Combined cycles, which use rejected heat from a high-temperature cycle to drive a lower-temperature cycle to supplement the power output, typically offer higher thermal efficiencies (potentially exceeding 60%), and have been used in traditional power cycles for decades [308]. Such high performance cycles have been shown, or considered to be adaptable to CSP systems [309, 310].

6.2 Carnot Cycle & Thermodynamic Limitations

When assessing power block cycles, it is important to have a relative fundamental thermodynamic basis by which to compare them. The Carnot cycle provides an upper limit for thermodynamic efficiency that any classical thermodynamic engine can achieve during the conversion of heat into work, or conversely, the efficiency of a refrigeration system in creating a temperature difference to facilitate work to the system. Every thermodynamic system exists in a particular state, where a Carnot cycle exhibits the different states a system can go through, where it can eventually be

returned to its initial state. In the process of going through this cycle, the system may perform work on its surroundings, thereby acting as a heat engine, Fig. 6.2.

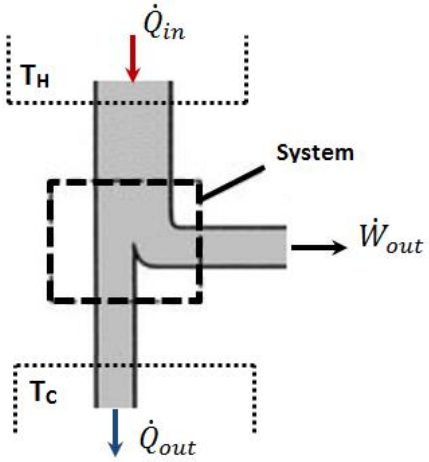

Figure 6.2. Carnot cycle work and thermal power transfer between two heat reservoirs

The process states of a Carnot cycle as depicted by the *PV* and *TS* diagrams in Fig. 6.3, when acting as a heat engine.

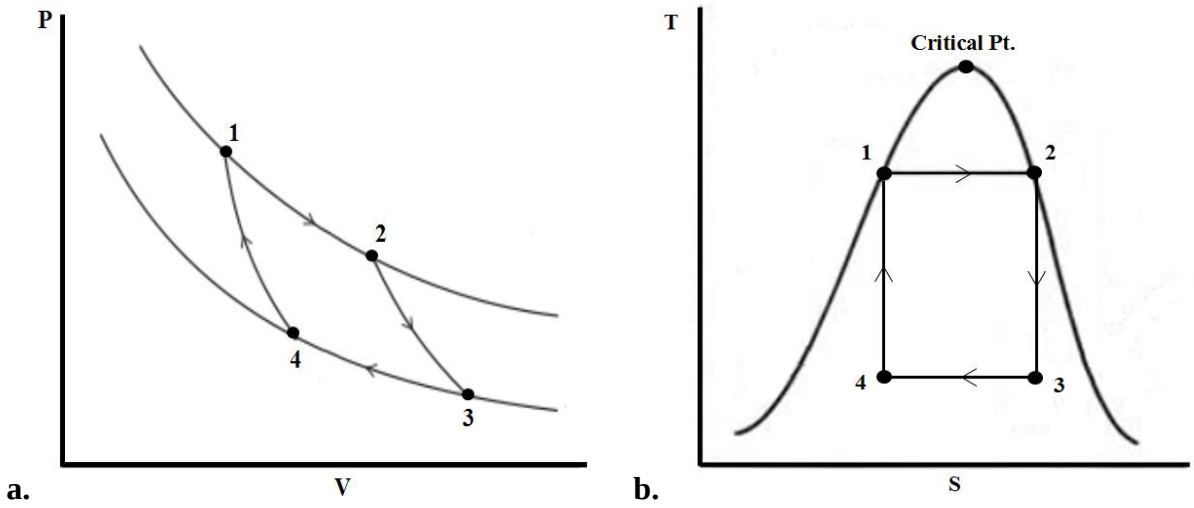

Figure 6.3. Carnot cycle thermodynamic P-V and T-S diagrams.

Process 1-2: Reversible isothermal expansion of a gas at a temperature, T_H (*isothermal heat addition or absorption*). During this step the gas is allowed to expand, where it does work on the surroundings. The temperature of the gas does not change during this process, and thus the expansion is isothermal. The expansion of gas is facilitated by absorption of thermal energy $\dot{Q}_{in}$ and entropy $dS = \dot{Q}_{in}/T_H$ from the high temperature reservoir.

Process 2-3: Isentropic (*reversible adiabatic*) expansion of the gas (*isentropic work output*). For this step the mechanisms of the engine are assumed to be thermally insulated, thus they neither gain nor lose heat. The gas continues to expand, doing work on the surroundings, and losing an equivalent amount of internal energy. The gas expansion causes it to cool to the temperature T_C. For this process the system entropy remains unchanged.

Process 3-4: Reversible isothermal compression of the gas at temperature T_C. (*isothermal heat rejection*). Here the ambient surroundings do work on the working fluid facilitating heat energy $\dot{Q}_{out}$ and entropy $dS = \dot{Q}_{out}/T_C$ to flow out of the working fluid to the low temperature reservoir. For this theoretical cycle, this would be the same amount of entropy absorbed in process 1-2, as can be seen from the Clausius inequality for an irreversible cyclic process:

$$\int \frac{\delta \dot{Q}}{T} \leq 0 \tag{6.1}$$

Process 4-1: Isentropic compression of the working fluid (*isentropic work input*). Here, just as with process 2-3, the mechanisms of the heat engine are assumed to be thermally insulated. During this process the surroundings do work on the working fluid, increasing its internal energy and compressing it, causing the temperature to rise to T_H. The entropy for this process remains unchanged.

From the Clausius inequality Eqn. 6.2, the amount of entropy *S* added to the system during the cycle is defined as:

$$\Delta S = \int \frac{\delta \dot{Q}}{T} \tag{6.2}$$

As prescribed by the 2nd law of thermodynamics, entropy is a state function since it depends only upon the state of the system and not what path the system took to get there. This however is in contrast to thermal energy added as heat ($\delta \dot{Q}$) and work ($\delta \dot{W}$), which may vary depending on the path. If the amount of energy added by heating can be measured during the process, and the temperature can be measured during the process, the Clausius inequality can be used to determine whether the process is reversible or irreversible by carrying out the integration in the Clausius inequality. In a cyclic process, the entropy of the system at the beginning of the cycle must equal the entropy at the end of the cycle. In the irreversible case, entropy will be created in the system, and more entropy must be extracted ($\Delta S < 0$) than was added in order to return the system to its original state. In the reversible case, no entropy is created and the amount of entropy added is equal to the amount extracted. However, for real systems, irreversibility *I* exists and accounts for the amount of exergy destroyed, or work wasted in a closed system. Irreversibility as it relates to the exergy in a closed system, with respect to entropy generated, is described by:

$$I = T_0 s_{gen} \tag{6.3}$$

where $I > 0$ if irreversibilities are present in the system thereby defining the actual work as:

$$\dot{W}_{act} = \dot{W}_{max} - I \tag{6.4}$$

With the relation $\dot{W}_{max} = \Delta B = B_{in} - B_{out}$ the available work or exergy is related to the irreversibility of a closed, real system as:

$$\Delta B = \dot{W}_{act} - I \tag{6.5}$$

For a Carnot engine with an unlimited reservoir that remains unaltered by the system, the exergy of a system heading towards equilibrium with respect to time is described by following expressions:

$$\frac{dB}{dt} \leq 0 \tag{6.6}$$

$$\frac{dS_{tot}}{dt} \geq 0 \tag{6.7}$$

From further integration, the area under the curve of Eqn. 6.8 can then be interpreted as the thermal power transferred into or out of the system.

$$\dot{Q} = \int_H^B TdS \tag{6.8}$$

If a process moves to a state of greater entropy, the area under the curve will be the amount of heat absorbed by the system, conversely if the process moves towards a state of reduced entropy it will correspond to heat removal. The area inside the cycle will then be the difference between the two, however since internal energy of the system must return to its initial value, the difference will correspond to the amount of work done by the system over the cycle. These relationships can be understood analytically by assessing a closed-system reversible process where the amount of work done over a cyclic is:

$$\dot{W} = \int PdV = \int(d\dot{Q} - dU) = \int(TdS - dU) = \int TdS - \int dU = \int TdS \tag{6.9}$$

Here since d*U* is an exact differential, where its integration over a closed loop is zero, it follows that the area inside the loop on a *T*-*S* diagram is equal to the total work performed if the loop is traversed in a clockwise direction, and is equal to the total work done on the system if the loop is traversed in a counterclockwise direction. Finally, the theoretical Carnot efficiency can be written in terms of output work and heat input, as well as the volumes at different states by:

$$\eta_{Carnot} = \frac{\dot{W}_{out}}{\dot{Q}_{in}} = 1 - \frac{\dot{Q}_C}{\dot{Q}_H} = 1 - \frac{T_C[ln(V_4/V_3)]}{T_H[ln(V_2/V_1)]} \tag{6.10}$$

The processes from states 2 to 3 and from 4 to 1 are both adiabatic and reversible where the expression $PV^\gamma = constant$ holds. From the ideal gas equation of state, one is able to obtain $TV^\gamma = constant$, which provides:

$$T_H V_2^{\gamma-1} = T_C V_3^{\gamma-1} \text{ and } T_H V_1^{\gamma-1} = T_C V_4^{\gamma-1} \tag{6.11}$$

Therefore, with incorporation of these expressions into Eqn. 6.10:

$$\left(\frac{V_4}{V_3}\right)^{\gamma-1} = \frac{(T_H/T_C)}{(T_H/T_C)}\left(\frac{V_1}{V_3}\right)^{\gamma-1} \rightarrow \frac{V_4}{V_3} = \frac{V_1}{V_3} \tag{6.12}$$

By evaluation of Eqn. 6.10, one is able to observe that heat received or rejected is related to the temperatures of the isothermal portions of the cycle by Eqn. 6.13, and a final form of Carnot efficiency Eqn. 6.14:

$$\frac{\dot{Q}_L}{T_L} + \frac{\dot{Q}_H}{T_H} = 0 \tag{6.13}$$

$$\eta_{Carnot} = 1 - \frac{T_C}{T_H} \tag{6.14}$$

For more realistic, less efficient cycles that contain irreversibilities, the average high and low cycle temperatures $\langle T_H \rangle$ and $\langle T_C \rangle$ will be lower than T_H and T_C respectively.

$$\langle T_H \rangle = \frac{1}{\Delta S} \int_{\dot{Q}_{in}} T dS \tag{6.15}$$

$$\langle T_C \rangle = \frac{1}{\Delta S} \int_{\dot{Q}_{out}} T dS \tag{6.16}$$

6.3 Rankine Cycle

6.3.1 Overview and Theory

A single Rankine power cycle represents one of the simplest power block configuration, and can be the baseline for identifying high-efficiency CSP systems. The water vapor with condensed droplets that emanate from power station cooling systems represents the potential for low-temperature waste heat to be used as an addition heat source that can be converted to useful work or power. Exhaust heat is represented by $\dot{Q}_{out}$ flowing from of the lower side of the *T-s* diagram Fig. 6.4, where processes 1-2 and 3-4, represented by vertical lines, closely resemble that of the Carnot cycle. For this cycle, vapor is prevented from the superheated region after the expansion in the turbine, which reduces the energy removed by the condensers. The actual vapor power cycle differs from an ideal Rankine cycle due to irreversibilities inherent within the components by fluid friction and heat losses to the ambient. Additionally, fluid friction also facilitates pressure drops (or head losses) within the heat input stage (generally also known as the "boiler"), the condenser, and system piping, which can result in steam leaving the boiler at a lower pressure, where heat losses reduce work output. For the Rankine cycle, Fig. 6.4 presents these four principal stages:

- **Process 1-2**: Compression of the liquid working fluid to high pressure. The working fluid is pumped from low to high pressure. As the fluid remains liquid at this stage, the pump requires relatively low input energy.

- **Process 2-3**: Heating and subsequent vaporization of the working fluid that is driven by a heat source. The high pressure liquid enters a heat input stage where it is heated at constant pressure by an external heat source to become a dry saturated vapor. The input energy required can be calculated by an *h-s* chart (Mollier diagram), or numerically using pre-defined tables.

- **Process 3-4**: Expansion through a turbine to a lower pressure for generating mechanical work. The dry saturated vapor expands through a turbine, generating power, which decreases the temperature and pressure of the vapor.

- **Process 4-1**: Cooling of the working fluid back to its initial state. The wet vapor then enters a condenser where it is condensed at constant pressure to become a saturated liquid.

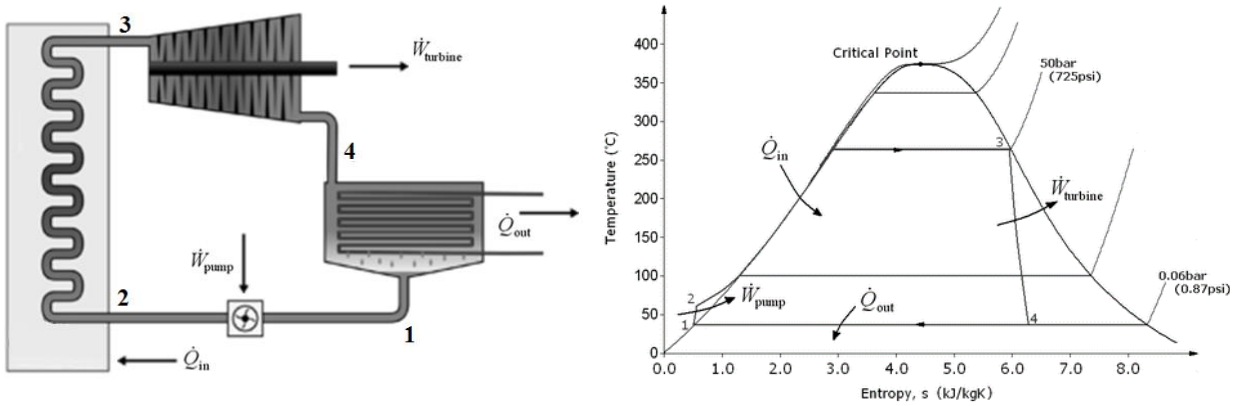

Figure 6.4. Ideal Rankine cycle components and T-s diagram [315].

In an ideal Rankine cycle the pump and turbine would be isentropic (i.e., the pump and turbine would not generate entropy and therefore maximize the net work output). The efficiency of the Rankine cycle is limited by the high heat of vaporization of the working fluid. Unless pressure and temperature reach super critical levels within the heat input stage, the temperature range the cycle can operate over is quite small. For water as the working fluid, steam turbine entry temperatures are typically around 565 °C and steam condenser temperatures are around 30 °C [315]. This gives a theoretical maximum Carnot efficiency for the steam turbine alone of about 63% compared with an actual overall thermal efficiency of up to 42% for a modern coal-fired power station. This low steam turbine entry temperature (compared to a gas turbine system) is why the Rankine cycle is often used as a bottoming cycle to recover otherwise rejected heat in combined-cycle gas turbine power stations [203]. Additionally, subcritical steam Rankine cycles used in solar facilities such as Solar One or SEGS [316] operate within the efficiency range of 37-42% [66, 317]. This type of cycle, used for CSP parabolic troughs, have typically been limited to turbine inlet temperatures of less than 400 °C due to limitations of oil, and relatively low solar flux levels provided by concentrating optics [203]. The utility of molten salt used as a working fluid systems that do not use an intermediate HTF (such as those that generate steam directly) have previously been explored [318]. These systems have been shown to raise turbine inlet temperature above 400 °C for trough systems [318, 319].

Cooling towers operate as large heat exchangers by absorbing the latent heat of vaporization of the working fluid, while simultaneously evaporating cooling water to the atmosphere. In traditional Rankine cycles, water is typically used due to its favorable properties, such as its non-toxic and unreactive chemistry, abundance, low cost, and favorable thermodynamic properties. By condensing steam vapor to a liquid, the pressure at the turbine outlet is lowered and the energy required by the feed pump consumes only 1% to 3% of the turbine output power where these factors contribute to a higher overall efficiency [203]. Gas turbines traditionally experience entry temperatures approaching 1500 °C. However, thermal efficiencies of actual large steam power stations and large modern gas turbine stations have been found to be similar [203].

For CSP, molten-salt power tower plants are limited to receiver outlet temperatures of approximately 565–600 °C and employ heat exchangers to produce superheated steam at approximately 540 °C and 130 bar, with reheated steam at 538 °C and 28 bar [202]. The result in

gross thermal efficiencies are typically 42% with wet cooling [202]. Typical steam Rankine cycles are limited to operational temperatures of up to approximately 600 °C, where higher efficiency can be achieved with supercritical steam Rankine cycles, with temperatures up to 760 °C [139]. Supercritical steam cycles have the potential to operate at higher temperatures and pressures, increasing the thermal efficiency to above 45% [250, 320].

Operating with steam in the supercritical regime allows for higher temperatures and fluid behavior that shares the compressibility traits of a liquid (reducing compressor work and enhancing regenerative heat exchange) while avoiding complications due to multiphase heat exchangers. However, concern has been expressed when steam temperatures exceed 627 °C due to the limitations of standard ferritic steels; these higher temperatures are expected to require the use of high-nickel composition alloys [203, 320, 323]. Organic Rankine Cycles (ORC) have been studied in-depth for their use in medium-temperature, and waste heat recovery applications [321, 322], though they typically have efficiencies of approximately 10–20%, and are most often used as bottoming cycles when the exit stream from a high temperature cycle still possesses high availability.

Additionally, alkali metals have been proposed for high-temperature topping cycles in a Rankine–Rankine combined cycle configuration [220]. This system provides good temperature-matching with a bottoming steam cycle with high heat transfer coefficients due to liquid metal phase change in the condenser. Thermal efficiencies of an alkali metal Rankine topping cycle and steam Rankine bottoming cycle have been shown to reach 56% for 1000 °C maximum working fluid temperature, with the potential to reach 60% [203]. However, turbomachinery for metal vapor cycles is estimated to be large, with a 50 MW turbine tip diameter of about 3.9 m for potassium and 2.8 m for rubidium [220]. Finally, although organic Rankine cycles have been well studied, primarily for medium temperature systems [321], they typically only have seen efficiencies of approximately 10-20%, where they are most often used in bottoming cycles when the exit steam from a high temperature cycle still possesses high availability [320].

6.4 Brayton Cycle

6.4.1 Overview & Theory

A Brayton cycle behaves similar to a Rankine cycle with the exception that the working fluid remains in the gas phase throughout the cycle [203]. Brayton cycles are able to operate at much higher temperatures, which can increase potential thermal efficiencies. Innovative receiver concepts have been proposed and demonstrated which can heat gases to temperatures above 1000 °C [68, 324]. However, the compression stage of gas-Brayton cycles requires much more power [203]. Although CSP trough systems typically operate at approximately 400 °C and Rankine cycle power towers operate at temperatures up to approximately 540 °C, Brayton thermodynamic cycles can operate at temperatures approaching 1,000 °C, offering development opportunities for greatly increased efficiency [66]. Higher efficiencies on the order of 50% are predicted for advanced, high-power, multiple-reheat, helium Brayton cycles which could operate with a turbine inlet temperature from 750 to 850 °C [203]. These temperatures are significantly higher than those used in subcritical steam Rankine cycles, but are achievable by current high-concentration solar tower technology. Helium possesses good heat transfer characteristics which also could be beneficial in

the design of the solar receiver. Angelino and Invernizzi [220] note that the closed helium cycle could be useful in cogeneration applications, as the rejected heat is typically available at relatively high temperatures. In 2002, a hybrid open solar Brayton cycle was operated for the first time consistently and effectively with relevant papers published, in the frame of the EU SOLGATE program [349]. The air was heated from 570 K to over 1000 K into the combustor chamber. Further hybridization was achieved during the EU Solhyco project running a hybridized Brayton cycle with solar energy and Biodiesel only [350]. This technology was scaled up to 4.6 MW within the project Solugas located near Seville where it is currently demonstrated at pre-commercial scale.

The premise of a Brayton cycle system is to extract energy from a flowing gas and fuel to generate useable work to power jet-powered aircraft and utility power block generators by providing thrust to a turbine. The cycle as shown in Fig. 6.5a can employ a heat exchanger or regenerator for heat removal, or it can be absent, as shown in Fig. 6.5b where the hot gas is exhausted directly to the ambient.

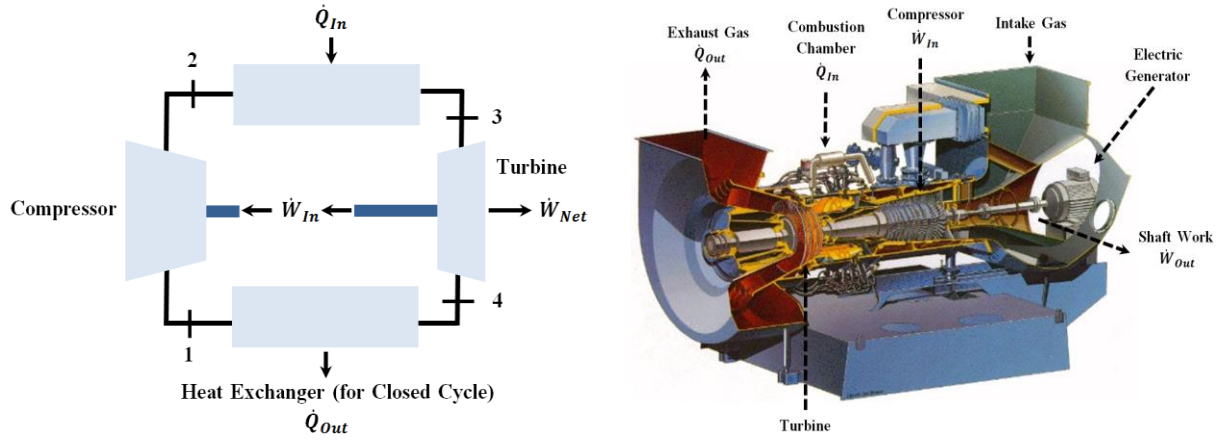

Figure 6.5. a. Closed loop ideal Brayton cycle and b. illustration of an open Brayton cycle system [326].

The most basic steps within a Brayton cycle in extracting energy is compression of flowing air, combustion, and then expansion of that air to create work and also power the compression at the same time. Although many irreversibilities exist within real systems, an ideal approach can be employed, Fig. 6.6 to quickly assess power production and efficiency, based on the following state processes:

- **Process 1-2:** Inlet gas enters and contacts the compressor which causes the pressure and temperature to dramatically rise. The rise in pressure comes from work being facilitated by the compressor which packs the gas into the mixer/combustion chamber. The rise in pressure accelerates a rise in temperature of the gas molecules due to the volume staying constant. For an ideal process ($PV = nRT$), entropy is assumed to be relatively constant (isentropic process) due to the flow of the gas.

- **Processes 2-3:** As the gas is compressed into the combustion chamber, it is typically mixed with a fuel to facilitate ignition, however for CSP applications, this process can be partially or fully omitted as hot gas is allowed to enter from a high-temperature receiver. For combustion

processes, once the gas-fuel mixture is ignited a steep rise in temperature and entropy is facilitated. The energy from the chemical bonds in the fuel are broken due to ignition, which is highly exothermic which raises entropy and raises the temperature due to increased ambient energy from the reaction.

- **Process 3-4:** The pressurized (and elevated temperature) fuel and air leave the combustion chamber to an expansion chamber, where a rapid drop in pressure is facilitated due to an increased volume change. The energy from combustion (increased *P* and *T*) is used to exert a force on a turbine/generator system and to the compressor for continuous Brayton cycle operation. The remaining energy from this process can be leveraged as a higher energy level input in an intermediate process for enhancing efficiency, or will be lost to surroundings (isobaric process).

- **Process 4-1:** Cooler exhaust gas from the turbine may enter into a heat exchanger which facilitates heating of the working fluid from a high-temperature receiver or from TES. Additionally, this process may be omitted if the working fluid is directly heated from a receiver.

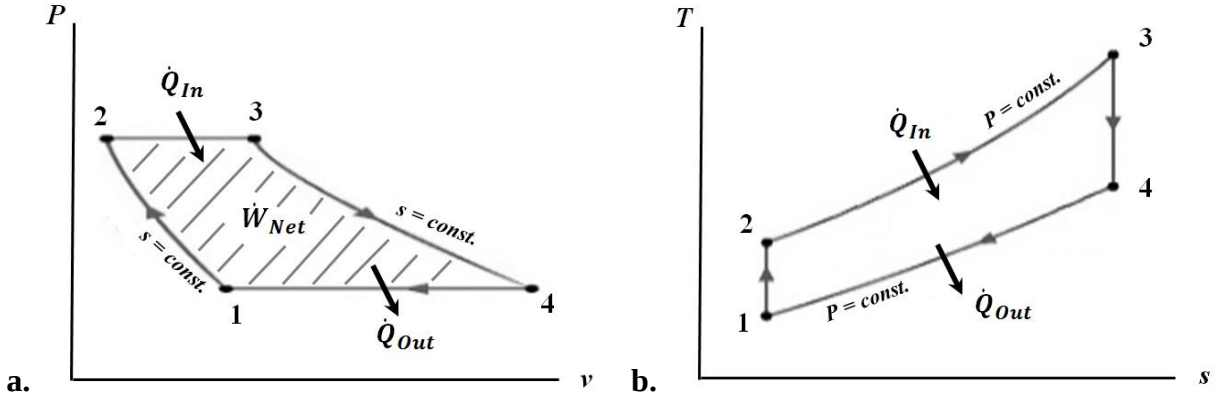

Figure 6.6. Ideal Brayton Cycle a. P-V Diagram and b. T-S Diagram.

The thermal efficiency of the cycle can be determined from the net output work and the heat absorbed. Tracing the path shown around the cycle from *a-b-c-d*, the first law, in terms of unit mass, provides:

$$\Delta u_{a-b-c-d-a} = 0 = q_2 + q_1 - w \tag{6.17}$$

Here Δu is approximated as zero where u is a function of state, and where any cycle returns the system to its starting state [326]. The net work is therefore:

$$w = q_2 + q_1 \tag{6.18}$$

where q_1 and q_2 are defined as heat received and rejected by the system respectively. For a constant pressure, quasi-static process the heat exchange per unit mass is defined by writing the first law in terms of enthalpy:

$$dh = C_p dT = dq \tag{6.19}$$

In general, heat exchange can be expressed in terms of enthalpy differences between respective states, where the working fluid can be idealized as a perfect gas with constant heat capacity values. Therefore, the heat addition from the combustor can be expressed as:

$$q_2 = h_c - h_b = C_p(T_c - T_b) \tag{6.20}$$

Similarly, the heat rejected can be expressed as:

$$q_1 = h_a - h_d = C_p(T_a - T_d) \tag{6.21}$$

The net work per unit mass is provided by:

$$Net\ Work\ per\ Unit\ Mass = \ q_1 + q_2 = C_p[(T_c - T_b) + (T_a - T_d)] \tag{6.22}$$

The Brayton cycle thermal efficiency can then be expressed in terms of state temperatures:

$$\eta = \frac{Net\ Work}{Heat\ In} = \frac{C_p[(T_c - T_b) - (T_d - T_a)]}{C_p[T_c - T_b]} = 1 - \frac{(T_d - T_a)}{(T_c - T_b)} = \frac{T_a\left(\frac{T_d}{T_a} - 1\right)}{T_b\left(\frac{T_c}{T_b} - 1\right)} \tag{6.23}$$

To assess temperature relationships between the states within the cycle it is important to note that points *a* and *d*, as well as states *b* and *c*, operate on a constant pressure processes, where P_a=P_d, P_b=P_c. The other processes of the cycle are adiabatic and reversible, where:

$$\frac{P_d}{P_c} = \frac{P_a}{P_b} \quad \rightarrow \quad \left(\frac{T_d}{T_c}\right)^{\gamma/(\gamma-1)} = \left(\frac{T_a}{T_b}\right)^{\gamma/(\gamma-1)} \tag{6.24}$$

Accordingly, T_d/T_c=T_a/T_b and T_d/T_a=T_c/T_b. Using this relation in the expression for thermal efficiency, the above equation yields an expression for the thermal efficiency of a Brayton cycle:

$$Ideal\ Brayton\ Cycle\ Efficiency\text{: } \eta_{Brayton} = 1 - \frac{T_a}{T_b} = 1 - \frac{T_{atm}}{T_{comp,o}} \tag{6.25}$$

The efficiency of the Brayton cycle be determined based of the temperature ratio across the compressor, TR=T_b/T_a, the pressure ratio PR, and the relation for an adiabatic reversible process:

$$\eta_{Brayton} = 1 - \frac{1}{TR} = 1 - \frac{1}{PR^{(\gamma-1)/\gamma}} \tag{6.26}$$

As prescribed by Eqn. 6.26, to achieve a high thermal efficiency, with system parameters prescribed by [326], the pressure ratio of the cycle should be increased as demonstrated by Fig. 6.7.

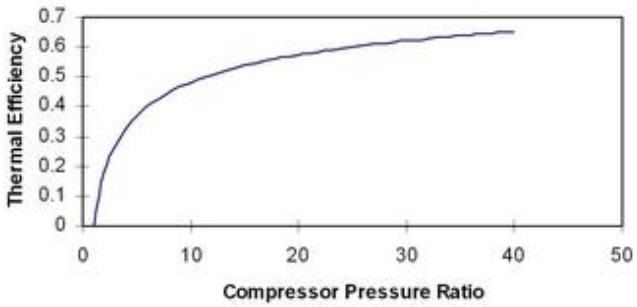

Figure 6.7. Ideal Brayton Cycle Compressor Pressure Ratio versus Thermal Efficiency [326].

6.4.2 Supercritical Brayton Cycles

Supercritical operation can permit an enhanced capture and utilization of heat, taking advantage of both latent and sensible HTFs in the two-phase regime as well as in the supercritical regime, while also reducing the required volume by taking advantage of high compressibility. Additionally, for supercritical systems storage performance and pressures can be optimized by judicious selection of fluids, such as sCO_2, with the following properties:

1. High latent heat of vaporization
2. High specific heat
3. High critical point
4. Low vapor pressure

For supercritical CO_2 systems, a heat source or CSP receiver can be incorporated within the loop as illustrated by the simple sCO_2 layout and T-s diagram provided by Goswami [332], Fig. 6.8.

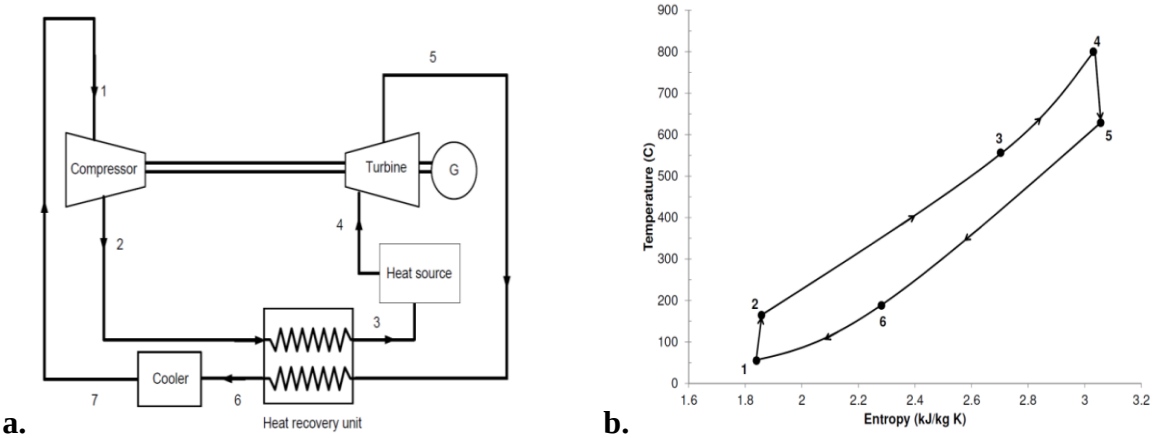

Figure 6.8. Simple sCO_2 Brayton cycle a. component layout and b. *T-s* diagram [332].

Supercritical gases can be advantageous working fluids for use in power generating turbines as they offer high efficiency with a compact footprint that can be matched to many different heat sources in CSP. In addition to increasing interest in nuclear and renewable energy, sCO_2 is becoming an important commercial and industrial solvent due to its advantages in chemical

extraction, low toxicity, stability and environmental impact. Previous research has shown promise for sCO_2 transport in pipelines, in addition to energy storage, as illustrated in Fig. 6.9 [327].

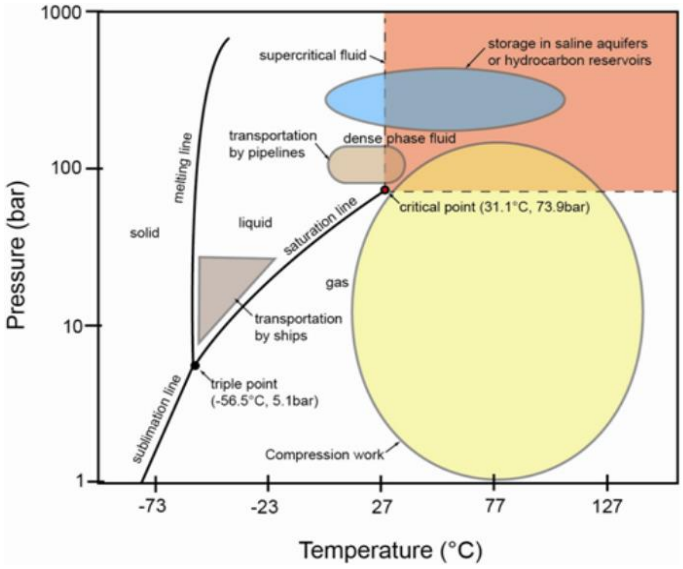

Figure 6.9. sCO_2 phase diagram with various CCS operations with superimposed pressure/temperature operating domains [327].

In an sCO_2 system, the fluid is compressed where the high turbine inlet temperature can be utilized with less material issues compared with steam Rankine cycles. However, the cycle pressure ratio of the sCO_2 Brayton cycle is much smaller than the steam Rankine cycle where the turbine outlet temperature is relatively high. Therefore, a large amount of heat must be recuperated to increase thermal efficiency, where the recuperation process greatly influences the thermal efficiency.

The CO_2 critical condition is achieved at 30.98 °C and 7.38 MPa where the fluid becomes more incompressible near the critical point as illustrated by Fig. 6.10 based on Eqn. 4.7.

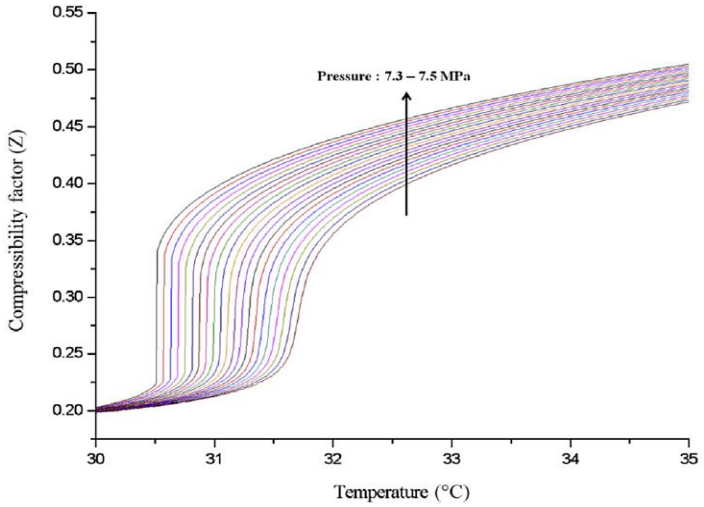

Figure 6.10. CO_2 compressibility factor as a function of temperature [328].

In the supercritical region, fluids exhibit compressibility and heat transfer characteristics more like liquids while still reaching high temperatures. This allows for reduced compressor work and more

efficient regenerative heat exchange [328]. CO_2 behaves like an ideal gas when the compressibility factor (molecular volumetric ratio of a fluid compared with ideal gas) is unity and is considered to be an incompressible fluid when it is zero. For operation near the critical point, the compressibility factor decreases to values between 0.2-0.5 where the compression work can therefore be substantially decreased [328]. Additionally, previous research within the aerospace and nuclear industries has demonstrated unique thermodynamic performance enhancements of Brayton systems with the utility of sCO_2 as the working fluid. As shown in Fig 6.11, for constant pressure conditions, heat capacity and enthalpy of CO_2 has remarkable thermodynamic property advantages over other readily available gases for employment in high temperature power systems [329].

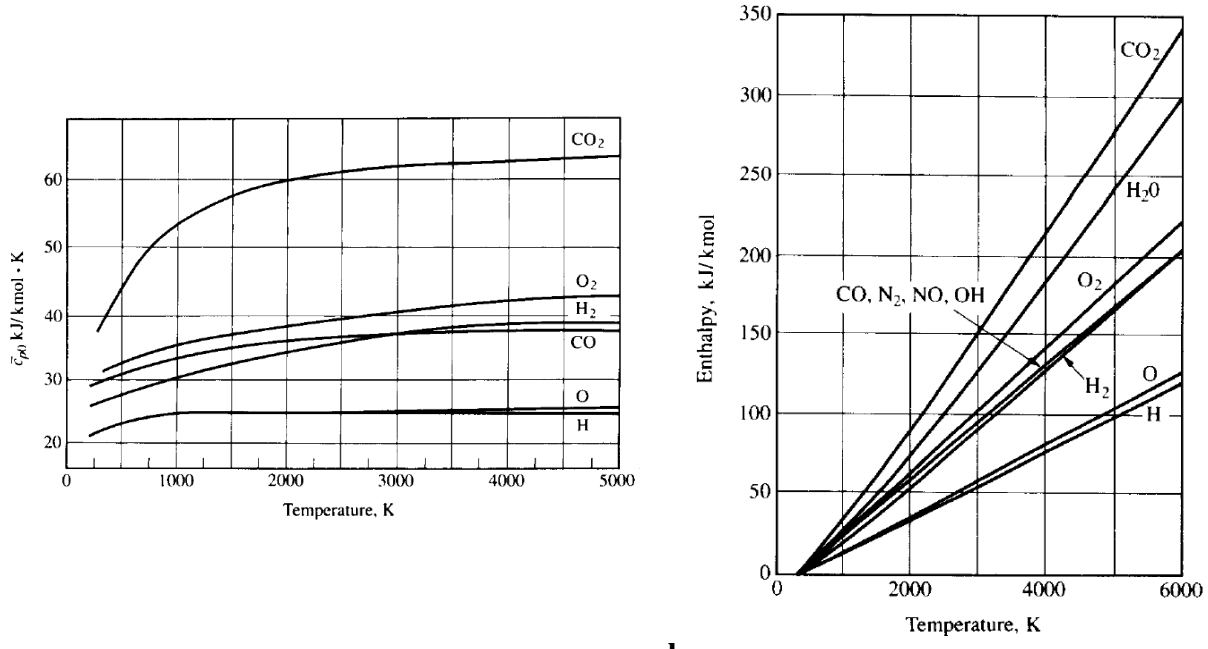

a. **b.**

Figure. 6.11. Comparisons of gases under constant pressure for a. specific heat and b. enthalpy [329].

As illustrated by Fig. 6.12, during operation in a CSP system, an sCO_2 bottoming cycle is first pumped up to a supercritical pressure, and then heated by a gas or heat from a solar receiver. The heated sCO_2 gas will then expand in the turbine producing work, where the vapor is then discharged from the turbine outlet to be cooled and condensed within a condenser (typically a gas cooler). The internal heat exchanger (regenerator) is typically included to optimize the performance. Provided that the compressor inlet conditions are kept in the vicinity of the critical point the specific compressor work is low and the compressor absorbs a small part of the work produced by the turbine [330].

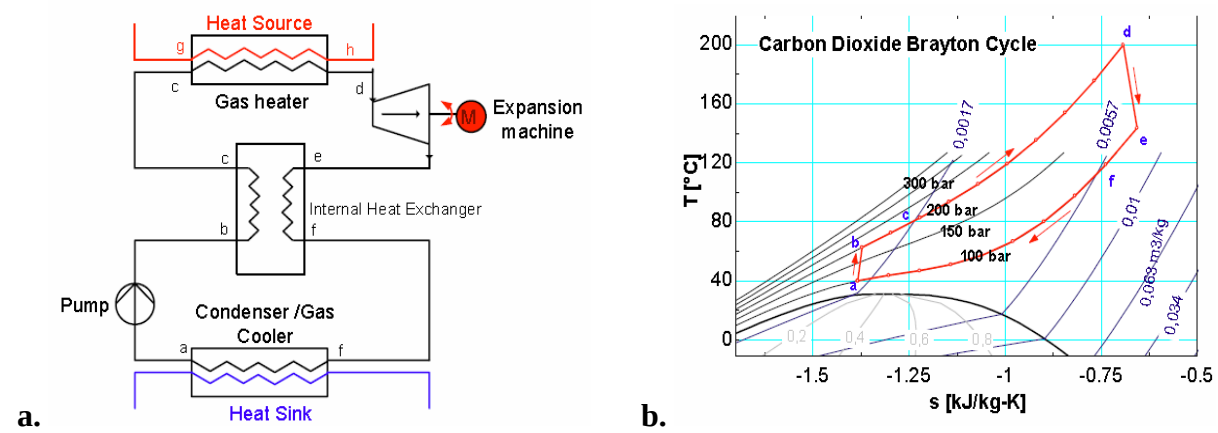

Figure 6.12. a. Carbon dioxide power system schematic and b. Carbon dioxide Brayton cycle *T-s* diagram [331].

Additionally, a notable thermodynamic characteristic of sCO_2 is its specific heat with respect to temperature as illustrated by Fig. 6.13. During operation the cold-side recuperator can have specific heat values that can be as high as two to three times that of the hot-side recuperator, which can have a negative impact on performance [328]. Therefore, design measures can be taken to split the sCO_2 flow to compensate for this specific heat difference to maximize recuperation for a recompression design, which reduces waste heat and improves thermal efficiency [328].

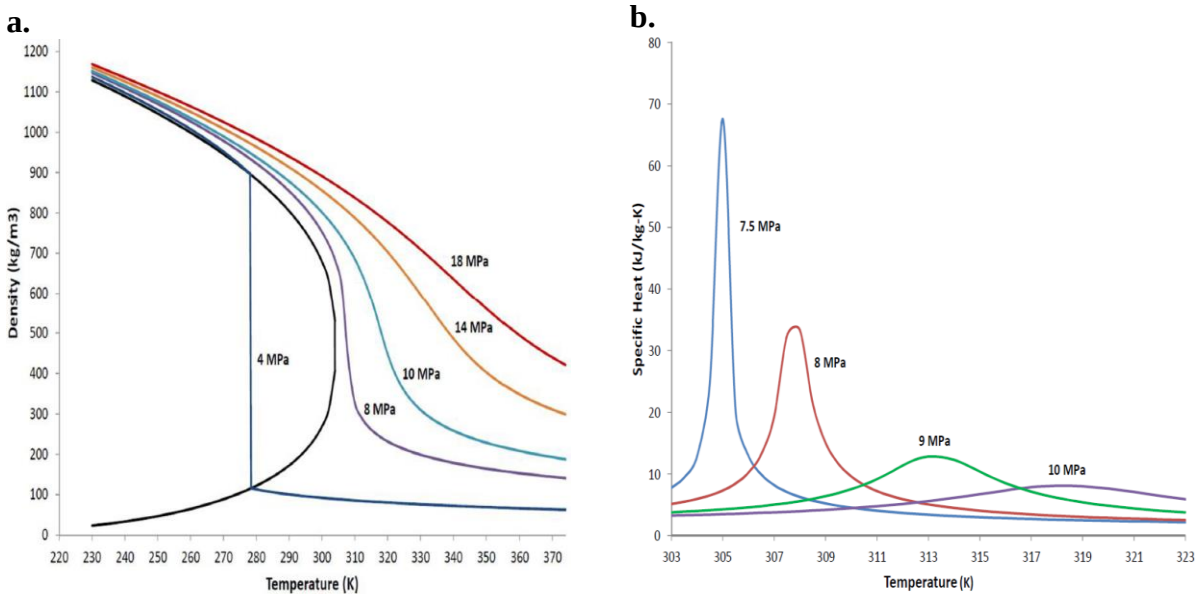

Figure 6.13. Specific heat and density properties of sCO_2 around the critical point [332].

The region near the CO_2 critical point is marked by rapid fluctuations in thermodynamic properties which may present a challenge in the design and operation of turbomachinery, particularly for a transient heat source from concentrated solar energy [203]. An incentive for using sCO_2 in turbine power cycles is also based on its favorable thermal stability compared to steam which allows for much higher power output in a much smaller package than comparable steam cycles [64]. The sCO_2 cycle is inherently efficient due to its operation near its respective critical point and the

ability of the working fluid to tolerate very high inlet temperatures. The high fluid density of sCO_2 enables extremely compact turbomachinery designs that can be highly efficient with simple, single casing body designs. Fig. 6.14 demonstrates the relative size difference for two 10 MW_e systems, where the overall size of sCO_2 turbo-machinery is significantly smaller than either conventional steam or helium turbines [338]. Additionally, due to its relative smaller size, many of the components for the sCO_2 system can be manufactured with advanced adaptive manufacturing technology [339].

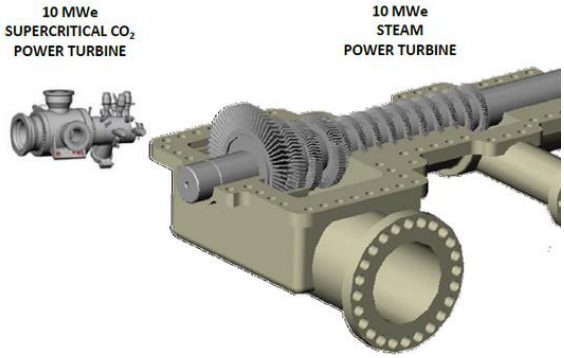

Figure 6.14. Comparison of Echogen 10 MW_e sCO_2 turbine with 10 MW_e traditional steam turbine [338].

More conventional steam turbines require multiple stages (e.g. low, medium and high-pressure) with associated casings, which can lead to a corresponding increase in inlet/outlet systems packaging complexity and O&M issues [338]. sCO_2 is effective at capturing waste heat from sources that have an approximately constant heat capacity, such as turbine exhaust or other hot gases due to the character of its heat capacity in the supercritical region. This can provide superior matching to the heat source temperature profile compared with boiling processes with other working fluids (steam or organic working fluids) used in organic Rankine cycle systems [338].

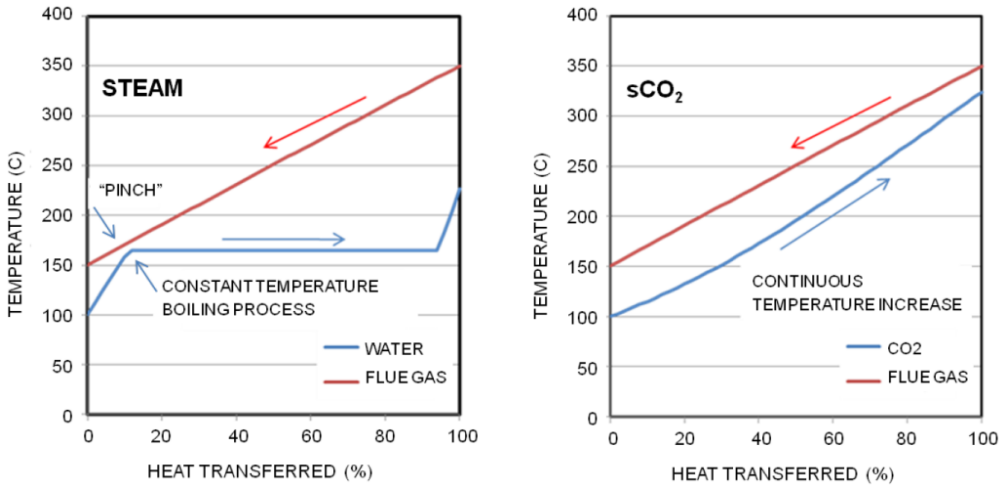

Figure 6.15. a. Steam and b. supercritical CO_2 working HTFs during heating in an exhaust heat exchanger [338].

As shown in Fig. 6.15 in comparing gas heat exchanger performance between CO_2 and steam that undergoes constant-temperature phase change, Persichilli *et* al. demonstrated the pinch point

phenomenon, which limits the maximum fluid temperature and resulting cycle efficiency [338]. The investigators determined that for steam-based systems, the boiling process limits the maximum fluid temperature and can require multiple heat recovery steam generators (HRSG) to get close to the same CO_2 gas temperature thereby reducing heat exchanger effectiveness.

Angelino found that single-heating sCO_2 cycles above 650 ^oC have a higher efficiency than reheat steam Rankine cycles [220]. Dostal *et* al. showed a thermal efficiency of 46.07% for an sCO_2 Brayton cycle with a turbine inlet temperature of 550 ^oC, and 49.25% for a helium Brayton cycle with turbine inlet temperature of 880 ^oC [334]. The volumetric flow rate for sCO_2 is much less than that for helium by approximately a factor of 5 [203], leading to relatively smaller turbomachinery requirements. Moisseytsev and Sienicki examined an sCO_2 cycle for a lower-temperature nuclear-driven process which operated between 31.25 ^oC/7.4 MPa and 470 ^oC/20.0 MPa with a thermal efficiency of 39.1% [334]. An increase in thermal efficiency to 43.1% was found by reducing the minimum temperature and pressure to 20 ^oC/5.75 MPa so the cycle operated as a condensation cycle. However, the low condensation temperature requires heat rejection to a relatively low temperature that may not be possible in environments where the ambient temperature is high. The sCO_2 Brayton cycle has been considered for use in CSP in studies of transient behavior by a cyclic, solar-driven heat source [335]. Garg *et* al. [336] concluded that by operating in the supercritical regime, the same thermal efficiency can be achieved with a lower maximum temperature, suggesting the potential for cost savings. Ma and Turchi suggested a modular tower design to capitalize on small sCO_2 turbomachinery where the entire power block would be placed on a power tower rather than transport high-pressure fluid to an externally located power block or incur large financial costs with a single large tower [261]. Additionally, Singh *et* al. [337] have also found promise for employment of sCO_2 in parabolic trough concentrators.

Challenges for using sCO_2 for CSP applications are generally focused on materials that can handle elevated temperatures/pressures, manufacturing turbo machinery, valves, pumps, seals, and high costs. Compatible heat exchangers that can effectively transfer heat from a receiver HTF to a sCO_2 working fluid is also a significant challenge that has garnered much research over the last decade [340]. An analysis by Dunham and Iverson [203] performed a review of several high-efficiency thermodynamic cycles and the applicability to CSP systems, where they found in comparison to He-Brayton, regenerated CO_2 Brayton, CO_2 recompression Brayton and CO_2-ORC combined cycles that steam Rankine cycles showed higher thermal efficiencies at temperatures up to 600 ^oC. Above this temperature, CO_2 recompression Brayton cycles were shown to have a very high superior thermal efficiency, potentially even exceeding 60% at 30 MPa maximum pressure and above 1000 °C maximum temperature with wet cooling [203]. For these cycles, HTF salts have also been investigated, such as the work by Forsberg *et* al. [341], who proposed high operating temperature molten salts (>700 °C) for use in power towers with direct thermocline TESS and graphite as a filer material. The multi-reheat Brayton cycle utilized helium and nitrogen as the working fluid and was able to achieve operating temperatures between 700 °C and 1000 °C [341]. However, liquid metals have the capability of operating at low pressures and potential for reaching the temperatures required for next-generation Rankine or supercritical Brayton power cycles.

6.4.3 Brayton Cycle Components & Advanced Designs

The output power of a Brayton Cycle can be significantly improved through the addition of heat transfer components that can facilitate increased temperatures, pressures and subsequent thermal efficiency. Several sCO_2 Brayton cycle layouts have been previously investigated [220, 225] to improve efficiency with respect to particular included processes:

1. Reheat
2. Recuperation and Recompression
3. Intercooling and Regeneration

6.4.3.1 Reheat

To bring the average temperature closer to the peak temperature, heat can be added by a reheat stage. As shown in Fig. 6.16, a reheater is a heat exchanger that increases the power output without increasing the maximum operating temperature. Here, excess working fluid is extracted and fed into a second stage combustor and turbine where the turbine outlet temperature is increased with reheat ($T_6 > T_4$). This increases the potential for regeneration which can in turn significantly increase thermal efficiency [346].

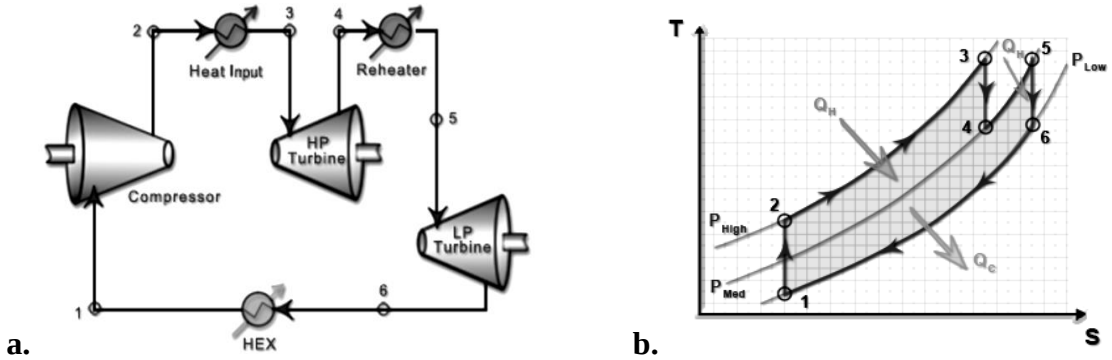

Figure 6.16. Ideal Brayton Cycle Reheat Process with heat exchanger (HEX) with a. Component Diagram and b. *T-s* Diagram [246].

In this layout the working fluid expands through a series of turbines, which then passed through a second combustion chamber before expanding to ambient pressure through a final set of turbines. This has the advantage of increasing power output for a given compression ratio without exceeding any metallurgical constraints (at approximately 1000 °C [345]). Reheat is most often used to improve the specific power (per throughput of air), and is usually associated with a drop in efficiency [345]. However, this process does not directly increase the efficiency of the cycle.

6.4.3.2 Recuperation & Recompression

The efficiency of a Brayton power cycle can also be improved by means of increasing the pressure ratio and utility of a recuperator. Recuperator performance can be expressed in terms of

effectiveness (percentage of possible heat transfer achieved) or pinch (minimum temperature differences at the two ends of the recuperator) [347]. Within a recompression cycle that employs a recuperator, this configuration differs from the simple Brayton cycle in that before cooling, some fraction of the flow does not pass through the precooler and the main compressor. Instead it is recompressed and then rejoins the main flow between the two parts of the divided recuperator, Fig. 6.17a. It is assumed that at this point the two flows are at the same temperature. The flow, which passes the low temperature recuperator should have the same pressure and temperature as the other, where both streams are later mixed again into one stream. This prevents the pinch point issue due to lower mass flow at the high pressure side of the low temperature recuperator since the heat capacity mass flow, weighted on both sides, are equal. This system will therefore reject less heat, and because re-compressor input work is lower than saved heat, thermal efficiency is improved [348].

Increasing the pressure ratio also has the capability of increasing the compressor discharge temperature, which can cause the temperature of the gasses leaving the combustor to exceed the metallurgical limits of the turbine. Additionally, the diameter of the compressor blades becomes progressively smaller in higher pressure stages of the compressor. This causes the gap between the blades and the engine casing to increase in size as a percentage of the compressor blade height as the blades get smaller in diameter. Therefore, a greater percentage of the compressed air can leak back past the blades in higher pressure stages, which can cause a drop in compressor efficiency, and is most likely to occur in smaller gas turbines (since their blades are inherently smaller to begin with).

In an analysis by Ahn *et* al. [328] who investigated thermodynamic properties of sCO_2 around the critical point, the authors' computational results suggest that for increasing pressures, the density was found to increase substantially (Fig. 6.17) which can influence the minimum pressure for turbine operation as compared to a traditional Gas-Brayton cycle (approximately 7,400 kPa compared to approximately 100 kPa) [347].

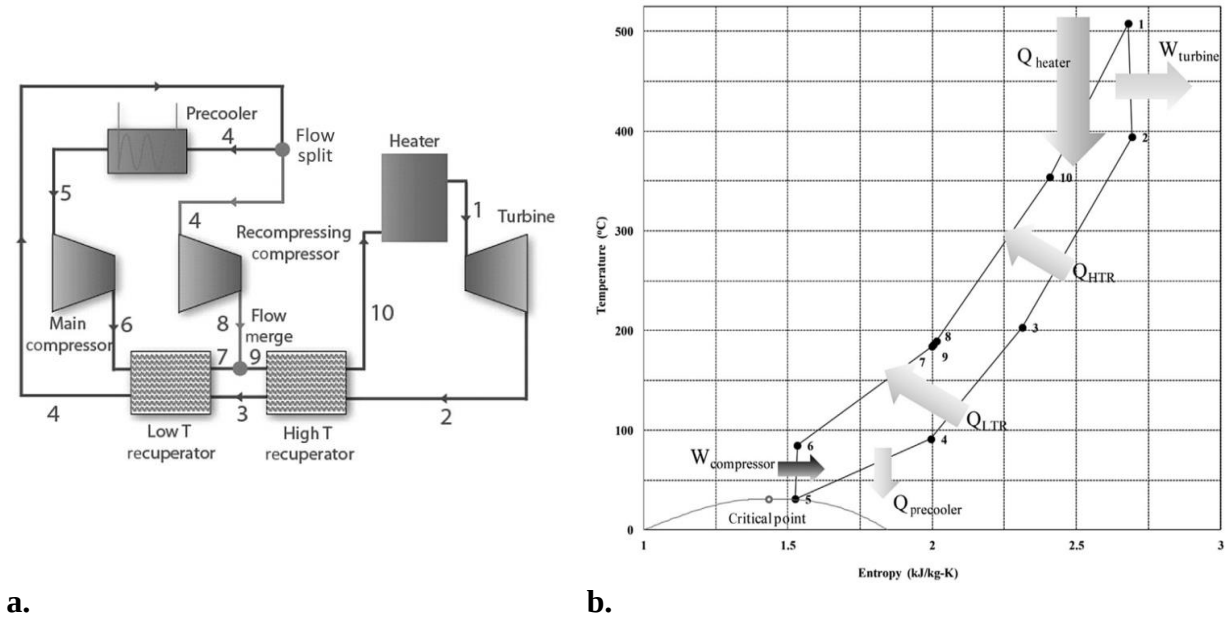

a. **b.**

Figure. 6.17. sCO_2 recompressing cycle with low and high-temperature recuperators [328].

If the Brayton power system is run at a low enough pressure ratio, the turbine outlet gas after the second turbine may still be hotter than the compressed inlet gas after the first turbine. Here, a heat exchanger can be used to transfer thermal energy from the turbine exhaust to the already compressed gas before it enters the combustion chamber. The thermal energy transferred is effectively re-used, thus increasing efficiency. However, this form of heat recycling is only possible if the engine is run in a low efficiency mode with a low pressure ratio. Note, that transferring heat from the 2nd turbine outlet to the inlet of the first turbine would reduce efficiency, as a hotter inlet gas would require more volume and in turn more work for the compressor turbine [328].

6.4.3.3 Intercooling & Regeneration

A Brayton Cycle with Intercooling uses two or more compression stages with one or more intercoolers, as shown in Fig. 6.18. With this configuration, although the power requirement for compression is reduced, the heat quality also increases. For this layout, a regenerator is used as a heat exchanger, used to recover heat from the turbine exhaust that would otherwise be wasted. This is accomplished by connecting the relatively hot turbine effluent gas with a relatively cool compressor outlet gas.

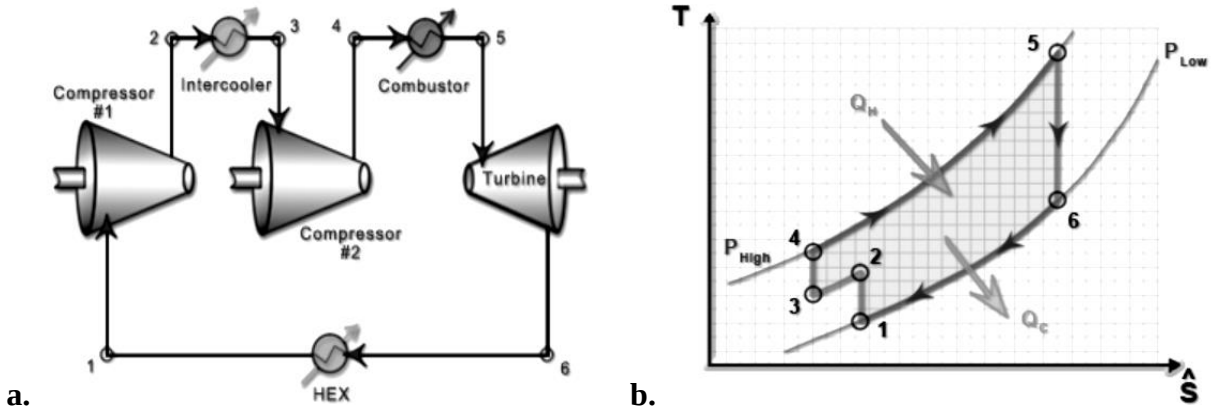

Figure 6.18. Ideal Brayton Cycle with Intercooling and heat exchanger (HEX) with a. component diagram and b. *T-S* Diagram [246].

Additionally, sCO_2 is often more sensitive to the critical point of working fluids within Brayton cycle systems than other working fluids [420] since compressor work is significantly decreased slightly above the critical point due to high density CO_2 fluid near the boundary between the supercritical state and its subcritical state. To address this challenge and increase the efficiency of sCO_2 Brayton systems, a second compressor (or recompressor) can be added to the simple Brayton cycle [421]. Although the two parallel compressors have different inlet conditions, they must operate at nearly the same pressure ratio to avoid impacting the performance of the other compressor, where a relatively small difference in pressure ratio can overload one of the compressors and shutdown the system. The addition of a regenerator and recompression within a CSP Brayton system has previously been explored by Dunham and Iverson [203] where the investigators first assessed a closed regenerative Brayton cycle with one stage of intercooling, Fig 6.19a. Here, a fluid at the minimum system temperature enters the first-stage compressor at state

(1) and is compressed to a higher pressure and temperature, state (2). A heat exchanger (HEX) removes heat from the fluid before it enters the second-stage compressor at state (3).

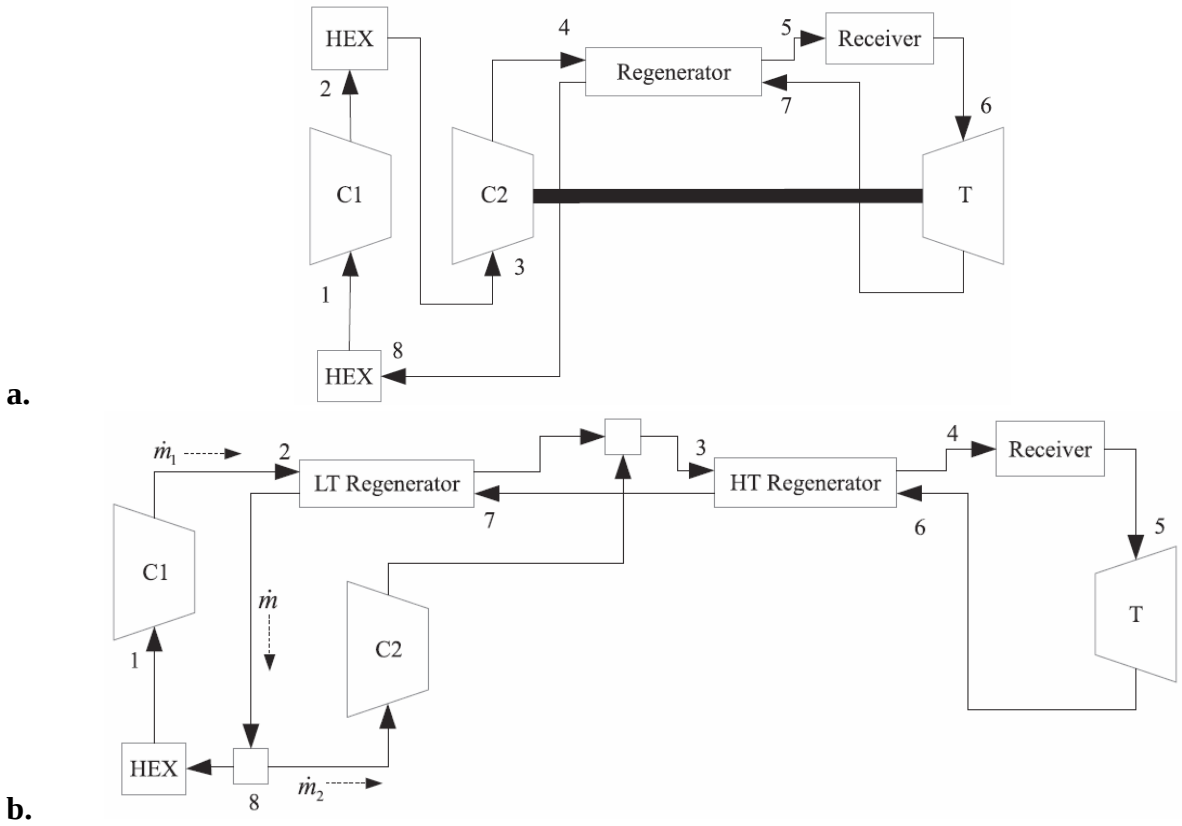

Figure 6.19. Brayton thermodynamic schematics with a. regeneration and b. recompression [203].

This intercooling process serves two primary purposes: it reduces the total work required for compression as well as reducing the compressed fluid outlet temperature which allows for more substantial regeneration, Fig. 6.19b. The compressed gas then enters the cold side of the regenerator at state (4) where it is preheated before entering the receiver at state (5). Now at its highest temperature, the compressed gas enters the turbine at state (6) where it is expanded to low pressure. At state (7), the hot turbine outlet stream enters the hot side of the regenerator, preheating the cold-side fluid. Finally, the gas enters a heat exchanger at state (8) through which it is returned to the minimum cycle temperature. In their investigation Dunham and Iverson [203] suggested the following compression ratio of each compressor in a two-stage intercooled process with known minimum and maximum pressures and a constant pressure drop within the intercooler, Eqn. 6.27.

$$P_{r,2-stage} = \frac{P_{loss,HEX} + \sqrt{\left(P_{loss,HEX}\right)^2 - 4P_{min}P_{max}}}{2P_{min}} \tag{6.27}$$

Additionally, from Fig. 6.18a the investigators also suggest using Eqn. 6.28 for regenerator effectiveness, calculated using the state enthalpies [333].

$$\varepsilon_{regenerator} = \frac{h_5 - h_4}{h_7 - h_{(T_4, P_7)}} \tag{6.28}$$

where the term $h_{(T_4,P_7)}$ is necessary for supercritical applications, though can commonly be approximated to be the same as h_4 under ideal gas systems [422].

As illustrated in Fig. 6.18b the recompression Brayton cycle is typically designed to have a fraction (~10-40%) of hot steam returned to the minimum cycle temperature while the remaining flow bypasses the cooler and is recompressed from the higher temperature [203]. Previous research of the recompression cycle has primarily been focused on sCO_2 [264], especially as the operation of the compressor near the critical point reduces the work required for gas compression. This is due to the fluid's unique thermodynamic properties as it transitions to a supercritical state [203]. Since CO_2 behaves less like an ideal gas than He under most conditions, the efficiency is more significantly-impacted by pressure. In their investigation, Dunham and Iverson [203] also analyzed a regeneration Brayton cycle system under dry-cooling and wet cooling conditions. Their results suggested that a high-temperature CO_2- Brayton cycle shows more resilience to the effects of dry-cooling than does the He-Brayton cycle, although the thermal efficiencies were found to be lower. However, the authors suggested that more careful consideration of pressure may be required during the design of a solar receiver for CO_2 systems than with He systems. Performance results for a CO_2 recompression Brayton cycle under wet-cooling conditions revealed that the recompression cycle showed the potential for very high thermal efficiencies, particularly at high temperatures and pressures. For 20 MPa conditions, the compressor inlet condition was supercritical for all temperatures with wet-cooling and was supercritical at a temperature of 1000 °C for dry-cooling. At 30 MPa, a 50% thermal efficiency was reached with a maximum temperature slightly above 650 °C for wet-cooling, and slightly under 800 °C for dry-cooling [203]. Their results also found for the regenerated He-Brayton cycle, under wet-cooling conditions, that as long as the minimum pressure is free to vary, the maximum pressure has relatively minimal impact on the thermal efficiency. This was found under operating conditions where the thermal efficacy rose from 55.0% at a maximum pressure of 10 MPa to only 55.7% at 30 MPa for a maximum temperature of 1100 °C. The maximum temperature has a significant impact on the system, causing the cycle thermal efficiency to rise from 29.3% at 500 °C, to 55.7% at 1100 °C and 30 MPa maximum pressure. This suggests that lower system pressures may be employed with relatively minimal effects on performance, providing fewer constraints on thermal optimization of the solar receiver [203].

6.4.3.4 Combined Cycle

Another method for enhancing sCO_2 power cycle performance is through the utility of a combined cycle which utilizes multiple thermodynamic cycles: one primary high-temperature cycle (topping) and one or more lower-temperature cycles (bottoming) driven by the heat rejected from the higher-temperature cycle. While significant steps have been made towards high-efficiency single cycles, it has been widely believed that operation above 50% thermal efficiency [68, 308] may require the implementation of binary or combined cycles [313], though it has been suggested that advanced sCO_2 and helium Brayton cycles could potentially reach to levels greater than 50%. Furthermore, combined cycles have been shown to be techno-economically effective, despite increased capital costs [310]. Brayton-topped, combined cycles allow for optimum use of highly concentrated solar energy where the ideal operating temperature is beyond what can be used in subcritical Rankine cycles [314]. An sCO_2 combined cycle that's been previously studied is a configuration that consists of a topping Brayton cycle with a bottoming ORC for waste heat

recovery [342, 343]. A study with an air-ORC/sCO_2 combined cycle showed that 50% thermal efficiency was possible for gas turbine inlet temperatures above 1027 °C, with the best combination at this temperature being air-toluene with an efficiency of 53.75% [342]. The peak temperature of toluene in the bottoming cycle was found to be 297 °C at the turbine inlet. A high-temperature combined cycle based on a closed-loop CO_2 Brayton cycle and driven by concentrated solar radiation was examined and found to produce a thermal efficiency of 47.51% for a turbine inlet temperature of 827 °C when combined with an isopentane bottoming cycle [343]. A variety of working fluids proposed for use in low-temperature or bottoming cycles were compared by Chen *et* al. [321]. It was determined that the critical temperature and classification as a "dry" or "wet" fluid (defined by the slope of the *T–s* diagram) were significant in determining the fluid's suitability for a given application. Further, dry fluids actually perform better when not superheated at the turbine inlet, which can reduce the need for additional heated sections. Johnson examined power cycle performance with a nuclear source and concluded that a single sCO_2 or cascaded sCO_2 cycle had benefits over a combined helium Brayton and supercritical steam Rankine cycle in terms of performance and turbo-machinery size [344]. For a topping cycle turbine inlet temperature of 850 °C, Johnson calculated the net thermal efficiency to be 49.8% for a cascaded sCO_2 configuration [203].

6.4.3.5 Overspray

For traditional Brayton cycle power systems, an overspray method can also be utilized which occurs during a first stage compressor, where a working fluid is injected into the compressor, thus increasing the mass-flow rate which increases the turbine output power significantly, thereby reducing compressor outlet temperatures [3]. For a second stage compressor with non-gas working fluids, the fluid is completely converted to a vapor form offering some intercooling via its latent heat of vaporization.

6.5 Stirling Cycles

Stirling cycles are used frequently during CSP dish applications [352]. In a Stirling cycle, air, helium or hydrogen are used as working fluids where all processes of this cycle are assumed to be reversible, therefore when the working fluid is heated the engine produces work or power. Conversely as illustrated by Fig. 6.20, if the engine is driven by a motor, and the process curves in the *T-s* and *P-v* diagrams run counter-clockwise, the Stirling cycle operates as a refrigerator and/or heat pump. For the Stirling cycle, Carnot cycle's compression and expansion isentropic processes are replaced by two constant-volume regeneration processes. During the regeneration process heat is transferred to a thermal storage device (regenerator) and is transferred back to the working fluid in another part of the cycle. Here, the regenerator can be a wire, ceramic mesh or any kind of porous plug with a high thermal mass [352].

Unlike other combustion engines, a Stirling cycle does not exchange the working gas in each cycle, therefore the gas is permanent. The heat is supplied externally, and can have the potential of achieving higher thermal efficiencies than even Otto and Diesel engines, since heat transfer occurs at constant temperatures. This type of heat transfer can be particularly suitable for systems with latent HTFs since they transfer thermal energy under constant temperature operation.

In this cycle, the pressure changes are very smooth and its torque is uniform where the system does not require any valves. Therefore, Stirling cycle systems are quiet and require little maintenance. To achieve competitive efficiency, the system needs to work at high pressures which could contribute to sealing issues. The temperature difference T_L - T_H should be maintained high for acceptable thermal efficiencies, this results in large thermal stresses in the cylinder (hot and cold ends). Consequently, high strength materials should be used such as Inconels and Haynes 230. The working fluid has to be an inert gas, where Helium could be ideal for this cycle due to its high heat capacity and low molecular mass, which lead to enhanced heat transfer [353].

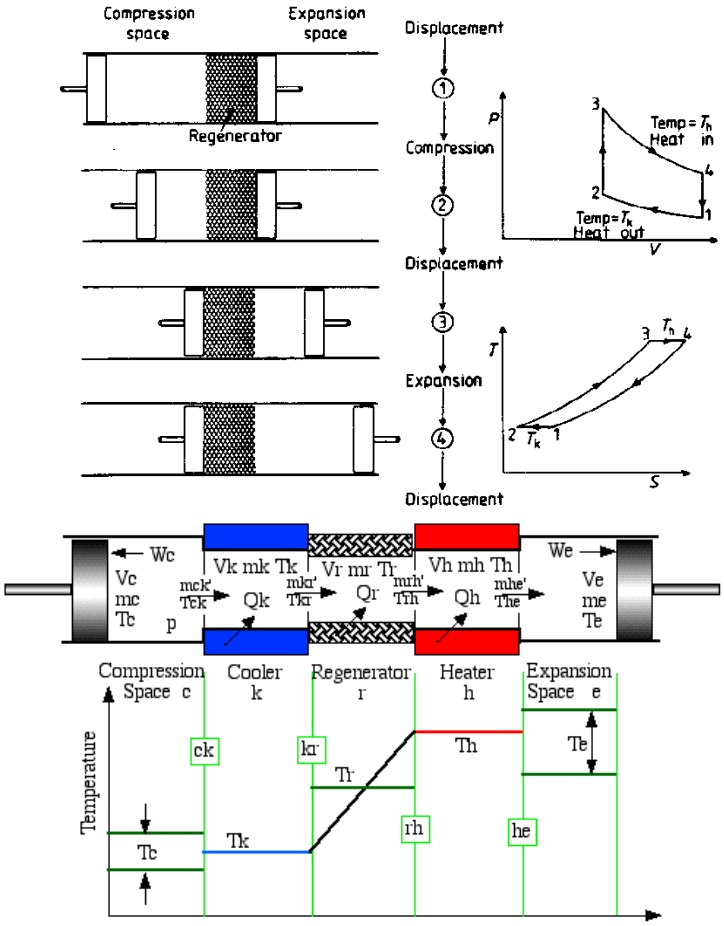

Figure 6.20. Stirling cycle operation and *P-V*, *T-s* thermodynamics [344].

6.6 Other CSP Cycles

Novel thermodynamic cycles not traditionally used in either CSP or fossil fuel plants, have also been theoretically explored for CSP application, though primarily for use in combined cycles [203]. A fringe cycle has been explored using a water-ammonia HTF where this cycle utilizes differing boiling points to fit fluid thermodynamics to the heat source, which allows for an increase in overall efficiency as high as 52% [355]. This type of cycle however generally has lower operating temperatures and has been considered for bottoming cycles, with working fluid properties tuned to the topping cycle heat rejection [356]. However, further study by Chen *et* al.

[321] found compared to an ORC cycle, this type of bottoming cycle requires more complex equipment.

Kribus proposed a system involving a triple "cycle" for solar energy conversion that is much like a typical combined cycle but with an additional energy conversion above the topping cycle [203]. Feeding the topping cycle is the waste heat from an MHD cycle, which uses extremely hot ionized air, heated to approximately 2000 °C to directly induce an electric current using magnets [357]. Very high efficiencies are possible in this configuration, theoretically approaching 70%. However, concentration ratios of approximately10,000 suns are also needed, requiring a power tower system with a complex and high-precision secondary concentrator, as well as high-temperature receiver materials [203]. Organic Flash Cycles (OFC) for CSP have also been recommended for power generation with a medium-temperature heat source [358].

Another potential thermodynamic CSP cycle is the OFC which uses organic fluids, similar to the ORC however with inherent advantages of a dry fluid as well as increased turbomachinery performance from the higher molecular weight when compared with water. In an OFC all of the heat is provided in the liquid phase, and the saturated liquid is throttled to a saturated vapor state at lower pressure [203], which then passes through a turbine for power generation. This system design reduces heating irreversibilities due to the temperature profile mismatch during isothermal/isobaric phase change, allowing for closer matching of the source and sink temperature profiles as in a single-phase heat exchanger. The OFC was previously shown to have higher utilization efficiency than basic ammonia-water Rankine and transcritical CO_2 cycles, favoring its use as a bottoming cycle [203].

7. CSP POWER BLOCK HEAT EXCHANGE COMPONENTS

7.1 Heat Exchangers

Techno-economic analyses have shown a significant potential for cost reduction in CSP systems through efficiency improvement of the power block, with particular focus to its stage components [66, 307]. Heat exchangers are devices used to transfer enthalpy between two or more fluids through a solid surface and a fluid, or between solid particles and a fluid. This occurs based on the fluids operating at different temperatures, where traditionally there is no externally-applied heat or work interactions. The portion of the surface that is in direct contact with both hot and cold fluids, which transfers heat between them, is referred to as the primary or direct surface. To increase the heat transfer area, supplemental attachments may be extended from the primary surface to provide a secondary, or indirect surface. These extended surface elements are referred to as fins. Thus, heat is conducted through the fin and convected (and/or radiated) from the fin (through the surface area) to the surrounding fluid, or vice versa, depending on whether the fin is being cooled or heated. As a result, the addition of fins to the primary surface reduces thermal resistance on that side and thereby increases the total heat transfer from the surface for the same temperature difference. Typically, in CSP applications, heat exchangers are used to recover or reject heat, distill, concentrate, fractionate or control a process fluid.

Combustion and chemical reaction may take place within the exchanger, such as in boilers, fired heaters, and fluidized-bed exchangers. Mechanical devices may be used in some exchangers such as in scraped surface exchangers, agitated vessels, and stirred tank reactors. Heat transfer in the separating wall of a recuperator generally takes place by conduction. If no phase change occurs in any of the fluids within the exchanger, it is referred to as a sensible heat exchanger. Conversely, a heat pipe heat exchanger not only acts as a separating wall, but also facilitates heat transfer by phase change condensation and evaporation processes. In general, if the fluids are immiscible, the separating wall may be eliminated, and the interface between the fluids replaces a heat transfer surface, as in a direct-contact heat exchangers [359]. In his book Shah [359] provided classifications of heat exchangers according to their transfer processes, heat transfer mechanisms, construction type and flow arrangements. Fig. 7.1 provides a breakdown of these types, including a classification for compact/non-compact heat exchangers which includes their heat transfer surface area/volume ratio.

a.

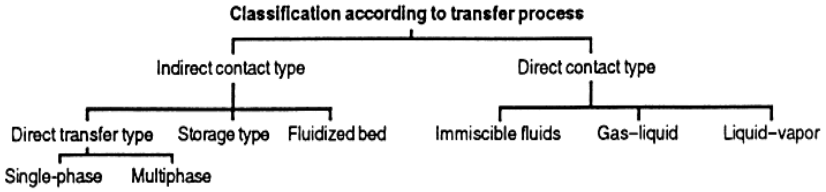

b.

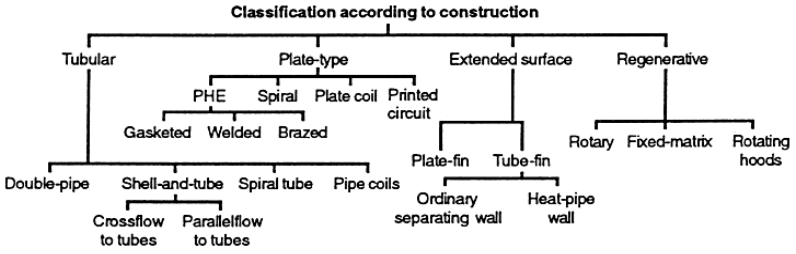

c.

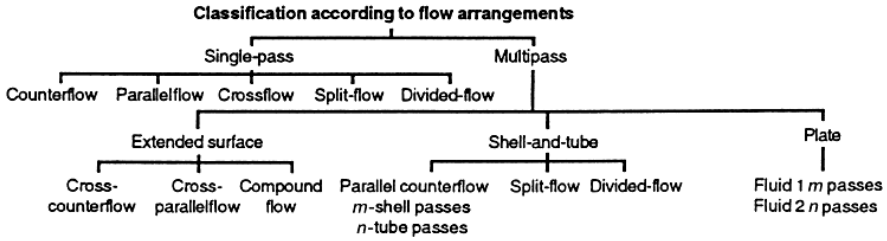

d.

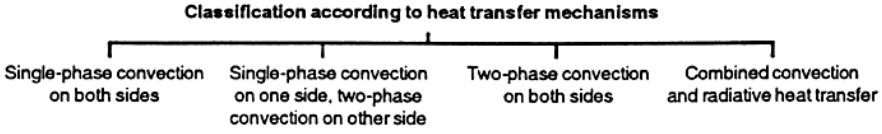

e.

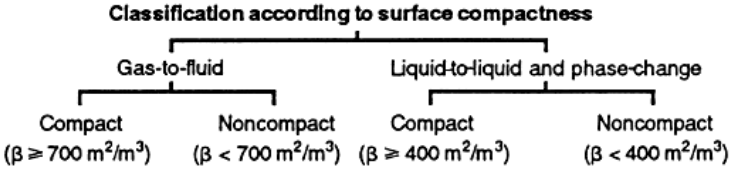

Figure 7.1. Heat exchanger classifications according to a. heat transfer process, b. construction, c. flow arrangements, d. heat transfer mechanisms and e. surface compactness [359].

Overall, heat exchangers can be categorized according to their process function and whether they are either indirect- and direct-contact types. In an indirect-contact heat exchanger, the fluid streams remain separate where the heat transfers continuously through an impervious dividing wall or into and out of a wall in a transient manner. Although a simultaneous flow of two (or more) fluids is required within the exchanger, there is no direct mixing of the two (or more) fluids since each fluid flows through separate fluid passages. Further categorization of these indirect/direct heat exchangers according to their process functions can be seen in Fig. 7.2, as prescribed by Shah [359].

a.

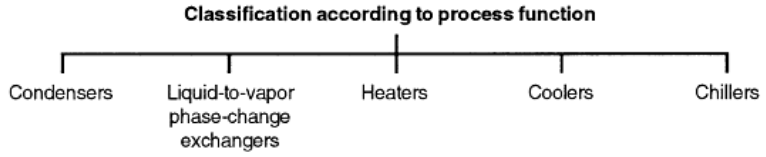

b.

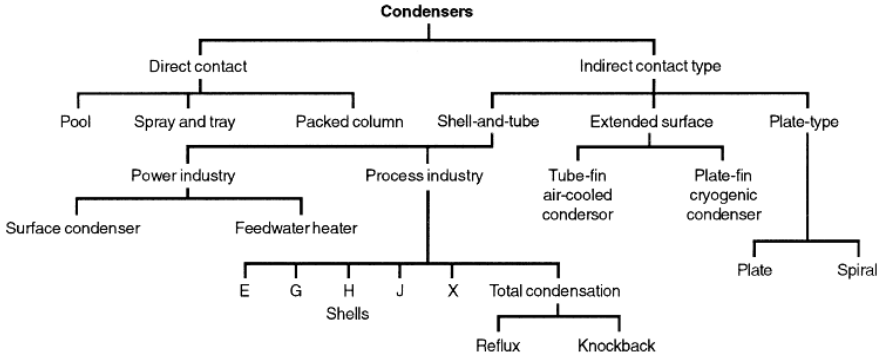

c.

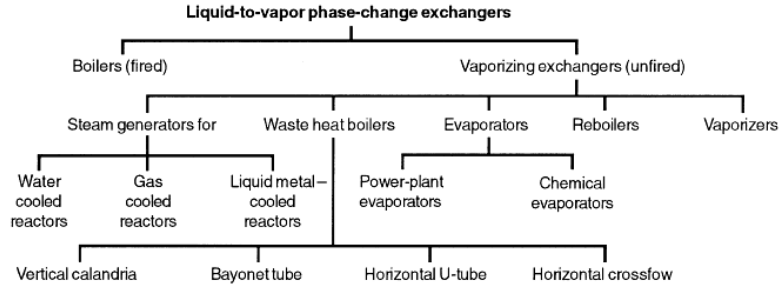

d.

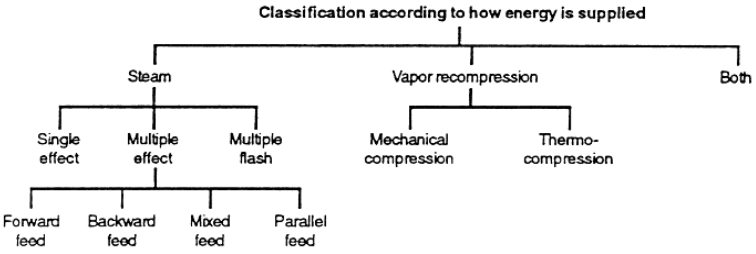

e.

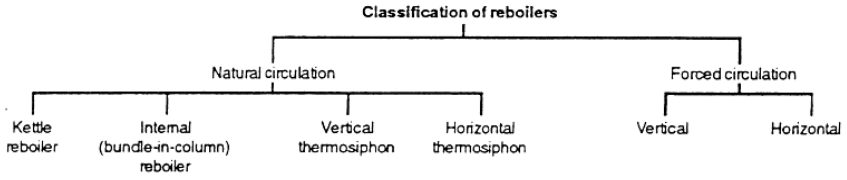

Figure 7.2. Heat exchanger categorization according to a. process function, b. classification of condensers and c. liquid-vapor exchangers [359].

Overall Shah and Sekulic [360] provide design criteria for facilitating successful heat exchanger design:

1. The process requirements which accomplish thermal change on the streams within respective allowable pressure drops, while retaining the capability to do this in the presence of fouling until the next scheduled maintenance period.
2. The heat exchanger must withstand service conditions of the plant environment.

3. The exchanger must be maintainable, to facilitate a configuration that permits cleaning and replacement of any component that is especially vulnerable to corrosion, erosion, vibration, or aging.
4. The designer can consider advantages of a multishell arrangement with flexible piping and valve designs, provided to allow one unit to be taken out of service for maintenance without significant disturbance to the rest of the plant.
5. The heat exchanger should cost as little as possible provided that the above criteria are satisfied.
6. Limitations on the heat exchanger length, diameter, weight, and/or tube specifications due to site requirements, lifting and servicing capabilities must be all taken into consideration in the design.

Two general heat exchanger designs used in analysis are parallel flow and cross-flow. For parallel flow heat exchangers, as shown in Fig. 7.3, the temperature difference between hot and cold fluids varies with position within the heat exchanger as: $\Delta T = T_H - T_C$. The temperature variations in heat exchanger fluid-to-fluid heat transfer processes depend on flow path arrangement, where typical configurations are: A. Parallel flow, B. Counterflow and C. Crossflow. In a parallel-flow configuration the hot and cold fluids enter, flow and exit in the same directions versus a counterflow heat exchanger where the two fluids flow in opposing directions, Fig. 7.4. These two configurations are used extensively in two of the simplest heat exchangers: a concentric tube or double-pipe configuration.

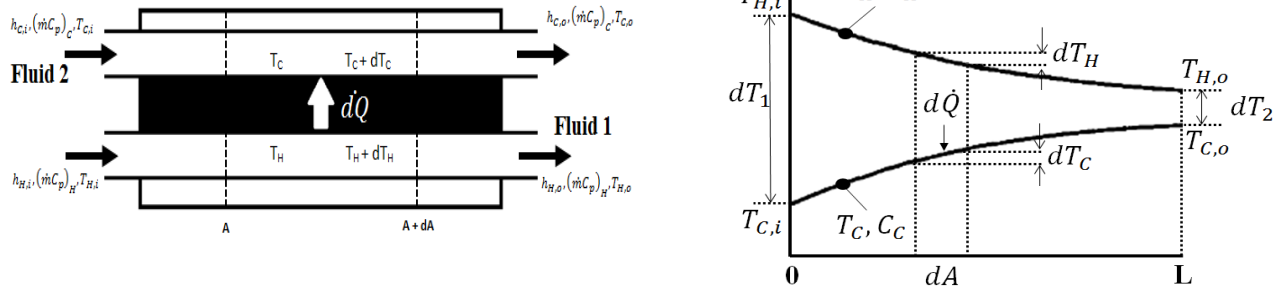

a. **b.**

Figure 7.3. Fluid a. heat transfer and b. temperature distributions for a parallel flow heat exchanger.

From the first law of thermodynamics for an open system with steady state and flow conditions, as well as with negligible changes in potential and kinetic energy, the heat transfer rate to the fluid based on an enthalpy change from inlet to outlet locations A and B respectively is provided by:

$$\dot{Q} = \dot{m}(h_A - h_B) \tag{7.1}$$

For two streams passing through a heat exchanger, one stream enters with a higher temperature, *H* and one with a cooler temperature *C*, where if the fluids do not undergo a phase change process and have constant specific heat values with $dh = C_p dT$, then the following equations apply to the system:

$$\dot{Q}_H = \left(\dot{m}C_p\right)_H \left(h_{H,A} - h_{H,B}\right) \tag{7.2}$$

$$\dot{Q}_C = \left(\dot{m}C_p\right)_C\left(h_{C,A} - h_{C,B}\right) \tag{7.3}$$

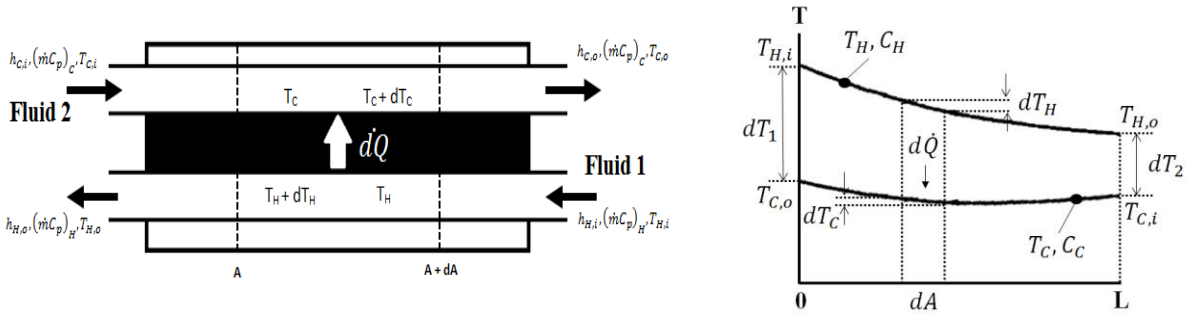

a. **b.**

Figure 7.4. Fluid a. heat transfer and b. temperature distributions for a counter flow heat exchanger.

Another common configuration is cross flow where heat exchange fluids flow perpendicular to each other, which is typical of finned tubular heat exchangers that are considered to have mixed or unmixed motion over the tubes. As shown in Fig. 7.5 if the fins inhibit motion in a direction that is traverse to the main-flow direction then it is considered to be mixed where turbulence and relatively higher heat transfer coefficients are possible. However, if the fluid flow passes through the channel without significant obstruction then the flow is considered unmixed where temperature variations are primarily in the main-flow direction [12].

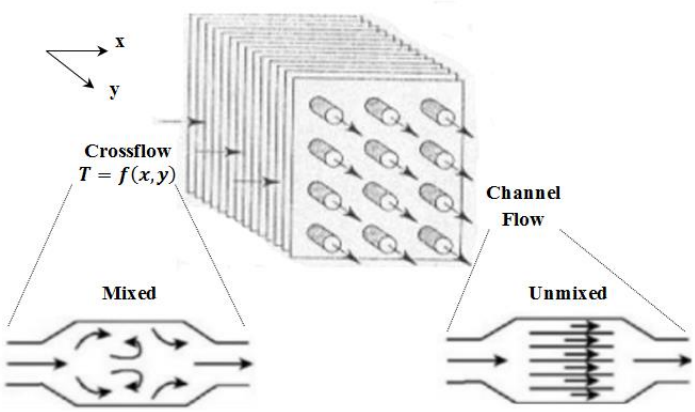

Figure 7.5. Cross-flow heat exchanger with mixed and unmixed fluid transport [12].

As discussed in section 2.3 one method for computing the temperature difference between two fluid streams is by computation of the log-mean temperature difference (LMTD), or ΔT_{lm}. This parameter can then be used to determine the rate of heat transfer by Eqn. 7.4, where *U* is the overall heat transfer coefficient, used in place of a single convection coefficient *h*.

$$\dot{Q} = UA\Delta T_{lm} \tag{7.4}$$

When the inlet and outlet fluid temperatures are unknown however the LMTD method becomes challenging as iterative procedures are then required [12]. Accordingly, the performance of a heat exchanger may be also expressed with respect to the number of heat transfer units (NTU) of which the heat exchanger is capable, where an NTU is defined by:

$$NTU = \frac{UA}{\dot{C}_{min}} \tag{7.5}$$

A commonly used metric for evaluating heat exchanger performance is the effectiveness, defined as the ratio of the actual heat transfer rate to the maximum heat transfer rate possible:

$$\varepsilon = \frac{\dot{Q}}{\dot{Q}_{max}} = \frac{C_H(T_{H,in} - T_{H,out})}{C_{min}(T_{H,in} - T_{C,in})} = \frac{C_C(T_{C,out} - T_{H,in})}{C_{min}(T_{H,in} - T_{C,in})} \tag{7.6}$$

It is then possible to express ε as a function of NTU, the heat capacity rate ratio C^* and the flow arrangement for any heat exchanger:

$$\varepsilon = f(NTU, C^*, Flow\ Arrangement) \tag{7.7}$$

where dimensionless heat capacity ratio and NTU are respectively defined as $C^* = C_{min}/C_{max}$, Eqn. 7.5. It should be noted also that $C_{min}/C_{max} = C_C/C_H = C_H/C_C$. For different heat exchanger flow arrangements, Incropera and DeWitt provide various relations, Table 7.1 for effectiveness [12] where the nature of the resulting temperature profiles depends on mass-heat capacity $(\dot{m}C_p)$ ratios of the fluids. In this table NTU equations are also provided for simplicity.

As illustrated by Shah [359] in Fig. 7.6, these classifications provide a variety of heat exchanger designs with thin-walled circular tubes and varying surface area densities. Also included are different heat exchanger surface types with respective β values for plate, plate-fin and regenerators:

$$\beta = \frac{A_{H\ or\ C}}{V_{H\ or\ C}} \tag{7.8}$$

where the porosity between plates or of a matrix surface is approximated as 0.8333, which provides the relation $\beta = 3333/D_h$. For tube-fin and shell-and-tube heat exchangers, β is defined as:

$$\beta = \frac{A_{H\ or\ C}}{V_{total}} \tag{7.9}$$

where A and V are the heat transfer area and exchanger volume respectively, while H and C denote either hot or cold fluid sides. According to Shah [359]. Compact surface heat exchangers can gain specified heat exchanger performance by q/T_m, within acceptably low mass and box volume constraints, where this metric can be expressed in terms of the overall heat transfer coefficient as:

$$\frac{q}{\Delta T_m} = UA = U\beta V \tag{7.10}$$

where ΔT_m is the true mean temperature difference, where a high β value minimizes exchanger volume for a specified value of q/T_m. As compact surfaces can achieve structural stability and strength with thinner-gauge material, the gain in a lower exchanger mass is even more pronounced than the gain in a smaller volume [359].

Table 7.1. Heat exchanger effectiveness correlations [12].

Flow Arrangement	Relation	
Concentric Tube		
Parallel Flow	$\varepsilon = \frac{1-exp[-NTU(1+C_r)]}{1+C_r}$	(7.11)
	$NTU = -\frac{ln[1-\varepsilon(1-C_r)]}{1-C_r}$	(7.12)
Counter Flow	$\varepsilon = \frac{1-exp[-NTU(1+C_r)]}{1-C_r exp 1-exp[-NTU(1+C_r)]}\ for\ C_r < 1$	(7.13)
	$\varepsilon = \frac{NTU}{1+NTU}\ for\ C_r = 1$	(7.14)
	$NTU = \frac{1}{C_r-1} ln\left(\frac{\varepsilon-1}{\varepsilon C_r-1}\right)\ for\ C_r < 1$	(7.15)
	$NTU = \frac{\varepsilon}{1-\varepsilon}\ for\ C_r = 1$	(7.16)
Shell & Tube		
One Shell Pass	$\varepsilon_1 = 2\left\{1 + C_r + (1+C_r^2)^{1/2}\frac{1+exp\left[-NTU\left(1+C_r^2\right)^{1/2}\right]}{1-exp\left[-NTU\left(1+C_r^2\right)^{1/2}\right]}\right\}^{-1}$	(7.17)
	$NTU = -(1+C_r^2)^{-1/2} ln\left(\frac{E-1}{E+1}\right)$ $E = \frac{2/\varepsilon_1-(1-C_r)}{\left(1+C_r^2\right)^{1/2}}$	(7.18)
n shell passes	$\varepsilon = \left[\left(\frac{1-\varepsilon_1 C_r}{1-\varepsilon_1}\right)^n - 1\right]\left[\left(\frac{1-\varepsilon_1 C_r}{1-\varepsilon_1}\right)^n - C_r\right]^{-1}$	(7.19)
	Use Eqns. 7.15 and 7.16 with: $\varepsilon_1 = \frac{F-1}{F-C_r}, F = \left(\frac{\varepsilon C_r-1}{\varepsilon-1}\right)^{1/n}$	(7.20)
Cross Flow (Single Pass)		
Both Fluids are Unmixed:	$\varepsilon - 1 - exp\left[\left(\frac{1}{C_r}\right) NTU^{0.22}\{exp[-C_r(NTU)^{0.78}] - 1\}\right]$	(7.21)
C_{Max} (Mixed)	$\varepsilon = \left(\frac{1}{C_r}\right)\{1 - exp[-C_r(1 - exp(-NTU))]\}$	(7.22)
C_{Min} (Mixed)	$NTU = -ln\left[1 + \left(\frac{1}{C_r}\right) ln(1 - \varepsilon C_r)\right]$	(7.23)
C_{Max} (Unmixed)	$\varepsilon = 1 - exp(-C_r^{-1}\{1 - exp[-C_r(NTU)]\})$	(7.24)
C_{Min} (Unmixed)	$NTU = -\left(\frac{1}{C_r}\right) ln[C_r ln(1-\varepsilon) + 1]$	(7.25)
All Exchangers (C_r = 0)	$\varepsilon = 1 - \exp(-NTU)$	(7.26)
	$NTU = -ln(1-\varepsilon)$	(7.27)

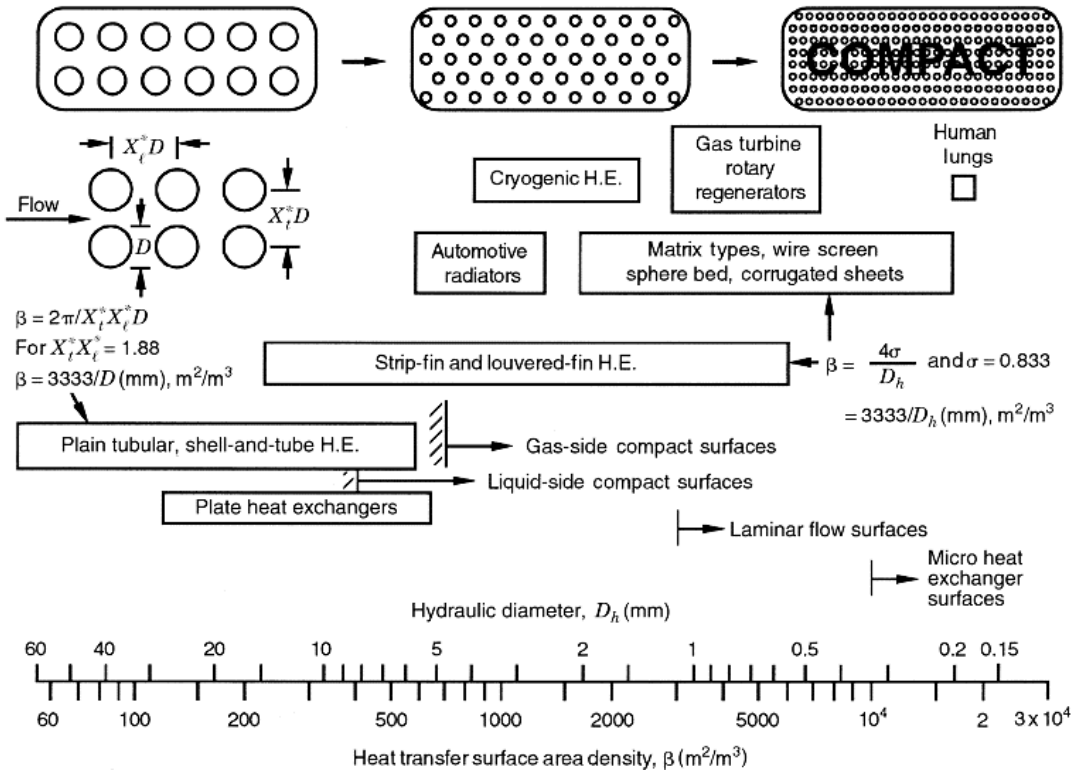

Figure 7.6. Heat transfer surface area density spectrum of heat exchanger surfaces [359].

For gas-to-fluid exchangers, the heat transfer coefficient *h* for gases is generally one or more orders of magnitude lower than for liquids such as water or oil. To minimize size, weight and overall costs, thermal conductances (*ha* products) for both sides of the exchanger should be in value, where the heat transfer surface on the gas-side needs to have a larger surface area and be more compact to facilitate this [359].

7.1.1 Gasketed-Plate Heat Exchangers

Gasketed plate heat exchangers utilize metal plates to transfer heat between fluids where its advantage over other heat exchanger designs is that the fluids are exposed to a much larger surface area since the fluids spread out over the plates. This facilitates the transfer of heat, which greatly increases the rate of temperature change. Plate heat exchangers fundamentally differ where their design replaces pipes that would pass through a chamber for heat transfer. Instead there are two alternating chambers, separated at their largest surface by a corrugated metal plate. These heat exchangers are highly configurable due to the variety of designs available for the plates and arrangements that are possible to suit a variety of applications. Unlike tubular heat exchangers for which design data and methods are easily available [360], gasketed-plate heat exchanger designs continue to be proprietary in nature where attempts have been made to develop heat transfer and pressure drop correlations. However, most of these cannot be generalized to give a high degree of prediction accuracy [360]. For these heat exchangers, the fluids are much closer to countercurrent flow than in shell-and-tube heat exchangers. Further, another permutation of this design is a gasketed plate-and-frame heat exchanger, which can provide efficient heat transfer in compact

equipment with a small footprint. These devices have been shown to have flexible design and are easy to service and maintain [361]. Stainless steel is commonly used for the plates due to its ability to withstand high temperatures, its high strength and corrosion resistance [362]. The plates are often spaced by rubber sealing gaskets which are cemented into a section around the edge of the plates. The plates are pressed to form troughs at right angles to the direction of flow of the liquid which runs through the channels in the heat exchanger. These troughs are arranged so that they interlink with the other plates which forms the channel with gaps of approximately 1.3–1.5 mm between the plates [363]. The plates are compressed together in a rigid frame to form an arrangement of parallel flow channels with alternating hot and cold fluids. The plates, with their large surface area, can facilitate high heat transfer rates. Making each chamber thin ensures that the majority of the volume of liquid contacts the plate, again aiding exchange. The troughs also create and maintain a turbulent flow, even at low flow rates, to maximize heat transfer coefficients [363].

Compared to shell and tube heat exchangers, the temperature approach in a plate heat exchanger may be as low as 1 °C, where shell and tube heat exchangers require an approach of 5 °C or more. Therefore, for the same amount of heat exchange, plate heat exchanger size can be smaller due to the large heat transfer area afforded by the plates. Increase and reduction of the heat transfer area is relatively simple with plate heat-exchangers through the addition or removal of plates from the stack [363] where heat transfer enhancement will strongly depend on the Chevron inclination angle β, relative to flow direction, as well as the friction factor that increases with β. The Chevron angle typically has a range between 25°-65° [360], and as shown in Fig. 7.7, adjustment of the corrugation pitch and depth increases the flat or projected plate area.

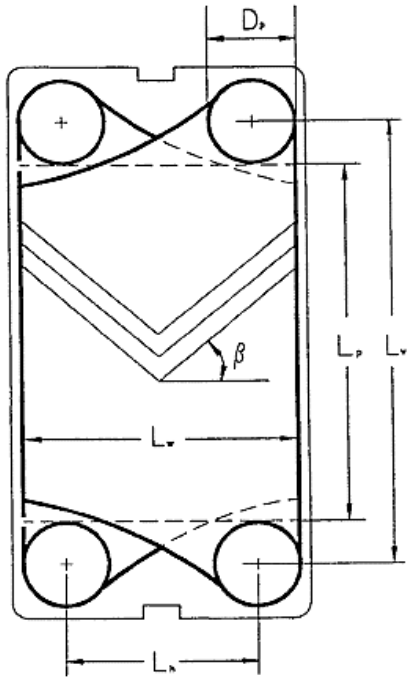

Figure 7.7. Gasketed-plate with chevron design grooves [360].

The increase of the developed length with respect to the projected length, can be described by an enlargement factor ϕ which can vary between 1.1 and 1.25 [422].

$$\phi = \frac{developed\ length}{projected\ length} \tag{7.28}$$

Another definition of ϕ is the ratio of the actual effective area to the projected plate area where the projected area can be approximated by $L_P \cdot L_w$. The determination of other geometrical performance parameters, such as the mean channel flow gap and channel flow area can be found by Kakaç *et* al. [360]. For gasketed-plate exchangers, heat transfer enhancement is determined based on the Chevron inclination angle β, relative to flow direction, which influences friction factor. However, performance of a Chevron plate also depends on the surface enlargement factor ϕ, corrugation profile, and temperature dependent physical properties, such as viscosity [360]. Comprehensive analyses of various gasketed-plate heat transfer correlations are provided and compared by Manglik [423] and Kakaç *et* al. [360] where discrepancies originate from differences in plate surface geometries such as: surface enlargement factor ϕ, metal-to-metal contact pitch, wavelength, amplitude, and profile or shape of the surface corrugation. A well accepted correlation for Chevron plates, based on an extensive data by Muley and Manglik [424-426] provide a heat transfer coefficient based on β and Re.

$$\left.\begin{aligned} Nu = \frac{2hb}{k} = 0.44\left(\frac{\beta}{30}\right)^{0.38} Re^{0.5} Pr^{1/3}\left(\frac{\mu_b}{\mu_w}\right)^{0.14} \\ f = \left(\frac{\beta}{30}\right)^{0.83}\left[\left(\frac{30.2}{Re}\right)^5 + \left(\frac{6.28}{Re^{0.5}}\right)^5\right]^{0.2} \end{aligned}\right\} for\ Re \le 400 \tag{7.29}$$

$$\left.\begin{aligned} Nu = [0.2668 - 0.006967\beta + 7.244\times10^{-5}\beta^2]Re^{\zeta} Pr^{1/3}\left(\frac{\mu_b}{\mu_w}\right)^{0.14} \\ \zeta = 0.728 + 0.0543 sin[(2\pi\beta/90) + 3.7] \\ f = [2.917 - 0.1227\beta + 2.016\times10^{-3}\beta^2]Re^{-\{0.2+0.0577 sin[2\pi\beta/90+2.1]\}} \end{aligned}\right\} for\ Re \le 800 \tag{7.30}$$

The investigators also developed prediction correlations for flat-plate channels, Eqns. 7.31 and 7.32.

$$\begin{aligned} Nu &= 1.849(L/d_e)^{-1/3}(RePr)^{1/3}(\mu_b/\mu_w)^{0.14} \quad for\ \le 2000 \\ Nu &= 0.023Re^{0.8}Pr^{1/3}(\mu_b/\mu_w)^{0.14} \quad for\ > 4000 \end{aligned} \tag{7.31}$$

$$\begin{aligned} f &= 24/Re \quad for\ Re \le 2000 \\ f &= 0.1268Re^{-0.3} \quad for\ Re > 2000 \end{aligned} \tag{7.32}$$

Muley and Manglik compared these correlations with those of Kakaç, with a Chevron angle of $\beta = 1.29$ with a channel aspect ratio of $2b/P_c$, where they found with respect to Re, the Chevron plates were able to produce up to five times higher Nu values than flat-plate channels, however with a considerably higher pressure drop. In general, various correlations are available for plate heat exchangers for various fluids depending on flow characteristics and plate geometries [360].

Finally, designed thermal mixing between stacked pates can provide additional flexibility in utilization of the available pressure drop without excessive surface area, and with fewer standard plate patterns [360]. The level of mixing is sensitive to β where a pack of plates may be composed of all high angles, low angles, and may be arranged alternately to provide an intermediate level of performance.

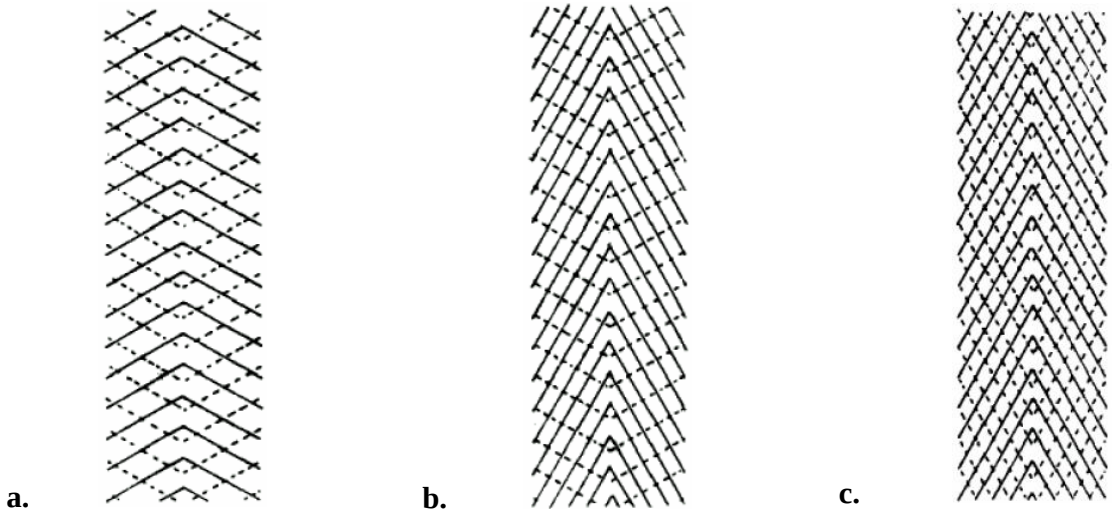

Figure 7.8. Thermal mixing configurations for a. low-low β angles, b. mixed β angles and c. high-high β angles [360].

7.1.2 Shell and Tube Heat Exchangers

In contrast to compact heat exchangers, general industry-standard shell and-tube exchangers have a surface area density of less than 100 m^2/m^3 on one side with plain tubes, and a surface area density two to three times greater with high-fin-density, low-finned tubing [359]. Additionally, for water/water applications [365], a typical plate heat exchanger has approximately twice the average heat transfer coefficient *h* on one fluid side for a shell and-tube exchanger. Plate-fin, tube-fin, and rotary regenerators are examples of compact heat exchangers for gas flow on one, or both fluid sides. Additionally, gasketed, welded, brazed-plate and printed-circuit heat exchangers are examples of compact heat exchangers for liquid flows. Basic flow arrangements of two-fluid compact heat exchangers are single-pass crossflow, counterflow, and multipass cross-counterflow for non-compact heat exchangers. The last two flow arrangements for compact or non-compact heat exchangers can yield very high exchanger effectiveness values or very small temperature differences between the fluid streams [365].

Shell-and-tube exchangers are traditionally custom designed for virtually any capacity and operating condition, from high vacuums to ultrahigh pressure systems; from cryogenics to high temperatures, and for any temperature/pressure differences between fluids limited only by respective structural materials. They can be designed for special operating conditions: vibration, highly viscous fluids, erosion, corrosion, toxicity, radioactivity, multicomponent mixtures, where are made from a variety of metal and nonmetal materials, and in surface areas from less than 0.1 to 100,000 m^2 [364]. Generally, shell-and-tube heat exchangers are an order of magnitude less surface area per unit volume than the compact exchangers, where they also require considerable space, weight, support structure, and footprint [169]. Fig. 7.9 by Kakaç *et* al. [364] provides a graphical illustration for a shell-and-tube heat exchanger that comprises tube bundles, baffles and the shell. Stream B is the main cross flow stream which passes from one window, across the cross flow section, and out through the opposite window. Additionally, there are four other streams because of the mechanical clearances required in a shell-and-tube heat exchanger. One is the A stream that leaks through the clearance between the tubes and the baffle, from one baffle

compartment to the next. There is also a C stream which is the bundle bypass stream which flows around the tube bundle between the outermost tubes and the inside of the shell. The E stream flows through a clearance between the baffles and the inside diameter of the shell. The F stream flows through any channels within the tube bundle, facilitated by the provision of pass dividers in the exchanger header [364].

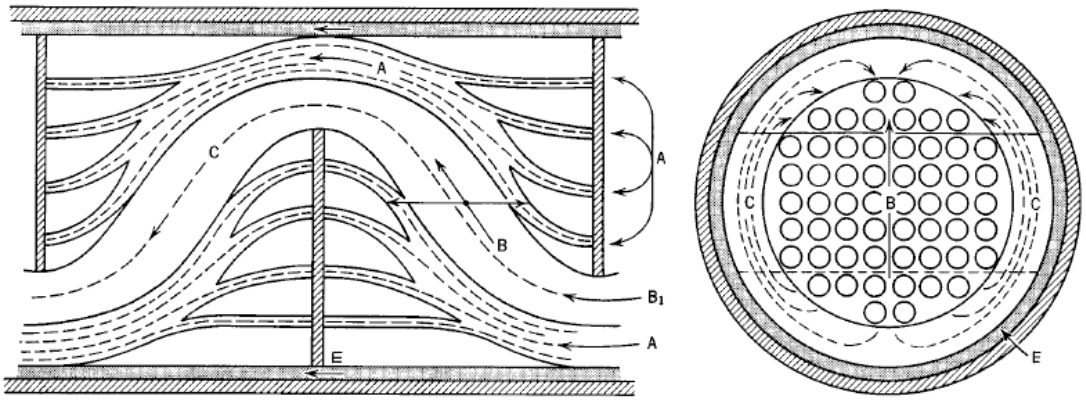

Figure 7.9. Generalized shell-in-tube heat exchanger, which portrays leaking paths for flow bypassing the tube matrix through the baffle clearances between the tube matrix and the shell [364].

For heat transfer analysis, two prominent methods used in industry are the Bell-Delaware method [366] which is most-widely used, and the Kern method [367], which offers simplicity though with some notable restrictions and limitations [364]. Here the Kern method will be discussed, which was developed as an attempt to correlate data for standard exchangers by a simple equation analogous to equations for flow in tubes. However, this method is restricted to a fixed baffle and cannot adequately account for baffle-to-shell and tube-to-baffle leakages [364]. For this method, thermal analysis begins by calculating the mass flow rate as a function of the number of tubes N_t and by considering the cross sectional area $A_c = \pi D_i^2/4$ where D_i is the inner tube diameter.

$$\dot{m}_t = \rho_t u_t A_c N_t \tag{7.33}$$

For laminar flow the Sieder and Tate correlation [431] can be used where Re_t and Pr_t are defined for the tube-side fluid and L_c is the tube characteristic length.

$$Nu_t = 1.86\left(\frac{Re_t Pr_t D_i}{L_c}\right)^{1/3} \quad for \begin{matrix} 0.48 < Re_t < 16700 \\ (Re_t Pr_t D_i/L_c)^{1/3} > 2 \end{matrix} \tag{7.34}$$

For turbulent flow, the Nusselt number can be analyzed by the Petukhav-Kirillov correlation [430].

$$Nu_t = \frac{(f/2)Re_t Pr_t}{1.07+12.7(f/2)^{1/2}\left(Pr_t^{2/3}-1\right)} \quad for \begin{matrix} 10^4 < Re_t < 5\times 10^6 \\ 0.5 < Pr_t < 2000 \end{matrix} \tag{7.35}$$

where $(f/2)$ is assumed to be 0.0029 and the friction factor determined by:

$$f_t = (1.58 ln Re_t - 3.28)^{-2} \tag{7.36}$$

For the shell-side, the number of tubes required is determined by taking the quotient of the shell circle by the projected area of the tube layout, Eqn. 7.37:

$$N_t = CTP\,\frac{\pi D_S^2}{4A_{1tube}} \tag{7.37}$$

From Eqn. 7.37 the projected area A_{1tube} corresponds to the area of one tube, which can be expressed as:

$$A_{1tube} = (CL)P_t^2 \quad \begin{matrix} for\ 90°\ and\ 45° \rightarrow CL = 1.0 \\ for\ 30°\ and\ 60° \rightarrow CL = 0.87 \end{matrix} \tag{7.38}$$

D_s is the shell inner diameter and CTP is the tube count calculation constant that accounts for incomplete coverage of the shell diameter by tubes, which for different number of tube passages can be provided by [364]:

$$\begin{matrix} one-tube\ pass \rightarrow CTP = 0.93 \\ two-tube\ pass \rightarrow CTP = 0.90 \\ three-tube\ pass \rightarrow CTP = 0.85 \end{matrix}$$

The shell equivalent diameter is determined along the long axes of the shell as four times the net flow area as layout on the tube sheet divided by the wetted perimeter [364]:

$$D_e = \frac{4\times free-flow\ area}{wetted\ perimeter} \tag{7.39}$$

As shown in Fig. 7.10 there are two general configurations for the flow over the tubes, where for the square pitch and triangular pitch, the perimeter is determined by the pitch size P_T which is the outside tube diameter:

$$\begin{matrix} Square\ Pitch: & D_e = \frac{4\left(P_t^2 - \frac{\pi D_O^2}{4}\right)}{\pi D_o} \\ Triangular\ Pitch: & D_e = \frac{4\left(\frac{P_t^2\sqrt{3}}{4} - \frac{\pi D_O^2}{8}\right)}{\pi d_o/2} \end{matrix} \tag{7.40}$$

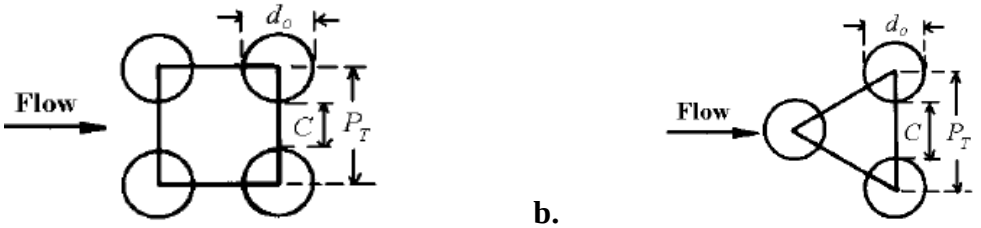

Figure 7.10. Tube layouts for a. square-pitch and b. triangular-pitch [364].

To determine the shell-side heat transfer coefficient, the correlation by McAdams [428], Eqn. 7.41 is provided for the shell-side.

$$\frac{h_o D_e}{k} = 0.36\left(\frac{D_e \dot{m}_s}{\mu A_s}\right)^{0.55}\left(\frac{C_p \mu}{k}\right)^{1/3}\left(\frac{\mu_b}{\mu_w}\right)^{0.14} \quad for\ 2\times 10^3 < Re_s < 1\times 10^6 \tag{7.41}$$

where:
$$\mathrm{Re_s} = \left(\frac{\dot{m}_s}{A_s}\right)\frac{D_e}{\mu_s} \tag{7.42}$$

and D_e is the equivalent diameter of the shell side. As prescribed by [364] the pressure drop encountered by the fluid making N_p passes through the heat exchanger is a multiple of the kinetic energy of the flow:

$$\Delta P_t = \left(4f_t\frac{LN_p}{D_i} + 4N_p\right)\frac{\rho_t u_t^2}{2} \tag{7.43}$$

where f_t is determined from Eqn. 7.36, and the second term represents the additional pressure drop introduced by the change of direction in the respective passages [364]. For the shell-side, the fluid experiences a pressure drop as it passes through the exchanger, over the tubes and around the baffles. If the shell fluid nozzles are on the same side of the heat exchanger, then the shell-side fluid can make an even number of tube bundle crossings, which is therefore dependent on pressure drop [364]. From experiments, the pressure drop experienced by the shell-side fluid is determined by Eqn. 7.44 [429].

$$\Delta P_s = \frac{f_s G_s^2 (N_b+1) D_s}{2\rho_s D_e \phi_s} \tag{7.44}$$

where N_b is the number of baffles, D_s is the inner shell diameter and:

$$f_s = e^{0.576-0.19 ln Re_s} \;\; for \;\; 400 < Re_s = \frac{G_s D_e}{\mu} \leq 1\times 10^6 \tag{7.45}$$

$$\phi_s = (\mu_b/\mu_w)^{0.14} \tag{7.46}$$

7.1.3 Compact Heat Exchangers

As shown in Fig. 7.6 a gas-to-fluid heat exchanger is referred to as a compact heat exchanger (CHE) if it incorporates a heat transfer surface having a surface area density above approximately 700 m^2/m^3 on at least one of the fluid sides, which usually has gas flow. It is referred to as a laminar flow heat exchanger if the surface area density is above about 3000 m^2/m^3, and as a micro heat exchanger if the surface area density is above approximately 10,000 m^2/m^3 [169]. A liquid/two-phase heat exchanger is referred to as a CHE if the surface area density on any one fluid side is above about 400 m^2/m^3 [169]. A typical process industry shell-and-tube exchanger has a surface area density of less than 100 m^2/m^3 on one fluid side with plain tubes, and two to three times that with the high-fin-density low-finned tubing. Plate-fin, tube-fin, and rotary regenerators are examples of CHEs for gas flows on one or both fluid sides, and gasketed and welded plate heat exchangers are examples of compact heat exchangers for liquid flows [169]. A detailed overview of heat exchanger types can be found by Hesselgreaves [368]. For compact extended surface heat exchangers, important design and operating considerations suggested by Kreith [169] are:

1. At least one of the HTFs is a gas or specific liquid with low *h* values.
2. Fluids must be clean and relatively noncorrosive because of small hydraulic diameter D_h flow passages with generally no easy techniques for cleaning.
3. The fluid pumping power (pressure drop) design constraint is often equally as important as the heat transfer rate with respect to performance.

4. Operating pressures and temperatures are somewhat limited compared with shell-and-tube heat exchangers as a result of the joining of the fins to plates or tubes such as brazing, mechanical expansion, etc.
5. With respect to the use of highly compact surfaces, the resultant shape of a gas-to-fluid exchanger is one having a large frontal area and a short flow length (the header design of a CHE is thus important for a uniform flow distribution among the very large number of small flow passages).

Some advantages of plate-fin exchangers over conventional shell-and-tube exchangers are that CHEs, generally fabricated from thin metallic plates can yield a large heat transfer surface area per unit volume, typically up to ten times greater than the 50-100 m^2/m^3 density provided by a shell and- tube exchanger for general process application, from 1000 to 6000 m^2/m^3 for highly compact gas side surfaces [169].

With regards to heat exchange limitations, small flow passages have two effects, a tendency for facilitating laminar flow within the channels, and a high pressure drop. Laminar flow is associated with low heat transfer coefficients, and therefore the efficiency is necessarily improved by various heat transfer enhancement techniques, which have facilitated a variety of CHE designs. A CHE provides a tighter temperature control and can provide rapid heating or cooling of a process stream, thus improving the product quality. CHEs are characterized by a large heat transfer surface area per unit volume of exchanger, resulting in reduced space, weight, support structure, energy requirements and cost, as well as improved process design, processing conditions and low fluid inventory. Its high-surface area density design is able to facilitate higher heat transfer coefficients, which make it inherently a smaller less-bulky device compared to other heat exchangers. Traditionally, this type of heat exchangers can be classified according to respective surface area densities and hydraulic diameters, with approximate values given in Table. 7.2 [365].

Table 7.2. Compact heat exchanger classification [365].

Excahnger Type	Surface Area Density [m^2/m^3]	Hydraulic Diameter
Gas-to-Fluid Compact Heat Exchanger (Gas Stream Operation)	700	$D_h \leq 6\text{mm}$
Gas-to-Fluid Compact Heat Exchanger (Liquid or Phase-Change Operation)	400	$D_h \leq 6\text{mm}$
Laminar Flow ("Meso Heat Exchanger")	3000	$100\mu\text{m} \leq D_h \leq 1\text{mm}$
Micro Heat Exchanger	15,000	$1\mu\text{m} \leq D_h \leq 100\mu\text{m}$

For CO_2 applications, compact heat exchangers such as the RANOTOR as described by Chen [331], are designed to be counter current with laminar flow at the heat exchanger gas side, and composed of concentric conical plates, which are comprised of several tubes arranged in parallel as shown in Fig. 7.11. This design has the advantages of high power densities, a low pressure drop and flexible installation [331].

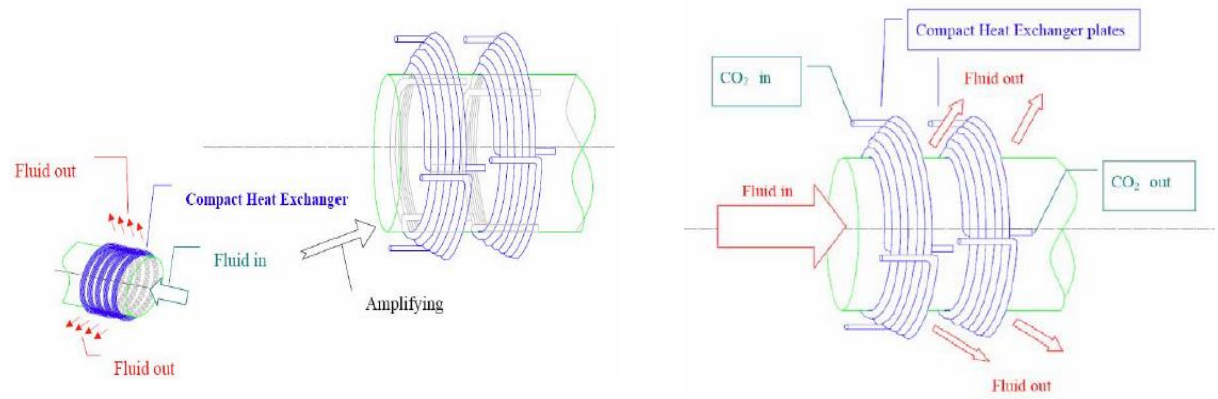

a. **b.**

Figure 7.11. RANOTOR compact heat exchanger [331].

From an O&M point of view, compact heat exchangers are used in a variety of configurations, such as high temperature (<850°C), high pressure applications (>200 bars), and in applications that encompass a moderate amount of fouling. However, a large majority of reported applications do not involve both aforementioned high temperature and pressure conditions simultaneously. For many compact exchangers except for plate heat exchangers, fouling is a significant challenge. For an exchanger with a large frontal area, flow maldistribution could be another potential issue. Additionally, because of short transient times, a careful design of controls is required for startup of compact heat exchangers compared with shell-and-tube exchangers [331].

7.1.4. Plate Heat Exchangers

There are a variety of locations where CHEs can be employed throughout a CSP system from receivers [369] to the power block [371]. One type of CHE is a plate heat exchanger (PHE), Fig. 7.12 [370], which consists of a series of corrugated plates supported by a rigid frame. The corrugations on adjacent plates contact or cross each other forming highly interrupted and tortuous channels. Sealing between streams is accomplished by gaskets. In addition, multi-pass configurations can be accommodated by blanking plates within the stack. Various system specifications can be matched by adding or removing plates or inclusion of plates with differing patterns.

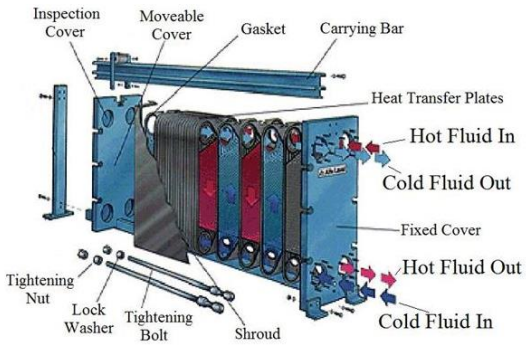

Figure 7.12. Generalized plate heat exchanger configuration [370]

The plate-fin exchangers can accommodate multiple fluid streams in one exchanger with proper manifolding, which allows process integration and cost effective compact design solutions. Fouling can be a major operational challenge with compact heat exchangers (except for plate-and frame heat exchangers), particularly those having a variety of fin geometries or very fine circular or noncircular flow passages that cannot be cleaned mechanically. Chemical cleaning may be possible, where thermal baking and subsequent rinsing is possible for small-size units. Therefore, extended surface compact heat exchangers may not be optimal for use in heavy fouling applications [169]. One advantage of PHEs is the greatly reduced space requirements.

The space required for a PHE can be 30–50% of a shell-and-tube heat exchanger for a given heat duty, [372]. Additionally, for the same effective heat transfer area, the weight and volume of PHEs are approximately only 30% and 20%, respectively, of shell-and-tube heat exchangers [372]. They can have 50% less volume than a fined tube heat exchanger, and 60% less than a serpentine design for the same thermal performance [373]. Choice of gasket materials is also critical to reliable operation of PHEs [375], where gaskets are generally comprised of a variety of elastic and formable materials, such as rubber [372]. Gasket materials restrict the utility of PHEs in highly corrosive applications which however limit the maximum operating temperature to avoid higher costs. The thermal conductivity of the plate is an important consideration for thermal–hydraulic design of a PHE, therefore plate materials with higher thermal conductivity are preferred. A wide variety of plate materials are available such as those suggested by Li [369]: Stainless steel (types 304, 316, 317, 304L, 316L, 317Ti), Alloy AL6XN, Alloy 904L, Alloy 27- 7MO, Alloy 254 SMO; Nickel 200, Alloy G-30, Alloy B-2, Alloy C-22, Alloy C-276, Alloy C-2000, Alloy 33; Titanium (Gr. 1), Titanium palladium (Gr. 7&11), tantalum. Of these, stainless steel is the most commonly used for plates due to its ability for enduring high temperatures, as well as its strength, and corrosion resistance [372, 375].

7.1.5. Plate-Fin Exchangers

A plate-fin heat exchanger (PFHE) is a CHE consisting of alternating layers of corrugated sheets (fins), separated by parting sheets, and enclosed at the edges by side bars to create a series of finned chambers.

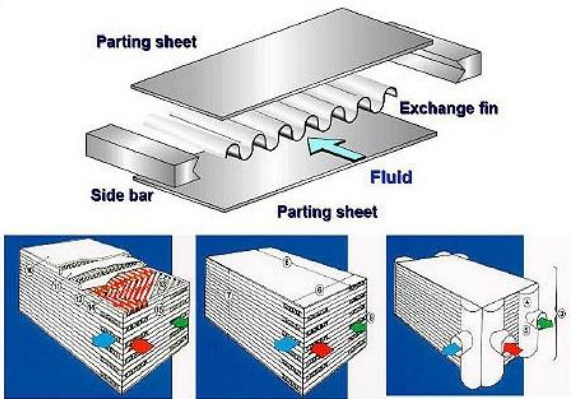

Figure 7.13. Plate-fin heat exchanger qualitative illustration [367].

As illustrated in Fig. 7.13, the fins and the parting sheets are assembled by brazing in a vacuum furnace to become a single rigid core, where this heat exchanger design can be comprised of one or more cores. Performance optimization is generally facilitated based on the number of plate and

fin layers, the size of the plate and fin, the height of the fin and the type of fin [377, 378]. During PFHE operation, heat is transferred from the hot fluid through the fin interface to the separator plate and through the next set of fins into the adjacent cold fluid. The fins have two functions: 1. first, to act as the secondary (or indirect, extended) heat transfer surface to increase the effective heat transfer surface area and increase the total heat transfer from the surface, and 2. to withstand the design pressure at the design temperature as a structural component [369]. Appendix A.1 provides general information on common application for each type of fin. In a PFHE, fins can be easily rearranged, which allow the device to operate in cross-flow, counter-flow, cross-counterflow flow. A simple cross-flow layout is generally suitable for low or moderate duties, which is nominal when one side consists of a low pressure gas. For heavier duties, the counter-flow pattern is generally a more productive solution, which also can be more efficient for most lower-temperature applications.

For plain fins, heat transfer enhancement is generally achieved due to an increased area density, rather than any increase in heat transfer coefficient [369]. Herringbone fins can enhance heat transfer by promoting mixing due to generated complex secondary flows and boundary layer separation. Serrated and perforated fins can be categorized as interrupted fins, which can enhance heat transfer through two mechanisms. First, surface interruption can prevent continuous growth of the thermal boundary layer by periodically interrupting it [379]. Secondly, the thicker thermal boundary layer in continuous fins offer higher thermal resistance to heat transfer, and is maintained thin and the resistance to heat transfer is reduced. This thermal enhancement mechanism occurs even at low Reynolds numbers when the flow is steady and laminar. Above a critical Reynolds number, the interrupted surfaces offer an additional mechanism of heat transfer enhancement by inducing self-sustained oscillations in the flow in the form of shed vortices [369], which are facilitated near the leading edge of the fins and travel downstream along the fin surface. Von Karman vortices are also observed to form at the trailing edge of the fins and travel downstream in the wake before encountering the next fin element. They act as large scale mixers and continuously bring in fresh fluid from the free-stream on their downstream side towards the fin surface [380, 381] and eject the fluid on their upstream side away from the fin surface. This however facilitates an associated increased pressure drop and pumping power due to higher skin friction associated with the hydrodynamic boundary layer resuming [369]. In addition, in the unsteady flow regime, the time-dependent flow behavior associated with vortex shedding increases frictional loss through the Stokes layer dissipation and form drag through Reynolds stresses [382]. The two independent mechanisms simultaneously influence both the overall heat transfer and the pumping power requirement [369].

For PFHEs, heat transfer performance is based on fin efficiency, Eqn. 7.47, which is determined by the surface area weighted average of finned section, $\eta_{f,i}$.

$$\eta_f = \frac{\sum_{i=1}^{n} \eta_{f,i} A_{f,i}}{\sum_{i=1}^{n} A_{f,i}} \tag{7.47}$$

According to Huang and Shah [383], Eqn. 7.47 is not valid in when the fin is thick, subject to variable heat transfer coefficients or variable ambient fluid temperature, or when it has a temperature depression at the fin base. However, for thin rectangular fins of constant cross-section, Shah [169] provides fin efficiencies for various cross-sectional plate-fin and tube-fin geometries.

7.1.6. Printed Circuit Heat Exchanger

Printed-circuit heat exchangers (PCHE), Fig. 7.14, are a category of CHEs due to their high surface density area (>2500 m^2/m^3) [384], where plate sizes can be as high as 1.2 m × 0.6 m [377]. PCHEs are strong candidate heat exchangers for CSP receiver and power block loops as they can achieve high power densities with far less material than comparable shell-and-tube heat exchangers [385]. The high temperatures within intermediate loops require heat exchangers that retain their strength at high temperatures [386], where PCHE's can be strong candidates. Their fluid passages are approximately semicircular in cross-section, being typically 1.0–2.0 mm wide, 0.5–1.0 mm in depth [387], with approximately 0.5–2.0 mm hydraulic diameters in size. PCHEs employ the same manufacturing processes as for printed circuit boards which involves photo-chemically etched grooves on a flat metal plate to form fluid passages. The etched-out plates are thereafter alternately joined by diffusion bonding, which can result in a compact, strong, all-metal heat exchanger core.

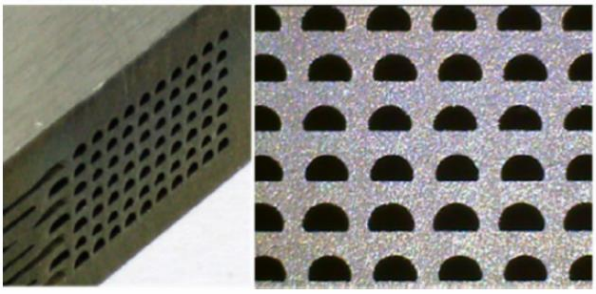

Figure 7.14. Cross-sectional view of a microchannel PCHE [388].

The diffusion bonding process includes a thermal soaking period to allow grain growth, thereby potentially eliminating the interface at the joints, which provides base-material strength and very high pressure containment capability throughout the entire exchanger, in addition to corrosion resistance [369]. Because of diffusion bonding, its expected lifetime exceeds that of most heat exchangers based on a brazed structure [289]. The complete heat exchanger core, can be tuned by welding together multiple blocks as required by a desired thermal duty (flow capacity) of the heat exchanger. The most commonly employed flow configurations include counter-flow, cross-flow or co-flow, where other advanced characteristics can be added to contribute to further improving PCHE performance [369].

In addition to its wide operating range, PCHEs also have enhanced safety features as they characteristically do not contain any gaskets or brazed material. Consequently, the risk of leaks or fluid incompatibility is substantially reduced [390]. According to Sabharwall [391] the risk of leaks in a PCHE is approximately two orders of magnitude lower than for any other heat exchanger due to its continuous passage [391]. PCHEs have been rated to operate under a temperature range from cryogenic to 900 °C, while withstanding pressures as high as 60 MPa [392]. The design of PCHEs enable operation under high purity or corrosive streams, and are not susceptible to flow induced oscillations and vibrations, like that experienced by conventional shell and tube heat exchangers. According to Heatric™ [393], PCHEs require low maintenance if used in flows with particulate size limited to 300 μm.

Characteristic continuous zigzag PCHE flow paths do not allow boundary layer growth and encourage into turbulent flow. By enhancing heat transfer area and increasing local flow velocity at channel bending points, this zigzag channel shape enhances thermal performance

compared with heat exchangers that have straight channels [394]. Compared to straight ducts, wavy geometries provide little advantage at low Reynolds numbers, although maximum advantage at transitional Reynolds numbers. Gschwind [395] described the important flow mechanisms associated with wavy channels, where low $Re < 200$ values facilitate steady recirculation zones that form in the troughs of the wavy passages, which do not enhance heat transfer. However, for higher Reynolds numbers, the free shear layer becomes unstable where subsequent vortices are advected downstream. Additionally, at higher Reynolds numbers, periodic shedding of transverse vortices increases the Nusselt number with a considerable increase in the friction factor [369].

According to Urquiza *et* al. [386] although PCHE heat exchangers can achieve high effectiveness, they can also be susceptible to very large thermal stresses that occur during flow transients, which can be significantly higher than those predicted under steady state conditions. Peak stresses occur at the feature scale where the fin roots and the flow channel geometry concentrate stresses resulting from thermal expansion [386].

7.1.7. Spiral Heat Exchangers

A spiral heat exchanger (SHE) is characterized by a helical tube configuration as illustrated by Fig. 7.15 where the circular heat exchanger has two long metal strips rolled together to form a pair of concentric spiral channels of rectangular cross-section, one for each fluid [396].

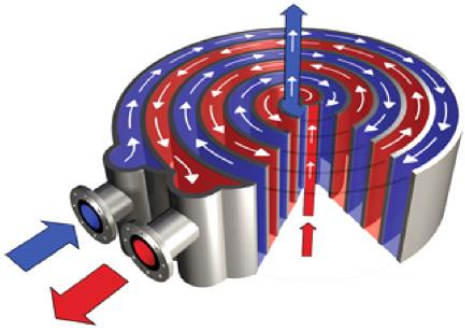

Figure 7.15. Spiral heat exchanger [396].

SHE passages can either be smooth or corrugated to enhance turbulent mixing, and in some cases studs are welded onto one side of each strip to fix the spacing between the plates, providing improved mechanical strength and increased turbulence and subsequent heat transfer [396]. Alternating passage edges are sealed either by welding at each side of the channel [368] or by providing a gasket at each end cover to obtain the following configurations of the two fluids: (1) both in spiral counter-flow; (2) one in spiral flow, with the other in cross-flow across the spiral; or (3) one in spiral flow, with the other in a combination of cross-flow and spiral flow. With countercurrent SHEs, an LMTD correction factor of 1.0 does not have an LMTD penalty like other exchangers [396].

In non-corrugated SHE devices, heat transfer coefficients are not as high as in PHEs, which are designed for operation at temperatures up to 540 °C, where SHEs are conventionally designed to operate up to 200 °C [369]. As with gasketed PHEs, the temperature limit is dependent on the gasket material used to seal the gaps between the open channel ends and the end covers. The fluid in a SHE is fully turbulent at a much lower velocity than in straight tube heat exchangers due to the studs and the concentric shape of the flow passages. As fluid flows, the curvature of the

passages facilitates a centrifugal force, which also impose secondary flow effects (eddy currents and vortices) which significantly enhance heat transfer [397]. SHE heat transfer characteristics can be improved by adjusting channel dimensions, such as variation of the diameter, surface modification or by adding roughness to the channel walls. SHE devices conventionally have relatively large diameters and a channel spacing range between 5 mm and 25 mm (representing hydraulic diameters of 10–50 mm), where engineers can leverage their high heat transfer surface area densities, and low propensities for blockage by fouling. Picon-Nunez *et* al. [398] presented a shortcut method for the sizing of spiral plate heat exchangers with single-phase processes, where SHEs can also be made compact. The internal void volume is lower (< 60%) than a shell-and-tube heat exchanger [365], which can facilitate a compact, space-saving construction that can be readily integrated in any plant, reducing installation costs. The heat transfer surface traditionally ranges from 0.05 m^2 for refrigeration applications, up to approximately 500 m^2 with a maximum shell diameter of 1.8 m and sheet metal thickness between 1.8–4 mm for industrial processes [377]. The surface area requirement is about 20% lower than that for shell-and-tube heat exchangers for the same heat duty [365].

7.1.8. Ceramic Heat Exchangers

Ceramic heat exchangers (CHE), Fig. 7.16, are mostly fin-and-tube or plate-type designs where advances in ceramic materials are providing novel designs for high temperature applications [369]. According to Li *et* al. [369] the ceramic material is defined as a glazed/unglazed body of crystalline or partly crystalline structure, or of glass. Here the structure is produced from essentially inorganic, nonmetallic substances and is either formed from molten mass which solidifies on cooling [399].

Figure 7.16. Industrial ceramic heat exchanger [400].

Currently, CHEs are primarily constructed by replacing tube and fin materials with ceramic. Manufacturing procedures include forming primary components from raw materials with subsequent machining, joining, bonding, and assembling, in either a monolithic and non-monolithic approach. Because individual components are bonded together permanently without an internal joint, there are no sealing problems in a monolithic assembly, but stress concentrations can arise under extreme operating conditions. In a non-monolithic assembly, individual components can be disassembled and repaired easily, however sealing issues can arise due to the brittleness of ceramics and challenges of forming a resilient metal–ceramic or ceramic–ceramic joint due coefficient of thermal expansion (CTE) differences [401]. Consequently, advanced fabrication techniques like laser supported brazing [402] are often employed to improve joint integrity. Primary advantages for using ceramic materials over traditional metallic materials in

CHE construction are their extremely high temperature stability, low material cost and excellent corrosion resistance. CHEs can withstand operating temperatures that potentially can far exceed those of conventional metallic alloys, Silicon carbide (SiC) 1400 °C, Silicon nitride (Si_3N_4) 1900 °C, Alumina 1500–1700 °C, and Aluminium nitride (AlN) 1300 °C [401]. At elevated operating temperatures, CHEs possess high fouling resistance and resistance to corrosion and chemical erosion.

Among the ceramics materials for CHEs, SiC ceramics that have been extensively investigated [403], which has been treated as a promising material for high-temperature heat exchanger applications, primarily because of its excellent thermal stability and corrosion resistance in severe environments, as well as sufficient thermal conductivity at elevated temperatures [404]. Steen [405] investigated the short and long term mechanical properties of a sintered silicon carbide heat exchanger within advanced gas turbine coal-fired power plants. Amirthan *et* al. [406] prepared four different types of Si/SiC ceramic composites by a liquid-silicon infiltration technique and measured their thermal conductivities at different temperatures by a laser flash thermal conductivity method. The investigators found that the presence of free carbon and voids notably affect the thermal conductivity of these materials. Investigations of ceramic CHEs involved in liquid-to-liquid heat exchangers [407], liquid-to-gas heat exchangers and gas-to-gas heat exchangers [408] could be leveraged for use in heat sinks and volumetric solar receivers. Schulte-Fischedick *et* al. [409] proposed a sintered SiC ceramic PFHE coated with an environmental barrier coating based on the "Offset Strip Fin" design, where the investigators studied it for use in a high temperature heat exchanger for an externally-fired combined cycle (EFCC), as well as for other applications that required extreme temperature operation up to 1250 °C. The thermal design was conducted by using empirical correlations drawn from literature via the LMTD-method, while the stress distribution of the selected design during operation was investigated by means of finite element method (FEM). Islamoglu [408] analyzed the temperature distribution for steady-state heat transfer, as well as the thermal stresses, where were induced by temperature difference in a silicon carbide (SiC) ceramic tube. The employment effects of annular fins with different profiles (rectangular and triangular) [410] and the axial non-uniform convective heat transfer coefficient [408] on the temperature and thermal stresses have also been investigated. Fend *et* al. [411] measured thermal conductivity, convective heat transfer coefficients and efficiency of selected materials made from various oxide/non-oxide ceramics, ceramic foams and metal structures, where they also experimentally investigated how the properties of the porous materials affect flow stability. It was concluded that introduction of materials based on ceramic foams and ceramic fabrics in solar tower technology would offer the potential for more effective and reliable operation compared to current open volumetric receiver technology. They presented test results for two novel porous materials, for an application as a volumetric receiver using a double-layer silicon carbide foam and a screen-printed porous silicon carbide material. Both ceramic technologies are future options with properties required for use in a high-performance solar receiver [412].

7.1.9 Fluidized-Bed Heat Exchangers

For fluidized-bed heat exchangers one characteristic type consists of tube bundles immersed in a bed of finely divided solid material, as shown in Fig. 7.17. If the upward fluid velocity on the bed side is low, the solid particles will remain fixed within the bed and the fluid will flow through the

interstices of the bed. If the upward fluid velocity is high, the solid particles will be carried away with the fluid.

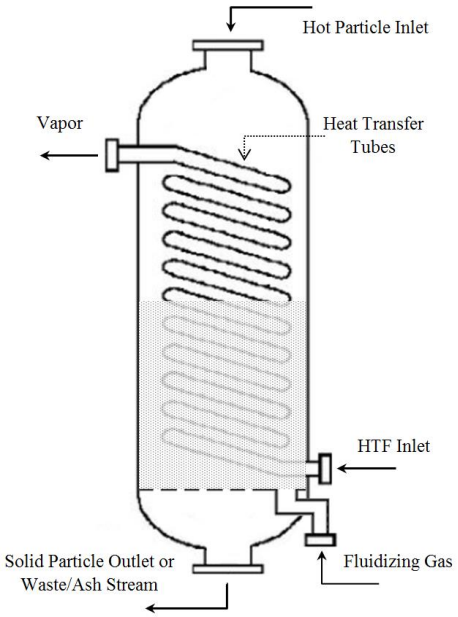

Figure 7.17. Fluidized-bed heat exchanger.

At high fluid velocities, the upward drag force is slightly higher than the weight of the bed particles which will cause the solid particles to float with an increase in bed volume causing the bed to behave as a liquid [413]. This is referred to as a fluidized condition where the pressure drop through the bed remains almost constant and independent of the flow rate. Under this condition a strong mixing of the solid particles occurs, especially for small particle diameters that are less than 1 mm, which results in a homogeneous temperature distribution of both gas and solid media [359]. Very high heat transfer coefficients are achieved on the fluidized-side compared to particle-free or dilute-phase particle gas flows. Chemical reaction can also be facilitated on the fluidized side depending on the level of oxygen and activation energy of the particles [414]. Since the initial temperature difference, between the hot fluid and fluidized bed, $T_{h,0}$-$T_{f,0}$ is reduced due to fluidization, the exchanger effectiveness is therefore lower [415].

For CSP combustion applications, input media with high reactivity have greater combustion or reaction efficiency, where previous studies have demonstrated the amount of combustible losses in fly ash is inversely proportional to the heating value of the fuel [417]. Typical combustion temperatures for fluidized beds falls within the range of 800 – 900 °C [417]. Although this temperature range minimizes the formation of sulfur and nitrogen oxides, higher temperatures will ensure reduced combustible losses in escaping unburned fuel particles with incomplete combustion. In fluidized bed combustors, the residence time of carbon particles is affected by the type of feed, particle size and fluidizing velocity. The residence time becomes shorter for particles with significantly lower velocities, favoring a high percentage of unburned carbon [417].

Principally, when an upward flowing gas moving with a relative velocity is passed through a static bed of particles, they will be partially suspended once the gas velocity reaches a certain minimum fluidization velocity [418], therefore the minimum fluidization velocity is that required to move the static bed. The quality of fluidization obtained varies from one bed media to another, where intrinsic properties including particle density, particle size and surface characteristics affect the outcome of fluidization [419]. The operating velocity of the fluidized bed must be maintained

between the minimum fluidization velocity and the terminal velocity, which is the maximum gas velocity beyond which particles will be entrained.

7.2 Recuperators

In most heat exchangers, heat transfer between fluids takes place through a separating wall, or into and out of a wall in a transient manner, where the fluids are separated by a heat transfer surface. However, in some design configurations direct-transfer type exchangers are required to enhance heat transfer between fluids where one fluid recovers (recuperates) heat from a second fluid. Some examples of recuperators can be seen in Fig. 7.18, where direct transfer designs can also include tubular, plate-type, and extended surface exchangers. Recuperators can be added between pump and expander outlets to preheat a liquid before the evaporator, which increases cycle efficiency.

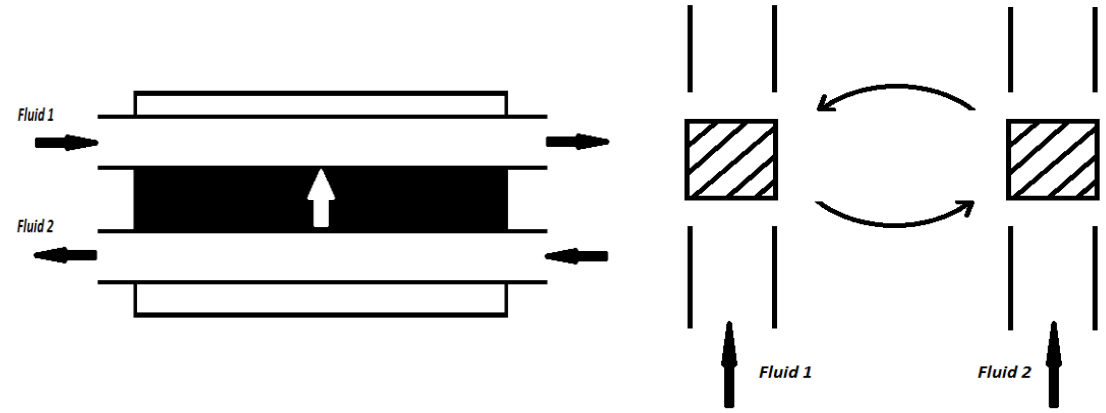

Figure 7.18. Generalized recuperator heat transfer modes.

7.3 Regenerators

In contrast to recuperators, regenerator heat exchangers are storage-type exchangers, which facilitate intermittent heat exchange between hot and cold fluids, via thermal energy storage and release through an exchanger surface or matrix. As shown in Fig. 7.19, there are several characteristic variations that transfer heat indirectly, where these devices usually have fluid interaction from one fluid stream to the other due to pressure differences or matrix rotation/valve switching. In general, a stationary heat exchanger is usually referred to as a recuperator, and a dynamic or rotating heat exchanger as a regenerator [359].

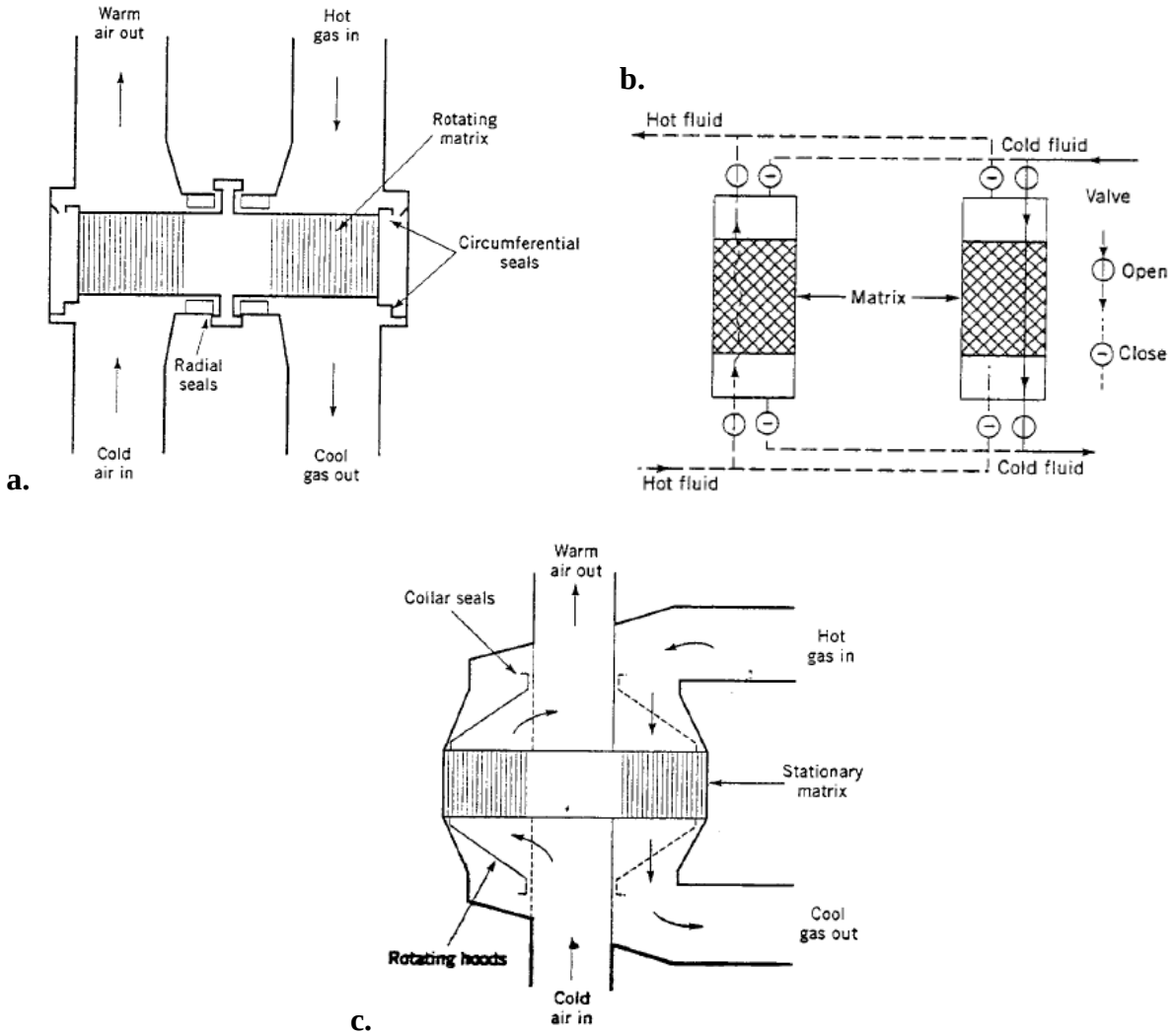

Figure 7.19. Regenerator types: a. rotary, b. fixed-matrix and c. Rothemuhle [169].

According to Kreith [169] in order to facilitate continuous regenerator operation, the internal matrix must be moved periodically within the fixed streams of gases, as in a rotary regenerator, or the gas flows must be diverted through valves to and from the fixed matrices. This can be accomplished with a fixed-matrix regenerator, also known as a periodic-flow regenerator or reversible heat accumulator. Rotary regenerators are advantageous for highly compact forms, where the cost of the regenerator surface per unit of heat transfer area is usually substantially lower than that for the equivalent recuperator. A major disadvantage of a regenerator is an unavoidable carryover of a small fraction of the fluid trapped in the passage to the other fluid stream just after periodic flow switching [169]. Since fluid contamination (small mixing) is prohibited with liquids, the regenerators are used exclusively for gas-to-gas heat or energy recovery applications. Cross contamination can also be minimized significantly by providing a purge section in the disk and using double-labyrinth seals [169]. Rotary regenerators have been designed for a surface area density of up to approximately 6600 m^2/m^3, with an exchanger effectivenesses exceeding 85% for a number of applications. These devices can additionally employ thinner stock material, resulting in minimal volumes of material necessary for a given effectiveness and pressure drop. Metal rotary regenerators have been designed for continuous inlet temperatures of up to approximately 790 °C,

and pressures differences up to 400 kPa between hot and cold gases, where ceramic matrices can potentially achieve even higher temperature applications [169]. Finally, another type of regenerator is a Rothemuhle regenerator which is used commonly as an air preheater in some power-generating plants, which has a fixed matrix, where the gases pass through rotating hoods to the matrix [169].

In storage heat exchangers both fluids flow alternatively through the same flow passages, where heat transfer is intermittent. The heat transfer flow passages generally have a cellular structure (matrix), or is a permeable solid material (packed bed). When hot gas flows over the heat transfer surface through flow passages, thermal energy is stored in the matrix wall, where the gas is cooled during the matrix heating period. As cold gas flows through the same passages thereafter, it absorbs thermal energy from the matrix wall. This storage type heat exchanger is also referred to as a regenerator. The actual time hot gas takes to flow through a cold regenerator matrix is called the hot period, and the time that cold gas flows through the hot regenerator matrix is called the cold period. There is a small fraction of carryover of the fluid trapped in the passage to the other fluid stream just after switching of the fluids, referred to as carryover leakage. In addition, if the hot and cold fluids are at different pressures, pressure leakage from the high-pressure fluid to the low-pressure fluid past the radial, peripheral, and axial seals, or across the valves. Over time leaks can be unavoidable where regenerators are used exclusively in gas-to-gas heat transfer sensible applications. Finally, in some applications, regenerators may transfer moisture from humid air to dry air up to approximately 5% [169].

8. CONCLUDING REMARKS

The novelty of CSP is that it captures and concentrates the sun's incident irradiant energy to provide heat required to generate electricity, where CSP plants can be equipped with heat storage to generate electricity even when the sky is cloudy or dark. This provides tremendous potential for impacting the base load of an electric grid by significantly increasing the capacity factor compared with solar photovoltaics by providing dispatchable electricity, which can facilitate both grid integration and economic competitiveness. Heat transfer in solar thermal systems are guided by five basic principles: heat gain; thermal-fluid transport; heat storage; heat losses; and heat insulation. CSP maximum efficiency can be enhanced and shifted towards higher temperatures when solar irradiation is further concentrated by CSP collectors, where high-absorption receivers are able to transfer large thermal loads to a heat transfer fluid for power block electricity generation. CSP technologies today benefit from new field concentrator layouts and optics, as well as advances in heat transfer to achieve even higher concentration ratios, as well as thermal storage technologies, while other components of CSP plants can benefit from thermal-fluid advances in heat exchangers and power block system technologies. Although CSP performance increases with higher temperatures, thermal losses also increase however especially at temperatures above 600 °C where radiation effects can become dominant for most surfaces. The utility of fundamental heat transfer phenomena at varying temperature/pressure scales has contributed to enhanced HTF materials that span solids, liquids and gases, which can achieve higher material temperatures while remaining stable. Novel supercritical gases have also been explored that can attain properties close to those of liquids for enhanced energy transfer, storage and power block system interactions. Novel development of HTFs has contributed to enhancement of their ability to also store and transfer heat through means of novel heat exchange equipment that also allow for higher thermal absorption to achieve even higher thermal efficiencies. However, system component equipment and HTF limitations still exist, such as losses, which require further heat transfer study. However, current advancements have contributed to the ability of transferring and retaining heat within innovative thermal cycles. Such cycles like the supercritical Brayton cycle, take advantage of components such as regenerators, recuperators and cascaded designs, as well as novel materials and coatings. These and other advancements demonstrate the potential for achieving even higher temperatures and pressures to facilitate further LCOE reductions for CSP competitiveness, to enable cost-effective energy sufficiency in a carbon-neutral future.

9. REFERENCES

[1] Krothapalli, A. and Greska, B. "Concentrated solar thermal power." USA: Florida State University, 2011.

[2] IRENA Report, Concentrating Solar Power, Technology Brief E10, IEA-ETSAP, 2013.

[3] Fichtner, "Technology Assessment of CSP Technologies for a Site Specific Project in South Africa Final Report," *The World Bank and ESMAP*, Washington D.C., 2010.

[4] Henry, A., & Prasher, R., The prospect of high temperature solid state energy conversion to reduce the cost of concentrated solar power. Energy & Environmental Science, 7, No. 6, pp. 1819-1828, 2014.

[5] Hinkley, J., Curtin, B., Hayward, J., Wonhas, A., Boyd, R., Grima, C., ... & Mikhail, A. (2011). Concentrating solar power–drivers and opportunities for cost-competitive electricity. Clayton South: CSIRO.

[6] Hoffschmidt, B., "Receivers for solar tower systems", SFERA, Font Romeu, France, 2014

[7] Mehos, M., Turchi, C., Jorgenson, J., Denholm, P., Ho, C., & Armijo, K.M., "On the Path to SunShot: Advancing Concentrating Solar Power Technology, Performance, and Dispatchability", No. NREL/TP-5500-65688; SAND2016-2237 R, Golden, CO, USA, 2016

[8] Molenbroek, E., "Concentrating Solar Power Status and Potential", ECOFYS Report, 2008.

[9] Duffie, J.A., Beckman, W.A., "Solar engineering of thermal processes", 4th Ed., Wiley & Sons, New Jersey, USA, 2013.

[10] Armijo, K. M., Harrison, R. K., King, B. H., & Martin, J. B. (2014, September). Spectral derates phenomena of atmospheric components on multi-junction CPV technologies. In AIP Conference Proceedings (Vol. 1616, pp. 264-271).

[11] Iqbal, M., An Introduction to Solar Radiation, Academic, Toronto, 1983.

[12] Incropera, F. P., & Dewitt, D. P., "Fundamentals of Mass and Heat Transfer", Wiley & Sons, New Jersey, USA, 2002

[13] Ibarra-Castanedo, C., Sfarra, S., Genest, M., & Maldague, X., "Infrared vision: Visual inspection beyond the visible spectrum", In: "Integrated imaging and vision techniques for industrial inspection", pp. 41-58. Springer London, 2015.

[14] Duffie, J. A., and Beckman, W. A., "Solar engineering of thermal processes*"* 4th Edition, Wiley & Sons, New York, USA, 2013.

[15] Tada, H., "Gourmet Engineering Lecture Notes", Tufts School of Engineering, 2002.

[16] Chirkin, V. S., "Thermal conductivity of industrial materials", Mashgiz, Moscow, 1962.

[17] Andraka, C. E. (2014). Dish Stirling advanced latent storage feasibility. *Energy Procedia*, *49*, 684-693.

[18] Hashmi, A., Tahir, F. R. A. A. Z., and Hameed, U. "Empirical Nusselt number correlation for single phase flow through a plate heat exchanger", In" *Proceedings of the 9th WSEAS International Conference on Heat and Mass Transfer*, Cambridge, MA, USA, pp. 25-27, 2012.

[19] J. Fernandez-Seara, J., Sieres, U.J., Campo, A., "A general review of the Wilson plot method and its modifications to determine convection coefficients in heat exchange devices", *Applied Thermal Engineering*, **27**, pp. 2745–2757, 2007.

[20] Edwards, M.F., Changal Vaie, A.A., and Parrott, D.L., "Heat transfer and pressure drop characteristics of a plate heat exchanger using non-Newtonian liquids", *The Chemical Engineer*, **285**, pp. 286–288, 293, 1974.

[21] Muley A. and Manglik, R.M., "Experimental study of turbulent flow heat transfer and pressure drop in a plate heat exchanger with chevron plates", *J. of Heat Transfer*, **121**, no. 1, pp. 110–117, 1999.
[22] Gnielinski, V. "New equations for heat and mass-transfer in turbulent pipe and channel flow", *International chemical engineering*, **16**, no.2, 359-368, 1976.
[23] Gourdon, M., Innings, F., Jongsma, A., & Vamling, L., "Qualitative investigation of the flow behaviour during falling film evaporation of a dairy product", *Experimental Thermal and Fluid Science*, **60**, pp. 9-19, 2015.
[24] Zhukauskas, A., "Heat transfer from tubes in cross flow", In: J.P. Hartnett and T.F. Irvine Jr., Eds., *Advances in Heat Transfer*, **8**, Academic Press, New York, USA, 2972.
[25] Carey, V.P., "Liquid-vapor phase-change phenomena", 2nd Ed., Taylor & Francis, New York, USA, 2008.
[26] Ramé-Hart, "Contact angle goniometers and tensionometers", Ramé-Hart Instrument Co., 2015: http://www.ramehart.com/contactangle.htm
[27]Eistron, "Contact angle meter", Weiston Co. LTD., 2014: http://www.weistron.com/products/contact-angle-meter/
[28] Pfleger, N., Bauer, T., Martin, C., Eck, M., and Wörner, A. "Thermal energy storage–overview and specific insight into nitrate salts for sensible and latent heat storage", *Beilstein journal of nanotechnology*, **6**, No. 1, pp. 1487-1497, 2015.
[29] Rohsenow, W.M., "A method of correlating heat transfer data for surface boiling of liquids", *Trans. ASME*, **84**, pp. 969–975, 1962.
[30] Faghri, A., Zhang, Y., & Howell, J. R., "Advanced heat and mass transfer", Global Digital Press, Columbia, MO, USA, 2010.
[31] Dwyer, O. E., "Boiling liquid-metal heat transfer", American Nuclear Society, Hinsdale, Ill., 1976.
[32] Subbotin, V.I., Ushakov, P.A., Kirillov, P.L., Ibragimov, M.K., Ivanovski, M.N, Nomophilov, E.V., Ovecnkin, D.M., Sorokin, D.N. and Sorokin, V.P., "Heat removal from the reactor fuel elements cooled by liquid metals", In: *Proc. UN Intern. Conf. Peaceful Uses of Atomic energy*, Geneva, Sept. 3rd 1964, **8**, pp. 192, United Nations, NY, USA, 1965.
[33] Edwards, J.A. and Hoffman, H.W., "Superheat with boiling alkali metals", In: *Proc. Conf. Application of high-temperature instrumentation to liquid-metal experiments*, Argonne national Laboratory, ANL-7100, 1065.
[34] Chen, J.C., "Incipient boiling superhets in liquid metals", *Trans. ASME Series C, J. of Heat Transfer*, **90**, 1968.
[35] Logan, A.D., Baroczy, C.J., Landoni, J.A. and Morewitz, H.A., "Effects of velocity, oxide level, and flow transients on boiling initiation in sodium", *Proc. ASME Symp. Liquid-Metal Heat Transfer and Fluid Dynamics*, pp. 116, 1970.
[36] Collier, J.G. and Thome, J.R., "Convective boiling and condensation", 3rd Ed., Oxford University Press, Oxford, U.K., 1994.
[37] Wright, R.M., "Downflow forced convection boiling of water in uniformly heated tubes", Univ. of California, Report No. UCRL-9744, 1961.
[38] Gungor, K.E. and Winterton, R.H.S., "A general correlation for flow boiling in tubes and annuli", *Int. J. Heat & Mass Transfer*, **29**, pp. 351-358, 1986.
[39] Bjorge, R.W., Hall, G.R. and Rohsenow, W.M., "Correlation of forced convection boiling heat transfer data", *Int. J. Heat & Mass Transfer*, **25**, pp. 753-757, 1982.

[40] Kandlikar, S.G., "A general correlation for saturated two-phase flow boiling heat transfer inside horizontal and vertical tubes", *J. of Heat Transfer*, **112**, pp. 219-228, 1990.
[41] Kandlikar, S.G., "Development of a flow boiling map for subcooled and saturated flow boiling of different fluids in circular tubes", *J. of Heat Transfer*, **113**, pp. 190-200, 1991.
[42] Gunther, F.C., "Photographic study of surface-boiling heat transfer to water with forced convection", *Trans. ASME*, **73**, pp. 105-107, 1951.
[43] Tong, L.S., "Boundary layer analysis of the flow boiling crisis", *Int. J. of Heat and Mass Transfer*, **11**, pp. 1208-1211, 1968.
[44] Tong, L.S., "A pheonomenological study of critical heat flux, ASME paper 75-HT-68, *National Heat Transfer Conference*, Sn Francisco, CA, USA, 1975.
[45] Thompson, B. and Macbeth, R.V., "Boiling water heat transfer – Burnout in uniformly heated round tubes: A compilation of world data with accurate correlations", *Report AEEW-R-356*, U.K. Atomic Energy Authority, Winfrith, England, 1964.
[46] Biasi, L., Clerici, G.C., Gariloben, S., Sala, R. and Tozzi, A., "Studies on burnout. Part 3", *Energia Nucleare*, **14**, No. 9, pp. 530-536, 1967.
[47] Katto, Y. and Ohno, H., "An improved version of the generalized correlation of critical heat flux for the forced convective boiling in uniformly heated vertical tubes", *Int. J. of Heat and Mass Transfer*, **27**, pp. 1641-1648, 1984.
[48]Stine, W. and Geyer, M., "Power from the sun", Ch. 9, 2001, http://www.powerfromthesun.net/Book/chapter09/chapter09.html
[49] Duffie, J. A. and Lof, G.O.G., ''Focusing Solar Collectors for Power Generation'', Paper 207 III.7/5, presented at the World Power Conference, Melbourne, Australia, 1962.
[50] Grange, B., "Solar Receiver modeling central receiver", SFERAII Presentation, Odeillo, France, 2014.
[51] Treadwell, G. W. "Design Considerations for Parabolic Cylindrical Solar Collectors", SAND76-0082, Sandia National Laboratories, Albuquerque, 1976.
[52] Ratzel, A C. "Evaluation of the Evacuated Solar Annular Receivers Employed at the Midtemperature Solar Systems Test Facility", *SAND78-0983*, Sandia National Laboratories, Albuquerque, 1979.
[53] Ratzel, A. C. "Receiver Assembly Design Studies for 2-m 90 Degree Parabolic Cylindrical Solar Collectors", *SAND79-1026*, Sandia National Laboratories, Albuquerque, 1979.
[54] Ratzel, A.C., and C.E. Simpson, "Heat Loss Reduction Techniques for Annular Receiver Designs", *SAND 78-1769*, Sandia National Laboratories, Albuquerque, 1979.
[55] Kalogirou, S.A., "Solar thermal collectors and applications", *Prog. Energy & Comb. Sci.*, **30**, pp. 231-295, 2004.
[56]Stine, W. and Geyer, M., "Power from the sun", Ch. 5, 2001, http://www.powerfromthesun.net/Book/chapter05/chapter05.html
[57] Bejan, A., Kearney, D.W. and Kreith, F., "Second law analysis and synthesis of solar collector systems", *J. of Solar Energy Engng.*, 103, pp. 23-28, 1981.
[58] Bejan, A., "Entropy generation minimization", 2nd Ed., CRC Press, Boca Raton, FL, USA, 1995.
[59] Petela, R., "Exergy of heat radiation", ASME J Heat Transfer, **68**, pp. 187, 1964.
[60] McDonald, G. E. "Spectral reflectance properties of black chrome for use as a solar selective coating", *Solar Energy*, **17**, No. 2, pp.119-122, 1975.
[61] Hollands, K. G. T., ''Directional selectivity, emittance and absorptance properties of V_{ee} Corrugated Specular Surfaces'', *Solar Energy*, **7**, pp. 108, 1963.

[62] Trombe, F., Foex, M. and LePhat Vinh, M., ‘‘Research on Selective Surfaces for Air Conditioning Dwellings.’’, *Proc. UN Conf. New Sources of Energy*, **4**, pp. 625-638, 1964.
[63] V. E. Dudley, G. J. Kolb, M. Sloan, and D. Kearney, “Test Results: SEGS LS-2 Solar Collector”, SAND94-1884, Sandia National Laboratories, Albuquerque, NM, USA, 1994.
[64] Ho, C. K., & Iverson, B. D., “Review of high-temperature central receiver designs for concentrating solar power”, *Renewable and Sustainable Energy Reviews*, **29**, pp. 835-846, 2014.
[65] Prakash, M., Kedare, S. B., & Nayak, J. K., “Investigations on heat losses from a solar cavity receiver”, Solar Energy, **83**, No. 2, pp.157-170, 2009.
[66] Kolb, G. J., Ho, C. K., Mancini, T. R., & Gary, J. A. “Power tower technology roadmap and cost reduction plan”, *SAND2011-2419*, Sandia National Laboratories, Albuquerque, NM, 2011.
[67] Becker, M. and Vant-Hull, L. L., “Thermal receivers, Solar Power Plants”, Springer, Berlin, Germany, 1991.
[68] Kribus, A., Doron, P., Rubin, R., Karni, J., Duchan, S. and Taragan, E., “A multistage solar receiver: the route to high temperature”, *Solar Energy*, **67**, No. 1, pp.3–11, 1999.
[69] Kugath, D. A. Drenker, G. and Koenig, A. A. “Design and development of a paraboloidal dish solar collector for intermediate temperature service,” *Proc. of Int. Solar Energy Soc.*, Silver Jubilee Congress, **1**, pp. 449–453, Atlanta, Ga, USA, 1979.
[70] Kedare, S. B., Nayak, J. K. and Paranjape, A. D., “Development, installation and evaluation of large scale concentrating solar collector for medium temperature industrial thermal applications,” *Final Report of R&D Project No. 15/9/2002-ST*, Ministry of New and Renewable Energy, Government of India, 2006.
[71] Lovegrove, A. Zawadski, and J. Coventy, “Taking the anu big dish to commercialization,” *Proc. of Solar 2006: Clean Energy? -Can Do!*, (ANZSES ’06), Canberra, Australia, 2006.
[72] F. Nepveu, A. Ferriere, and F. Bataille, “Thermal model of a dish/stirling systems,” *Solar Energy*, **83**, No. 1, pp. 81–89, 2009.
[73] A. Steinfeld and R. Palumbo, “Solar thermochemical process technology,” *Encyclopedia of Physical Science & Technology*, **15**, pp. 237–256, 2001.
[74] Harris, J. A., & Lenz, T. G., “Thermal performance of solar concentrator/cavity receiver systems”, *Solar Energy*, **34**, No.2, pp. 135-142, 1985.
[75] Dudley, V. E., and Workhoven, R. M., “Performance Testing of the Suntec- SLATS Solar Collector,” *SAND78-0623*, Sandia National Laboratories, Albuquerque, NM, USA, 1978.
[76] Ma, R. Y. “Wind effects on convective heat loss from a cavity receiver for a parabolic concentrating solar collector,” SAND92-7293, Sandia National Laboratories, Albuquerque, NM, USA, 1993.
[77] Prakash, M., “Numerical study of natural convection heat loss from cylindrical solar cavity receivers,” *ISRN Renewable Energy*, 2014.
[78] Taumoefolau, T., Paitoonsurikarn, S., Hughes, G. and Lovegrove, K.,“Experimental investigation of natural convection heat loss from a model solar concentrator cavity receiver,” *J. of Solar Energy Eng.*, **126**, No. 2, pp. 801–807, 2004.
[79] Sendhil Kumar, N. and Reddy, K.S., “Numerical investigation of natural convection heat loss in modified cavity receiver for fuzzy focal solar dish concentrator,” *Solar Energy*, **81**, no. 7, pp. 846–855, 2007.
[80] Stine, W.B., and McDonald, C.G., “Cavity receiver convective heat loss,” *Proc. of Int. Solar Energy Soc. Solar World Cong.*, **2**, pp. 1318–1322, Kobe, Japan, 1989.

[81] Sendhil Kumar, N. and Reddy, K. S., "Comparison of receivers for solar dish collector system," *Energy Conversion and Management*, **49**, No. 4, pp. 812–819, 2008.
[82] Kistler, B. L. "A user's manual for DELSOL3: a computer code for calculating the optical performance and optimal system design for solar thermal central receiver plants," *SAND86-8018*, Sandia National Laboratories, Albuquerque, NM, USA, 1986.
[83] Koenig, A.A., Marvin, M., "Convection heat loss sensitivity in open cavity solar receivers," Final Report, DOE Contract No. EG77-C-04-3985, D.O.E., Oak Ridge, Tennessee, USA, 1981.
[84] Siebers, D.L. and Kraabel, J.S., "Estimating convective energy losses from solar central receivers," *SAND84-8717*, Sandia National Laboratories, Albuquerque, NM, USA, 1984.
[85] Kraabel, J.S., "An experimental investigation of natural convection from a side-facing cubical cavity," *ASME-JSME Thermal Eng. Joint Conf. Proc.*, **1**, pp. 299-306, Honolulu, Hawaii, USA, 2983.
[86] LeQuere, P., Penot, F. and Mirenayat, M., "Experimental study of heat loss through natural convection from an isothermal cubic open cavity," *SAND81-8014*, Sandia National Laboratories, Albuquerque, NM, USA, 1981.
[87] Clausing, A.M., "An analysis of convective losses from cavity solar central receviers," Solar Energy, 27, No. 4, pp. 295-300, 1981.
[88] McMordie, R.K., "Convection heat loss from a cavity receiver, "*ASME J. of Solar Energy Eng.*, 106, pp. 98-100, 1984.
[89] Faust, K.M., Plate, E.J. and Kuezera, M., "Experimental Investigation of the convective losses from the cavity receiver of the project GAST," *SAND81-8014*, Sandia National Laboratories, Albuquerque, NM, USA, 1981.
[90] Paitoonsurikarn, S., Lovegrove, K., Hughes, G. and Pye, J., "Numerical investigation of natural convection loss from cavity receivers in solar dish applications," J. of Solar Energy Eng., **133**, No. 2, 2011.
[91] Prakash, M., Kedare, S. B., & Nayak, J. K., "Determination of stagnation and convective zones in a solar cavity receiver," *Int. J. of Therm. Sci.*, **49**, No. 6, pp. 680-691, 2010.
[92] Flamant, G., Gauthier, D., Benoit, H., Sans, J. L., Garcia, R., Boissière, B. and Hemati, M. "Dense suspension of solid particles as a new heat transfer fluid for concentrated solar thermal plants: on-sun proof of concept", *Chemical Engineering Science*, **102**, pp. 567-576, 2013.
[93] Röger, M., Amsbeck, L., Gobereit, B. and Buck, R., "Face-down solid particle receiver using recirculation," *J. of Solar Energy Eng.*, **133**, No. 3, 2011.
[94] Wu, W., Gobereit, B., Singer, C., Amsbeck, L. and Pitz-Paal, R., "Direct absorption receivers for high temperatures," 2011.
[95] Ho, C. K., Christian, J. M., Yellowhair, J., Siegel, N., Jeter, S., Golob, M., and Al-Ansary, H., "On-sun testing of an advanced falling particle receiver system," *SOLARPACES 2015: International Conference on Concentrating Solar Power and Chemical Energy Systems*, **1734**, No. 1, 2016.
[96] Chen, H., Chen, Y., Hsieh, H. T., and Siegel, N., "Computational fluid dynamics modeling of gas-particle flow within a solid-particle solar receiver," *Journal of solar energy engineering*, **129**, No. 2, pp. 160-170, 2007.
[97] Penner, A., "High temperature falling particle receiver reaches new limits," *Sandia National Laboratories: Energy & Climate*, Accessed: August, 2015, http://energy.sandia.gov/high-temperature-falling-particle-receiver-breaks-reaches-new-limits/.

[98]. Jones, P.D., *Radiation and convection heat trasnfer in particle-laden fluid flow*. Dissertation Doctoral Thesis, Rice University, 1991.
[99]. R. Yamazaki, N.U.a.G.J., "Mechanism of incipient fluidization and fluidized bed at elevated temperature", *J. of Chemical Engineering of Japan***19**: p. 251-257, 1986.
[100]. C.E. Davies, S.G.B.D.a.R.B.F., "Fluidization VI. An investigation of thermal agglomeration in fluidized beds", Engineering Foundation, New York, USA, 1989.
[101]. Shimizu, T.T.a.A., "*Advances in Multiphase Flow*. Prediction of turbulence modulation by using k-e model for gas-solid flow," *Elsevier Science*, Amsterdam, NL,1995.
[102]. Basu, P.K.N., "An investigation into heat trasnfer in CFB's," *J. of Heat and Mass Trans*., **30**, p. 2399, 1987.
[103]. C. Heered, A.P.V.a.D.W.V., "Mechanism of heat trasnfer in FBs," *Industrial and Chemistry Research*, **45, *No.*** 6, p. 1237, 1953.
[104]. Kolar, M.M.a.A.K., "Emulsion layer model for wall heat transfer in CFB,"*AlChe Journal*, **37**, p. 1139, 1991.
[105]. Mickley, D.F.F., "Mechanism of heat trasnfer in FBs," *AlCheE Journal*, **1**, p. 374, 1960.
[106]. Basu, D.S.a.P., "A model for heat transfer in CFBs," *Int. J. of Heat and Mass Transfer*, **29**: p. 487, 1986.
[107]. Williams, J.S.B.a.J.R., "The mechanism of heat transfer in gas-FBs," *Trans. of Inst. of Chem. Eng.*, **41**, p. 217, 1963.
[108]. Martin, H., "Heat transfer between gas fluidized beds of solid particles and the surfaces of immersed heat exchanger elements *Part II," Chem. Eng. & Proc.: Proc. Intensification*, **18**, No. 4, p. 199-223, 1984.
[109]. Drake, E.R.G.E.a.R.M., "Analysis of Heat and Mass Transfer," McGraw-Hill, New York: 1972.
[110]. Miller, C.Y.W.a.E.N., "Heat transfer in solid-gas transport lines," *J. of Ind. and Eng. Chem.*, **53**, p. 51, 1961.
[111] Ma, Z., Glatzmaier, G., & Mehos, M., "Fluidized bed technology for concentrating solar power with thermal energy storage," *Journal of Solar Energy Engineering*, **136**, No. 3, 2014.
[112] Zhou, Z., Hou, Q. and Yu, A., "Particle scale simulation of heat transfer in fluid bed reactors," *INTECH Open Access Publisher*, Ch. 15, 2011.
[113] Loth, E., Tryggvason, Tsuji, Y., Elghobashi, S.E., Crowe, C.T., Berlemont, A., Reeks, M., Simonin, O., Frank, Th., Onishi, Y., van Wachem, B., "Multiphase Flow Handbook: Modeling", Ch. 13, Taylor & Francis, Boca Raton, FL, 2006.
[114] Anderson, T.B. and Jackson, R., "Fluid mechanical description of fluidized bed sequations of motion," *Ind. Eng. Chem. Fund.*, **6**, pp. 527-539, 1967.
[115] Ishii, M., "Thermo-fluid dynamic theory of two-phase flow," *Eyrolles*, Paris, FR, 1975.
[116] Gidaspow, D., "Multiphase Flow and Fluidization," Academic Press, San Diego, USA, 1994.
[117] Tsuji, Y., Tanaka, T. & Ishida, T., "Lagrangian numerical simulation of plug flow of cohesionless particles in a horizontal pipe,"*Powder Technol*., **71**, pp. 239-250, 1992.
[118] Xu, B.H. & Yu, A.B., "Numerical simulation of the gas-solid flow in a fluidized bed by combining discrete particle method with computational fluid dynamics," *Chem. Eng. Sci.*, **52**, 1997.
[119] Crocker, A. and Miller, F., "Fluid flow and radiation modeling of a cylindrical small particle solar receiver," *SolarPACES 2011*, Granada, Spain, 2011.

[120] Ho, C.K., "Sandia advanced concepts," Technical Report 505, Sandia National Laboratories, Washington D.C., 2010.
[121] Zhou, Z.Y., Yu, A.B. and Zulli, P., "Particle scale study of heat transfer in packed and bubbling fluidized beds," *AIChE J.*, **55**, pp.868-884, 2009.
[122] Zhou, Z.Y., Yu, A.B. and Zulli, P., "A new computational method for studying heat transfer in fluid bed reactors," *Powder Technol.*, **197**, pp. 102-110, 2010.
[123] Zhu, H.P., Zhou, Z.Y., Yang, R.Y. and Yu, A.B., "Discrete particle simulation of particulate systems: Theoretical developments," *Chem. Eng. Sci.*, **62**, 2007.
[124] Ergun, S., "Fluid flow through packed columns," *Chem. Eng. Prog.*, **48**, pp. 89-94, 1952.
[125] Di Felice, R., "The voidage function for fluid-particle interaction systems," *Int. J. Multiphase Flow*, **20**, pp. 153-159, 1994.
[126] Wakao, N. and Kaguei, S., "Heat and Mass Transfer in Packed Beds," Gordon and Breach Science Publishers, New York, USA, 1982.
[127] Kunii, D. and Levenspiel, O., "Fluidization Engineering," Butterworth-Heinemann, 978-0-409-90233-4, Boston, USA, 1991.
[128] Holman, J.P., "Heat Transfer," McGraw-Hill Company, New York, USA, 1981.
[129] Yagi, S. and Kunii, D., "Studies on effective thermal conductivities in packed beds," *AIChE J.*, **3**, pp. 373-381, 1957.
[130] Cheng, G.J., Yu, A.B. and Zulli, P., "Evaluation of effective thermal conductivity from the structure of a packed bed," *Chem. Eng. Sci.*, **54**, 1999.
[131] Sun, J. & Chen, M.M., "A theoretical analysis of heat transfer due to particle impact," *Int. J. Heat Mass Transfer*, **31**, pp. 969-975, 1998.
[132] Parmar, M.S. and Hayhurst, A.N., "The heat transfer coefficient for a freely moving sphere in a bubbling fluidized bed," *Chem. Eng. Sci.*, **57**, 2002.
[133] Collier, A.P., Hayhurst, A.N., Richardson, J.L. and Scott, S.A., "The heat transfer coefficient between a particle and a bed (packed or fluidised) of much larger particles," *Chem. Eng. Sci.*, **59**, 2004.
[134] Scott, S.A., Davidson, J.F., Dennis, J.S. and Hayhurst, A.N., "Heat transfer to a single sphere immersed in beds of particles supplied by gas at rates above and below minimum fluidization," *Ind. Eng. Chem. Res.*, **43**, pp. 5632-5644, 2004.
[135] Armijo, K. M., Ho, C., Anderson, R., Christian, J., Babiniec, S., and Ortega, J., "Magnetic field flow phenomena in a falling particle receiver," *SOLARPACES 2015*, **1734**, No. 1, AIP Publishing, 2006.
[136] E. Gedik, H. Kurt and Z. Recebli, "CFD simulation of magnetohydrodynamic flow of a liquid-metal Galinstan fluid in circular pipes," FDMP, **9**, pp. 23-33, 2013.
[137] Nakatsuka, K., Jeyadevan, B., Neveu S., and Koganezawa, H., "The magnetic fluid for heat transfer applications," *J. of Magnetism & Magnetic Mats.*, **252**, pp. 360-362, 2002.
[138] Jones, P.D., "Radiation and convection heat transfer in particle-laden fluid flow," Ph.D. Thesis, Rice University, 1991.
[139] Weinstein, L.A., Loomis, J., Bhatia, B., Bierman, D.M., Wang, E.N. and Chen, G., "Concentrating solar power," *Chem. Rev.*, **115**, pp. 12797-12838, 2015.
[140] Yong, S., Fu-Qiang, W., Xin-Lin, X., He-Ping, T., and Ying-Chun, L., "Radiative properties of a solar cavity receiver/reactor with quartz window," *International journal of hydrogen energy*, **36**, No. 19, pp. 12148-12158, 2011.

[141] Fleming, A., Ma, Z., Wendelin, T., Ban, H., and Folsom, C., "Thermal modeling of a multi-cavity array receiver performance for concentrating solar power generation," *ASME 2015 9th Int.l Conf. Energy Sus.*, ASME, 2015.
[142] Kim, H. N., Lee, H. J., Lee, S. N., Kim, J. K., Chai, K. K., Yoon, H. K., and Cho, H. S., "Experimental evaluation of the performance of solar receivers for compressed air," *J. of Mech. Sci. & Tech.*, **28** No. 11, pp. 4789-4795, 2014.
[143] Ahn, Y., Lee, J., and Lee, J. I., "Preliminary studies on the heat exchanger option for S-CO {sub 2} power conversion cycle coupled to water cooled SMR," American Nuclear Society, La Grange Park, IL, USA, 2012.
[144] Escandell, J., Wurm, D. J., Belleville, M. P., Sanchez, J., Harasek, M., and Paolucci-Jeanjean, D., "Enzymatic synthesis of butyl acetate in a packed bed reactor under liquid and supercritical conditions," *Catalysis Today*, **255**, pp. 3-9, 2015.
[145].Hesham G. Ibrahim, M.A.-M., Abubket A. Alshuiref, Abdulmajed R. Alagata and Mohamed A. Adali, "Radial heat transfer in packed-beds-II: Mathematical modeling of heat transfer through packed beds at elevated temperatures," *Int. J. of Eng. & App. Sci.*, **4**, No. 2, pp. 24-36, 2013.
[146]. Noorman, S., M. van Sint Annaland, and J.A.M. Kuipers, "Experimental validation of packed bed chemical-looping combustion," Chem. Eng. Sci., **65**, No. 1, pp. 92-97, 2010.
[147]. Louge, M., J.M. Yusof, and J.T. Jenkins, "Heat transfer in the pneumatic transport of massive particles," *Int. J. of Heat and Mass Transf*., 1993. **36**, No. 2, pp. 265-275, 1993.
[148]. A. Berlemont, O.S., M. Sommerfeld, "Validation of interparticle collision models based on large Eddy simulation," *ASME/FED Symp. Fluids Eng. Div. Gas Particle Flows*, **228**, pp. 359-369, 1995.
[149]. Ahmadi, G. and D. Ma, "A thermodynamical formulation for dispersed multiphase turbulent flows—1: Basic theory," Int. J. of Multiphase Flow, **16**, No. 2, pp. 323-340, 1990
[150]. Simonin, O., "Prediction of the dispersed phase turbulence in particle-laden jets," *ASME/FED Symp. Fluids Eng. Div., Gas Solid Flows*, **121**, pp. 197, 1991.
[151]. J. Lavieville, E.D. and O. Simonin, "Large Eddy simulation of interactions between colliding particles and a homogeneous isotropic turbulence field," *ASME/FED Symp. Fluids Eng. Div., Gas Solid Flow*s, No. 228, pp. 347, 1995.
[152]. Cao, J. and G. Ahmadi, "Gas-particle two-phase turbulent flow in a vertical duct," Int. J. of Multiphase Flow,**21**, No.6, pp. 1203-1228, 1995.
[153]. Cao, J. and G. Ahmadi, "Gas–particle two-phase turbulent flow in horizontal and inclined ducts," Int. J. of Eng. Sci., **38**, No.17, pp. 1961-1981, 2000.
[154]. Berlemont, A., P. Desjonqueres, and G. Gouesbet, "Particle lagrangian simulation in turbulent flows," Int. J. of Multiphase Flow, **16**, No.1, pp. 19-34, 1990
[155]. T. Tanaka, Y.T., "Numerical simulation of gas-solid two-phase flow in a vertical pipe: on the effect of inter-particle collision," ASME/FED Symp. Fluids Eng. Div., Gas Solid Flows, **121**, pp. 123, 1991.
[156]. Y. Yamamoto, M.P., T. Tanaka, T. Kajishima and Y. Tsuji, "Large-eddy simulation of turbulent gas-particle flow in a vertical channel: effect of considering inter-particle collisions," J. of Fluid Mech., **442**, pp. 303-334, 2001.
[157]. Zivkovic, M.S.a.G., "Recent advances in the numerical simulation of pneumatic conveying through pipe systems," *Comp. Methods and App. Sci*., Brussels, Belgium, pp. 201, 1992.
[158]. Oesterle, B. and A. Petitjean, "Simulation of particle-to-particle interactions in gas solid flows," Int. J. of Multiphase Flow, **19**, No. 1, pp. 199-211, 1993.

[159]. Sommerfeld, M., "The importance of inter-particle collisions in horizontal gas-solid channel flows," *ASME/FED Symp. Fluids Eng. Div., Gas Particle Flows*, **228**, pp. 335, 1995.
[160]. Lain, S., D. Bröder, and M. Sommerfeld, "Experimental and numerical studies of the hydrodynamics in a bubble column," Chem. Eng. Sci., **54**, No. 21, pp. 4913-4920, 1999.
[161]. Manohar, A.A.A.a.K., "Theoretical and experimental investigation of heat transfer in packed beds," Research J. of App. Sci., **4**, No. 5, pp. 166-177, 2009
[162]. Flamant, G., et al., "A New Heat Transfer Fluid for Concentrating Solar Systems: Particle Flow in Tubes," Energy Procedia, **49**, No. 0, pp. 617-626, 2014.
[163] Mansoori, Z., Saffar-Avval, M., Tabrizi, H. B., Dabir, B., & Ahmadi, G. "Inter-particle heat transfer in a riser of gas–solid turbulent flows," *Powder technology*, **159**, No. 1, pp. 35-45, 2005.
[164] Mansoori, Z., Saffar-Avval, M., Basirat-Tabrizi, H., Ahmadi, G., & Lain, S., "Thermo-mechanical modeling of turbulent heat transfer in gas–solid flows including particle collisions," *Int. J. of Heat & Fluid Flow*, **23**, No. 6, pp. 792-806, 2002.
[165] Mansoori, Z., Saffar-Avval, M., Tabrizi, H. B., and Ahmadi, G. "Experimental study of turbulent gas–solid heat transfer at different particles temperature," *Exp. Therm. & Fluid Sci*, **28**, No.6, pp. 655-665, 2004.
[166] Awad, M. M., and Muzychka, Y. S. "Two-phase flow modeling in microchannels and minichannels," *Heat Transfer Engineering*, **31**, No. 13, pp.1023-1033, 2010.
[167] Lim, K. S., Zhu, J. X., and Grace, J. R., "Hydrodynamics of gas-solid fluidization," *International journal of multiphase flow*, **21**, pp.141-193, 1995.
[168] Rosenweig, R. E., "Fluidization: hydrodynamic stabilization with a magnetic field," *Science*, **204**, pp. 57-60, 1979.
[169] Kreith, F., Boehm, R.F., et al., "Heat and mass transfer," Ch. 4, *Mechanical Engineering Handbo*ok, Ed. Frank Kreith, Boca Raton, FL, USA, CRC Press LLC, 1999.
[170] Grace, J. R., "Contacting modes and behavior classification of gas-solid and other two-phase suspensions," *Can. J. Chem. Eng.* **64**, pp. 353-363, 1986.
[171] Wen, C.Y. and Yu, Y.H., "A generalized method for predicting the minimum fluidization velocity," *J. AIChE*, **12**, No. 2, pp. 610–612, 1966.
[172] Biyikli, K., Tuzla, K., and Chen, J.C., "Heat transfer around a horizontal tube in freeboard region of fluidized beds," *J. AIChE*, **29**, No. 5, 712–716, 1983.
[173] Wen, C.Y. and MIller, E.N., "Heat transfer in solid-gas transport lines," *Ind. Eng. Chem.*, **53**, pp. 51–53, 1961.
[174] Lucas, A., Arnaldos, J., Casal, J. and Puigjaner, L., "Improved equation for the calculation of minimum fluidization," *Ind. Eng. Chem. Proc. Des. Dev.*, **25**, pp. 426-429, 1986.
[175] Adanez, J. & Abanades, J. C., "Minimum fluidization velocities of fluidized-bed coalcombustion solids," *Powder Technol.* **67**, pp. 113-119, 1991.
[176] Chirone, R., Massimilla, L. and Russo, S., "Bubbling fluidization of a cohesive powder in an acoustic field," *Fluidization VII*, pp. 545-553. Engineering Foundation, New York, USA, 1992.
[177] Chirone, R., Massimilla, L. & Russo, S., "Bubble-free fluidization of a cohesive powder in an acoustic field," *Chem. Eng. Sci.* **48**, pp. 41-52, 1993.
[178] Penchev, I. P. and Hristov, J. Y., "Behaviour of fluidized beds of ferromagnetic particles in an axial magnetic field," *Powder Technol.* **61**, pp. 103-118, 1990.
[179] Bienert, W.B., Rind, H., Wolf, A.A., "Conceptual design of an open cycle air Brayton Solar Receiver: Phase 1 final report," DTM-79, contract no. 955135 for California Institute of

Technology Jet Propulsion Laboratory, Dynatherm Corporation, Cockeysville, MD, USA, 1979.
[180] Heller, P., "Solar-hybrid power and cogeneration plants" SOLHYCO, Project No. 019830, 2011.
[181] Heller, P., Pfander, M., Denk, T., Tellez, F., Valverde, A., Fernandez J, et al., "Test and evaluation of a solar powered gas turbine system," *Solar Energy*, **80**, No. 10, pp.1225–1230, 2006.
[182] Amsbeck, L., Buck, R., Heller, P., Jedamski J, and Uhlig R., "Development of a tube receiver for a solar-hybrid microturbine system," *SolarPACES 2008*, Las Vegas, NV, USA, 2008
[183] Amsbeck, L., Denk, T., Ebert, M., Gertig C, Heller P, Herrmann P, et al., "Test of a solar-hybrid microturbine system and evaluation of storage deployment," *SolarPACES 2010*, Perpignan, France, 2010.
[184] Uhlig, R., "Transient stresses at metallic solar tube receivers," *SolarPACES 2011*, Granada, Spain, 2011
[185] Kolb, G.J., "An evaluation of possible next-generation high-temperature molten-salt power towers," Sandia National Laboratories, *SAND2011-9320*, Albuquerque, NM, USA 2011.
[186] Becker, M., and Boehmer, M., "GAST: The Gas Cooled Solar Tower Technology Program," *Springer*, Berlin, Germany, 1989.
[187] Romero-Alvarez, M., & Zarza, E., "Concentrating solar thermal power," *Handbook of energy efficiency and renewable energy*, Ch. 21, 2007.
[188] Hennecke K, Schwarzbozi P, Alexopoulos S, Gottsche J, Hoffschmidt B, Beuter M, et al., "Solar power tower Julich: the first test and demonstration plant for open volumetric receiver technology in Germany," *SolarPACES 2008*, Las Vegas, NV, 2008.
[189] Avila-Marin, A.L., "Volumetric receivers in solar thermal power plants with central receiver system technology: a review," *Solar Energy*, **85**, No. 5, pp. 891-910, 2011.
[190] Zunft S., Hanel M., Kruger M, Dreissigacker V., Gohring F., and Wahl E. Julich, "Solar power tower-experimental evaluation of the storage subsystem and performance calculation," *J. of Sol. Energy Eng.-Trans. ASME*, **133**, No. 3, 2011.
[191] Menigault T., Flamant G., and Rivoire B., "Advanced high-temperature 2-slab selective volumetric receiver," *Solar Energy Materials*, **24**, pp.192–203, 1991.
[192] Pitzpaal R., Morhenne J. and Fiebig M.A., "New concept of a selective solar receiver for high-temperature applications," *Solar Energy Materials*, **24**, pp. 293–306, 1991.
[193] Kribus, A., Ries, H. and Spirkl, W., "Inherent limitations of volumetric solar receivers," *J. of Sol. Energy Eng.-Trans. ASME*, **118** No. 3, 1996.
[194] Karni, J., Kribus, A., Rubin, R. and Doron, P., "The porcupine: a novel high-flux absorber for volumetric solar receivers," *J. of Solar Energy Eng.-Trans. ASME*, **120**, No. 2, 1998.
[195] Modi, A., Knudsen, T., Haglind, F., and Clausen, L. R., "Feasibility of using ammonia-water mixture in high temperature concentrated solar power plants with direct vapour generation," *Energy Procedia*, **57**, pp. 391-400, 2014.
[196] Becker, M., "Comparison of heat transfer fluids for use in solar thermal power stations," *Electric Power Systems Research*, **3**, pp. 139-150, 1980.
[197] Heller, L., "Literature review on heat transfer fluids and thermal energy storage systems in CSP plants," *STERG Report*, 2013.
[198] Invernizzi, C.M., "The thermodynamic properties of working fluids," Ch. 2, *Lecture Notes in Energy 11*, Springer-Verlag, London Ltd., 2013.

[199] Pitzer, K.S., Lippmann, D.Z., Curl, R.F., Huggins, C.M., and Petersen, D.E., "The volumetric and thermodynamic properties of fluids. II. Compressibility factor, vapour pressure and entropy of vaporization," *J. Am. Chem. Soc.*, **77**, No. 13, pp. 3433–3440, 1955.
[200] NREL, "Concentrating solar power projects,", 2015, http://www:nrel :gov/ csp/ solarpaces/ by technology:cfm.
[201] Dow Chemical Company, "`Synthetic Organic Heat Transfer Fluid Liquid and Vapor Phase Data," 2015, http://www:dow:com/ webapps/ lit/ litorder:asp? _lepath=heattrans/ pdfs/noreg/ 176-01463 :pdf&pdf=true.
[202] Pacheco, J.E., Moursund, C., Rogers, D., Wasyluk, D., "Conceptual design of a 100MWe modular molten salt power tower plant," *SolarPACES2011*, Granada, Spain, 2011.
[203] Dunham, M. T., and Iverson, B. D., "High-efficiency thermodynamic power cycles for concentrated solar power systems," *Renewable and Sustainable Energy Reviews*, **30**, pp. 758-770, 2014.
[204] Pacheco, J. E., Reilly, H. E. and Gregory, J., "Summary of the solar two test and evaluation program, Technical report, Sandia National Laboratories, SAND2000-0372C, 2000.
[205] Yang, Z. and Garimella, S. V., "Molten-salt thermal energy storage in thermoclines under different environmental boundary conditions," *Applied Energy*, **87**, No. 11, pp. 3322-3329, 2010.
[206] Garbrecht, O., Al-sibai, F., Kneer, R. and Wieghardt, K., "Numerical Investigation of a new molten salt central receiver design," *SolarPACES 2012*, Marrakech, Morocco, 2012.
[207] Pacheco, J. E. and Dunkin, S. R., "Assessment of Molten-Salt Solar Central- Receiver Freeze-Up and Recovery Events," Technical report SAND96-0331C, Sandia National Laboratories, Albuquerque, USA, 1996.
[208] Kelly, B., "Advanced Thermal Storage for Central Receivers with Supercritical Coolants," Technical report DE-FG36-08GO18149, Abengoa Solar, Lakewood, Colorado, 2010.
[209] Raade, J. W. and Padowitz, D., "Development of Molten Salt Heat Transfer Fluid with Low Melting Point and High Thermal Stability," *J. of Solar Energy Eng*. **133**, No. 3, pp. 31013-31016, 2011.
[210] Das, A. K., Clark, M. M., Teigen, B. C., Fiveland, W. A., and Anderson, M. H., "Heat transfer behavior of molten nitrate salt," *SOLARPACES 2015*, **1734**, No. 1, 2016.
[211] J.W. Cooke and B. Cox, "Forced-Convection Heat-Transfer Measurements with a Molten Fluoride Salt Mixture Flowing in a Smooth Tube," Oak Ridge National Lab, 1973.
[212] Silverman, M.D., Huntley, W.R. and Robertson, H.E., "Heat transfer measurements in forced convection loop with two molten-fluoride salts: LiF-BeF2-ThF4-UF4 and eutectic NaBF4-NaF," Oak Ridge National Lab, 1976.
[213] Hoffman, H.W., "Turbulent forced convection heat transfer in circular tubes containing molten sodium hydroxide," Oak Ridge National Lab, 1952.
[214] Grele, M.D., Gedeon, L., "Forced-convection heat-transfer characteristics of molten sodium hydroxide," NACA, 1953.
[215] Hoffman, H.W., Cohen, S.I., "Fused Salt Heat Transfer - Part III: Forced-Convection Heat Transfer in Circular Tubes Containing the Salt Mixture NaNO2-NaNO3-KNO3," Oak Ridge National Lab, 1960.
[216] W. Yu-ting, L. Bin, M. Chong-fang, G. Hang, "Convective heat transfer in the laminar-turbulent transition region with molten salt in a circular tube," *Exp. Therm. Fluid Sci.*, **33**, pp. 1128–1132, 2009.

[217] Gnielinski, V., "New equations for heat and mass-transfer in turbulent pipe and channel flow," *Int. chem. Eng.*, **16**, No. 2, pp. 359-368, 1976.
[218] Andraka, C.E., Rawlinson, K.S., Moss, T.A., Adkins, D.R., Moreno, J.B. and Gallup, D.R., "Solar Heat Pipe Testing of the Stirling Thermal Motors 4-120 Stirling Engine," *IECEC 96*, **1292**, pp. 1295-1300, 1996.
[219] Andraka, C.E., Rawlingson, K.S. and Siegel, N.P., "Technical feasibility of storage on large dish Stirling systems," *Sandia Report SAND2012-8352*, Sandia National Laboratories, Albuquerque, NM, USA, 2012.
[220] Angelino, G., and Invernizzi, C., "Binary conversion cycles for concentrating solar power technology," *Solar Energy*, **82**, No. 7, pp.637-647, 2008.
[221] Goswami, D.Y., Kreith, F., Kreider, J.F., "Principles of solar engineering," 2nd Ed., Taylor & Francis, Philadelphia, PA, USA, 1999.
[222] Boerema, N., Morrison, G., Taylor, R. and Rosengarten, G.,"Liquid sodium versus Hitec as a heat transfer fluid in solar thermal central receiver systems," *Solar Energy*, 86, No. 9, pp. 2293-2305, 2012.
[223] Lata, J. M., Rodriguez, M. and de Lara, M. A., "High Flux Central Receivers of Molten Salts for the New Generation of Commercial Stand-Alone Solar Power Plants," *J. of Solar Energy Eng*. **130**, No. 2, 2008.
[224] Coventry, J., Pye, J., Andraka, C.E., Blanco, M. and Fisher, J., "Sodium receivers for solar power towers: a review," *Energy Procedia*, **00**, 2015.
[225] J.P. Kotze, T.W. von Backstrom and P.J. Erens, "NaK as a Primary Heat Transfer Fluid in Thermal Solar Power Installation," SASEC 2012, South Africa, 2012.
[226] Armijo, K. M., and Andraka, C. E. "Phenomenological studies on sodium for CSP applications: A safety review," *SOLARPACES 2015*, **1734**, No. 1, 2016.
[227] Morozov, Yu.D., Prisniakov, V.F., Privalov, A.N., Trofimenko, A.V., Gabrinets, V.A., Gontarev, Yu.K., "Solar dynamic Rankine space power plant using vapour–liquid metallic techniques," *Space Technology*, **16**, No. 4, pp. 169–176, 1996.
[228] Fraas, A.P., "A potassium-steam binary vapor cycle for better fuel economy and reduced thermal pollution," *Trans. ASME J. of Energy & Power*, pp. 53–63, 1973.
[229] Foust, O. J., "Sodium-NaK Engineering Handbook," *Gordon and Breach, Science Publishers Inc*., New York, USA, 1972.
[230] Diver, R. B., Adkins, D. R. and Moss, T. A., "Trends in Dish-Stirling Solar Receiver Designs," *Energy Conv. Eng. Conf*., pp. 303-310, 1990.
[231] Chopra, O.K., Smith, D.L., Tortorelli, P.F., DeVan, J.H., and Kai Sze, D., "Liquid–metal corrosion," *Fusion Technology*, **8**, pp. 1956–1969, 1985.
[232] Song, J.S., Louis, J.F. and Wendte, J.C., "Liquid lithium thermal energy storage for solar dynamic power systems," *Proc. of 23rd Intersociety Energy Conv. Eng. Conf.*, Denver, CO, USA, **2**, pp. 187–193, 1988.
[233] Davis, J.P. and Kikin, G.M., "Lithium-boiling potassium Rankine cycle test operating experience," *Adv. in Energy Conv. Eng., Intersoc. Energy Conv. Eng. Conf.*, Miami Beach, Florida, USA, pp. 87–95, 1967.
[234] International Energy Agency, "Central Receiver System (CRS)," Small Solar Power Systems Project (SSPS), **1**, Springer, USA, 1986.
[235] International Energy Agency, "Book of Summaries," **4**, Springer, USA 1986.

[236] D.R. Adkins, C.E. Andraka, J.B Moreno, K.S. Rawlinson, S.K. Showalter and T.A Moss, "Heat pipe solar receiver development activities at Sandia National Laboratories," Renewable and Advanced Energy Conference for the 21st Century, Maui, Hi, 1999.
[237] Olivier, T.J., Radel, R.F., Nowlen, S.P., Blanchat, T.K. and Hewson, J.D., "Metal fire implications for advanced reactors, Part 1: Literature review," Sandia Report, SAND2007-6332, Sandia National Laboratories, Albuquerque, NM, USA, 2007.
[238] Griffin, C.W. and Piccot, A.R., "Sodium-NaK Engineering handbook – Sodium Flow, Heat Transfer, Intermediate Heat Exchangers, and Steam Generators," Ch. 2, **3**, Gordon and Breach Inc., New York, 1976.
[239] Wegrzyn, J. and Jhaw, D.T., "Experimental investigation of aerosol behavior in Post LMFBR accident reactor containment atmosphere," NUREG/CR-0799.R7-38.45, U.S. Nuclear Regulatory Commission, 1979.
[240] Baqué, F. and Beauchamp, F., "Sodium – Water reaction in steam generators," ESFR SP5, 2009.
[241] Schulenberg, T., Cheng, X., and Stieglitz, R., "Thermal-hydraulics of Lead-Bismuth for Accelerator Driven Systems," *NURETH11*, Avignon, France, 2005.
[242] Fazio, C., Sobolev, V. P., Aerts, A., Gavrilov, S., Lambrinou, K., Schuurmans, P. and Gosse, S. "Handbook on Lead-bismuth Eutectic Alloy and Lead Properties, Materials Compatibility, Thermal-hydraulics and Technologies-2015 Edition" No. NEA--7268, 2015.
[243] Kim, J. S., Dawson, A., Wilson, R., Venkatesan, K., and Stein, W., "High-Temperature Heat Transport and Storage Using LBE Alloy for Concentrated Solar Power System," *ASME 2015 9th Int. Conf. on Energy Sus.*, 2015.
[244] Pacio, J. and Wetzel, T., "Assessment of liquid metal technology status and research paths for their use as efficient heat transfer fluids in solar central receiver systems," *Solar Energy*, **93**, pp. 11-22, 2013.
[245] Hennecke, K., Schwarzbözl, P., Hoffschmidt, B., Göttsche, J., Koll, G. and Beuter, M., "The Solar Power Tower Jülich: A solar thermal power plant for test and demonstration of air receiver technology," *Proc. of ISES World Congress*, 2009.
[246] Koll, G., Sahraoui, T., Höschmidt, B., Khedim, A., Pomp, S., Schwarzbözl, P. and Dillig, M., "ALSOL Solar Thermal Tower Power Plant Algeria," SolarPACES 2011, Ganada, Spain 2011.
[247] Wilson Solarpower, "Wilson's concentrated solar power (CSP) system targets 5-6 cents/kilowatt-hour," 2015, http://wilsonsolarpower.com/
[248] Frutschi, H.U., "Closed-cycle Gas Turbines," Operating Experience and Future Potential," ASME Press, New York, USA, pp. 200–228, 2005.
[249] Tsiklauri, G.,Talbert, R., Schmitt, S., Filippov, G., Bogoyavlensky, R., Grishanin, E, *et* al., "Supercritical steam cycle for nuclear power plant," *Nucl. Eng. Des.*, **235**, 2005.
[250] Forsberg, C.W., Peterson P.F. and Zhao, H. "High-temperature liquid-fluoride-salt closed-Brayton-cycle solar power towers," *J. Sol. Energy Eng.*, **129**, 2007.
[251] Fleming, D., Kruizenga, A., Pasch, J., Conboy, T., and Carlson, M., "Corrosion and Erosion Behavior in Supercritical CO2 Power Cycles," *ASME Turbo Expo 2014: Turbine Technical Conference and Exposition*, 2014.
[252] Boss, M., Gadoury, T., Feeny, S. and Montgomery, M., "Recent Advances in Ultra Super Critical Steam Turbine Technology," *Technical report*, 2007.
[253] Weitzel, P. S., "Steam Generator for Advanced Ultra-Supercritical Power Plants 700 to 760C," *ASME 2011 Power Conference*, Denver, CO, USA, 2011.

[254] Coventry, J. and Pye, J., "Coupling Supercritical and Superheated Direct Steam Generation with Thermal Energy Storage," *Technical report*, Wizard Power, 2010.
[255] Ahn, Y., Bae, S. J., Kim, M., Cho, S. K., Baik, S., Lee, J. I., and Cha, J. E., "Review of supercritical CO2 power cycle technology and current status of research and development," *Nuclear Engineering and Technology*, **47**, No. 6, pp. 647-661, 2015.
[256] Persichilli, M., Kacludis, A., Zdankiewicz, E., and Held, T., "Supercritical CO2 Power Cycle Developments and Commercialization: Why sCO2 can Displace Steam Ste," *Power-Gen India & Central Asia*, 2012.
[257] Wright, S. A., Conboy, T. M., Parma, E. J., Tom G. Lewis, Gary A. Rochau and Ahti J. Suo-Anttila, "Summary of the Sandia Supercritical CO2 Development Program," *SCO2 Power Cycle Symposium*, Boulder, CO, 2011.
[258] Turchi, C. S., "Supercritical CO2 for Application in Concentrating Solar Power Systems," *Proc. of SCO2 Power Cycle Symp.*, Troy, NY, USA, 2009.
[259] Gary, J., Turchi, C. and Siegel, N., "CSP and the DOE SunShot Initiative," *SolarPACES 2011*, **1**, Granada, Spain, 2011.
[260] Chapman, D. J. and Arias, D. A., "An Assessment of the Supercritical Carbon Dioxide Cycle for Use in a Solar Parabolic Trough Power Plant," *Proc. of SCO2 Power Cycle Symp.*, Troy, NY, USA, 2009.
[261] Ma, Z. and Turchi, C. S., "Advanced Supercritical Carbon Dioxide Power Cycle Configurations for Use in Concentrating Solar Power Systems," *Supercritical CO2 Power Cycle Symp.*, Boulder, CO, 2011.
[262] Cox, T. L., "Preliminary Results of Heat Transfer Experiments with Supercritical Carbon Dioxide in the Small System Test Loop," *Proc. of SCO2 Power Cycle Symp.*, Troy, NY, 2009.
[263] Rouillard, F., Charton, F. and Moine, G., "Corrosion behaviour of different metallic materials in supercritical CO2 at 550 C and 250 bars," *Proc. of SCO2 Power Cycle Symp.*, Troy, NY, 2009.
[264] Dostal, V., Driscoll, M. J. and Hejzlar, P., "A Supercritical Carbon Dioxide Cycle for Next Generation Nuclear Reactors," Technical report, Massachusetts Institute of Technology, Cambridge, MA., 2004.
[265] Spiers, D.J., and Rasinkoski, A.D., "Predicting the service lifetime of lead/acid batteries in photovoltaic systems," *J. of Power Sources*, **53**, No. 2, pp. 245–253, 1995.
[266] Li, P. W., Chan, C. L., Stephens, J., James. E. O'Brien, Van Lew, J., and Karaki, W., "Transient heat transfer and energy transport in packed bed thermal storage systems," *INTECH Open Access Publisher*, 2011.
[267] Herrmann, U. and Kearney D.W., "Survey of thermal energy storage for parabolic trough power plants," *J. of Sol. Energy Eng.*, **124**, No. 2, pp. 145–152, 2002.
[268] Kuravi, S., Trahan, J., Goswami, D. Y., Rahman, M. M., & Stefanakos, E. K., "Thermal energy storage technologies and systems for concentrating solar power plants," *Prog. in Energy & Comb. Sci.*, **39**, No. 4, pp. 285-319, 2013.
[269] Sioshansi, R. and Denholm, P., "The value of concentrating solar power and thermal energy storage," *NREL-TP-6A2-45833*, NREL, Golden, CO, USA, 2010.
[270] Reilly, H.E. and Kolb, W.J., "Evaluation of molten salt power tower technology based on the experience of solar two," *SAND2001-3674*, Sandia National Laboratories, Albuquerque, NM, USA, 2001.
[272] Jorgenson, J., Denholm, P., and Mehos, M., "Quantifying the Value of Concentrating Solar Power in a Production Cost Model," *ASME 2014 8th Int. Conf. on Energy Sus.*, 2014.

[272] Sioshansi, R., and Denholm, P., "The value of concentrating solar power and thermal energy storage," *IEEE Transactions on Sustainable Energy*, **1**, No. 3, pp. 173-183, 2010.
[273] CPUC, "2015 Filing Guide for System, Local and Flexible Resource Adequacy (RA) Compliance Filings," Issued: September 9, 2014, 2014.
[274] Mehos, M., Turchi, C., Jorgenson, J., Denholm, P., Ho, C., and Armijo, K., "On the Path to SunShot: Advancing Concentrating Solar Power Technology, Performance, and Dispatchability," *No. NREL/TP-5500-65688; SAND2016-2237*, NREL, Golden, CO, USA, 2016.
[275] Miller, N.W., M. Shao, S., Pajic, and R. D'Aquila, "Western Wind and Solar Integration study phase 3-Frequency Response and Transient Stability," *Technical Report NREL/SR-5D00-62906*, 2014.
[276] Madaeni, S. H., Sioshansi, R., and Denholm, P., "Capacity value of concentrating solar power plants," *Contract*, **303**, pp. 275-3000, 2011.
[277] Mills, A., and R. Wiser, "An Evaluation of Solar Valuation Methods Used in Utility Planning and Procurement Processes," *Environmental Energy Technologies Division*, LBNL, LBNL-5933E, 2012.
[278] Michels, H., and Pitz-Paal, R., "Cascaded latent heat storage for parabolic trough solar power plants," *Solar Energy*, **81**, No. 6, pp. 829-837, 2007.
[279] Ma, Z., Glatzmaier, G. C., Wagner, M., and Neises, T., "General Performance Metrics and Applications to Evaluate Various Thermal Energy Storage Technologies," *ASME 2012 6th Int. Conf. on Energy Sus.*, pp. 345-351, 2012.
[280] Zhao, C.Y., Wu, C.G., "Thermal property characterization of a low melting-temperature ternary nitrate salt mixture for thermal energy storage systems," *Sol. Energy Mater. Sol. Cells*, **95**, pp. 3341–3346, 2011.
[281] Herrmann U. and Kearney D.W., "Survey of thermal energy storage for parabolic trough power plants," *Solar Energy Engineering*, **124**, pp. 145-152, 2002.
[282] Baumann, T., and Zunft, S., "Properties of granular materials as heat transfer and storage medium in CSP application," *Solar Energy Materials and Solar Cells*, **143**, 38-47, 2015.
[283] Seyf, H. R., and Henry, A., "Thermophotovoltaics: a potential pathway to high efficiency concentrated solar power," *Energy & Env. Sci.*, **9**, No. 8, pp. 2654-2665, 2016.
[284] H Abedin, A., and A Rosen, M., "A critical review of thermochemical energy storage systems," *The Open Renewable Energy Journal*, **4**, No. 1, 2011.
[285] Lacy, D.E., Coles-Hamilton, C. and Juhasz, A., "Selection of high temperature thermal energy storage materials for advanced solar dynamic space power systems," *NASA Technical Memorandum 89886, 22nd Int. Energy Conv. Eng. Conf.*, Philadelphia, PA, USA, 1987.
[286] Wallin, W.E. and Dustin, M.O., "Advanced space solar dynamic power systems beyond IOC space station," Energy New Frontiers, 22nd Intersoc. *Energy Conv. Eng. Conf.*, **1**, Philadelphia, PA, USA, pp. 145–155, 1987.
[287] Kesseli, J.B. and Lacy, D.E., "Advanced solar receiver conceptual design study," Energy New Frontiers, 22nd Intersoc. *Energy Conv. Eng. Conf.*, Philadelphia, PA, USA, **1**, pp. 162–168, 1987.
[288] Misra, A.K. and Whittenberg, J.D., "Fluoride salts and container materials for thermal energy storage applications in the temperature range 973–1400 K," Energy New Frontiers, 22nd Intersoc. *Energy Conv. Eng. Conf.*, Philadelphia, PA, USA, **1**, pp. 188–201, 1987.

[289] Shabgard, H., Bergman, T. L., and Faghri, A., "Exergy analysis of latent heat thermal energy storage for solar power generation accounting for constraints imposed by long-term operation and the solar day," *Energy*, **60**, pp. 474-484, 2013.
[290] Regin, A. F., Solanki, S. C., and Saini, J. S., "Heat transfer characteristics of thermal energy storage system using PCM capsules: a review," *Renewable and Sustainable Energy Reviews*, **12**, No. 9, pp. 2438-2458, 2008.
[291] Nithyanandam, K., and Pitchumani, R., "Cost and performance analysis of concentrating solar power systems with integrated latent thermal energy storage. *Energy*," **64**, pp. 793-810, 2014.
[292] Andraka, C. E., Kruizenga, A. M., Hernandez-Sanchez, B. A., and Coker, E. N., "Metallic phase change material thermal storage for dish Stirling," *Energy Procedia*, **69**, pp. 726-736, 2015.
[293] Petrone, G., Spagnuolo, G., Teodorescu, R., Veerachary, M., and Vitelli, M., "Reliability issues in photovoltaic power processing systems," *IEEE Transactions on Industrial Electronics*, **55**, No. 7, pp. 2569-2580, 2008.
[294] Weber, R. and Dorer, V. "Long-term heat storage with NaOH," *Vacuum*, **82**, No. 7, pp. 708-716, 2008.
[295] Mouromtseff, I.E., "Water and forced-air cooling of vacuum tubes nonelectronic problems in electronic tubes," *Proc. IRE*, **40**, No. 4 pp. 190-205, 1942.
[296] Bonilla, C., Baumeister, T. and Dunning, J.R., "Nuclear Engineering," McGraw-Hill, New York, USA, 1975.
[297] Lenert, A., Nam, Y. and Wang, E.N., "Heat transfer fluids," *Annu. Rev. Heat Transfer*, **15**, pp. 93-129, 2012.
[298] Bales, C., Setterwall, F. and Bolin G., "Development of the thermo-chemical accumulator (TCA)," *Proc. of Eurosun*, Freiburg, Germany, 2004.
[299] Mauran, S., Lahmidi, H. and Goetz, V. "Solar heating and cooling by a thermochemical process: first experiments of a prototype storing 60 kWh by a solid/gas reaction," *Solar Energy*, **82**, No. 7, pp. 623-636, 2008.
[300] Zondag, H., van Essen, M., He, Z., Schuitema, R. and van Heldan, W., "Characterization of MgSO4for Thermochemical Storage," *2nd Int. Ren. Energy Storage Conf. (IRES II)*, Bonn, Germany, 2007.
[301] Azpiazu, M.N., Morquillas, J.M. and Vazquez, A. "Heat recovery from a thermal energy storage based on the Ca(OH)2/CaO cycle," *Appl. Therm. Eng*., **23**, No. 6, pp. 733-741, 2003.
[302] Lovergrove, K., Luzzi, A. and Kreetz, H. "A solar-driven ammonia-based thermochemical energy storage system," *Solar Energy*, **67**, No. 4, pp. 309-316, 1999.
[303] Kreetz, H. and Lovergrove, K. "Theoretical analysis and experimental results of a 1 kW_{chem} ammonia synthesis reactor for a solar thermo-chemical energy storage system," *Solar Energy*, **67**, No. 4, pp. 287-296, 1999.
[304] Winter, C. J., Sizmann, R. L., and Vant-Hull, L. L., "Solar Power Plants", Springer, Berlin, Germany, pp. 21–27. 1991.
[305] Kodama, T. "High-temperature solar chemistry for converting solar heat to chemical fuels," *Prog. in Energy and Comb. Sci.*, **29**, pp. 567–597, 2003.
[306] Seinfeld, A., "Solar thermochemical production of hydrogen-a review," *Solar Energy*, **78**, pp. 603–615, 2005.
[307] Finch, N.S. and Ho, C.K., "Stochastic modeling of power tower sand evaluation of technical improvement opportunities," *SolarPACES 2011*. Granada, Spain, 2011.

[308] Bolland O., "A comparative evaluation of advanced combined cycle alternatives," Proc. of Int. Gas Turbine & Aeroengine Congress & Exhibition, Brussels, Belgium, 1990.
[309] Mittelman, G., Epstein, M., "A novel power block for CSP systems," *SolEnergy*, **84**, pp. 1761–71, 2010.
[310] Spelling, J., Favrat, D., Martin, A., Augsburger, G., "Thermoeconomic optimization of a combined-cycle solar tower power plant," *Energy*, **41** pp.113–120, 2012.
[311] Glatzmaier, G., "Summary Report for Concentrating Solar Power Thermal Storage Workshop: New Concepts and Materials for Thermal Energy Storage and Heat-Transfer Fluids," NREL/TP-5500-52134, NREL, Golden, CO., 2011.
[312] Haywood, R.W., "Analysis of engineering cycles," 3rd Ed., New York, USA, Pergamon Press, 1991.
[313] Kehlhofer, R., Bachmann, R., Nielson, H., Warner, J., "Combined-cycle gas and steam turbine power plants," 2nd Ed., Tulsa, OK, USA, Pennwell Publishing; 1999.
[314] McGovern, R.K., Smith, W.J., "Optimal concentration and temperatures of solar thermal powerplants," *Energy Conver. Manag*., **60** pp. 226–232, 2012.
[315] Omer, L. M., and Mustafa, N. M., "Performance Of Laboratory Small Scale Power Plant Based On Rankine Cycle For Rural Area Power Generation," Ph.D. Dissertation, University of Khartoum, 2015.
[316] Kribus, A., Zaibel, R., Carey, D., Segal, A., and Karni, J., "A solar-driven combined cycle power plant," *Solar energy*, **62**, No. 2, pp. 121-129, 1998.
[317] Barigozzi, G., Bonetti, G., Franchini, G., Perdichizzi, A., Ravelli, S., "Thermal performance prediction of a solar hybrid gas turbine," *SolEnergy*, **86**, pp. 2116–2127, 2012.
[318] Price, H., Lupfert, E., Kearney, D., Zarza, E., Cohen, G., Gee, R., *et* al., "Advances in parabolic trough solar power technology," *SolEnergy Eng*., **124**, pp. 109–125, 2002.
[319] Zarza, E., Rojas, M.E., Gonzalez, L., Caballero, J.M., Rueda, F., "INDITEP: The first pre-commercial DSG solar power plant," *SolEnergy*, **80**, pp. 1270–1276, 2006.
[320] Wheeldon, J.M., "Engineering and economic evaluation of 1300°F series ultra- supercritical pulverized coal power plants: phase 1," No. 1015699. PaloAlto, CA, USA, Electric Power Research Institute, 2008.
[321] Chen, H., Goswami, D.Y., Stefanakos, E.K., "A review of thermodynamic cycles and working fluids for the conversion of low-grade heat," *Renew. Sustain. Energy*, **14** pp. 3059–3067, 2010.
[322] Fernández, F.J., Prieto, M.M., Suárez, I., "Thermodynamic analysis of high-temperature generative organic Rankine cycles using siloxanes as working fluids," *Energy*, **36**, pp. 5239-5249, 2011.
[323] Yeo, W.H., Fry, A.T., Purbolaksono, J., Ramesh, S., Inayat-Hussain, J.I., Liew, H.L., and Hamdi, M., "Oxide scale growth and presumed exfoliation in a 700° C or higher steam condition: A simulation study for future operations of ultra-supercritical power plants,"*The J. of Supercritical Fluids*, **92**, pp. 215-222, 2014.
[324] Ries, H., Kribus, A., Karni, J., "Non-isothermal receivers," *J. SolEnergy Eng.*, **117**, pp. pp. 259–261, 1995.
[325]Thermonet, "Brayton Cycle Irreversibilities," Wiley, 2001, http://www.wiley.com/college/moran/CL_0471465704_S/user/tutorials/tutorial9/tut9m_content.html

[326] Greitzer, E.M., Spakovszky, Z.S. and Waitz, I.A., "Unified: Thermodynamics and propulsion," Ch. 16 Lecture Notes, MIT, Accessed: Aug. 2016: http://web.mit.edu/16.unified/www/FALL/thermodynamics/notes/notes.html
[327] Paul, S., Shepherd, R., & Woollin, P. (2012). Selection of materials for high pressure CO2 transport. *TWI*. 2012, http://www.twi.com.uk.
[328] Ahn, Y., Bae, S. J., Kim, M., Cho, S. K., Baik, S., Lee, J. I., and Cha, J. E., "Review of supercritical CO2 power cycle technology and current status of research and development," *Nuclear Engineering and Technology*, **47**, No. 6, 647-661, 2015.
[329] Hill, P. G., and Peterson, C. R., "Mechanics and thermodynamics of propulsion," *Addison-Wesley Publishing Co.*, **764**, 1992.
[330] J. C. *Bryant*, H. Saari, and K. Zanganeh, "An Analysis and Comparison of the Simple and Recompression Supercritical CO2 Cycles," *Supercritical CO2 Power Cycle Symposium*, 2011.
[331] Chen, Y., "Novel cycles using carbon dioxide as working fluid," Licentiate Thesis, Universitetsservice US AB, Stockholm, Sweden, 2006
[332] Goswami, D.Y., "Thermodynamic cycles for CSP," Clean Energy Center Presentation, Univ. of South Florida, 2015.
[333] Dostal, V., Driscoll, M.J. and Hejzlar, P., "A Supercritical Carbon Dioxide Cycle for Next Generation Nuclear Reactors," MITANP-TR-100, MIT, Cambridge (MA), 2004. Available from: http://hdl.handle.net/1721.1/17746.
[334] Moisseytsev, A. and Sienicki, J.J., "Investigation of alternative layouts for the supercritical carbon dioxide Brayton cycle for a sodium-cooled fast reactor," *Nucl. Eng. Des.*, **239**, pp. 1362–1371, 2009.
[335] Iverson, B.D., Conboy, T.M., Pasch, J.J. and Kruizenga, A.M., "Supercritical CO2 Brayton cycles for solar-thermal energy," *Appl. Energy*, **111**, pp. 957–970, 2013.
[336] Garg, P., Kumar, P. and Srinivasan, K., "Supercritical carbon dioxide Brayton cycle for concentrated solar power," *J. of Supercrit. Fluids*, **76**, pp. 54–60, 2013.
[337] Singh, R., Rowlands, A.S., Miller, S.a., "Effects of relative volume-ratios on dynamic performance of a direct-heated supercritical carbon-dioxide closed Brayton cycle in a solar-thermal power plant," *Energy*, **55**, pp. 1025–1032, 2013.
[338] Persichilli, M., Kacludis, A., Zdankiewicz, E. and Held, T. "Supercritical CO2 Power Cycle Developments and Commercialization: Why sCO2 can Displace Steam," *Ste. Power-Gen India & Central Asia*, 2012.
[339] Ames, R., Driscoll, D. and Narayanan, V., "Design, Fabrication and Characterization of Microchannel Heat Exchangers for Fossil-Fired Supercritical CO2 Cycles," DOE Project FE0024064, NETL, 2016, https://www.netl.doe.gov/research/coal/project-information/proj?k=FE0024064
[340] Neises, T. and Turchi, C., "A comparison of supercritical carbon dioxide power cycle configurations with an emphasis on CSP applications," *Energy Procedia*, **49**, pp. 1187-1196, 2014.
[341] Forsberg, C. W., Peterson, P. F. and Zhao, H., "High-Temperature LiquidFluoride-Salt Closed-Brayton-Cycle Solar Power Towers," "*J. of Solar Energy Eng*. **129**, No. 2, 2007.
[342] Dunham, M.T. and Lipinski, W., "Thermodynamic analyses of single Brayton and combined Brayton-Rankinecycles for distributed solar thermal power generation," *J. of Sol. Energy Eng*., **135**, 2013.

[343] Chacartegui, R., Munoz de Escalona, J.M., Sanchez, D., Monje, B. and Sanchez, T., "Alternative cycles based on carbon dioxide for central receiver solar power plants," *Appl. Therm. Eng.*, **31**, pp. 872-879, 2011.
[344] Johnson, G.A., "Power conversion system evaluation for next generation nuclear plant," Nuclear, Tech., 175, pp. 371-387, 2011.
[345] Sabharwall, P., Kim, E. S., Mckellar, M. and Patterson, M., "Small Modular Molten Salt Reactor (SM-MSR)," *ASME 2011 Small Modular Reactors Symp.*, pp. 31-39, 2011
[346] B-Cubed, "The Brayton Cycle," Accessed Aug. 2016, http://www.learnthermo.com/
[347] Bryant, J. C., Saari, H., and Zanganeh, K., "An analysis and comparison of the simple and recompression supercritical CO2 cycles," *Supercritical CO2 Power Cycle Symposium*, Boulder, CO, 2011.
[348] Kulhanek, M., & Dostal, V., "Supercritical carbon dioxide cycles thermodynamic analysis and comparison," *Supercritical CO2 Power Cycle Symposium*, Boulder, CO, 2011.
[349] Sugarmen, C., Tellez, F., Buck, R., Medina, J. E., Altwegg, P., Ring, A., and Schwarzbözl, P., "SOLGATE: Solar Hybrid Gas Turbine Electric Power System," Final Report, 2002.
[350] Behar, O., Khellaf, A., Mohammedi, K., Ait-Kaci, S., and Beghdadi, F., "Global CSP market trends: the case of solar tower technology," *CIGE 2013*, 2013.
[351] Bhargava, R. and Meher-Homji, C. B., "Parametric analysis of existing gas turbines with inlet evaporative and overspray fogging," *ASME Turbo Expo 2002: Power for Land, Sea, and Air*, pp. 387-401), 2002.
[352] Thombare, D. G. and Verma, S. K., "Technological development in the Stirling cycle engines," *Renewable and Sustainable Energy Reviews*, **12**, No. 1, pp. 1-38, 2008.
[353] Thombare, D. G. and Verma, S. K., "Technological development in the Stirling cycle engines," *Renewable and Sustainable Energy Reviews*, *12*(1), 1-38, 2008.
[354]Urielie, I., "Ideal adiabatic analysis," Ch. 4a, Lecture Notes – Ohio Univ., https://www.ohio.edu/mechanical/stirling/adiabatic/adiabatic.html
[355] Kalina, A.I., "Combined-cycle system with novel bottoming cycle," J. Eng. Gas Turbines Power, 106, pp. 737–42, 1984.
[356] Goswami, D.Y., Vijayaraghavan, S., Lu, S., Tamm, G., "New and emerging developments in solar energy," *SolEnergy*, **76**, pp. 33–43, 2004.
[357] Kribus, A., "A high-efficiency triple cycle for solar power generation," *SolEnergy*, **72**, pp. 1–11, 2002.
[358] Ho, T., Mao, S.S. and Greif, R., "Comparison of the Organic Flash Cycle (OFC) to other Advanced vapor cycles for intermediate and high temperature waste heat reclamation and solar thermal energy," *Energy*, **42**, pp. 213–23, 2012.
[359] Shah, R.K., "Classification of heat exchangers" In Heat Echanger: Thermal-Hydraulic Fundamentals and Design, S., Kakaç, Bergles, A.E. and Mayinger, F., Editors, Hemisphere Publishing, Washington, D.C., pp. 9-46, 1981.
[360] Kakac, S., Liu, H. and Pramuanjaroenkij, A., "Gasketed-plate heat exchangers," Ch. 11, *Heat exchangers: selection, rating, and thermal design*, CRC press, 2012.
[361] Alfa Laval, "Gasketed plate-and-frame heat exchangers," Accessed Aug. 2016, http://www.alfalaval.us/products/heat-transfer/plate-heat-exchangers/Gasketed-plate-and-frame-heat-exchangers/
[362] Vlasogiannis, P., Karagiannis, G., Argyropoulos, P., and Bontozoglou, V., "Air–water two-phase flow and heat transfer in a plate heat exchanger," *Int. J. of Multiphase Flow*, **28**, No. 5, pp. 757-772, 2002.

[363] Zohuri, B., "Application of Compact Heat Exchangers for Combined Cycle Driven Efficiency in Next Generation Nuclear Power Plants: A Novel Approach," Springer, Switzerland, 2015.
[364] Kakac, S., Liu, H. and Pramuanjaroenkij, A., "Gasketed-plate heat exchangers," Ch. 9, *Heat exchangers: selection, rating, and thermal design*, CRC press, 2012.
[365] Shah, R.K. and Sekulic, "Classification of Heat Exchangers," *Fundamentals of Heat Exchanger Design*, Ch. 1, John Wiley & Sons, Hoboken, New Jersey, USA, 2003.
[366] Serna, M., and Jiménez, A., "A compact formulation of the Bell–Delaware method for heat exchanger design and optimization," *Chemical Engineering Research and Design*, **83**, No. 5, pp. 539-550, 2005.
[367] Selbaş, R., Kızılkan, Ö., and Reppich, M., "A new design approach for shell-and-tube heat exchangers using genetic algorithms from economic point of view," *Chemical Engineering and Processing: Process Intensification*, **45**, No. 4, pp. 268-275, 2006.
[368] Hesselgreaves, J. E., "Compact heat exchangers: selection, design and operation," Gulf Professional Publishing, Oxford, UK, 2001.
[369] Li, Q., Flamant, G., Yuan, X., Neveu, P., and Luo, L., "Compact heat exchangers: A review and future applications for a new generation of high temperature solar receivers," *Renewable and Sustainable Energy Reviews*, **15**, No. 9, pp. 4855-4875, 2011.
[370] Bengtson, H., "Features and characteristics of the flat plate heat exchanger," Bright Hub Engineering, Accessed Aug 2016, http://www.brighthubengineering.com/hvac/61791-features-and-characteristics-of-the-flat-plate-heat-exchanger/#imgn_1
[371] Carlson, M. D., Kruizenga, A. K., Schalansky, C., and Fleming, D. F., "Sandia Progress on Advanced Heat Exchangers for S-CO2 Brayton Cycles," *4th Int. Symp. Supercritical CO2*, **2**, pp. 9-10, 2014.
[372] Wang, L., Sunden, B., Manglik, R.M., Plate heat exchangers: design, applications and performance," WIT Press, Southampton, UK, pp. 8-45, 2007.
[373] Lozano A, Barreras F, Fueyo N and Santodomingo S. "The flow in an oil/water plate heat exchanger for the automotive industry," *Appl. Therm. Eng*., **28**, No. 10, pp. 1109–1117, 2008.
[374] Katzel, J., "Heat exchanger basics - A Plant Engineering Exclusive," *Plant Engineering*, 2000.
[375] Durmus A, Benli H, Kurtbas I and Gul H. "Investigation of heat transfer and pressure drop in plate heat exchangers having different surface profiles," Int. J. Heat Mass Trans., 52, pp. 1451–7, 2009.
[376] Vermeulen, T. N. "Knowledge Sharing Report-CO 2 Liquid Logistics Shipping Concept (LLSC)," *Overall Supply Chain Optimization*, Global CCS Institute, 2011 *http://hub.globalccsinstitute.com/publications/co2-liquid-logistics-shipping-concept-llsc-overall-supply-chain-optimization/53-co2*
[377] Thonon B and Breuil E, "Compact heat exchangers technologies for HTRs recuperator application. In: Proceedings of the technical committee meeting on gas turbine power conversion systems for modular HTGRs," IAEA-TECDOC, Palo Alto, CA, USA, pp. 1–11, 2001.
[378] Sherman, S.R., Chen, Y., "Heat exchanger testing requirements and facility needs for the NHI/NGNP project," *WSRC-STI-2008-00152*, STI, 2008.
[379] Zhang, L.W., Balachandar, S., Tafti, D.K. and Najjar, F.M., "Heat transfer enhancement mechanisms in inline and staggered parallel-plate fin heat exchangers," *Int. J. Heat Mass Trans*., **40**, No. 10, pp. 2307–25, 1997.

[380] Jacobi, A.M. and Shah, R.K., "Heat transfer surface enhancements through the use of longitudinal vortices: a review of recent progress," *Exp. Therm. Fluid Sci*., **11** pp. 295–309, 1995.
[381] Valencia, A., Fiebig, M. and Mitra, N.K., "Heat transfer enhancement by longitudinal vortices in a fin-tube heat exchanger element with flat tubes," *J. Heat Trans*., **118**, pp. 209–11, 1996.
[382] Mittal, R. and Balachandar, S., "Effect of three-dimensionality on the lift and drag of nominally two-dimensional cylinders," *Phys. Fluids*, **7**, pp. 1841–65, 1995.
[383] Huang, L.J. and Shah, R.K., "Assessment of calculation methods for efficiency of straight fins of rectangular profiles," *Int. J. Heat Fluid Flow*, **13**, pp. 282–293, 1992.
[384] Focke, W.W., Zachariades, J. and Oliver, I., "The effect of the corrugation inclination angle on the thermo hydraulic performance of plate heat exchangers," *Int. J. Heat Mass Trans*, **28**, No. 8, pp. 1469–79, 1985.
[385] Heatric, http://www.heatric.com/diffusion_bonded_exchangers.html
[386] Urquiza, E., Lee, K., Peterson, P. F., and Greif, R., "Multiscale transient thermal, hydraulic, and mechanical analysis methodology of a printed circuit heat exchanger using an effective porous media approach," *J. of Therm. Sci. & Eng. Apps.*, **5**, No. 4, 2013.
[387] Pieve, M.A., "Calculation method for the optimized thermal-fluid dynamic sizing of heat exchangers," *Heat Trans. Eng*., **29**, No. 6, pp. 556–64, 2008.
[388] Seo, J. W., Kim, Y. H., Kim, D., Choi, Y. D. and Lee, K. J., "Heat transfer and pressure drop characteristics in straight microchannel of printed circuit heat exchangers," *Entropy*, **17**, No. 5, pp. 3438-3457, 2015.
[389] Dewson, S.J., "The development of high efficiency heat exchangers for helium gas cooled reactors," Paper No. 3213, *Int. Conf. Adv.Nuclear Power Plants (ICAP)*, Cordoba, Spain; 2003.
[390] Ravindran, P., Sabharwall, P. and Anderson, N. A., "Modeling a printed circuit heat exchanger with RELAP5-3D for the next generation nuclear plant," Technical report, Idaho National Laboratory, 2010.
[391] Sabharwall, P., "Engineering design elements of a two-phase thermosiphon to transfer NGNP thermal energy to a hydrogen plant," *INL/EXT-09-15383*, 2009.
[392] Li, X., Kininmont, D., Pierres, R.L. and Dewson, S.J., "Alloy 617 for the High Temperature Diffusion- Bonded Compact Heat Exchangers," *ICAPP 2008*, pp. 7, 2008.
[393] Li, X., Le Pierres, R. and Dawson, S., "Heat exchangers for the next generation of nuclear reactors," *ICAPP 2006*, **6**, pp. 4–8, 2006.
[394] Kim, D.E., Kim, M.H., Cha, J.E. and Kim, S.O., "Numerical study for heat transfer and pressure drop of supercritical carbon dioxide fluid with channel bending angle in Printed Circuit Heat Exchanger," Korean Society of Mechanical Engineering, Division of Thermal Engineering; 2008.
[395] Gschwind, P., Regele, A., and Kottke, V. "Sinusoidal wavy channels with Taylor-Goertler vortices," *Experimental thermal and fluid science*, **11**, No. 3, pp. 270-275, 1995.
[396] Sabharwall, P., Gunnerson, F., Tokuhiro A., Utgikar, V., Weaver, K. and Sherman S., "Theoretical design of a thermosyphon for a process heat removal from Next Generation Nuclear Plant (NGNP) for production of hydrogen," *INL/EXT-07-13433*, DOE, 2007.
[397] Mellouli, S., Askri, F., Dhaou, H., Jemni, A. and Ben Nasrallah, S. "A novel design of a heat exchanger for a metal-hydrogen reactor," *Int. J. Hydrogen Energy*, **32**, No. 15, International Symposium on Solar-Hydrogen-Fuel Cells, pp. 3501–3507, 2007.

[398] Picon-Nunez, M., Canizalez-Davalos, L., Martinez-Rodriguez, G. and Polley, G.T., "Shortcut design approach for spiral heat exchangers," *Food Bioproducts Process*, **85**, No. 4, pp. 322–327, 2007.
[399] ASTM Standard C242-01, "Standard Terminology of Ceramic Whitewares and Related Products," ASTM International, West Conshohocken, PA, USA, 2007.
[400] Westabe, J., "Heat transfer international turns manure into power," MLive Media Group, 2009, http://www.mlive.com/business/west-michigan/index.ssf/2009/02/heat_transfer_international_tu.html
[401] Sommers, A., Wang, Q., Han, X., T'Joen, C., Park, Y. and Jacobi, A., "Ceramics and ceramic matrix composites for heat exchangers in advanced thermal systems—a review," *Appl. Therm. Eng.* **30**, pp. 1277–91, 2010.
[402] Lippmann, W., Knorr, J., Wolf, R., Rasper, R., Exner, H., Reinecke, A.-M., "Laser joining of silicon carbide—a new technology for ultra-high temperature resistant joints," *Nucl. Eng. Des.*, **231**, pp. 151–161, 2004.
[403] Snead LL, Katoh Y, Kohyama A, Bailey JL, Vaughn NL, Lowden RA. Evaluation of neutron irradiated near-stoichiometric silicon carbide fiber composites, Journal of Nuclear Materials, Volumes 283–7, Part 1, 9th Int. Conf. on Fusion Reactor Materials, December; 2000. p. 551–5.
[404] Greil, P., Lifka, T., and Kaindl, A., "Biomorphic cellular silicon carbide ceramics from wood: II. Mechanical properties," *J. Eur. Ceram. Soc*., **18**, No. 14, pp.1975–1983, 1998.
[405] Steen M, Ranzani L. Potential of SiC as a heat exchanger material in combined cycle plant. Ceram Int 2000;26(8):849–54.
[406] Amirthan G, Udaya kumar A, Balasubramanian M. Thermal conductivity studies on Si/SiC ceramic composites. Ceram Int 2011;37(1):423–6.
[407] Alm, B., Imke, U., Knitter, R., Schygulla, U., and Zimmermann, S., "Testing and simulation of ceramic micro heat exchangers," *Chem. Eng. J.*, **135**, Supplement 1., pp. S179–S184, 2008.
[408] Islamoglu, Y., "Finite element model for thermal analysis of ceramic heat exchanger tube under axial non-uniform convective heat transfer coefficient," *Mater Des.*, **25**, No. 6, pp. 479–82, 2004.
[409] Schulte-Fischedick, J., Dreißigacker, V., and Tamme, R., "An innovative ceramic high temperature plate-fin heat exchanger for EFCC processes," *App. Therm. Eng.*, **27**, No. 8, pp. 1285-1294, 2007.
[410] Islamoglu, Y., "Numerical analysis of the influence of a circular fin with different profiles on the thermal characteristics in a ceramic tube of heat transfer equipment," *Int. J. Press. Vessels Piping*, **81**, No. 7, pp. 583–587, 2004.
[411] Fend, T., Hoffschmidt, B., Pitz-Paal, R., Reutter, O. and Rietbrock, P., "Porous materials as open volumetric solar receivers: experimental determination of thermophysical and heat transfer properties," *Energy*, **29**, pp. 823–33, 2004.
[412] Fend, T., Pitz-Paal, R., Reutter, O., Bauer, J. and Hoffschmidt, B., "Two novel high porosity materials as volumetric receivers for concentrated solar radiation," *Solar Energy Mater Solar Cells*, **84**, pp. 291–304, 2004.
[413] Subramanian, R.S., "Flow through packed beds and fluidized beds," *Clarkson University*, 2004, *http://web2.clarkson.edu/projects/subramanian/ch301/notes/packfluidbed.pdf*
[414] Szent-Gyorgyi, A., "Diffusion and Reaction," Forler, Editor, Ch. 12, Elements of Chemical Reaction Engineering, Univ. of Michigan, 2008.

[415] Suo, M., "Calculation methods for performance of heat exchangers enhanced with fluidized beds," *Lett. Heat Mass Transfer*, **3**, pp. 555–564, 1976.
[416] Folyan, C.O., Pam, G.Y. and Habib, Y.B., "Fluidized bed combustion: Towards alternative ways of energy recovery in rural Nigeria," *J. Energy Tech. & Policy*, **5**, No. 2, 2015.
[417] Vos, J., "Biomass Energy for Heating and Hot Water Supply in Belarus," *BTG Biomass Technology Group BV, University of Twente*, 2005.
[418] Gadgil P.R., "Survey on Fluidization Techniques and Its Advancements," *MGV's Pharmacy College*, Nashik, 2009.
[419] Johari, A. and Taib, M.R., "Effect of Sand Sizes on the Fluidisation Behaviour in Circular and Rectangular Columns," *J. of Chem. & Nat. Res. Eng.*, **2**, pp. 14-21, 2007.
[420] Jeong, W. S., Lee, J. I., and Jeong, Y. H., "Potential improvements of supercritical recompression CO 2 Brayton cycle by mixing other gases for power conversion system of a SFR," *Nucl. Eng. & Design*, **241**, No. 6, pp. 2128-2137, 2011.
[421] Hexemer, M.J., "Supercritical CO_2 Brayton Recompression Cycle Design and Control Features to Support Startup and Operation," *sCO₂ Power Cycle Symp.*, 2014.
[422] Edwards, M.F., Changal, A.A. and Parrott, D.L., "Heat transfer and pressure drop characteristics of a plate heat exchanger using Newtonian and non-Newtonian liquids," Chem. Eng., pp. 286-293, 1974.
[423] Manglik, R.M., "Plate heat exchangers for process industry applications: enhanced thermal-hydraulic characteristics of chevron plates," *Process Enhanced and Multiphase Heat Transfer*, Manglik, R.M. and Kraus, A.D., Eds., Begel House, New York, USA 1996.
[424] Muley, A. and Manglik, R.M., "Experimental investigation of heat transferenhancement in a PHE with $\beta = 60°$ chevron plates, in *Heat and Mass Transfer*, Tata McGraw-Hill, New Delhi, India, 1995.
[425] Muley, A. and Manglik, R.M., "Enhanced heat transfer characteristics of singlephase flows in a plate heat exchanger with mixed chevron plates," *J. Enhanced Heat Trans.*, **4**, No. 3, 1997.
[426]. Muley, A., Manglik, R.M. and Metwally, H.M., "Enhanced heat transfer characteristicsof viscous liquid flows in a chevron plate heat exchanger," *J. Heat Trans.*, **121**, No. 4, 1999.
[427] Kakaç, S., Shah, R. K., and Aung, W., *Handbook of Single-Phase Convective Heat Transfer*, John Wiley & Sons, New York, 1987.
[428] Fraas, A.P., "Heat exchanger design," John Wiley & Sons, New Your, USA, 1989.
[429] Kern, D.Q., "Process heat transfer," McGraw-Hill, New Yourk, USA, 1950.
[430] Petukhov, B.S., "Heat transfer and friction in turbulent pipe flow with variable physical properties," *Advances in heat transfer*, **6**, pp. 503-564, 1970.
[431] Sieder, E.N. and Tate, G.E., "Heat transfer and pressure drop of liquids in tubes," *Industrial and Engineering Chemistry*, **28**, pp. 1429-1435, 1936.
[432] Lang, C., and B. Lee, "Heat Transfer Fluid Life Time Analysis of Diphenyl Oxide/Biphenyl Grades for Concentrated Solar Power Plants." *Energy Procedia*, **69**, pp. 672-680, 2015.
[433] W.O. Walter, "Heat transfer technique with organic media," In: Heat transfer media, second ed. Graefelfing, Germany: Maria-Eich-Straβe; Ch.2, pp. 4–58, 1997.
[434] Ho, C.K., "Computational fluid dynamics for concentrating solar power systems," *Wiley Interdisciplinary Reviews: Energy and Environment*, **3.3**, pp.290-300, 2014.
[435] Cabeza, L.F., "Lithium in thermal energy storage: A state-of-the-art review," *Renewable and Sustainable Energy Reviews*, **42**, pp. 1106-1112, 2015.

[436] Fernández, Á. G., Gomez, J. C., Galleguillos, H., & Fuentealba, E., "Thermophysical properties and corrosion characterization of low cost lithium containing nitrate salts produced in northern Chile for thermal energy storage," *SOLARPACES 2015,* **1734**, No. 1, AIP Publishing, 2016.
[437] Mohanty, B. P. and Shores, D.A., "Role of Chlorides in Hot Corrosion of a Cast Fe–Cr–Ni Alloy. Part I: Experimental Studies," *Corros. Sci.,* **46**, No.12, pp. 2893–2907, 2004.
[438] Meier, G. H., and Pettit, F. S., 1989, "High-Temperature Corrosion of Alumina-Forming Coatings for Superalloys," *Surf. Coat. Technol.,* **39/40**, pp. 1–17.
[439] Ma, J., Jiang, S. M., Gong, J. and Sun, C., "Behavior and Mechanisms of Alkali-Sulfate-Induced Hot Corrosion on Composite Coatings at 900°C," *Corros. Sci.*, **58**, pp. 251–259, 2012.
[440] Glatzmaier, G. C. and Gomez, J.C., "Determining the Cost Benefit of High-Temperature Coatings for Concentrating Solar Power Thermal Storage Using Probabilistic Cost Analysis," *J. of Solar Energy Eng*., **137**, No. 4, 2015.
[441] Kruizenga, A. M., "Corrosion mechanisms in chloride and carbonate salts," Sandia National Laboratories, Livermore, *CA Report No. SAND2012-7594*, 2012.
[442] Pfleger, N., Bauer, T., Martin, C., Eck, M., and Wörner, A., "Thermal energy storage–overview and specific insight into nitrate salts for sensible and latent heat storage," *Beilstein Journal of Nanotechnology*, **6**, No. 1, pp. 1487-1497, 2015.
[443] Ho, C. K., Christian, J. M., Yellowhair, J., Ortega, J., & Andraka, C., "Fractal-like receiver geometries and features for increased light trapping and thermal efficiency," *SOLARPACES 2015*, **1734**, No. 1, AIP Publishing, 2016.
[444] Ortega, J. D., Khivsara, S. D., Christian, J. M., Yellowhair, J. E. and Ho, C. K., "Coupled Optical-Thermal-Fluid Modeling of a Directly Heated Tubular Solar Receiver for Supercritical CO2 Brayton Cycle," *ASME 2015 9th International Conference on Energy Sustainability*, American Society of Mechanical Engineers, San Diego, CA, USA, 2015.
[445] D. A. Kugath, G. Drenker, and A. A. Koenig, "Design and development of a paraboloidal dish solar collector for intermediate temperature service," *Int. Solar Energy Soc*., 1, pp. 449–453, Atlanta,Ga, USA, 1979.
[446] Nagarajan, P. K., Subramani, J., Suyambazhahan, S., & Sathyamurthy, R., "Nanofluids for solar collector applications: a review," *Energy Procedia*, **61**, pp. 2416-2434, 2014.
[447] Frankel, A., Iaccarino, G., & Mani, A. "Convergence of the Bouguer–Beer law for radiation extinction in particulate media," *J. Quant. Spec. & Radiative Trans*., **182**, pp.45-54, 2016.
[448] Kostinksi, A., "On the extinction of radiation by a homogeneous but spatially correlated random medium," *J. Opt.Soc. Am. A.*, **33**, pp. 18-1929, 2001.
[449] Davis, A., Mineev-Weinstein, M., "Radiation propagation in random media: from positive to negative correlations in high-frequency fluctuations," *J. Quant. Spectrosc. Radiation Trans*., **112**, pp. 632–45, 2011.
[450] Coelho, P., Teerling, O. and Roekaerts, D., "Spectral radiative effects and turbulence/radiation interaction in an on-luminous turbulent jet diffusion flame," Combust Flame, 133, pp. 75–91, 2003.
[451] Wu, Y., Haworth, D., Modest, M., Cuenot, B., "Direct numerical simulation of turbulence/radiation interaction in premixed combustion systems," *Proc. Combustion Inst*., **30**, pp. 639–46, 2005.

[452] Moens, L., and Blake, D. M., "Mechanism of hydrogen formation in solar parabolic trough receivers," *J. Solar Energy Eng.*, **132**, No. 3, 2010.
[453] de Miguel, M. T., Encinas-Sánchez, V., Lasanta, M. I., García-Martín, G. and Pérez, F. J., "Corrosion resistance of HR3C to a carbonate molten salt for energy storage applications in CSP plants," *Solar Energy Materials and Solar Cells*, **157**, pp. 966-972, 2016.
[454] Ren, N., Wu, Y., Wang, T. and Ma, C. "Experimental study on optimized composition of mixed carbonate for phase change thermal storage in solar thermal power plant," *J. Therm. Anal. Calorim.*, **104**, pp. 1201–1208, 2011.
[455] Olivares, R. Chen, C. and Wright, S., "The thermal stability of molten lithium-sodium-potassium carbonate and the influence of additives on the melting point, *J. Sol.Energy Eng*., **134**, 2012.
[456] Flores, E., "A review of latent heat thermal energy storage for concentrated solar plants on the grid," *J. Undergraduate Research*, **5**, No. 1, 2015.
[457] Stekli, J., Irwin, L. and Pitchumani, R., "Technical challenges and opportunities for concentrating solar power with thermal energy storage," J. Therm. Sci. & Eng. Apps., **5**, No. 2, 2013.
[458] Bonan, G., "Ecological climatology," Cambridge University Press, Cambridge U.K., 2002.

10. APPENDIX

Appendix A.1. Plate-fin and tube-fin heat exchanger fin efficiencies for geometries of uniform fin thickness [169].

Geometry	Fin Efficiency Formula
	$m_i = \left[\frac{2h}{k_f \delta_i}\left(1+\frac{\delta_i}{l_f}\right)\right]^{1/2} \quad E_1 = \frac{\tanh(m_i l_1)}{m_i l_1} \quad i = 1, 2$
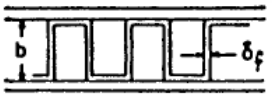 Plain, wavy, or offset strip fin of rectangular cross section	$\eta_f = E_1$ $l_1 = \frac{b}{2} - \delta_1 \quad \delta_1 = \delta_f$
 Triangular fin heated from one side	$\eta_f = \frac{hA_1(T_0 - T_a)\frac{\sinh(m_1 l_1)}{m_1 l_1} + q_e}{\cosh(m_1 l_1)\left[hA_1(T_0 - T_a) + q_e \frac{T_0 - T_a}{T_1 - T_a}\right]}$
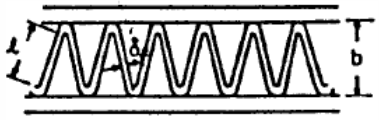 Plain, wavy, or louver fin of triangular cross section	$\eta_f = E_1$ $l_1 = \frac{l}{2} \quad \delta_1 = \delta_f$
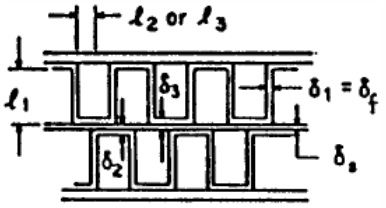 Double sandwich fin	$\eta_f = \frac{E_1 l_1 + E_2 l_2}{l_1 + l_2} \frac{1}{1 + m_1^2 E_1 E_2 l_1 l_2}$ $\delta_1 = \delta_f \quad \delta_2 = \delta_3 = \delta_f + \delta_s$ $l_1 = b - \delta_f + \frac{\delta_s}{2} \quad l_2 = l_3 = \frac{p_f}{2}$
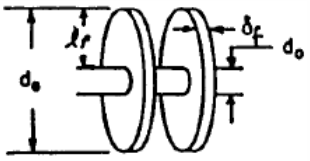 Circular fin	$\eta_j = \begin{cases} \frac{a(ml_e)^{-\delta}}{\Phi} & \text{for } \Phi > 0.6 + 2.257(r^*)^{-0.4455} \\ \frac{\tanh\Phi}{\Phi} & \text{for } \Phi \le 0.6 + 2.257(r^*)^{-0.4455} \end{cases}$ $a = (r^*)^{-0.2346} \quad \Phi = ml_e(r^*)^{\exp(0.13ml_e - 1.3863)}$ $b = \begin{cases} 0.9107 + 0.0893 r^* & \text{for } r^* \le 2 \\ 0.9706 + 0.17125 \ln r^* & \text{for } r^* > 2 \end{cases}$ $m = \left(\frac{2h}{k_f \delta_f}\right)^{1/2} \quad l_e = l_j + \frac{\delta_f}{2} \quad r^* = \frac{d_e}{d_o}$
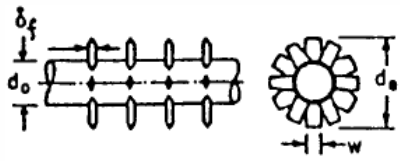 Studded fin	$\eta_j = \frac{\tanh(ml_e)}{ml_e}$ $m = \left[\frac{2h}{k_f \delta_f}\left(1+\frac{\delta_f}{w}\right)\right]^{1/2} \quad l_e = l_j + \frac{\delta_f}{2} \quad l_f = \frac{(d_e - d_o)}{2}$

DISTRIBUTION

1	MS6123	Kenneth M. Armijo	6123
1	MS6123	Subhash Shinde	6123
1	MS0899	Technical Library	9536 (electronic copy)


Sandia National Laboratories